HARVARD UNIVERSITY
Graduate School of Arts and Sciences



DISSERTATION ACCEPTANCE CERTIFICATE

The undersigned, appointed by the

Department of Physics

have examined a dissertation entitled

Local electronic and optical phenomena in two-dimensional materials

presented by Trond Ikdahl Andersen

candidate for the degree of Doctor of Philosophy and hereby certify that it is worthy of acceptance.

Signature _____

Typed name: Professor Mikhail Lukin, Chair

Signature _____

Typed name: Professor Philip Kim

Signature _____

Typed name: Professor Amir Yacoby

Date: December 6, 2021

Local electronic and optical phenomena in two-dimensional materials

A dissertation presented

by

TROND IKDAHL ANDERSEN

to

The Department of Physics

in partial fulfillment of the requirements

for the degree of

Doctor of Philosophy

in the subject of

Physics

Harvard University

Cambridge, Massachusetts

December 2021

©2022 TROND IKDAHL ANDERSEN
All rights reserved.

Dissertation Advisor: Professor MIKHAIL D. LUKIN TROND IKDAHL ANDERSEN

Local electronic and optical phenomena in two-dimensional materials

Abstract

Two-dimensional (2D) materials, consisting of a single layer of atoms, have proven to be a tremendously valuable platform for studying novel physical phenomena. Besides representing the ultimate thickness limit, these materials exhibit new optical, electronic, and mechanical properties often not present in the bulk, rendering them exciting candidate systems for a wide variety of technological applications, ranging all the way from DNA sequencing to solar cells. A major challenge in fully understanding the physical behavior of two-dimensional materials and realizing their technological potential, is that many of the phenomena occur locally and on length scales that are too small to be interrogated with conventional techniques. In this thesis, I present studies of such phenomena in two different 2D materials systems, namely graphene and transition metal dichalcogenides (TMDs), using novel techniques to understand their local behavior. Specifically, we first employ spin defects in diamond as nanoscale noise sensors to locally probe current fluctuations in biased, ultraclean graphene devices. At high electronic drift velocities, we observe a dramatic increase in GHz current noise that grows exponentially across the device. We attribute our observations to an electron-phonon instability driven by Cherenkov amplification of acoustic phonons, which arises when the electronic drift velocity exceeds the speed of sound. Next, we study the optical properties of excitons in twisted TMDs and introduce a new technique for

imaging the emergent nanoscale moiré patterns in these devices. By correlating the optical response of the excitons with the local moiré structure, we observe signatures of an exciton array containing two spatially alternating exciton species that can be tuned independently through electrostatic gating. We also study the chiral exciton response in the same system, and demonstrate that twisted TMDs is a promising platform for valleytronic devices. Our work provides new important insights into the local electronic and excitonic behaviors of graphene and TMDs respectively, and demonstrates the immense value of local investigations in 2D materials.

Contents

List of figures ..... **ix**
Acknowledgments ..... **xxii**
Citations to previously published works ..... **xxv**
1 INTRODUCTION **1**
1.1 Background 2
1.1.1 Two-dimensional materials 2
1.1.2 Understanding two-dimensional materials on a local level 3
1.2 Overview 4
2 LOCAL PROBING OF ELECTRON-PHONON INSTABILITY IN GRAPHENE **6**
2.1 Graphene 7
2.1.1 Graphene band structure 7
2.1.2 Doping and low-bias excitation in graphene 9
2.2 Current noise 11
2.2.1 Thermal noise 11
2.2.2 Shot noise 13
2.2.3 $1/f$ (flicker) noise 13
2.3 Nitrogen vacancy (NV) centers in diamond 14
2.3.1 NV basics 14
2.3.2 NV centers as nanoscale noise magnetometers 16
2.3.3 Noise measurement pulse sequence 18
2.4 Electron-phonon instability in graphene revealed by global and local noise probes 20
2.5 Theory of Cherenkov instability 31
2.5.1 Coupled electron-phonon dynamics 31
2.5.2 Phonon emission rate 34
2.5.3 Phonon decay rate 37
2.5.4 AC conductivity in Cherenkov instability 39
2.5.5 Connection between global noise and phonon fluctuations 44
2.5.6 Dependence of global noise on charge density 45
2.5.7 Local noise 48
2.5.8 Alternative mechanisms 50

2.5.8.1 Optical phonon scattering 51
2.5.8.2 Plasmonic effects 51
2.5.8.3 Hydrodynamic instabilities 52
3 VALLEYTRONICS IN TWISTED TRANSITION METAL DICHALCOGENIDES 54
3.1 Transition metal dichalcogenides (TMDs) 55
3.2 Band structure and the valley degree of freedom 55
3.3 Gate control of excitons 58
3.4 Valleys for information storage: promises and challenges 59
3.5 Electrically tunable valley dynamics in twisted WSe_2/WSe_2 bilayers 61
4 CORRELATION OF MOIRÉ STRUCTURE AND EXCITON PROPERTIES IN TWISTED TMDS 73
4.1 Moiré patterns 74
4.2 Imaging moiré patterns – an important challenge 75
4.3 Interlayer excitons in small-angle twisted homobilayer $MoSe_2$ 76
4.4 Correlated moiré imaging and exciton spectroscopy in twisted bilayer WSe_2 78
4.4.1 Channeling modulated secondary electron imaging technique 81
4.4.2 Correlating reconstructed moiré patterns with optical measurements 86
4.4.3 Properties of the reconstructed superlattice 91
4.4.4 Outlook 94
4.5 Extended discussion of exciton properties in the small-domain limit 96
4.5.1 Enhanced exciton diffusion to lower energy states 96
4.5.2 Reduced lattice reconstruction 97
4.5.3 Exciton delocalization 100
Appendix A: ADDITIONAL DETAILS FOR GRAPHENE NOISE EXPERIMENT 103
A1 Device fabrication 104
A1.1 Devices on diamond substrate 104
A1.2 Devices on Si/SiO_2 substrate 105
A2 NV measurement setup 106
A3 High-frequency measurements 108
A3.1 AC conductivity calibration 109
A3.2 Noise calibration 113
A4 Additional noise and conductivity measurements 116
A4.1 Noise power vs. drift velocity 116

A4.2 Disordered device noise 117
A4.3 Length dependence in global noise measurements 119
A4.4 Global noise independent of carrier flow direction 120
A4.5 Independence of conductivity time scales on charge density and temperature 121
A5 Additional NV measurements 122
A5.1 Local noise spectroscopy 122
A5.2 NV measurement of lattice temperature 123
A5.3 Local doping dependence 124
A5.4 NV center orientation 125
A5.5 DC measurements of local current distribution 127
A6 Device overview 128
Appendix B: ADDITIONAL DETAILS FOR TWISTED TMD VALLEYTRONICS EXPERIMENT 129
B1 Materials and methods 130
B2 Exciton characterization based on DC Stark shift 130
B3 Spatial map of DOCP in a sample containing natural and twisted bilayer regions 131
B4 Fitting of lifetime data 132
B5 Intra- and interlayer K-Q excitons 133
B6 Data from additional devices 136
Appendix C: ADDITIONAL DETAILS FOR MOIRÉ IMAGING EXPERIMENT 139
C1 Polar angle dependence of imaging contrast 140
C2 Modelling of SEM signal 141
C3 Distinguishing multilayer polytypes 143
C4 Representative Raman spectra in multilayer graphene 144
C5 Dependence of SEM signal on acceleration voltage and hBN thickness 145
C6 Background compensation of SEM data 147
C7 Additional SEM data 148
C7.1 Monolayer TMD signal 148
C7.2 Imaging of monolayer on bulk TMD 149
C7.3 Imaging of stepped graphene and TMD flakes 151
C7.4 Applications to CVD-grown materials 152
C8 Parameters used for SEM imaging 154
C9 Procedure for co-alignment of SEM imaging and optical measurements 154

C10 Comparison of PL and absorption spectroscopy 155
C11 Extracting energy splitting between the exciton species 156
C12 PL measurements of additional devices 158
C13 Prevention of interlayer contamination 160
C14 Linear vs circular polarization measurements 162
C15 Doping dependence of additional small-angle devices 163
C16 DOLP measurements of additional small-angle device 164
C17 Density functional theory 165
References 166

List of figures

Figure 2.1: Graphene band structure. (A) First Brillouin zone of graphene, showing the location of the K and K' points. (B) Band structure calculated from the tight-binding model. The valence and conduction bands touch at the K and K' points (example shown by red circle). Near these points, graphene exhibits a linear dispersion relation. 8

Figure 2.2: NV center energy levels and transitions. The ground states are triplet states with a zero-field splitting of $hD = h \cdot 2.87$ GHz between the $m_s = 0$ and $m_s = \pm 1$ levels. A magnetic field B along the NV axis further splits the $m_s = \pm 1$ levels by $2\mu_B g B$. Green and red arrows indicate transitions via optical excitation and emission, respectively. The excited $m_s = \pm 1$ states readily become shelved into the dark, long-lived singlet state, from which they predominantly decay to the $m_s = 0$ state. 15

Figure 2.3: Spin-to-charge readout. (A) Pulse sequence for measuring relaxation rate of NV centers. A 532 nm pulse preferentially prepares the NV center in the NV− charge state and $m_s = 0$ spin state. The NV center spin is allowed to relax for a time τ before a strong yellow pulse shelves the $m_s = \pm 1$ population in the singlet state. An intense pulse of 637 nm light ionizes any population in the triplet state, while the singlet is protected. The resulting charge state is read out by resonant excitation of the NV− zero phonon line, and from this, the spin state before the yellow pulse is inferred. (B) Photon distribution from NV is fit as a 70%-30% mix of two Poisson distributions with different parameters, λ, corresponding to counts from NV− and NV0. (C) Post-selected photon distributions. The photon distributions for the two charge states are distinguishable, permitting single-shot charge state readout. 19

Figure 2.4: Nonequilibrium dynamics in graphene, probed both globally and locally. (A) Device schematic: hBN-encapsulated graphene device on diamond substrate containing NV centers for nanomagnetometry. (Inset) Optical image of clean hBN-encapsulated device A1 (6 μm by 5.4 μm). (B) Condition for Cherenkov emission of phonons: when $v_D > v_s$, stimulated phonon (ph) emission dominates over absorption (right). (C) Two-probe resistance versus carrier density of device A1 (T = 10 K). (D) Current density as a function of applied electric field (T = 80 K) in clean device A1 (blue) and disordered device B1 (7 μm by 18 μm, black). The gray dashed line indicates where $v_D = v_s$ for the longitudinal acoustic mode. (E) Global electronic noise PSD (averaged over 100 to 300 MHz) as a function of bias power in devices A1 (blue) and B1 (black). Blue curve satisfies $v_D > v_s$ for $P > 0.12$ mW/μm^2. (F) Local magnetic noise (measured by NV nanomagnetometry) versus applied bias power in clean device C1 on diamond substrate. Error bars represent 95% confidence intervals. 22

Figure 2.5: Spatially resolved local noise measurements with NV magnetometry. (A) Fluorescence image of NV centers underneath device C2, with false-colored contacts and borders added. (B) NV spin relaxation from polarized to thermal state (dashed line), when current densities j = 0 mA/μm (dark blue) and j = -0.19 mA/μm (light blue) are passed through the device. Solid lines are fits. m_s, spin quantum number. (C) Local magnetic noise near drain contact as a function of graphene current density (device C1) in electron (e)– and hole (h)–doped regime (blue and red, respectively). (D) Spatial map of the local magnetic noise (device C2) at j = 0.19 mA/μm and n =

$0.92 \cdot 10^{12}$ cm^{-2}. The spatial profile is consistent with the exponential growth of phonons due to Cherenkov amplification (cartoon, top). Dashed black curve shows the theoretically predicted excess phonon population (offset to account for background noise). a.u., arbitrary units. (E) The growth direction is reversed by changing the current direction (left) or the charge carrier sign (right). Error bars represent 95% confidence intervals. 24

Figure 2.6: Slow dynamics in global electronic measurements. (A) Global noise spectra at $n = 2 \cdot 10^{12}$ cm^{-2}. Colored curves: clean device A2 (9.5 μm by 11 μm) at bias ranging from 0 to 0.8 V (bottom to top). Black curve: disordered device B1 at maximum power applied to device A2 (scaled 7x). (B) AC differential conductivity spectra (excitation: −20 dBm) (see Appendix A3.1 for calibration technique) with biases 0 to 0.8 V (top to bottom, colors same as in (A)). The real (Re) component is suppressed at low frequencies. Gray curve: imaginary (Im) component at 0.8 V. Black curves are fits. (C and D) Features in noise and conductivity spectra shift to higher frequencies in a shorter (6 μm) device (device A1) under similar electric field as maximum in (A) and (B). (E and F) Extracted traversal time from (B) and (D) as a function of drift velocity and device length. Dashed curves correspond to speed of sound in graphene (light gray, transverse acoustic (TA); dark gray, longitudinal acoustic (LA)). (G) Cartoon of important rates in the driven electron-phonon system. During Cherenkov amplification, the correlation time observed in electronic measurements is limited by the phonon traversal time, $t_T = L/v_s$. 26

Figure 2.7: Dependence on bath temperature and charge density. (A) Global noise PSD as a function of bath temperature at constant drift velocities and $n = 2 \cdot 10^{12}$ cm^{-2}. (B) Calculated peak phonon emission frequency, which can be tuned via the graphene carrier density (blue: $T_e = 0$ K; red: $T_e = 320$ K). (C) Normalized global current noise as a function of carrier density for different device lengths ($j = 0.6$ mA/μm). Solid curves show predicted total phonon emission. (D) The charge density at which the noise peaks (n_{peak}) for a wider variety of samples than in (C), with fit (blue). Error bars represent sampling spacing of carrier densities..... 30

Figure 2.8: Spatial dependence. Normalized local emission rate of most amplified mode ($\Delta\gamma_{\boldsymbol{q}} n_{\boldsymbol{q}}(x) \propto n_{\boldsymbol{q}}(x)$, purple), and integrated over phonon modes (yellow), for the parameters used in Figure 2.5D (j=0.18 mA/μm, $n = 2 \cdot 10^{12}$ cm^{-2}, $\max(\Gamma^{amp}) = 10.9$ GHz). Due to the dominance of the most amplified modes, the two curves are very similar. The purple curve has a slightly sharper upturn due to the higher amplification rate. 34

Figure 2.9: Onset of Cherenkov emission. (A) Cartoon showing Cherenkov criterion for graphene. When $v_D > v_s$, the electronic population becomes inverted with respect to phonon-induced transitions. As a result, the phonon emission rate (red arrow) becomes greater than the absorption rate (yellow arrow). (B) Net emission rate $\Delta\gamma_{\boldsymbol{q}}$ vs. phonon wavevector $\boldsymbol{q}$ at various electronic drift velocities in the x-direction, $n = 2 \cdot 10^{12}$ cm^{-2} and zero electronic temperature. Once the drift velocity exceeds the speed of sound ($v_s = 21$ km s$^{-1} = 0.021 v_F$), we find regions of phononic phase space where $\Delta\gamma_{\boldsymbol{q}} > 0$ (red), indicating that stimulated emission dominates over absorption. This effect is strongest for the phonon modes moving along the current. The circle sector in which the amplification criterion is satisfied becomes wider as the drift velocity increases, and eventually saturates as a semi-circle. (C) Line cut along $q_y = 0$ for electronic temperatures $T_e = 0$ K and 350 K at $v_D = 5v_s$. 36

Figure 2.10: Phonon decay rate. Phonon decay rate (calculated from eqns. (2.32) and (2.33)) versus phonon wavevector q and energy $v_s q$. 39

Figure 2.11: Including angular spread of phonon emission. Blue: Measured AC differential conductivity spectrum at 0.8 V bias and $n = 2 \cdot 10^{12}$ cm^{-2} (identical data shifted to show multiple fits). Black curves: Fits by averaging the phonon emission angle up to varying θ_{max}. We find best agreement at $\theta_{max} = 60°$..... 44

Figure 2.12: Non-monotonic charge density dependence of phonon amplification. (A) The net emission rate Δn_q at constant current density $j = 0.6$ mA/μm, for various k_F (k_0=165 meV/$\hbar v_F$). The corresponding charge densities are $n = 2.1$, 4.5 and $8.0 \cdot 10^{12}$ cm^{-2}, including the effect of the non-zero v_D on n. Δn_q becomes zero near $2k_F$. (B) The integrand of eqn. (2.52), which is expected to be strongly related to the measured noise. The blue curve has the biggest area and thus corresponds to the highest expected noise, for device length $L = 2.5$ μm. (C) Same as (B), but for $L = 7$ μm. The longer device allows for more filtering, causing the noise to be maximized at a lower k_F (red curve). 48

Figure 3.1: Optical selection rules of TMDs. (a) Band edges at the K' and K points. Circularly polarized excitation with σ_- (σ_+) only couples to the K' (K) valley. (b) Spin-orbit coupling causes splitting of the bands (spin-up and spin-down indicated in cyan and magenta, respectively), giving rise to two spin-conserving transitions, A and B. While the lowest energy transition is spin-conserving in $MoSe_2$, it is not in WSe_2, causing stronger photoluminescence from the former.. 57

Figure 3.2: Gate-tunable exciton reflection in $MoSe_2$. The application of a gate voltage V_g allows for tuning the TMD out of the intrinsic (i) regime, into the p- and n-doped regimes. In the doped regimes, the intrinsic exciton resonance blue-shifts due to Pauli blocking and repulsive polaron formation, and a new red-shifted resonance appears due to attractive polarons. 58

Figure 3.3: Band engineering through twisting. (a) Side view and Brillouin zone alignment of natural (2H-stacked, top) and twisted homobilayer (bottom). The K and K' points are aligned in natural bilayers, but not in twisted structures. (b) Device schematic (top), illustration of a moiré pattern in a twisted WSe_2/WSe_2 bilayer (bottom left) and optical image of a device (bottom right). (c) Polarization-resolved PL spectra from bilayers with varying twist angle. All spectra are collected in the intrinsic regime. Solid (dashed) lines represent co- (cross-) polarized emission. X_0 and X_I indicate intra- and interlayer excitons, respectively. (d) Degree of circular polarization calculated from PL spectra in (c). While the natural bilayer (red) exhibits almost zero interlayer DOCP, the twisted devices show DOCP as high as 60%. 63

Figure 3.4: Gate tunability of DOCP. (a) Out-of-plane electric field dependence of intra- and interlayer exciton PL from the 17°-twisted bilayer. While the intralayer excitons (X_0) do not shift with electric field, the interlayer excitons (X_I) exhibit a Stark shift equivalent to an electron-hole separation of 0.37 nm. Opposite voltages are applied to the two gates (the hBN flakes have the same thickness) to apply an electric field while keeping the TMD intrinsic. (b) Electric field dependence of DOCP, showing that the DOCP is largely insensitive to electric field. (c) Doping dependence of PL emission for intra- and interlayer excitons. The same voltages are applied to the two gates to dope the sample without applying an electric field. (d) Doping dependence of DOCP,

showing switching from large (>80%) values in the *n*-doped regime, to almost zero (<5%) in the *p*-doped regime. 66

Figure 3.5: Exciton and valley dynamics in twisted WSe_2. (a) Time-resolved measurements of co- and cross-polarized photoluminescence (dark and light green markers, respectively) from the 17° twisted bilayer in the intrinsic regime. Black dotted lines are bi-exponential fits convolved with the instrument response (Appendix B4). The extracted slow and fast time scales are $\tau_1 = 0.1$ ns and $\tau_2 = 0.9$ (1.0) ns for co- (cross-) polarized emission. (b) and (c) Same as in (a), but at V_G=-8 V and V_G=8 V. Black dashed lines are fits based on the coupled linear model (Appendix B4). The extracted exciton and valley lifetimes are $\tau_1 = 0.1$ ns and $\tau_v = 30$ ps at $V_G = -8$ V, and $\tau_1 = 40$ ps and $\tau_v = 2.2$ ns at $V_G = 8$ V. (d) Time-resolved DOCP corresponding to measurements in (a)-(c). Black dotted and dashed curves are calculated from fits in (a)-(c). Inset: Zoomed-in version of long tail in intrinsic regime, fitted with the linear coupled model (dashed line). The extracted valley lifetime is $\tau_v = 44$ ns. Lines corresponding to $\tau_v = 5$ ns (light grey) and $\tau_v = 10$ ns (dark grey) are shown for comparison. 68

Figure 3.6: Depolarization mechanisms in natural and twisted WSe_2/WSe_2 bilayers. (a) Depolarization in natural bilayer WSe_2 occurs simply through two spin-flip transitions (curved arrows), causing low DOCP. Magenta (cyan) bands indicate spin up (down) for electrons. The thickness of the dashed lines qualitatively represents the relative dominance of the $\sigma+$ and $\sigma-$ recombination processes. Inset: Brillouin zone showing location of the degenerate K and Q points of a natural bilayer as a whole. (b) Depolarization in twisted bilayer WSe_2 requires both a phonon-induced momentum kick (straight arrows) and a spin-flip transition (curved arrows) for both carriers, resulting in high DOCP and long τ_v. (c)-(d) Since positively (negatively) charged excitons already have holes (electrons) at both the K and K' (Q and Q') points, only the electron (hole) must flip spin and shift in *k*-space. 70

Figure 4.1: Optically resolvable moiré domains with broken mirror symmetry in twisted $MoSe_2/MoSe_2$. **a**, TEM image of twisted $MoSe_2/MoSe_2$, showing large reconstructed AB- and BA-domains. **b**,**c**, Electric field dependence of photoluminescence from interlayer excitons in two different spots. Opposite Stark shifts in the two spots are explained by (opposite) preferential dipole moments in AB and BA domains. **d,** Same as **b** and **c**, but in location where both exciton species are observed. **e**, Mapping of $\eta = ((PL(+)-PL(-))/(PL(+)+PL(-))$ (see definition in text), demonstrating confocal imaging of the moiré domains. 77

Figure 4.2: SEM based imaging of stacking order in vdW heterostructures. a, Schematic of operating principle: an accelerated electron beam is focused onto the device at an azimuthal (polar) angle, ϕ (θ). Channeling of the incident electrons and subsequent secondary electron generation depend on the local stacking order. **b,c,** Optical (**b**) and SEM (**c**) images of a natural bilayer graphene flake ($\theta = 24°, \phi = 5°$). SEM reveals areas of different contrast. **d**, Dependence of SEM signal on ϕ in boxed locations in **c** (normalized to the mean). The two regions display 120° symmetry and 180° phase offset, consistent with AB and BA domains (inset schematics). The contrast decays due to gradual charging of the substrate. **e-g**, Same as **b-d**, in a few (~ 6) layer graphene flake. The more complex ϕ-dependence is consistent with our model of ABC and ABA stacking (dashed line, Appendix C2): while ABC stacking exhibits fully open channels every 120°, ABA stacking shows only partially open channels every 60°. **h**,

Difference between two SEM images with a 60° offset in azimuthal angle. **i,** Spatial map of Raman 2D-peak position, confirming the ABC/ABA stacking order. 81

Figure 4.3: Moiré superlattices in twisted homobilayers. a, Optical image of hBN-encapsulated twisted WSe_2 bilayer (device D1). Dashed white and teal lines indicate top and bottom TMD layer, respectively. **b**, SEM image of device D1, showing a reconstructed moiré pattern with triangular AB and BA (3R) stacking domains. ($\theta = 40°$). **c**, ϕ-dependence of signal from AB and BA domains (solid red and blue curves), along with model predictions (dashed curves). **d,** Top: Top view schematic of moiré pattern (5° twist angle) with and without reconstruction (right and left). Reconstruction was illustrated by reducing the local twist angle near AB and BA sites. Bottom: Side view of AB, AA and BA stacking orders. Purple: W, yellow: Se. 84

Figure 4.4: Correlating local superlattice structure and optical properties. a, Left: SEM image ($\theta = 40°$) of device D2, displaying reconstructed moiré pattern. λ_m increases from <10 nm to 60 nm from left to right. The moiré pattern is not visible left of the vertical dashed line. Dashed circle indicates optical beam spot size, crosses indicate beam spot centers. Right: Zoom-in of area indicated by dotted lines. **b**,**c**, Gate-dependent PL spectra collected from locations with $\lambda_m < 10$ nm (**b**) and $\lambda_m = 25 \pm 10$ nm (**c**), indicated by boxed crosses in **a**. While the left region only exhibits one intralayer peak in the *p*-doped regime, the right (larger λm) region exhibits two peaks. **d**, Raw PL spectra collected from the locations marked with crosses in **a**, at $V_G = -5$ V. The spectra are offset for clarity and the intensity is multiplied by 10 below 1.58 eV. The higher energy (type II) exciton peak emerges with increasing λ_m, and the interlayer exciton emission is blue-shifted for $\lambda_m < 10$ nm. 87

Figure 4.5: SEM correlation of PL peak splitting. a, Zoomed-out SEM image of D1 showing large (70-670 nm) reconstructed moiré domains in the entire twisted bilayer region. ($\theta = 40°$). **b,** Map of extracted exciton peak splitting overlaid with the SEM image from **a**. Inset: Example PL spectrum (blue) with double Lorentzian fit. **c**, Correlation of SEM and PL shows that the peak splitting is independent of domain size over a 30-fold range. Red: device D1, blue: device D2. 89

Figure 4.6: Valley coherence of the two exciton species. a, Gate-dependent PL spectra from device D1. Green dashed lines show fitted peak positions (Appendix C11). Inset: SEM image of measured spot ($\theta = 40°$). Scale bar: 200 nm. **b**, Gate-dependent DOLP, showing that type I excitons have nearly zero DOLP in the *p*-doped regime. **c**,**d**, Co- and cross-polarized PL (blue solid and dashed curves), and corresponding DOLP (orange) at $V_G = -3$ V (**c**) and $V_G = 2$ V (**d**). 90

Figure 4.7: Periodic exciton and doping landscape in reconstructed superlattice. a, Side view of AB and BA domains. Maroon and orange boxes indicate type I and II locations, respectively. **b**, Band structure schematic and wavefunction distribution at important points in *k*-space. **c**-**f**, Schematic of alternating properties in the two-dimensional triangular exciton array. For clarity, only excitons in the top layer are shown. **c**, Excitons have higher energies in type II locations due to larger optical band gap. **d**, Type I excitons are preferentially *p*-doped due to higher VBM. **e**, Only the type I exciton is observed in the small-domain regime due to relaxation of the higher energy exciton. **f**, The two alternating exciton species also have different valley coherence properties. **g**-**i**, Schematics of K/K' exciton recombination. Black horizontal lines indicate top and bottom layer. **g**, Since the resident hole must be in the opposite valley of the type I exciton, it

becomes correlated with the photon and breaks coherence. **h**, For the type II exciton, the resident hole is in a different layer and carries no information about the exciton valley, allowing for non-zero DOLP. **i**, DOLP is non-zero for both exciton types in the *n*-doped regime, because the electron is in a different valley (Q/Q') than the exciton (K/K'). 92

Figure 4.8: Effects of reconstruction. a, Lattice displacement profile for λ_m = 60 nm (twist angle 0.3°), showing that the lattice rotates locally to approach 3R-stacking. **b**-**k**, Calculated potential (**b-h**) and interlayer tunneling rate (**g-k**) at the valence band K-point for λ_m = 60 nm (**b,g**), 20 nm (**c,h**), 8 nm (**d,i**) and 4 nm (**e,f,j,k**). **b**-**e** and **g**-**j** are modeled based on the stacking fault energy, while **f** and **k** are fully non-reconstructed for reference. Weaker reconstruction effects are observed for smaller λ_m (larger twist angle), causing a smoother moiré potential and more interlayer tunneling. 99

Figure A.1: Device fabrication on diamond substrate. (A) Device schematic: Monolayer graphene (grey chain) was graphite contacted and encapsulated with hexagonal boron nitride (hBN). Few-layer graphene (FLG) was used as topgate. (B-H) Micrographs of device fabrication, with 40 μm scalebar in (B)-(G) and 500 μm in (H). (B) Exfoliated graphene. White dashed line indicates monolayer region. (C) Complete stack on diamond substrate with shallow implanted (40 − 60 nm deep) NV centers. (D) Initial contacts and wire for delivering reference noise (left-most electrode). (E) Device after etch to define geometry. (F) Edge contacts constructed through etching and subsequent thermal evaporation. (G) Device with etch mask for disconnecting topgate from edge contacts. Note that ripples visible in the image are entirely contained in the top gate graphene and are not expected to affect the transport properties of the channel graphene, due to the thick (∼ 90 nm) hBN dielectric. (H) Entire (2 × 2 mm^2) single crystal diamond, with wire bonded device. 105

Figure A.2: Device fabrication on Si/SiO_2 substrate. (A) Device schematic: Monolayer graphene (grey chain) was encapsulated with hexagonal boron nitride (hBN). Silicon substrate was used as a global backgate. (B)-(F) Micrographs of device fabrication, with 20 μm scalebar. (B) Exfoliated graphene. (C) Complete stack on substrate. (D) Initial contacts. (E) Edge contacts constructed through etching and subsequent thermal evaporation. (F) Device after geometry-defining etch..... 106

Figure A.3: NV measurement setup. The three laser beams used for spin-to-charge readout are combined before the galvonometric mirrors located at one focal point of a 4f system. Lasers are switched by acousto-optic modulators, except for the 637 nm high-powered ionization laser, which is a directly driven diode laser. The objective and sample are located inside a Janis ST-500 cryostat, which is used to keep the sample at ∼70 K by a combination of flowing liquid helium and a resistive heater in a PID loop. 107

Figure A.4: High frequency transport setup. Circuit diagram for the measurement of noise (red box) and AC differential conductivity (yellow box)..... 109

Figure A.5: Circuit diagram of wire bonded device. Wire bonds and bonding pads give rise to parasitic reactance. 110

Figure A.6: Changes in reflection during biasing. (A) Reflection spectrum in the biased (blue) and unbiased (orange) case. (B) Relative difference in reflection. The gate is used to keep the DC conductance equal (3.1 mS) in the two cases, and as expected, the DC reflection is approximately equal. At higher frequencies, however, the reflection coefficients differ significantly, indicating that the conductance varies with frequency. 111

Figure A.7: AC conductivity calibration. (A-B) Real (blue) and imaginary (orange) parts of the reflection coefficient at $\omega = 2\pi \cdot 0.2$ GHz (A) and $2\pi \cdot 1.2$ GHz (B), as a function of the conductance (swept through electrostatic gating at zero bias). Using L = 11 nH and C = 0.24 pF, we extract $r_{ext}(0.2\ \text{GHz}) = -0.011 + 0.085i$, $t_{ext}^2\,(0.2\ \text{GHz}) = 0.66 + 0.29i$, $r_{ext}(1.2\ \text{GHz}) = 0.041 - 0.048i$, and $t_{ext}^2(1.2\ \text{GHz}) = -0.43 - 0.17i$. (C) Total fit error (summed over all ω) as a function of parasitic capacitance and inductance. The error is minimized at $L \sim 11$ nH and $C \sim$ 0.24 pF. 112

Figure A.8: Noise calibration. In A-C, blue and orange dots represent data at f = 0.2 GHz and f = 1.2 GHz, respectively. (A) Measured noise S_{rec} vs. differential conductance $Z(G')$, at base temperature T_C = 10 K (bright dots) and an elevated temperature T_H = 50 K (dark dots). The noise is minimized when $Z(G')$ is closest to matching 50 Ω, because at such low temperatures, the noise is dominated by background noise reflected off the sample. As expected, the matching value of G' is above 12 mS (below $\sim 80\ \Omega$) at low frequencies, but shifts to $\sim$ 6 mS ($\sim 150\ \Omega$) at f=1.2 GHz, due to the emerging parasitic reactance. (B) Background noise $S0$ calculated according to eqn. (A.10). (C) Total gain A calculated according to eqn. (A.9). Sub-unity transmission and losses in the cables bring A below the 68 dB amplifier gain. (D-F) Same as (A)-(C), except as a function of frequency, $f = \omega/2\pi$. Purple and yellow curves show measurements at fixed G' = 3 mS. Green curve in (F) accounts for the frequency-dependence of $G'(\omega; j, n)$ for the particular driven case, j = 0.56 mA/μm and $n = 2 \cdot 10^{12}$ cm^{-2}. This is achieved using the technique outlined in the text. 115

Figure A.9: Linear relationship between gain and reflection. Gain $A(\omega, G')$ plotted against the reflection, $|r(\omega, G')|^2$ at $\omega = 2\pi \cdot 0.2$ GHz (blue) and $\omega = 2\pi \cdot 1.2$ GHz (orange). The different points are obtained by sweeping the charge density n (and thus also G') at zero bias. As expected, the two quantities are linearly related. The gain in the biased case $A(\omega, G'(\omega; j, n))$ can now be found by measuring the reflection $|r(\omega, G'(\omega; j, n))|^2$ while applying current, and inserting it into the fit. 116

Figure A.10: Noise versus drift velocity. (A) Measured noise power spectral density (averaged over 0.1-0.3 GHz) as a function of electronic drift velocity in clean device A1, at bath temperatures 10 K and 80 K (blue and red, respectively). We observe equivalent noise temperatures in excess of 15,000 K. (B) Zoomed-in version of (A) to highlight smooth transition into the excess noise regime. Lines are guides to the eye..... 117

Figure A.11: Johnson noise in a disordered device. Measured noise temperature (blue circles) as a function of input power for disordered device B1. The data agrees well with a fit based on disorder-assisted phonon cooling (black curve), and confirms that the dominant noise source is thermal Johnson-Nyquist noise..... 118

Figure A.12: Dependence of noise on device length. (A) Measured noise power spectral density from devices of different lengths, at $v_D = 3.3v_s$ and $n = 2 \cdot 10^{12}$ cm^{-2}. The noise power initially increases superlinearly with device length (inset), but appears to saturate in longer devices. (B) Current noise versus carrier density at constant current density $j = 0.6$ mA/μm (circles) and $j = 0.2$ mA/μm (squares). As shown in Figure 2.7, the cross-over density decreases with device length. 119

Figure A.13: Global electronic transport and noise under current inversion. (A) Absolute value of current density versus absolute applied field at $n = 2 \cdot 10^{12}$ cm^{-2} and $T = 10$ K, for positive (orange) and negative (blue) fields. The $I - V$ curve is observed to be highly symmetric. (B) Global noise power spectral density as a function of (absolute) current density. Changing the sign of the current has almost no effect on the measured noise power. Lines are guides to the eye. 120

Figure A.14: Global conductivity for different charge densities and temperatures. (A) The normalized real part of the conductivity spectrum for $v_D = 0.125v_F$ at different doping levels. The curves are normalized to have the same vertical spread, and are offset to avoid overlap. The general shape of the conductivity spectrum, as well as the extracted time scales (B) are unchanged by varying the charge density. (C) The normalized real part of the conductivity spectrum measured at bath temperatures of 300 K (blue) and 10 K (red), at $v_D = 0.125v_F$ and $n = 2.2 \cdot 10^{12}$ cm^{-2}. We again observe no clear frequency shifts, but the effect is much (~ 4 times) weaker at room temperature than at 10 K. 121

Figure A.15: Noise measured at different applied magnetic fields. Relaxation rates of an NV center at B = 0 (red) and B = 363 Gauss (blue), for positive and negative bias ($|j| = 0.2$ mA/μm) at $n = 0.92 \cdot 10^{12}$ cm^{-2}. 123

Figure A.16: Lattice heating during NV measurements. Scans of the optical line of an NV center located below device C2. The NV center zero phonon line is broadened by approximately the same amount when a high bias is applied (blue) as when the bath temperature is increased by 10 K at zero bias (green), suggesting that the increase in temperature near the NV during device operation is approximately 10 K. $\delta\lambda$ is approximate and is inferred from cavity piezo voltage and laser manufacturer's specifications (New Focus Velocity 6300). Center wavelength corresponds to ~ 637.4 nm 124

Figure A.17: Doping dependence of local magnetic noise. Locally probed magnetic noise as a function of graphene charge density. Light and dark blue points represent positive and negative source-drain current, respectively. The bias power was kept constant at 14 ± 0.1 mW. 125

Figure A.18: NV center orientation. (A) NV center orientation with respect to diamond surface. (B) Projection of the four possible NV axes onto the device plane. Our device is closely aligned along two of the projections, giving rise to two distinctive groupings of NV centers: those with *xy*-projections that are perpendicular to current flow (group I, blue) and those with *xy*-projections parallel to current flow (group II, red). (C) DC field measurements. Group I NVs measure a significant current-induced magnetic field, while group II NVs do not. (D) Relaxation rates of NVs in group I (blue) and II (red). The noise sensed by nearby NVs from different orientation groups is similar, despite measuring very different DC magnetic fields. $|j| = 0.2$ mA/μm, $n = 0.92 \cdot 10^{12}$ cm^{-2}. 126

Figure A.19: DC and AC current measurements. (A) DC current response of two NVs located a similar distance from the source electrode. While one of the NVs shows the expected linear local field dependence on global current (green), the other shows non-linear behavior at high drives (blue). (B) Local noise measurements for same NVs as in (A). Noise measurements taken at $|j|$ = 0.2 mA/μm, $n = 0.92 \cdot 10^{12}$ cm^{-2}. 127

Figure B.1: Spatial map of DOCP. (a) Optical image of an hBN-encapsulated heterostructure that contains both natural (180°, lower right) and twisted (∼0°, upper left) bilayer regions. (b) Spatial dependence of average interlayer exciton DOCP (photon energy below 1.6 eV). Consistent with PL spectra shown in Chapter 3, the twisted bilayer region exhibits much higher DOCP than the natural bilayer region. 132

Figure B.2: Electron (blue, Q-point) and hole (red, K-point) wavefunctions in natural and twisted bilayers (only the bottom layer hole wavefunction is shown for simplicity). (a) In natural bilayers, the wavefunction at the Q-point is completely delocalized between the layers, causing the inter- and intralayer K-Q exciton to be equivalent. The expected electron-hole separation is half the interlayer spacing ($d = d_0/2$). (b)-(c) In twisted bilayers, the hole wavefunction is concentrated near the AB(BA)-stacked sites in the bottom (top) layer. In contrast, the electron wavefunction is concentrated near the AB(BA)-stacked sites in the top (bottom) layer, although more layer delocalized. Thus, the electron-hole wavefunction overlap can be larger for the interlayer exciton (c) than the intralayer exciton (b). 134

Figure B.3: Photoluminescence from additional samples. Colored (grey) curves show PL from bilayer (monolayer) WSe_2, including additional twist angles of 0.5°, 4.5° and 5° not displayed in section 3.5. The devices with 4.5° and 5° twist angles show the same interlayer exciton blue-shift as was presented for the 17° sample in section 3.5. 136

Figure B.4: Electric field dependence of PL in device with 2° twist angle. While the intralayer exciton (∼ 1.7 eV) does not shift observably with electric field, the interlayer excitons (∼ 1.5 − 1.6 eV) exhibit a clear Stark shift (dashed white lines). The corresponding electron-hole separation is 0.36 nm, similar to the value extracted in the 17° device (0.37 nm)..... 137

Figure B.5: Doping dependence of DOCP in device with 2° twist angle. (a) Polarization-resolved photoluminescence spectra from 2°-twisted bilayer WSe_2 at gate voltages V_G = -4 V (left) and V_G=4 V (right). Solid and dashed curves show co- and cross-polarized emission, respectively. (b) DOCP calculated from PL spectra in (a). As in the 17° device presented in in section 3.5, the interlayer DOCP is much higher in the *n*-doped regime than in the *p*-doped regime. (c) Full gate dependence of DOCP. (d) DOCP of the brightest interlayer exciton peak as a function of gate voltage. Since this device exits the intrinsic regime at relatively low gate voltages, plateaus are only observed in the *p*- and *n*-doped regimes. 137

Figure B.6: Exciton lifetime in additional samples. (a)-(b) Time-resolved PL measurements from devices with 0° (a) and 5° (b) twist angles (colored dots). Dotted black lines are biexponential fits convoluted with the system response. The extracted fast and short timescales are τ_1=110 (60) ps and τ_2=2.0 (3.3) ns for the device with 0° (5°) twist angle. 138

Figure C.1: Polar angle variation. a-f, SEM images of few-layer graphene containing ABA- and ABC-stacked regions, at different polar ($\theta = 24°, 33°, 41°$) and azimuthal ($\phi = 0°, 60°$) angles. Schematics show channeling paths for ABA (red) and ABC (blue) stacking order at the different angle combinations. Since $\theta = 24°(41°)$ corresponds to a shift of one (two) carbon-carbon bond lengths per layer, these polar angles enable complete channeling in the ABC region (causing bright SEM signal), but at different azimuthal angles. Less contrast is observed at $\theta = 33°$, since this does not correspond to an integer number of bond lengths. 140

Figure C.2: Computational modeling of SEM imaging. Parallel primary beams (black lines) are positioned at Monte Carlo generated positions within an area corresponding to one unit cell, and their transmission probability through the lattice is calculated using a Lorentzian shaped scattering potential (inset) at each atom site..... 143

Figure C.3: Modelling signal from 5-layer graphene polytypes. Computational model of pure ABABA and ABCAB stacking orders along with the mixed ABABC ordering in graphene, modelled at $\theta = 24°$..... 144

Figure C.4: Representative Raman spectra for ABC stacking **(a)** and ABA stacking (**b**) in four different locations within each domain. 145

Figure C.5: Acceleration voltage and hBN thickness dependence of SEM contrast. a, Optical image of a naturally stepped WSe_2 flake stacked underneath a stepped hBN flake. Inset: AFM of stepped hBN thickness. **b,** SEM images of the sample in **a** at 1.5 keV (left) and 3 keV (right) primary acceleration voltage. Tuning the primary voltage alters the secondary electron energy spectrum, allowing for greater escape depth at higher acceleration voltage. For 1.5 keV, the escape depth is ∼10 nm, restricting collected secondary signal to the hBN. At 3 keV, the depth exceeds 30 nm, revealing the underlying stepped WSe_2 structure. **c,d**, Azimuthal angle dependence of secondary yield from bilayer (**c**) and trilayer (**d**) WSe_2 under varying thickness of hBN. The curves are normalized by dividing by the yield of bare silicon oxide underneath an equal thickness of hBN. **e**, RMS amplitude of the modulation signal for bi- and tri-layer WSe_2 (red and blue squares, respectively) as a function of encapsulating layer thickness. Our data indicate that domain contrast in bilayer TMDs is resolvable even through 27 nm of hBN. 147

Figure C.6: Compensation for channeling effects through top hBN. a,b, Azimuthal dependence of SEM signal from bi-layer TMD under hBN of varying thickness, before (**a**) and after (**b**) compensation for channeling effects in the hBN. We note that **b** is also shown in Fig. C.5. 148

Figure C.7: Imaging of monolayer TMD. a, SEM image of monolayer WSe_2 flakes on SiO_2 substrate, using acceleration voltage of 1 keV and $\theta = 40°$. **b,** Schematic of secondary emission in this system, showing stronger secondary signal from the TMD, due to its higher atomic mass. **c,** Azimuthal dependence of SEM signal from two separate monolayer WSe_2 flakes, indicated by boxes in **a**. Due to the 3D structure of TMDs, amplitude modulation can be observed even from monolayers. 149

Figure C.8: Imaging TMD monolayer on bulk. a, SEM image of a monolayer $MoSe_2$ flake placed on top of a thick $MoSe_2$ flake. **b**, Schematic of secondary generation from both the

monolayer and bulk flake. **c**, Azimuthal dependence of SEM signal from monolayer on bulk (blue) and only the bulk (red), collected from the boxed regions in **a**. The more complex structure of the former is due to the partial channels of the combined system. **d**, Difference between the two curves in **c**. 150

Figure C.9: Imaging of stepped graphite and $MoSe_2$. **a**, SEM image of stepped graphite flake using acceleration voltage of 500 eV and $\theta = 24°$. Alternating contrast is observed as the top two layers change between AB and BA stacking across the steps. **b,** Schematic of secondary generation, highlighting the sensitivity to the stacking order of the top few layers, which enables imaging of AB/BA domains on top of thick low-Z materials such as graphite or hBN. **c,** Azimuthal angle dependence of SEM signal in regions with AB (red) and BA (blue) surface stacking (solid lines). Dashed lines show predictions of model presented in Appendix C2. **d-f**, Same as **a-c**, but in stepped $MoSe_2$ underneath 10 nm Au. The more complex azimuthal dependence (**f**) is due to the 3D nature of the $MoSe_2$ layers, and also because the polar angle used here (30°) does not allow for maximal channeling. 152

Figure C.10: Modelling signal from TMD bilayer stackings. **a**, Schematics of three of the stacking orders that can be found in CVD-grown TMD bilayers (**a**,**c**,**e**), with corresponding computed azimuthal dependence (**b**,**d**,**f**). Computational modelling is performed for WSe_2 at $\theta = 24°$ 153

Figure C.11: Co-alignment of SEM and photoluminescence device images. **a**, SEM image of a twisted TMD device (D2). Dashed blue line indicates the border of features recognizable in both PL and SEM. **b,** Photoluminescence intensity scan showing that the twisted TMD area is darker than the surrounding monolayer TMD section. Once the scan is performed, one can select any spot within the sample to perform optical measurements. **c,** Overlaid PL and SEM images, which allow for correlation of moiré periodicity with optical signal. 155

Figure C.12: Comparison of absorption and photoluminescence spectra. a, Derivative of differential reflectance vs. gate voltage in device D4, showing strong intralayer exciton absorption, consistent with the momentum direct K-K transition. **b**, Corresponding gate-dependent photoluminescence spectra from device D4. 156

Figure C.13: Peak fitting in different doping regimes. a-c, Photoluminescence spectra (light blue lines) from devices D1 (**a-c**), D2 (**d-f**) and D3 (**g-i**) in the p-doped, intrinsic and n-doped regimes. In **a,c,d,i,g**, the spectra are fit with double Lorentzians (black), with contributions from the type I (II) excitons shown in maroon (orange). In **b,e,f,h** the positively charged type I exciton is observed even outside the p-doped regime (dashed maroon), likely due to localized charge defects. We therefore fit with a triple Lorentzian (black). The extracted peak splittings are 36 meV, 16 meV and 10 meV in **a**-**c**, and 36 meV, 16 meV and 9 meV in **d-f**, 35 meV, 16 meV and 10 meV in **g-i**. 157

Figure C.14: Photoluminescence measurements of devices with varying target twist angle in the intrinsic regime. The higher energy (type II) exciton is not observed in large angle devices (**a-c**), appears sporadically in intermediate twist angle devices (**d-f**), and is seen everywhere in small angle devices (**g-i**). 159

Figure C.15: Surface contamination. a, Zoomed-out SEM image of device D2. Red boxes show zoomed-in, contrast-enhanced versions of top surface contamination, and include a 200 nm scale bar. In the reconstructed moiré region (top right), top surface contamination causes variation in moiré contrast. **b**, SEM image of a single hBN flake, showing the same type of surface features. **c,d,** Variation in moiré contrast due to surface contamination is also observed in D1. **e**, Top surface contamination can also be seen with AFM. **f,g,** AFM images of device D1, including height (**f**) and phase (**g**) profiles. Blue dashed lines indicate twisted bilayer region. **h**, AFM height profile of region indicated by white box in **f**. Inset: Histogram of height profile, showing rms roughness of ~300 pm. 161

Figure C.16: Comparison of DOLP and DOCP. a,b, Orange: Line cuts of DOLP (**a**) and DOCP (**b**) at $V_G = -10$ V. Blue: Co- and cross-polarized emission components (solid and dashed curves). 162

Figure C.17: Doping dependent PL measurements of additional devices. a-e, Gate dependent photoluminescence from devices D1, D2, D3, D4 and D6 (left to right). Green lines show the extracted peak positions from double or triple Lorentzian fits. The dashed green line in **b** indicates that the charged type I exciton emission persists into the intrinsic regime, likely due to localized charge defects. The width of the intrinsic regime varies due to differences in contact quality and hBN thickness. **f-j**, Peak splitting calculated from green lines in **a-e**. Dashed horizontal lines highlight that the splitting is very similar across all five devices. 163

Figure C.18: DOLP measurements in device D3. a, Gate-dependent PL spectra from device D3. **b**, Corresponding DOLP, showing the same behavior as device D1 presented in Figure 4.6. **c**,**d**, Photoluminescence (blue) and corresponding DOLP (orange) at $V_G = -10$ V (**c**) and $V_G = 7$ V (**d**)..... 164

Figure C.19: Density functional theory calculations of AB (3R) stacked WSe_2 bilayers. a, Calculated band structure for 3R-stacked WSe_2 bilayers, with indicated Γ, K, and Q points. **b,** Top: electron density plots of the same-spin K-point valence and conduction bands, showing that the wavefunctions are localized in different layers and around the tungsten atoms. Below: calculated energy differences from the plot in **a**. **c,** Top: electron density plots of the conduction band minima at the Q point showing that the wavefunctions are more delocalized between the two layers than at the K point. Bottom: calculated dipole moments indicate that the wavefunctions at the Q points are still slightly preferentially localized in one of the two layers. 165

To Nicole.

Acknowledgments

The past six years in the Lukin group at Harvard University have been terrific. It has been very exciting to get to study novel physical phenomena in such an intellectually stimulating environment full of driven, intelligent colleagues and state-of-the-art facilities. It is truly amazing to be in a place where one can think of a new idea during the bike ride to campus in the morning, and be able to discuss the idea with world experts on the topic, locate the necessary measurement equipment, and even start preparing the first devices before the day is over.

There are numerous people I wish to thank, without whom the work presented in this thesis would not be possible. First of all, I want to thank my advisor, Professor Mikhail (Misha) Lukin, who has been an incredible mentor throughout my PhD. Misha has taught me a lot, about both physics and how to grow as a researcher. I want to especially thank Misha for being so supportive when I have proposed new research projects, enabling me to start taking the steps toward becoming an independent researcher myself. Next, I would like to thank the rest of my committee, Professor Philip Kim and Professor Amir Yacoby. I always really enjoy the discussions with Philip about our experimental data, and he provides a lot of very valuable insight. I am also very grateful for being able to fabricate devices and collect a lot of experimental data in Philip's lab. I truly appreciate the discussions that I have had with Amir, and I am amazed by his combined theoretical and experimental expertise. Next, I wish to thank Professor Hongkun Park, who was so kind to let me collaborate with his group on some very fruitful projects presented in this thesis. Hongkun has an incredible ability to provide us with brilliant advice on the experiments, and we always have great discussions about the data. Another professor who has meant a lot during my PhD is Professor Eugene Demler, who provided invaluable support in our theoretical work on the

Cherenkov instability discussed in Chapter 2. As someone who really enjoys the theoretical part of our projects, I feel very lucky to have gotten to work with Eugene.

During the first three years of my PhD, I worked very closely with (then postdoc) Javier D. Sanchez-Yamagishi and (then graduate student) Bo Dwyer, and I am forever grateful for the amazing time we had together in lab, leading to our discovery of a Cherenkov instability in graphene. Javier exemplified everything a postdoc should be, and I would like to thank him for teaching me so much, always keeping up the good mood when research was difficult, trusting me with a lot of responsibility, and making every day in lab a lot of fun. I also want to thank Bo for being a fantastic lab mate, teaching me a lot about NV centers, and sharing many funny moments with me. Moreover, I thank theorists Dominik, Rivka, Valentin and Joaquin for a lot of very fruitful discussions, and the whole Lukin group for sharing their expertise with me.

During my PhD, I was very lucky to also get to work with many amazing people in the Park group, including Gio, You, Jiho, Ryan and Elise, and in the Kim group, including Andy, Andres, Jonah and Artem. I would like to thank these people for all the great times we spent together in lab and for a lot of very interesting discussions. I want to especially thank Gio, who has not only been an amazing colleague to work with, but also become one of my closest friends. Gio's research talent and great humor have made our time together in lab both incredibly productive and a lot of fun. Collecting great data sets together while singing to loud European EDM songs, and going to conferences together around the world have really been some of the greatest highlights for me in my PhD.

I also want to make a special thanks to Qiong Ma, who was an amazing mentor for me during my undergraduate degree at MIT, and taught me so many skills that have helped me succeed during my PhD. I am very grateful that Qiong and I have managed to stay in close contact

throughout my PhD as well, and she has continued being a fantastic conversation partner with regards to both physics and career advice.

My experience at Harvard would not have been the same without the social activities with my colleagues, and I would like to thank Kristiaan, Dominik, Javier and Alexei for a lot of fun squash games, as well as everyone who participated in our soccer and volleyball games. I am also grateful to Tamara S., Tamara D., Mihir, Gio, Andrei, Paloma and Alex for many very fun nights out, including of course our legendary karaoke nights at The Hong Kong.

Moreover, thank you, Harvard staff members Silke Exner, Samantha Dakoulas, Lisa Cacciabaudo, Clare Ploucha, and Carol S. Davis for all your help and support throughout the last six years.

Finally, I want to thank the most important people of them all, namely my family at home in Norway and my girlfriend, Nicole. I would not be where I am today without my amazing family who always roots for me, and the vast amount of scientific discussions we have around the dinner table at home. My older brother Eirik has played a huge role, with his enthusiastic efforts to teach me mathematics and science from when I was very little, including teaching me differentiation with a stick in the sand at a beach in Sweden, many games of "blindfold tic-tac-toe", and countless intense science discussions. Most importantly, I wish to thank my girlfriend Nicole, for being the best friend I could ever have found, for always putting a smile on my face, for cheering me up when the experiments are challenging, and for celebrating with me when they are successful. This thesis is dedicated to her.

Citations to previously published works

The discovery of an electron-phonon Cherenkov instability presented in Chapters 2.4 and 2.5 has been published as:

> T. I. Andersen*, B. L. Dwyer*, J. D. Sanchez-Yamagishi*, J. F. Rodriguez-Nieva, K. Agarwal, K. Watanabe, T. Taniguchi, E. A. Demler, P. Kim, H. Park, M. D. Lukin. *Electron-phonon instability in graphene revealed by global and local noise probes*, Science **364**, 154-157 (2019).

The observations of tunable valley dynamics of excitons in twisted homobilayer WSe_2 discussed in Chapter 3.5 were published as:

> G. Scuri*, T. I. Andersen*, Y. Zhou*, D. S. Wild, J. Sung, R. J. Gelly, D. Bérubé, H. Heo, L. Shao, A. Y. Joe, A. M. Valdivia, T. Taniguchi, K. Watanabe, M. Lončar, P. Kim, M. D. Lukin, H. Park. *Electrically Tunable Valley Dynamics in Twisted WSe_2/WSe_2 Bilayers,* Physical Review Letters **124**, 217403 (2020).

The measurements of broken mirror symmetry in optically resolvable moiré domains discussed in Chapter 4.3 has been published as:

> Jiho Sung, You Zhou, Giovanni Scuri, Viktor Zólyomi, Trond I. Andersen, Hyobin Yoo, Dominik S. Wild, Andrew Y. Joe, Ryan J. Gelly, Hoseok Heo, Samuel J. Magorrian, Damien Bérubé, Andrés M. Mier Valdivia, Takashi Taniguchi, Kenji Watanabe, Mikhail D. Lukin, Philip Kim, Vladimir I. Fal'ko, Hongkun Park. *Broken mirror symmetry in excitonic response of reconstructed domains in twisted $MoSe_2$/$MoSe_2$ bilayers*, Nature Nanotechnology **15**, 750–754 (2020).

The correlation of moiré structure and exciton properties in twisted homobilayer WSe_2 discussed in Chapter 4.4 has been published as:

T. I. Andersen*, G. Scuri*, A. Sushko*, K. De Greve*, J. Sung, Y. Zhou, D. S. Wild, R. J. Gelly, H. Heo, D. Bérubé, A. Y. Joe, L. A. Jauregui, K. Watanabe, T. Taniguchi, P. Kim, H. Park, M. D. Lukin. *Excitons in a reconstructed moiré potential in twisted WSe_2/WSe_2 homobilayers,* Nature Materials **20**, 480-487 (2021).

1

INTRODUCTION

1.1 Background

1.1.1 Two-dimensional materials

Following the discovery of the first two-dimensional material, graphene in 2004 (*1*), numerous other atomically thin materials have been introduced in recent years. These come in many flavors, including semiconductors like the transition metal dichalcogenides (TMDs) (*2*), insulators such as hexagonal boron nitride (hBN) (*3*), and even superconductors (*4*) and magnetic materials (*5*). The family of two-dimensional materials provides us with the opportunity to study a very wide variety of interesting phenomena that are often not present in the bulk. For instance, graphene is famous for its fascinating electronic behavior involving massless Dirac fermions (*6*), the TMDs exhibit electron-hole pairs (excitons) that interact so strongly with light that a single atomic layer can exhibit almost perfect reflection (*7*), and hBN hosts interesting hybrid light-matter particles known as hyperbolic phonon-polaritons (*8*). In this thesis, I will present studies of device structures involving all three of these materials, with a predominant focus on the first two.

A very attractive feature of the two-dimensional materials is their great level of tunability, both during fabrication and measurements. By stacking different two-dimensional materials on top of each other, one can tune their properties, and even realize entirely new ones that were not present in the constituent materials. For instance, a graphene layer can be stacked on top of hBN to open a bandgap in the former (*9*), and two TMD layers can be combined to realize new types of excitons where the electron and hole reside in different layers (*10*). The relative twist angle between subsequently stacked flakes has attracted wide attention as a powerful tuning knob, allowing for tunable band structure engineering and the realization of exotic phenomena such as superconductivity in twisted bilayers of graphene (*11*). In addition to the incredible versatility available at the fabrication stage, the atomic thickness of the 2D materials greatly enhances the

ability to tune the entire material in-situ via electrostatic gating. In this thesis, we shall see examples of all the above-mentioned tuning mechanisms.

The wide variety and great tunability of physical phenomena in two-dimensional materials have three-fold value. First, these features allow us to realize new physical phenomena that do not exist elsewhere in nature. Second, they can be harnessed to develop new technological applications with tailored properties for their particular use case. Finally, these capabilities make two-dimensional materials an excellent platform for studying elusive physical phenomena that have proven difficult to study in other less controllable systems.

1.1.2 Understanding two-dimensional materials on a local level

While the 2D materials host a broad range of exciting physical phenomena, actually measuring these is often challenging. High-quality exfoliated flakes of two-dimensional materials are typically on the micrometer scale, and many of the interesting phenomena occur locally in the sample, at length scales that are inaccessible with conventional measurement techniques. For instance, while conventional electronic measurements can measure the net current that flows through a graphene device, they provide very little information about the spatial structure of the current. In the case of optical phenomena, confocal measurements provide a somewhat greater level of locality, but even these are limited by the diffraction limit, which often greatly exceeds the characteristic length scale of the phenomenon of interest.

As a consequence, many important insights in the field of 2D materials have relied on the use of new techniques that allow for understanding the phenomena locally. For instance, scanning single electron transistor (SET) and nitrogen vacancy measurements have provided invaluable knowledge in the study of hydrodynamic electron flow in graphene (*12, 13*), and scanning superconducting quantum interference devices (SQUIDs) allowed for understanding local

dissipation mechanisms in the same material (*14*). Moreover, near-field optical techniques have allowed for surpassing the diffraction limit (*8*), deepening our understanding of local optical phenomena on the subwavelength scale such as strain-localized exciton states (*15*).

1.2 Overview

In this thesis, I present studies where we take advantage of new techniques to understand local phenomena in two-dimensional materials, including local current fluctuations in graphene (Chapter 2) and the effects of local moiré structure in twisted TMDs (Chapters 3 and 4). The chapters are accompanied by appendices that provide additional supporting information, such as calibration techniques, fabrication details, and fitting procedures.

In Chapter 2, I discuss the study of local current noise in biased ultra-clean graphene devices, probed using nitrogen vacancy (NV) centers in diamond. Following introductions of graphene and NV center physics, as well as background about current noise, I present our results, which show a dramatic growth in local noise in the direction of the charge carrier flow. We attribute our observations to an electron-phonon instability driven by Cherenkov amplification of phonons, which occurs when the electronic drift velocity exceeds the speed of sound in graphene. Additional details are provided in Appendix A.

In Chapters 3 and 4, I turn to measurements of exciton properties in twisted homobilayer TMDs. First, in Chapter 3, I provide theoretical background about excitons in TMDs, their optical selection rules and potential valleytronic applications, before presenting our experimental demonstration of interlayer excitons with highly tunable and very long valley lifetimes in twisted homobilayer TMDs. Next, in Chapter 4, I discuss our new moiré imaging technique based on scanning electron microscopy, which allows for correlating the local moiré structure with the

exciton properties. Through these measurements, we observe signatures of an array of two spatially alternating exciton species that reside in different parts of the moiré bilayer system. We also demonstrate that the two species not only have different resonance energies, but can also be tuned independently via electrostatic gating. Supporting information to Chapters 3 and 4 is presented in Appendices B and C, respectively.

2

LOCAL PROBING OF ELECTRON-PHONON INSTABILITY IN GRAPHENE

2.1 Graphene

Graphene is a two-dimensional material consisting of carbon atoms arranged on a honeycomb lattice (*1*). In its multi-layer form, graphite, the graphene layers are held together by van der Waals interactions, which are much weaker than the covalent (sp^2) bonds within each layer. Indeed, it is the weakness of these interlayer bonds that allow us to smear graphite on a piece of paper when writing with a pencil. The isolation of single layers of graphene from bulk graphite is achieved by exfoliating graphite using scotch tape (*16*), which allows for overcoming the van der Waals interactions. Other than representing the fundamental atomic thickness limit of materials – and being the first material to do so – graphene has been described as the decathlete of materials, due to its remarkable performance over a wide range of properties, including material strength (elastic modulus) (*17*), thermal conductivity (*18*), impermeability (*19*), and electrical conductivity (*20*). As such, graphene carries promise for a wide variety of applications, ranging from infrared detection (*21*) and energy storage (*22*), to heat distribution solutions (*23*) and even water desalination (*24*). In this chapter, I will discuss the discovery of a phenomenon that arises due to the combination of particularly two of graphene's special properties. Specifically, we shall see that fascinating non-equilibrium effects occur when electrons are driven to very high drift velocities in a system with long-lived phonons (the origin of the high thermal conductivity).

2.1.1 Graphene band structure

The unit cell of graphene has a two-atom basis, giving rise to two inequivalent sublattices. A standard tight-binding model calculation considering hopping between p_z-orbitals of carbon atoms on different sublattices yields the following band structure (*25*):

$$\epsilon(k) = \pm t\sqrt{1 + 4\cos^2\left(\frac{k_x a}{2}\right) + 4\cos\left(\frac{k_x a}{2}\right)\cdot\cos\left(\frac{\sqrt{3}k_y a}{2}\right)}, \tag{2.1}$$

where ϵ is the energy, k is the wavevector, $t \sim 2.8$ eV is the hopping energy, and $a \sim 2.46$ Å is the lattice constant (see Figure 2.1). The plus and minus signs represent the conduction and valence bands, respectively. Importantly, the conduction and valence bands touch at the vertices of the hexagonal Brillouin zone, which are divided into two alternating (inequivalent) sets known as the K and K' points, respectively. Near these points, the band structure exhibits a linear dispersion given by:

$$\epsilon = \hbar v_{\mathrm{F}} \Delta k, \tag{2.2}$$

where $v_{\mathrm{F}} = 10^6\ \mathrm{ms}^{-1}$ is the Fermi velocity of carriers in graphene and Δk is the wavevector relative to the K/K'-point (simply referred to as k from here on). These cones in the band structure are known as Dirac cones, and the point at which they touch is commonly referred to as the Dirac point.

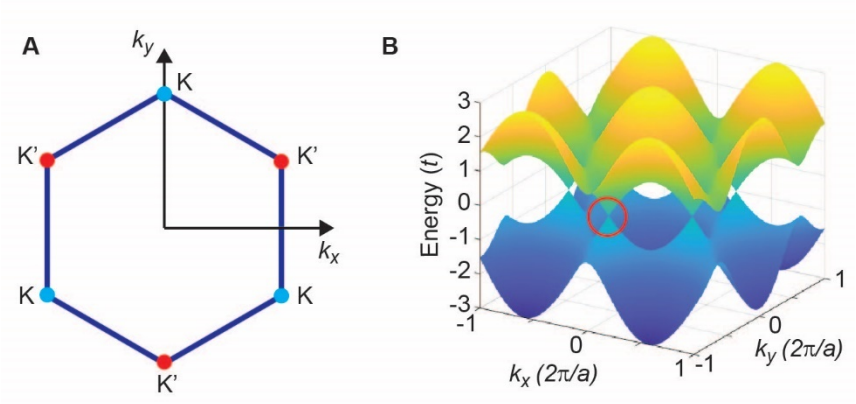


Figure 2.1: Graphene band structure. (A) First Brillouin zone of graphene, showing the location of the K and K' points. (B) Band structure calculated from the tight-binding model. The valence and conduction bands touch at the K and K' points (example shown by red circle). Near these points, graphene exhibits a linear dispersion relation.

2.1.2 Doping and low-bias excitation in graphene

Out of the four valence electrons of a carbon atom, three are part of the sp^2-bonds, leaving one electron in the p_z-orbital. Hence, in charge neutral graphene, the valence band is filled and the Fermi level lies at the Dirac point, causing the Fermi surface to be simply a point in k-space. (In practice, residual doping often causes a deviation from this point). When graphene is electron- or hole-doped, typically achieved through electrostatic gating, the Fermi surface moves up or down as $\epsilon_\mathrm{F} = \mathrm{sgn}(n) \cdot \hbar v_\mathrm{F} k_\mathrm{F} = \mathrm{sgn}(n) \cdot \hbar v_\mathrm{F} \sqrt{\pi n}$, where n is the charge density, and ϵ_F and k_F are the Fermi energy and wavevector, respectively. This can be found by simply integrating over the occupied states on the Dirac cone, including a factor 4 due to spin and valley (K/K') degeneracy. With the increasing size of the Fermi surface, the resistance decreases (conductivity increases), giving rise to a characteristic peak at $n = 0$ when measuring resistance versus charge density (applied gate voltage).

To describe the behavior of charge carriers in graphene when a bias voltage is applied across it, we consider the Boltzmann equation for fermions with a distribution function $f_{\boldsymbol{k}}$:

$$\partial_\mathrm{t} f_{\boldsymbol{k}} = -\boldsymbol{v_k} \cdot \nabla_{\boldsymbol{r}} f_{\boldsymbol{k}} - e\boldsymbol{E}/\hbar \cdot \nabla_{\boldsymbol{k}} f_{\boldsymbol{k}} + I_{\mathrm{coll},\boldsymbol{k}}[f], \tag{2.3}$$

where $\boldsymbol{v_k} = \partial_{\boldsymbol{k}} E = v_\mathrm{F} \widehat{\boldsymbol{k}}$, $\nabla_{\boldsymbol{k}(\boldsymbol{r})}$ is the gradient in momentum (position) space, $\boldsymbol{E}$ is the applied (in-plane) electric field, and $I_{\mathrm{coll},\boldsymbol{k}}[f]$ is the collision integral representing collisions with phonons and/or impurities. We here consider the degenerate regime, where the electronic temperature T is small compared to the Fermi energy ($T \ll \epsilon_\mathrm{F}/k_\mathrm{B}$), and do therefore not have to worry about more than one band. Next, we linearize the Boltzmann equation using $f_{\boldsymbol{k}} = f_{\boldsymbol{k}}^0 + \Delta f_{\boldsymbol{k}}$ where $f_{\boldsymbol{k}}^0 = \left(1 + e^{-\beta(\epsilon_{\boldsymbol{k}} - \epsilon_\mathrm{F})}\right)^{-1}$ is the Fermi-Dirac distribution ($\beta = (k_B T)^{-1}$ where k_B is the Boltzmann constant and T is the electronic temperature), and use a simple collision model $I_{\mathrm{coll},\boldsymbol{k}}[f] =$

$-\Delta f_{\boldsymbol{k}}/\tau_{\mathrm{mfp}}$, where τ_{mfp} is the ($\boldsymbol{k}$-independent) mean free scattering time. We also assume that the electric field is uniform (eliminating any $\boldsymbol{r}$-dependence), and obtain:

$$\partial_{\mathrm{t}}\Delta f_{\boldsymbol{k}} = -e\boldsymbol{E}/\hbar \cdot \nabla_{\boldsymbol{k}} f_{\boldsymbol{k}}^{0} - \Delta f_{\boldsymbol{k}}/\tau_{\mathrm{mfp}}. \tag{2.4}$$

For the steady state solution ($\partial_{\mathrm{t}}\Delta f_{\boldsymbol{k}} = 0$), we then find:

$$\Delta f_{\boldsymbol{k}} = e\tau_{\mathrm{mfp}}\boldsymbol{E} \cdot v_{\mathrm{F}}\hat{\boldsymbol{k}}\partial_{\epsilon} f^{0} \sim e\tau_{\mathrm{mfp}}\boldsymbol{E} \cdot v_{\mathrm{F}}\hat{\boldsymbol{k}}\delta(\epsilon - \epsilon_{\mathrm{F}}), \tag{2.5}$$

One can then find the current by summing over all carriers:

$$\boldsymbol{j} = \frac{2^2}{(2\pi)^2}\int e\boldsymbol{v}_{\boldsymbol{k}}\Delta f_{\boldsymbol{k}} d^2\boldsymbol{k} = \frac{e^2 v_{\mathrm{F}}\tau_{\mathrm{mfp}}}{\pi\hbar}\int \left(\boldsymbol{E}\cdot\hat{\boldsymbol{k}}\right)\hat{\boldsymbol{k}}\delta(k - k_{\mathrm{F}}) d^2\boldsymbol{k} = e^2 v_{\mathrm{F}}\tau_{\mathrm{mfp}}k_{\mathrm{F}}\boldsymbol{E}/\pi\hbar, \tag{2.6}$$

Where the factor 2^2 is due to the two valley and two spin flavors. Hence, we find the conductivity,

$$\sigma = \frac{j}{E} = \frac{e^2 v_{\mathrm{F}}\tau_{\mathrm{mfp}}k_{\mathrm{F}}}{\pi\hbar} = \frac{e^2\ell_{\mathrm{mfp}}k_{\mathrm{F}}}{\pi\hbar}, \tag{2.7}$$

where $\ell_{\mathrm{mfp}} = v_{\mathrm{F}}\tau_{\mathrm{mfp}}$ is the mean free path in graphene. Defining the electronic drift velocity as $v_{\mathrm{D}} = j/n$, we then find:

$$v_{\mathrm{D}} = \frac{j}{n} = \frac{e^2\ell_{\mathrm{mfp}}k_{\mathrm{F}}}{\hbar k_{\mathrm{F}}} \cdot E = \mu E, \tag{2.8}$$

where μ is the mobility, which describes the ability to drive the electrons to a high electronic drift velocity. Due to the high Fermi velocity of graphene and the low disorder scattering rate in today's ultra-clean, hBN-encapsulated devices, very high mobilities exceeding $10^5\ \mathrm{cm}^2/(\mathrm{Vs})$ can be achieved (*20*). As we shall see later in this chapter, this allows for driving the electrons to very high drift velocities, where new non-equilibrium phenomena occur. At such high drift velocities, the electron-phonon scattering rate increases, as further discussed in section 2.5.2.

2.2 Current noise

While the properties of electronic systems are typically studied by measuring the coherent current response to an applied DC or AC voltage, measurements of the current noise can in many cases provide additional information about the properties and dynamics of the system (*26*). For instance, thermal (Johnson) noise allows for measuring the electronic temperature of a system (*27*), measurements of shot noise in resonant tunneling structures provide information about correlations due to electron-electron interactions (*28*), and the 1/*f* noise can tell us about defects in the system (*29*).

An intuition for the information contained in the current noise can immediately be obtained by considering the definition of the noise spectral density:

$$S_a(\omega) = \int_{-\infty}^{\infty} \langle a(t)a(t+\tau)\rangle \cdot e^{-i\omega\tau} d\tau, \tag{2.9}$$

In other words, the noise spectrum of an observable quantity a is the Fourier transform of its autocorrelation function. Therefore, noise measurements provide insights into correlated dynamics that are not necessarily visible in conventional transport measurements. Below, we discuss various common types of current noise, including thermal (Johnson-Nyquist) noise, shot noise and 1/*f* (flicker) noise.

2.2.1 Thermal noise

While this thesis is mainly concerned with noise in systems driven strongly out of equilibrium, even equilibrium electronic systems exhibit current noise due to thermal fluctuations. The magnitude of these fluctuations can be found from the fluctuation-dissipation theorem, which connects the fluctuations in a quantity a to its linear response function χ. More specifically, in a

system with Hamiltonian $H = H_0 + a \cdot F$, where a responds to the "force" $F(t)$ according to $a(t) = \int_{-\infty}^{t} F(t')\chi(t-t')dt'$, the (single-sided) thermal noise in a is given by:

$$S_a(\omega) = \hbar \cdot \coth\left(\frac{\hbar\omega}{4k_{\mathrm{B}}T}\right) \cdot \mathrm{Im}\big(\chi(\omega)\big). \tag{2.10}$$

In the classical regime ($k_{\mathrm{B}}T \gg \hbar\omega$), one then finds:

$$S_a(\omega) = \frac{4k_{\mathrm{B}}T}{\omega}\,\mathrm{Im}\big(\chi(\omega)\big). \tag{2.11}$$

In the case of electronic systems, we can replace a with the voltage and F with the time integrated current. We then observe that the conductance $G(\omega)$ is given by:

$$G(\omega) = \frac{I(\omega)}{V(\omega)} = \frac{\dot{F}(\omega)}{\chi(\omega)F(\omega)} = \frac{i\omega}{\chi(\omega)}. \tag{2.12}$$

Hence, we find the voltage fluctuations:

$$S_V(\omega) = \frac{4k_{\mathrm{B}}T}{\mathrm{Re}\big(G(\omega)\big)} = 4k_{\mathrm{B}}T \cdot R(\omega). \tag{2.13}$$

Thus, at sufficiently low frequencies, where G and R are frequency independent, the thermal noise spectrum is white. As shown by Nyquist in 1928 (*30*), this expression can also be derived by considering the thermal occupation of electromagnetic modes in a transmission line of length l and characteristic impedance R, connecting two resistors with resistance R. The equipartition theorem entails that each electromagnetic mode of the transmission line has an energy of $k_{\mathrm{B}}T$ ($\frac{1}{2}k_{\mathrm{B}}T$ for electric and magnetic vibrations), moving from one resistor to the other at a rate of c/l, where c is the speed of light. Since the natural modes have wavelength $nl/2$ (for integer n), the spectral density of modes is $\frac{2l}{c}$. Hence, the power spectral density absorbed and emitted by each resistor is $k_{\mathrm{B}}T$, which means the current fluctuations are $S_I(\omega) = k_{\mathrm{B}}T/R$ and the voltage fluctuations are

$S_V(\omega) = (2R)^2 S_I(\omega) = 4k_B TR$. Hence, a resistor at temperature T is conveniently represented by an equivalent circuit consisting of a noiseless resistor in series with a white noise voltage source of rms voltage equal to $4k_B TR$. Because of Nyquist's theoretical work, combined with experimental work by Johnson, thermal noise in electronic systems is commonly referred to as Johnson-Nyquist noise.

2.2.2 Shot noise

Even at zero temperature, electronic currents exhibit fluctuations due to shot noise, arising from the fact that the current is carried by discrete particles (typically electrons) rather than a uniform "fluid" of charge. For instance, in the case of a Poissonian (low transmission) tunnel junction, the number of charge carriers N crossing the junction in a time interval dt has standard deviation, $\sigma_N = \sqrt{\overline{N}} = \sqrt{I \cdot dt/q}$, where $\overline{N}$ is the average of N, and q is the charge of the carriers. In the uncorrelated case, the noise spectrum is white with single-sided current spectral density given by $S_I = \sigma_I^2 \cdot \frac{1}{df} = \left(\frac{q\sigma_N}{dt}\right)^2 \cdot 2dt = 2qI$. Hence, shot noise measurements allow for probing the granularity of the charge flow, which has been used to show fractionalization of charge in the fractional quantum hall effect (*31*), as well as the existence of Cooper pairs ($q = 2e$) in superconductors (*32*). Correlations cause deviations from the Poissonian estimate: for instance, Coulomb interactions and the Pauli exclusion principle force the electrons to be spaced out more regularly than in a Poissonian process, and thus reduce the noise.

2.2.3 1/f (flicker) noise

Another source of current fluctuations are defect states nearby or inside the conductor, which impact the current by for instance changing the electronic scattering rate when the defect state is occupied. Since such defects remain occupied for some time, they cause current fluctuations with

non-zero correlation times. In particular, a defect with characteristic lifetime τ induces current correlations on the form $\langle \delta I(t)\delta I(t+\Delta t)\rangle \propto e^{-|\Delta t|/\tau}$, which gives a Lorentzian-shaped noise spectral density: $S_I \propto (1+(\omega\tau)^2)^{-1}$. Given a distribution of lifetimes, $P(\tau)$, the total noise is then given by $\int P(\tau)\,(1+(\omega\tau)^2)^{-1}d\tau$, which ends up being on the form $\omega^{-\alpha}$ for $P(\tau)$ in most materials. In particular, a normal distribution of τ gives $\alpha = 1$, thus $1/f$ noise.

2.3 Nitrogen vacancy (NV) centers in diamond

In order to measure the local current fluctuations in biased graphene, we placed the graphene devices on diamond substrates containing nitrogen vacancy centers (see Appendix A1.1), which were used as nanoscale noise magnetometers. While conventional noise measurements only measure the noise in the total source-drain current, thus averaging over the sample as a whole, the novel NV-based technique allows for studying the spatial distribution of the noise. In this section, we first describe the basic fundamentals of nitrogen vacancy centers, then their capability of measuring noise from nearby conductors, and finally the specific measurement technique used in our experiment to probe graphene devices.

2.3.1 NV basics

Nitrogen vacancy centers are defect centers in diamond consisting of a substitutional nitrogen atom and a vacancy on an adjacent lattice site (*33*). The NV center can exist in two different charge states, including the neutral (NV0) state with a zero-phonon line at 575 nm, and the negatively charged (NV^-) state with an optical resonance at 637 nm (simply referred to as NV from here on). The electronic ground state of NV centers is a spin triplet, in which the $m_s = \pm 1$ states are D =2.87 GHz higher in energy than the $m_s = 0$ state (at zero field) due to spin-spin interactions

(*34*). Including also non-zero magnetic fields, the Hamiltonian of the ground state manifold can be written as (in the case of zero electric field):

$$H = hDS_z^2 + g\mu_B \boldsymbol{B} \cdot \boldsymbol{S}, \tag{2.14}$$

where S_i are the Pauli matrices, $g \approx 2$ is the Landé g-factor, μ_B is the Bohr magneton and $\boldsymbol{B}$ is the applied magnetic field. Note that the z-axis is here aligned along the NV-axis, defined by the vector from the nitrogen atom to the vacancy site. There are four possible such axes, set by the tetrahedral lattice of the diamond. The second term represents the Zeeman effect, which splits the $m_s = \pm 1$ states by $\pm 2.8 \frac{\text{MHz}}{\text{Gauss}} \cdot B_z$.

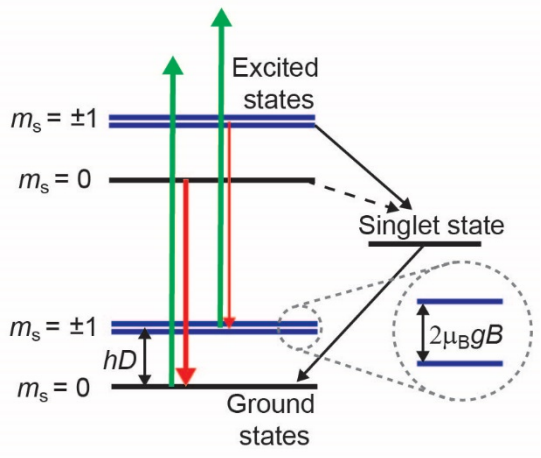


Figure 2.2: NV center energy levels and transitions. The ground states are triplet states with a zero-field splitting of $hD = h \cdot 2.87$ GHz between the $m_s = 0$ and $m_s = \pm 1$ levels. A magnetic field B along the NV axis further splits the $m_s = \pm 1$ levels by $2\mu_B gB$. Green and red arrows indicate transitions via optical excitation and emission, respectively. The excited $m_s = \pm 1$ states readily become shelved into the dark, long-lived singlet state, from which they predominantly decay to the $m_s = 0$ state.

Crucially, the optical excitation dynamics of the $m_s = \pm 1$ states are very different from that of the $m_s = 0$ state, due to preferential leakage from the excited $m_s = \pm 1$ states into a dark, longer-lived singlet state (*35*). Hence, while the excited $m_s = 0$ state mainly relaxes back to the

ground state with the emission of a photon, the excited $m_s = \pm 1$ states readily become shelved into the dark singlet state, and subsequently decay non-radiatively into the $m_s = 0$ ground state. These distinct dynamics have two central consequences. First, they allow for initialization of the NV center into the $m_s = 0$ state; by repeated optical cycling of the NV center, any initial population in the $m_s = \pm 1$ states eventually becomes shelved in the singlet state and thereafter transferred to the $m_s = 0$ state. It should of course be noted that these spin-dependent transitions are not perfectly preferential, causing a typical initialization contrast of about 80%. Another very useful effect of the spin-dependent optical dynamics is that the different spin states can be optically detected. Due to the eventual transition into the long-lived dark singlet state, optical cycling of the $m_s = \pm 1$ state generates less fluorescence than the $m_s = 0$ state.

2.3.2 NV centers as nanoscale noise magnetometers

As can be seen from eqn. (2.14), magnetic fields perpendicular to the NV-axis couple the $m_s = 0$ and $m_s = \pm 1$ states. Hence, following Fermi's Golden Rule, off-axis magnetic noise at the level splitting frequency causes decay from a polarized NV state to a thermalized state. In particular, the transition rate between the $m_s = \pm 1$ and $m_s = 0$ states is given by:

$$\Gamma_{0,\pm 1} = \frac{g^2 \mu_B^2}{\hbar^2} S_B^{ij}(\omega_{0,\pm 1}) \cdot |\hat{n}_{NV} \times \hat{n}_i| |\hat{n}_{NV} \times \hat{n}_j|, \tag{2.15}$$

where $\hat{n}_{NV}$ and $\hat{n}_i$ are unit vectors along the NV-axis and in the i-direction, respectively, and $S_B^{ij}(\omega_{0,\pm 1}) = \int_{-\infty}^{\infty} \langle B_i(t) B_j(t+\tau) \rangle e^{-i\omega_{0,\pm 1}\tau} d\tau$ is the noise spectral density at the splitting frequency $\omega_{0,\pm 1}$ between the $m_s = 0$ and $m_s = \pm 1$ states, which is typically diagonal.

At zero DC magnetic field, where the $m_s = \pm 1$ states are degenerate, the NV spin relaxation dynamics are governed by a single relaxation rate, $\Gamma = \Gamma_{0,+1} = \Gamma_{0,-1}$, and the populations ρ_i can be described by the following equations:

$$\frac{d}{dt}\begin{pmatrix}\rho_{+1}\\ \rho_0\\ \rho_{-1}\end{pmatrix} = \begin{pmatrix}-\Gamma & \Gamma & 0\\ \Gamma & -2\Gamma & \Gamma\\ 0 & \Gamma & -\Gamma\end{pmatrix}\begin{pmatrix}\rho_{+1}\\ \rho_0\\ \rho_{-1}\end{pmatrix}. \tag{2.16}$$

Hence, with initialization efficiency α (initial populations of $\rho_0(0) = \alpha$ and $\rho_{+1}(0) = \rho_{-1}(0) = (1-\alpha)/2$), the dynamics are given by:

$$\rho_0(t) = \frac{1}{3} + \left(\alpha - \frac{1}{3}\right)e^{-3\Gamma t}, \tag{2.17}$$

$$\rho_{\pm 1}(t) = \frac{1}{3} + \left(\frac{1}{6} - \frac{\alpha}{2}\right)e^{-3\Gamma t}. \tag{2.18}$$

Moreover, defining the fluorescence level of each state as I_{m_s}, one finds that the overall fluorescence is given by:

$$I(t) = \frac{I_0 + 2I_{\pm 1}}{3} + \left(\alpha - \frac{1}{3}\right)(I_0 - I_{\pm 1})e^{-3\Gamma t} \tag{2.19}$$

Hence, by measuring the time-dependent fluorescence, the local magnetic noise can be measured.

A particularly useful application of NV noise magnetometry is measurements of current noise in nearby conductors, since current fluctuations in the conductor give rise to fluctuations in the nearby magnetic field. In particular, for a 2D conductor, the Biot-Savart law can be used to show that:

$$\begin{aligned} S_B^{xx}(\omega) = {} & \frac{\mu_0^2}{4\pi}\int_0^\infty dq_x\, q_x e^{-2q_x z_{\mathrm{NV}}} \cdot S_j^{yy}(q_x, q_y = 0, \omega_{\mathrm{NV}}) \\ & + \frac{\mu_0^2}{4\pi}\int_0^\infty dq_y\, q_y e^{-2q_y z_{\mathrm{NV}}} \cdot S_j^{yy}(q_x = 0, q_y, \omega_{\mathrm{NV}}) \end{aligned} \tag{2.20}$$

$$S_B^{yy}(\omega) = \frac{\mu_0^2}{4\pi}\int_0^\infty dq_x\, q_x e^{-2q_x z_{\mathrm{NV}}} \cdot S_j^{xx}(q_x, q_y = 0, \omega_{\mathrm{NV}}) + \frac{\mu_0^2}{4\pi}\int_0^\infty dq_y\, q_y e^{-2q_y z_{\mathrm{NV}}} \cdot S_j^{xx}(q_x = 0, q_y, \omega_{\mathrm{NV}}) \tag{2.21}$$

$$S_B^{zz}(\omega) = \frac{\mu_0^2}{4\pi}\int_0^\infty dq_x\, q_x e^{-2q_x z_{\mathrm{NV}}} \cdot S_j^{yy}(q_x, q_y = 0, \omega_{\mathrm{NV}}) + \frac{\mu_0^2}{4\pi}\int_0^\infty dq_y\, q_y e^{-2q_y z_{\mathrm{NV}}} \cdot S_j^{xx}(q_x = 0, q_y, \omega_{\mathrm{NV}}) \tag{2.22}$$

where $S_j^{ii}(q_x, q_y, \omega)$ is the current noise spectral density in the i-direction of the mode with wavevector (q_x, q_y) at frequency ω. Importantly, the factor $qe^{-2qz_{\mathrm{NV}}}$ acts as a filter centered around $q = 2z_{\mathrm{NV}}$, where z_{NV} is the distance from the conductor to the NV-center. Hence, the distance to the NV can be varied in order to probe fluctuations at different wavevectors.

2.3.3 Noise measurement pulse sequence

Due to the slow NV decay rates (100s of ms) in most of our measurements, accurate read-out was essential to shortening the total averaging time of our measurements. We therefore employed a technique known as spin-to-charge conversion to reduce the readout noise to only 6.3 times the projection noise limit. The working principle behind spin-to-charge conversion is to map the $m_s = 0$ and $m_s = \pm 1$ states onto the two different charge states (NV0 and NV-, respectively), since their fluorescence contrast is much larger than that between the spin-states.

The NV centers were first initialized into the m_s = 0 spin state by shining a 1 mW pulse of 532 nm light for 25 μs (Figure 2.3A). This also preferentially prepared the NV center in the NV− charge state with ~70% fidelity, as shown in Figure 2.3B. To improve this further, we performed post-selection based on an initial charge state readout, using a low-power pulse from an external

cavity diode laser tuned to the NV− zero phonon line near 637 nm. Extremely low power (~nW) was used to avoid ionizing the NV center while determining its initial charge state. The NV was then allowed to relax for a variable amount of time in the dark, before the spin state was mapped onto a charge state.

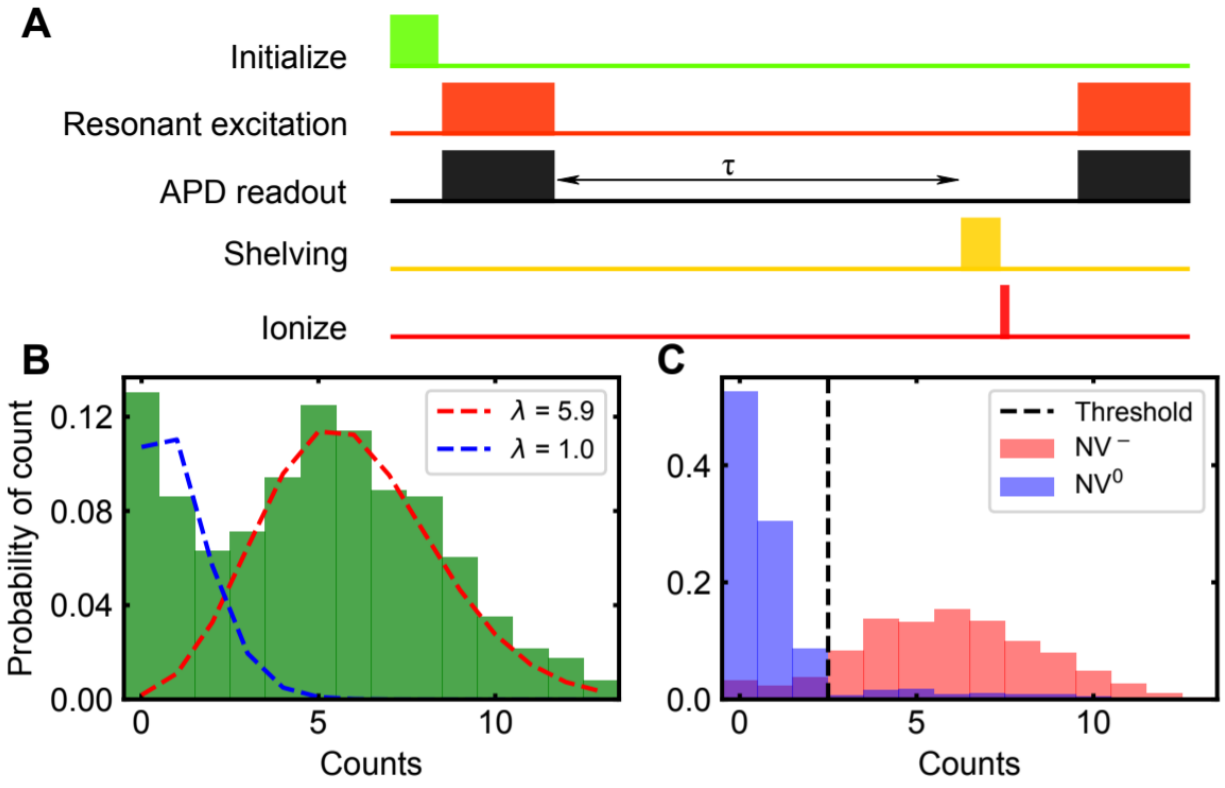


Figure 2.3: Spin-to-charge readout. (A) Pulse sequence for measuring relaxation rate of NV centers. A 532 nm pulse preferentially prepares the NV center in the NV− charge state and $m_s = 0$ spin state. The NV center spin is allowed to relax for a time τ before a strong yellow pulse shelves the $m_s = \pm 1$ population in the singlet state. An intense pulse of 637 nm light ionizes any population in the triplet state, while the singlet is protected. The resulting charge state is read out by resonant excitation of the NV− zero phonon line, and from this, the spin state before the yellow pulse is inferred. (B) Photon distribution from NV is fit as a 70%-30% mix of two Poisson distributions with different parameters, λ, corresponding to counts from NV− and NV0. (C) Post-selected photon distributions. The photon distributions for the two charge states are distinguishable, permitting single-shot charge state readout.

Spin-to-charge conversion was achieved by applying a strong (5 mW) pulse of 589 nm light for 40 ns to preferentially shelve any $m_s = \pm 1$ population in the metastable singlet state, and then using a 20 ns pulse of ~70 mW 637 nm light to efficiently ionize any population in the triplet state. The protected population in the singlet then relaxed back to the triplet manifold by an intersystem crossing so that only the $m_s = \pm 1$ population remained in the NV− charge state. The final charge state was then read out using the resonant laser, and the number of collected photons was used to assign a charge state. With an optimal threshold for photon counts, the single-shot charge state readout fidelity was 80%-99% depending on the NV center (Figure 2.3C), and the technique was limited primarily by spin-to-charge mapping efficiency.

2.4 Electron-phonon instability in graphene revealed by global and local noise probes

The following is reproduced from the manuscript "Electron-phonon instability in graphene revealed by global and local noise probes" by Trond I. Andersen, Bo L. Dwyer, Javier D. Sanchez-Yamagishi *et al*. (*36*)

Understanding and controlling nonequilibrium electronic phenomena is an outstanding challenge in science and engineering. By electrically driving ultraclean graphene devices out of equilibrium, we observe an instability that is manifested as substantially enhanced current fluctuations and suppressed conductivity at microwave frequencies. Spatial mapping of the nonequilibrium current fluctuations using nanoscale magnetic field sensors reveals that the fluctuations grow exponentially along the direction of carrier flow. Our observations, including the dependence on density and temperature, are consistently explained by the

emergence of an electron-phonon Cherenkov instability at supersonic drift velocities. These results offer the opportunity for tunable terahertz generation and active phononic devices based on two-dimensional materials.

Nonequilibrium phenomena in driven electronic and optical systems display rich dynamics that can be harnessed for applications such as Gunn diodes and lasers. Two-dimensional (2D) materials (*37*) constitute a new platform for exploring such nonequilibrium phenomena. In particular, modern ultraclean graphene devices exhibit high mobilities (*20*) and can be driven to high electronic drift velocities where instabilities have been predicted to occur. Examples include hydrodynamic instabilities (*38*) in electronic fluids (*27, 39*), as well as Dyakonov-Shur instabilities, where plasmons are amplified by driven electrons (*40, 41*). In addition to the potential use for high-frequency signal generation, understanding nonequilibrium dynamics is vital for many technological applications of graphene, including high-frequency transistors (*42*), ultrafast incandescent light sources (*43*), and flexible transparent interconnects (*44*). In practice, such electronic instabilities are difficult to realize owing to increased phonon scattering at high drift velocities. Although phonon scattering is typically an irreversible loss channel, long-lived phonons can themselves act as a source of instabilities. Specifically, when the electronic drift velocity (v_{D}) exceeds the sound velocity (v_{s}), stimulated phonon emission can dominate over absorption (Figure 2.4B), resulting in exponential growth of the phonon population known as phonon Cherenkov amplification (*45, 46*). This phenomenon has long been theoretically explored as a method to produce high-frequency acoustic waves (*47, 48*), with experimental evidence found in bulk systems and semiconductor superlattices via acoustic and optical measurements (*49-52*).

Our experiments make use of electrically gated graphene devices encapsulated in hexagonal boron nitride (hBN) (Figure 2.4A) and are conducted at cryogenic temperatures (T = 10

to 80 K). Figure 2.4C presents the low-bias transport properties of the ultraclean graphene system, with a mobility of 20 to 40 $\mathrm{m^2/V \cdot s}$ at a carrier density, n, of $2 \cdot 10^{12}$ $\mathrm{cm^{-2}}$, corresponding to nearly ballistic transport. Due to the high mobility, carriers can be accelerated by an electric field to high drift velocities ($v_D \gg v_s$ =21 km/s), where a nonlinear current response is observed (Figure 2.4D, blue). By contrast, a disordered device shows linear ohmic behavior (Figure 2.4D, black).

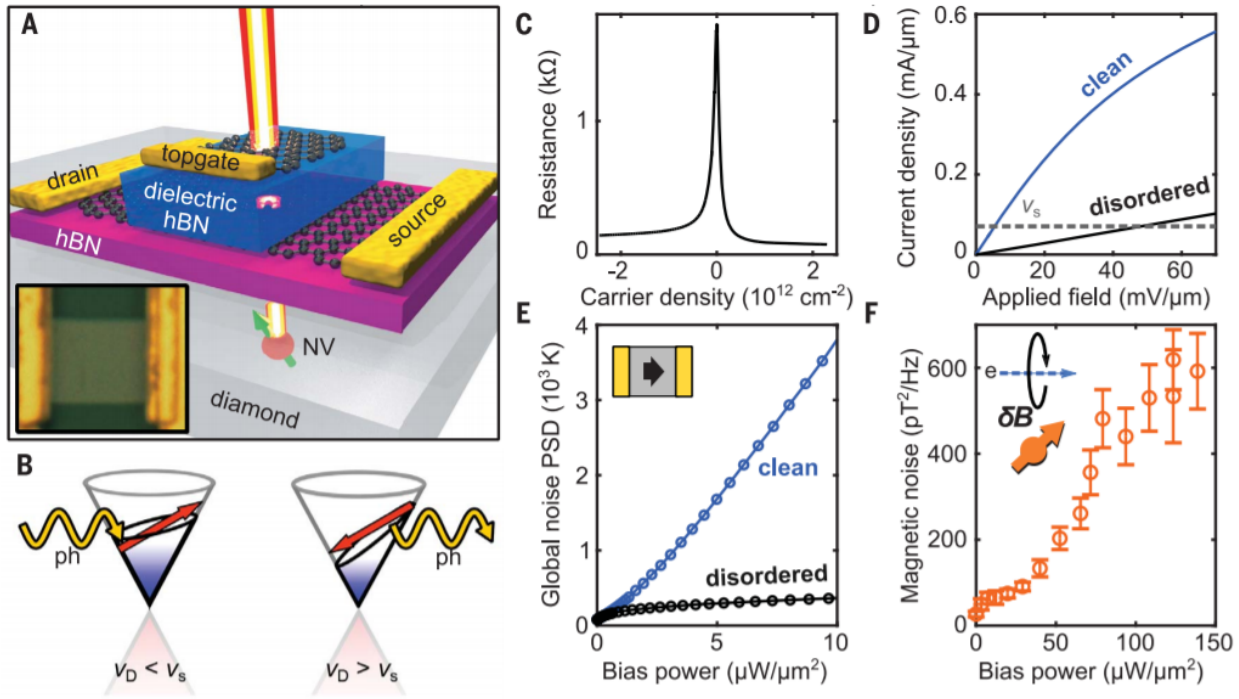


Figure 2.4: Nonequilibrium dynamics in graphene, probed both globally and locally. (A) Device schematic: hBN-encapsulated graphene device on diamond substrate containing NV centers for nanomagnetometry. (Inset) Optical image of clean hBN-encapsulated device A1 (6 μm by 5.4 μm). (B) Condition for Cherenkov emission of phonons: when $v_D > v_s$, stimulated phonon (ph) emission dominates over absorption (right). (C) Two-probe resistance versus carrier density of device A1 (T = 10 K). (D) Current density as a function of applied electric field (T = 80 K) in clean device A1 (blue) and disordered device B1 (7 μm by 18 μm, black). The gray dashed line indicates where $v_D = v_s$ for the longitudinal acoustic mode. (E) Global electronic noise PSD (averaged over 100 to 300 MHz) as a function of bias power in devices A1 (blue) and B1 (black). Blue curve satisfies $v_D > v_s$ for $P > 0.12$ mW/μm^2. (F) Local magnetic noise (measured by NV nanomagnetometry) versus applied bias power in clean device C1 on diamond substrate. Error bars represent 95% confidence intervals.

We first study the nonequilibrium behavior by measuring the global noise in the source-drain current with a spectrum analyzer (noise power spectral density, PSD, averaged over 0.1 to 0.3 GHz), while varying the applied bias power, *P*. The noise observed in disordered devices (Figure 2.4E, black) is in good agreement with increased thermal noise due to Joule heating and shows a characteristic $P^{1/3}$-dependence (*53*). Different behavior is observed in clean (hBN-encapsulated) devices, where the noise grows superlinearly with drive power and reaches values that are inconsistent with thermal noise. In particular, at higher biases, the noise increases to values equivalent to the thermal noise expected for a sample at 10,000 K (Appendix A4.1). This behavior, observed consistently in 12 devices, stands in stark contrast to that of more disordered (not hBN-encapsulated) devices studied here and elsewhere (*54*), indicating a new noise source in driven graphene devices with low disorder.

To gain insights into the origin of this anomalous noise, we perform spatially resolved noise measurements by fabricating graphene devices on diamond substrates that contain shallow nitrogen-vacancy (NV) color-center impurities (40 to 60 nm depth) (*55*). These atomlike spin qubits can be individually measured using confocal microscopy and can probe nanoscale current noise by measuring the resulting magnetic fields (*56*-*58*). The locally probed noise under a driven clean graphene device exhibits similar superlinear behavior as global measurements (Figure 2.4F).

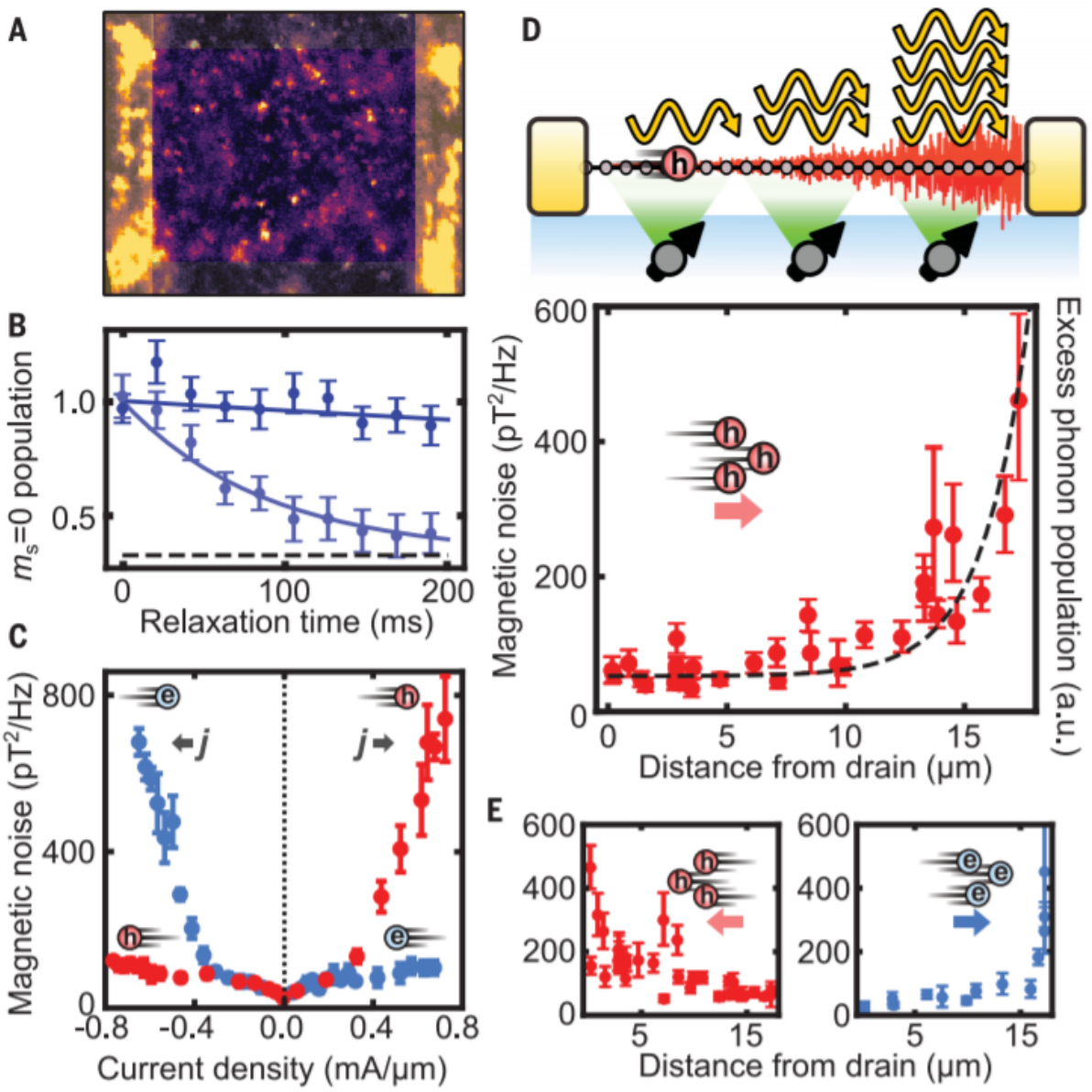


Figure 2.5: Spatially resolved local noise measurements with NV magnetometry. (A) Fluorescence image of NV centers underneath device C2, with false-colored contacts and borders added. (B) NV spin relaxation from polarized to thermal state (dashed line), when current densities j = 0 mA/μm (dark blue) and j = -0.19 mA/μm (light blue) are passed through the device. Solid lines are fits. m_s, spin quantum number. (C) Local magnetic noise near drain contact as a function of graphene current density (device C1) in electron (e)– and hole (h)–doped regime (blue and red, respectively). (D) Spatial map of the local magnetic noise (device C2) at j = 0.19 mA/μm and n = $0.92 \cdot 10^{12}$ cm^{-2}. The spatial profile is consistent with the exponential growth of phonons due to Cherenkov amplification (cartoon, top). Dashed black curve shows the theoretically predicted excess phonon population (offset to account for background noise). a.u., arbitrary units. (E) The growth direction is reversed by changing the current direction (left) or the charge carrier sign (right). Error bars represent 95% confidence intervals.

We probe the spatial dependence of the anomalous noise by optically addressing single NV centers along the device (Figure 2.5A) and measuring their spin relaxation rate (Figure 2.5B), which is determined by the local noise at 2.87 GHz (*56*). Far from the midpoint of the device, the noise exhibits a clear asymmetry with current direction (Figure 2.5C), with nearly an order of magnitude difference when the current is reversed. This is surprising given that the global noise and transport properties are independent of current direction (Appendix A4.4). Using the device gate, we invert the sign of the charge carriers and find that the asymmetric pattern also inverts, indicating that the local noise signal depends on the flow direction of momentum, not charge. Figure 2.5D shows the local noise profile along the source-drain direction when $v_{\mathrm{D}} = 5.8 v_{\mathrm{s}}$. We observe that the noise is small at the carrier entry point but then grows exponentially as the carriers flow down the 17-μm long device. The noise profile inverts when the current direction is reversed and flips back when the carrier sign is also switched (Figure 2.5E).

To explore the underlying dynamics, we measure the spectrum of the global current noise. When driven, the disordered graphene samples show 1/*f* noise and white thermal noise (Figure 2.6A, black curve), consistent with previous studies (*53, 59*). Clean devices, on the other hand, exhibit a peaked spectrum with a roll-off at ~1.5 GHz. The ac differential conductivity is suppressed at similar frequencies (Figure 2.6B). These gigahertz features are in stark contrast to the equilibrium graphene Drude spectrum, which is featureless up to terahertz frequencies (*60, 61*), thus indicating time scales much longer than the typical electronic lifetime. The frequencies of these nonequilibrium features are independent of drive voltage, doping, and temperature (Appendix A4.5), but they are upshifted in a shorter device (Figure 2.6C and D).

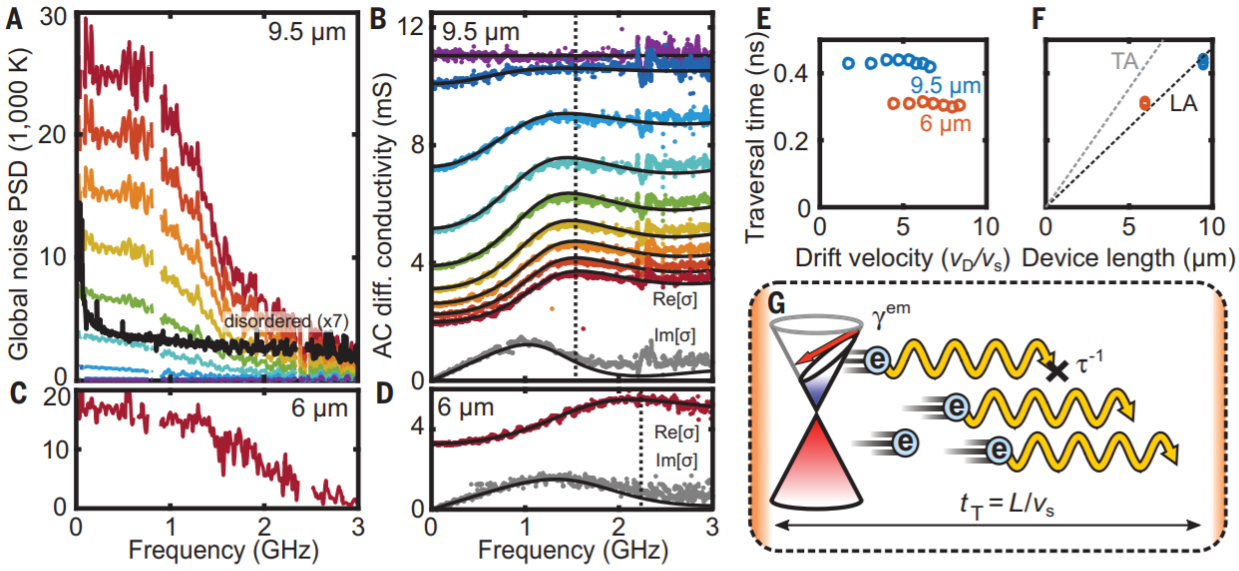


Figure 2.6: Slow dynamics in global electronic measurements. (A) Global noise spectra at $n = 2 \cdot 10^{12}$ cm^{-2}. Colored curves: clean device A2 (9.5 μm by 11 μm) at bias ranging from 0 to 0.8 V (bottom to top). Black curve: disordered device B1 at maximum power applied to device A2 (scaled 7x). (B) AC differential conductivity spectra (excitation: −20 dBm) (see Appendix A3.1 for calibration technique) with biases 0 to 0.8 V (top to bottom, colors same as in (A)). The real (Re) component is suppressed at low frequencies. Gray curve: imaginary (Im) component at 0.8 V. Black curves are fits. (C and D) Features in noise and conductivity spectra shift to higher frequencies in a shorter (6 μm) device (device A1) under similar electric field as maximum in (A) and (B). (E and F) Extracted traversal time from (B) and (D) as a function of drift velocity and device length. Dashed curves correspond to speed of sound in graphene (light gray, transverse acoustic (TA); dark gray, longitudinal acoustic (LA)). (G) Cartoon of important rates in the driven electron-phonon system. During Cherenkov amplification, the correlation time observed in electronic measurements is limited by the phonon traversal time, $t_T = L/v_s$.

The observed spectrum, spatial dependence, and scale of the anomalous noise are inconsistent with conventional noise sources (such as $1/f$ or white thermal/shot noise) (*62*). Our observations, especially the slow time scales and their independence on electronic parameters, are incompatible with many purely electronic mechanisms for AC signal generation (*38, 40, 63*) (see further discussion in section 2.5.8) and suggest that other, longer-lived excitations play a role. In particular, the time scales match well with the time it takes for acoustic phonons to traverse the device. Furthermore, the anomalous effects occur only when the electronic drift velocity is higher

than the speed of sound, but emerge at energies that are too low to excite optical phonons and plasmons ($2\hbar k_{\mathrm{F}} v_{\mathrm{D}}, k_{\mathrm{B}} T < 20$ meV, where $\hbar$ is the reduced Planck constant, k_{F} is the Fermi wavevector, and k_{B} is the Boltzmann constant).

All of our observations are consistently explained as an electron-phonon Cherenkov instability. The key insight is that when the electronic drift velocity exceeds the speed of sound, a cone of forward-moving acoustic phonon modes experiences a faster rate of stimulated emission ($\gamma_{\boldsymbol{q}}^{\mathrm{em}}$) than absorption ($\gamma_{\boldsymbol{q}}^{\mathrm{abs}}$) (*45-48*). For the emitted phonons to amplify, $\gamma_{\boldsymbol{q}}^{\mathrm{em}}$ must exceed the loss rate due to absorption and other decay sources. Pristine graphene exhibits long acoustic phonon lifetimes ($\tau_{\boldsymbol{q}}$) (*64*), thus an emitted phonon can stimulate the emission of more phonons, leading to exponential growth (Figure 2.6G). This process is seeded by a wide spectrum of spontaneously emitted and thermal phonons and is therefore expected to have limited coherence. Stochastic electronic scattering with the growing phonon population is expected to reduce the conductivity and increase noise.

To model these effects, we analyze the coupled electron-phonon dynamics by including the influence of the phonons on the electronic scattering rate, Γ_{e} (see section 2.5.1):

$$\partial_t \boldsymbol{j}(\boldsymbol{r}, t) = D\boldsymbol{E}(\boldsymbol{r}, t) - \Gamma_e(\{n_{\boldsymbol{q}}\})\boldsymbol{j}(\boldsymbol{r}, t), \tag{2.23}$$

$$\partial_t n_{\boldsymbol{q}} = -\frac{(n_{\boldsymbol{q}} - n_{\boldsymbol{q},0})}{\tau_{\boldsymbol{q}}} + \gamma_{\boldsymbol{q}}^{em}(\boldsymbol{j}) \cdot (n_{\boldsymbol{q}} + 1) - \gamma_{\boldsymbol{q}}^{\mathrm{abs}}(\boldsymbol{j}) \cdot n_{\boldsymbol{q}}^{\mathrm{abs}} - v_s \hat{\boldsymbol{q}} \cdot \nabla n_{\boldsymbol{q}}. \tag{2.24}$$

Here, $D = 2e^2 v_{\mathrm{F}} k_{\mathrm{F}}/h$ is the Drude weight of graphene, $E(\boldsymbol{r}, t)$ is the electric field, $n_{\boldsymbol{q}}$ is the phonon occupation at wavevector $\boldsymbol{q}$, $n_{\boldsymbol{q},0}$ is the equilibrium phonon occupation when the current density, $\boldsymbol{j}$, is zero, and $\tau_{\boldsymbol{q}}^{-1}$ is assumed to be dominated by anharmonic interactions. Although we describe the phonon population using second quantization, the results can also be obtained through a semiclassical treatment. Using known constants for the electron-phonon coupling and

anharmonic decay, we find that phonon amplification $\Gamma_{\boldsymbol{q}}^{\mathrm{amp}} = \gamma_{\boldsymbol{q}}^{\mathrm{em}} - \gamma_{\boldsymbol{q}}^{\mathrm{em}} - \tau_{\boldsymbol{q}}^{-1} > 0$ can be easily achieved for a wide range of parameters (see more detailed discussion in sections 2.5.2 and 2.5.3). For instance, the parameters used in Figure 2.5D ($v_{\mathrm{D}} = 5.8v_{\mathrm{s}}$) give a maximum $\gamma_{\boldsymbol{q}}^{\mathrm{em}} - \gamma_{\boldsymbol{q}}^{\mathrm{abs}} =$ 11 GHz at $q \sim 2\pi/(25\text{ nm})$, where $\tau_{\boldsymbol{q}}^{-1} = 0.02$ GHz. The amplification of stochastically emitted phonons is expected to cause large fluctuations in the local electronic scattering rate, thus generating current noise. Due to the Poissonian nature of phonon emission, the fluctuations are expected to scale with the mean emission rate, which is proportional to $n_{\boldsymbol{q}}$. We thus plot the spatial profile of the excess phonon population ($\sim e^{\Gamma_{\mathrm{amp}}\mathrm{x}/v_{\mathrm{s}}} - 1$) associated with Γ_{amp} ~11 GHz (dashed black curve) along with the noise profile in Figure 2.5D, and find good agreement with our experimental results. Integrating over more modes gives a similar profile, indicating the dominance of the most-amplified modes. This amplification behavior is also consistent with our global measurements, where the anomalous noise increases with device length (see Appendix A4.3).

The model also predicts that the electron-phonon Cherenkov instability gives rise to a conductivity spectrum of the form:

$$\sigma(\omega) = \frac{\sigma^{\mathrm{Drude}}(0)}{1 - \frac{iK}{\omega t_{\mathrm{T}}}(1 - e^{i\omega t_{\mathrm{T}}})}, \tag{2.25}$$

where $\sigma^{\mathrm{Drude}} = D/\Gamma_{\mathrm{e}}$ is the usual dc Drude conductivity and K is an increasing function of $\Gamma_{\boldsymbol{q}}^{\mathrm{amp}}$ (see derivation in section 2.5.4). Importantly, $\sigma(\omega)$ depends on the sample traversal time for phonons, $t_{\mathrm{T}} = L/v_{\mathrm{s}}$, where L is the device length. When Cherenkov amplification occurs, the correlation time probed in conductivity measurements is no longer limited by the individual electron and phonon lifetimes but by the traversal time, because the memory of an emission event is amplified until the phonons reach the edge (reflected, backward-moving modes are no longer

amplified). To account for the variation in t_T with phonon emission angle, we sum over a cone in phonon phase space in our fits. Our model gives excellent agreement with the observed conductivity spectra (Figure 2.6B and D, black curves) and even predicts the slight oscillatory behavior due to the sharp transit time cutoff. The extracted traversal time is independent of drift velocity (Figure 2.6E), and the corresponding speed matches that of the longitudinal acoustic mode in graphene (Figure 2.6F) (*65*).

The extension of the correlation time is expected to also cause noise in the same low-frequency range, consistent with our observations (Figure 2.6A and C). Whereas the stochastic emission of a phonon normally causes a small drop in current that only lasts for $\Gamma_e^{-1} \sim$ picoseconds, Cherenkov amplification both prolongs and magnifies the effect. The emitted phonon stimulates cascading emission of subsequent phonons, causing the current to continue decreasing until the phonon packet reaches the device edge. This should give strong current correlations $\langle \delta j(t) \delta j(t+\tau) \rangle$ for long τ (up to $t_T \sim 100$ ps) and thus noise at low frequencies $\lesssim 1/t_T$.

Cherenkov amplification is sensitive to the phonon lifetime, and the effect is therefore expected to intensify at lower temperatures because of slower anharmonic decay (*66*). We observe a strong increase in noise as the temperature is reduced from 300 to 10 K (Figure 2.7A), in clear contrast to the decreasing thermal noise observed at low drives ($v_D \lesssim v_s$). This suggests that the amplification process is limited by scattering with thermally occupied modes at energies similar to that of the amplified mode (7 THz ~ 50 K at $n = 2 \cdot 10^{12}$ cm^{-2}).

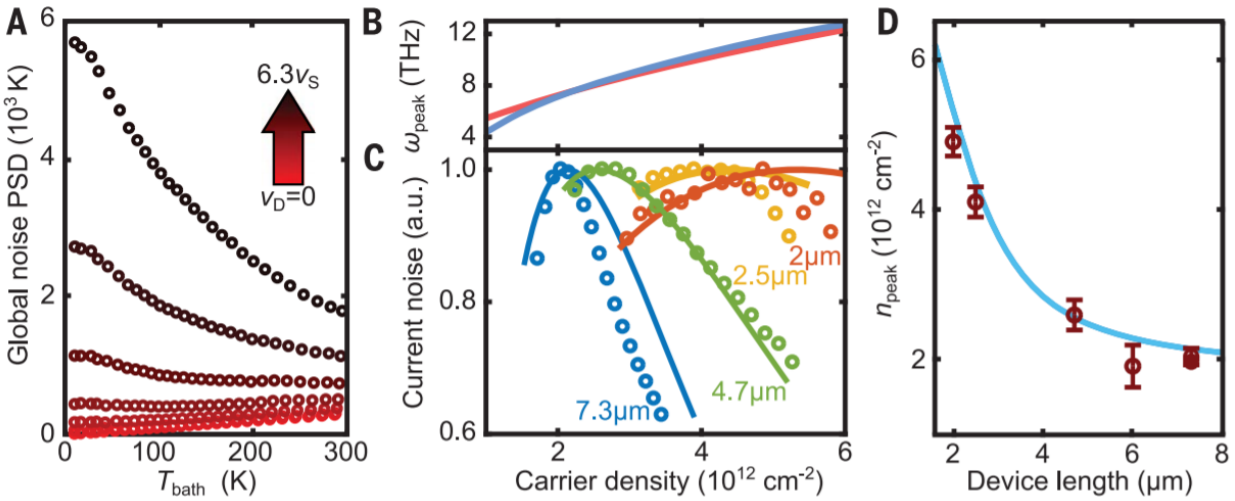


Figure 2.7: Dependence on bath temperature and charge density. (A) Global noise PSD as a function of bath temperature at constant drift velocities and $n = 2 \cdot 10^{12}$ cm^{-2}. (B) Calculated peak phonon emission frequency, which can be tuned via the graphene carrier density (blue: $T_e = 0$ K; red: $T_e = 320$ K). (C) Normalized global current noise as a function of carrier density for different device lengths ($j = 0.6$ mA/μm). Solid curves show predicted total phonon emission. (D) The charge density at which the noise peaks (n_{peak}) for a wider variety of samples than in (C), with fit (blue). Error bars represent sampling spacing of carrier densities.

Another important aspect of Cherenkov amplification in graphene is that the peak emission frequency is tunable via the carrier density, n (Figure 2.7B). This peak occurs just below the upper limit $\omega \sim 2v_s k_F$, corresponding to transitions across the entire Fermi surface. The frequency tunability manifests as a nonmonotonic dependence of the global current noise on n (Figure 2.7C, see unnormalized data in Appendix A4.3). Initially, the noise increases with n, because the larger Fermi surface permits emission of more (and higher-energy) modes. In other words, increasing n broadens Γ_q^{amp}. However, its maximum value decreases at constant current because $v_D = j/(ne)$, eventually causing a downturn in noise.

The crossover density, n_{peak}, is determined by the relative importance of the width and maximum of Γ_q^{amp}, which depends on the device length. Analogously to an active filter, the

amplification process narrows the excess phonon distribution $n_{\boldsymbol{q}} \sim e^{\Gamma_{\boldsymbol{q}}^{\mathrm{amp}} x/v_{\mathrm{s}}}$ as it traverses the device. In longer devices, the noise therefore depends more on the maximum of $\Gamma_{\boldsymbol{q}}^{\mathrm{amp}}$ than its width, causing a smaller n_{peak}. We observe such a length dependence, shown in Figure 2.7C and D in terms of current noise to facilitate comparison with the model. Plotting the predicted total phonon emission along with the data, we find that our model reproduces both the peak shift and narrowing well (see theoretical discussion in section 2.5.6).

These considerations show that our observations are well explained as an electron-phonon Cherenkov instability in a 2D material. This driven electron-phonon system shows rich nonequilibrium dynamics that merit further exploration, potentially by developing new techniques to directly characterize the phonon spectrum. Prior theoretical work predicts that the amplified phonons in graphene have frequencies as high as 10 THz (*48*), substantially higher than those observed in other materials (*49, 50, 52*). Moreover, this system can offer purely electrical generation and amplification of phonons in a single micrometer-scale device, with wide frequency tunability. Future work could explore coupling to a mechanical cavity to develop a phononic laser, as well as outcoupling of the amplified sound waves to far-field terahertz radiation. Our results represent a promising step toward a new generation of active phononic and photonic devices based on 2D materials.

2.5 Theory of Cherenkov instability

2.5.1 Coupled electron-phonon dynamics

The dynamics of our system could in principle be modeled by a complete Boltzmann treatment of both electronic and phononic degrees of freedom. However, at the high electronic temperatures reached in our experiments, rapid e-e collisions ensure that the electronic system reaches local

equilibrium at much shorter timescales (< 1 ps) than those probed here. Therefore, a full Boltzmann framework is not necessary, and we can instead represent the electronic system by the three variables governing its equilibrium distribution. These include the electronic temperature T_e, charge density n, and drift velocity v_{D}. The electrostatic gate keeps the charge density spatially uniform, and we shall assume that the effects of variations in electronic temperature are negligible as well. Indeed, the temperature profile has been found to be relatively uniform in the high-bias regime (*67, 68*), and temperature-induced changes in chemical potential are suppressed in the degenerate regime ($\mu \gg k_{\mathrm{B}}T_{\mathrm{e}}$). Moreover, we show in section 2.5.2 that the net phonon emission rate is only weakly dependent on electronic temperature. In order to connect our theory to measured quantities, we will often refer to the current density $j = nev_{\mathrm{D}}$ instead of the drift velocity. We do not make the same equilibrium assumption about the phononic system, and will treat each phonon mode separately. Our model then takes the form of a modified Drude formula, which explicitly accounts for the dependence of the electronic scattering rate Γ_{e} on the phonon population $n_{\boldsymbol{q}}$:

$$\partial_t \boldsymbol{j}(\boldsymbol{r},t) = D\boldsymbol{E}(\boldsymbol{r},t) - \Gamma_e(\{n_{\boldsymbol{q}}\})\boldsymbol{j}(\boldsymbol{r},t), \tag{2.26}$$

$$\begin{aligned}\partial_t n_{\boldsymbol{q}} = -\frac{\left(n_{\boldsymbol{q}} - n_{\boldsymbol{q},0}\right)}{\tau_{\boldsymbol{q}}} + \gamma_{\boldsymbol{q}}^{em}(\boldsymbol{j}) \cdot \left(n_{\boldsymbol{q}} + 1\right) - \gamma_{\boldsymbol{q}}^{\mathrm{abs}}(\boldsymbol{j}) \cdot n_{\boldsymbol{q}}^{\mathrm{abs}} - v_s\hat{\boldsymbol{q}} \cdot \nabla n_{\boldsymbol{q}} = \\ \overbrace{\left(\gamma_{\boldsymbol{q}}^{\mathrm{em}}(\boldsymbol{j}) - \gamma_{\boldsymbol{q}}^{\mathrm{abs}}(\boldsymbol{j}) - \tau_{\boldsymbol{q}}^{-1}\right)}^{\equiv \Gamma_{\boldsymbol{q}}^{\mathrm{amp}}(\boldsymbol{j})} \cdot n_{\boldsymbol{q}} + n_{\boldsymbol{q},0}\tau_{\boldsymbol{q}}^{-1} + \gamma_{\boldsymbol{q}}^{em}(\boldsymbol{j}) - v_s\hat{\boldsymbol{q}} \cdot \nabla n_{\boldsymbol{q}},\end{aligned} \tag{2.27}$$

where $D = 2e^2 v_{\mathrm{F}} k_{\mathrm{F}}/h$ is the Drude weight of graphene, $\boldsymbol{E}(\boldsymbol{r},t)$ is the electric field, $D = 2e^2 v_{\mathrm{F}} k_{\mathrm{F}}/h$ is the Drude weight of graphene, $E(\boldsymbol{r},t)$ is the electric field, $n_{\boldsymbol{q}}$ is the phonon

occupation at wavevector $\boldsymbol{q}$, $n_{\boldsymbol{q},0}$ is the equilibrium phonon occupation when the current density, $\boldsymbol{j}$, is zero, and $\tau_{\boldsymbol{q}}^{-1}$ is assumed to be dominated by anharmonic interactions. $\gamma_{\boldsymbol{q}}^{\mathrm{em}}$ and $\gamma_{\boldsymbol{q}}^{\mathrm{abs}}$ are the stimulated emission and absorption rates per phonon (calculated in section 2.5.2). In the derivations shown here, the only assumptions made about the electronic scattering rate Γ_e are: 1) that it depends on the phonon population $n_{\boldsymbol{q}}$, and 2) that we can use an average electronic lifetime to write equations for the current. Both of these assumptions are well supported in the literature (*66, 69, 70*), and can simply be thought of as a phonon-dependent resistance. Although not used explicitly here, the specific form of $\Gamma_e(\{n_{\boldsymbol{q}}\})$ can be found in Refs. (*65, 69, 70*). In our experiment, we apply a DC voltage across the device (in addition to a weak AC excitation in conductivity measurements), and we will define $\hat{\boldsymbol{x}}$ to point along the applied field. Since the electric field is uniform in the transverse ($\hat{\boldsymbol{y}}$) direction, the steady state current $\langle \boldsymbol{j} \rangle = \langle j \rangle \hat{\boldsymbol{x}}$ and phonon occupation $\langle n_{\boldsymbol{q}} \rangle$ are too. (Here, and in what follows, we use $\langle\ \rangle$ to refer to temporal averages). Moreover, the high energy cost of local charge buildup entails that $\langle j \rangle$ is divergence-free and thus independent of x as well. We emphasize therefore that $\langle j \rangle$ is an entirely global property of the sample. The phonon occupation, on the other hand, will change along the sample due to the convective term in eqn. (2.27). We find the steady state spatial profile $\langle n_{\boldsymbol{q}}(x) \rangle$:

$$\langle n_{\boldsymbol{q}}(x) \rangle = n_{\boldsymbol{q},0} e^{\langle \Gamma_{\boldsymbol{q}}^{\mathrm{amp}} \rangle x / v_{\boldsymbol{q}}} + \frac{1}{\langle \Gamma_{\boldsymbol{q}}^{\mathrm{amp}} \rangle \tau_{\boldsymbol{q}}} (n_{\boldsymbol{q},0} + \tau_{\boldsymbol{q}} \langle \gamma_{\boldsymbol{q}}^{\mathrm{em}} \rangle) \left(e^{\langle \Gamma_{\boldsymbol{q}}^{\mathrm{amp}} \rangle x / v_{\boldsymbol{q}}} - 1 \right), \tag{2.28}$$

where $v_{\boldsymbol{q}} = v_s \hat{\boldsymbol{q}} \cdot \hat{\boldsymbol{x}}$. Clearly, the phonon population increases exponentially through the sample for wavevectors $\boldsymbol{q}$ that have $\Gamma_{\boldsymbol{q}}^{\mathrm{amp}} > 0$. This is the expression plotted in Figure 2.5D in section 2.4. Since we expect the measured local current noise to be due to local fluctuations in phonon emission (section 2.5.7), which is a Poissonian process, it should scale with the (local) mean emission rate. The latter is proportional to $n_{\boldsymbol{q}}$, so the current noise profile should be representative of the spatial

distribution of phonons. Seeing as the most amplified modes dominate strongly in long samples like the one shown in Figure 2.5D (L = 17 μm), we plot $n_{\boldsymbol{q}}(x)$ for the most amplified mode. Including background effects (thermal noise and intrinsic NV decay), we find that the current noise should be of the form $\langle \delta j^2 \rangle(x) = A + Be^{\Gamma_{\max}^{\mathrm{amp}} x/v_s}$. In Figure 2.8, we show that integrating over all modes gives a similar result, due to the dominance of the most amplified modes. Finally, we note that eqn. (2.28) breaks down for $\hat{\boldsymbol{q}}$ with large transverse components, due to the finite width of our samples. The treatment of these modes is discussed further in the end of section 2.5.4.

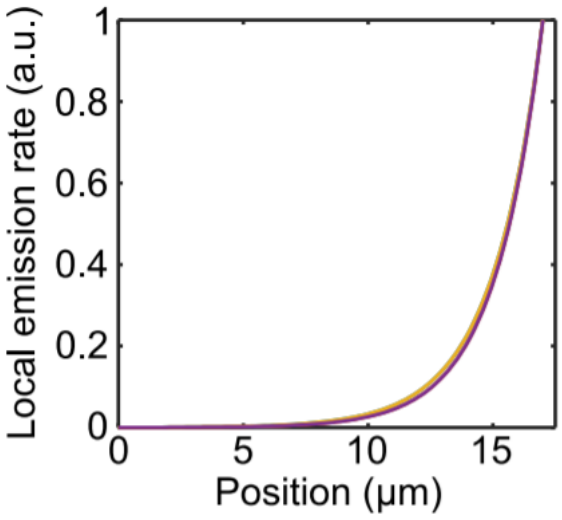


Figure 2.8: Spatial dependence. Normalized local emission rate of most amplified mode ($\Delta\gamma_{\boldsymbol{q}} n_{\boldsymbol{q}}(x) \propto n_{\boldsymbol{q}}(x)$, purple), and integrated over phonon modes (yellow), for the parameters used in Figure 2.5D (j=0.18 mA/μm, $n = 2 \cdot 10^{12}$ cm^{-2}, $\max(\Gamma^{\mathrm{amp}}) = 10.9$ GHz). Due to the dominance of the most amplified modes, the two curves are very similar. The purple curve has a slightly sharper upturn due to the higher amplification rate.

2.5.2 Phonon emission rate

In order to determine the net emission rate $\Delta\gamma_{\boldsymbol{q}} = \gamma_{\boldsymbol{q}}^{\mathrm{em}} - \gamma_{\boldsymbol{q}}^{\mathrm{abs}}$ of a phonon mode with wavevector $\boldsymbol{q}$, we sum over all electronic transitions accompanying the emission/absorption event:

$$\Delta\gamma_{\boldsymbol{q}} = \gamma_{\boldsymbol{q}}^{\mathrm{em}} - \gamma_{\boldsymbol{q}}^{\mathrm{abs}}$$

$$= \frac{2\pi N}{\hbar}\sum_{\boldsymbol{k},\boldsymbol{k}'}\left|C_{\boldsymbol{k},\boldsymbol{k}',\boldsymbol{q}}\right|^2\left(f_{\boldsymbol{k}}(1-f_{\boldsymbol{k}'}) - f_{\boldsymbol{k}'}(1-f_{\boldsymbol{k}})\right)\cdot\delta_{\boldsymbol{k}-\boldsymbol{k}',\boldsymbol{q}}\cdot\delta(\epsilon_{\boldsymbol{k}} - \epsilon_{\boldsymbol{k}'} - \hbar v_{\mathrm{s}}|\boldsymbol{q}|), \tag{2.29}$$

where the first term represents an electron moving from $\boldsymbol{k}$ to $\boldsymbol{k}'$ while emitting a phonon, and the second represents an electron moving from $\boldsymbol{k}'$ to $\boldsymbol{k}$ while absorbing a phonon. Here, v_{s} is the speed of sound, $N = 4$ is the number of valley/spin flavors, $\epsilon_{\boldsymbol{k}} = \hbar v_{\mathrm{F}}|k|$ is the electron energy, $f_{\boldsymbol{k}} = \left(e^{\beta(\hbar(v_{\mathrm{F}}|\boldsymbol{k}|-\boldsymbol{k}\cdot\boldsymbol{v_D})-\epsilon_{\mathrm{F}})}+1\right)^{-1}$ is the drifting Fermi-Dirac distribution with drift velocity v_{D}, and $\left|C_{\boldsymbol{k},\boldsymbol{k}',\boldsymbol{q}}\right|^2$ is the deformation potential coupling matrix element (*65, 69, 70*):

$$\left|C_{\boldsymbol{k},\boldsymbol{k}',\boldsymbol{q}}\right|^2 = \frac{D^2\hbar q}{2\rho A v_{\mathrm{s}}}\cos^2(\theta_{\boldsymbol{k},\boldsymbol{k}'}/2) \tag{2.30}$$

Here, D is the deformation potential, ρ is the (2D) mass density, A is the sample area, and $\theta_{\boldsymbol{k},\boldsymbol{k}'}$ is the angle between $\boldsymbol{k}$ and $\boldsymbol{k}'$. At zero drift velocity, $f_{\boldsymbol{k}}$ is simply a (decreasing) function of $\epsilon_{\boldsymbol{k}}$, and one therefore finds that every term in eqn. (2.29) is negative. At higher v_{D}, however, the Fermi surface becomes tilted (Figure 2.9A), causing higher-energy states on one side of the Dirac cone to have higher occupation than lower energy states on the other side. In order to achieve positive terms in eqn. (2.29), the Fermi surface must become steeper than the phonon-assisted transitions (red arrow), which gives the Cherenkov criterion, $v_{\mathrm{D}} > v_{\mathrm{s}}$. We here emphasize that this phenomenon is very different from the effects of high electronic temperatures. While the latter allows for the probabilistic occupation of higher energy states, the mean occupation is still a decreasing function of energy, causing $\Delta\gamma$ to remain negative. Figure 2.9B shows the numerically calculated net emission rate at various electronic drift velocities, using deformation potential $D = 20$ eV. When the drift velocity exceeds the speed of sound, stimulated emission dominates over absorption ($\Delta\gamma > 0$) for a cone in phonon phase space moving along with the carrier flow. We find

that the highest net emission rate exceeds 5 GHz already at $v_D = 2v_s$, and increases all the way up to 40 GHz at $v_D = 10v_s$. The net emission rates greatly exceeds the rate of phonon decay (section 2.5.2), as such $\Gamma_{\boldsymbol{q}}^{amp} > 0$ and phonon Cherenkov amplification is predicted to occur. At zero temperature, phonon amplification occurs for modes with wavevectors up to $2k_F$, corresponding to electronic transitions across the entire Fermi surface. As expected, this upper bound is found to be less sharp at higher temperatures (Figure 2.9C). However, the region near the peak (which dominates after nonlinear amplification) is relatively insensitive to electronic temperature, since absorption and stimulated emission change by a similar amount. Finally, we note that a different coupling rate may result from considerations of a gauge potential coupling (*71*). However, we expect this to only modify the scale of the coupling rate, and to result in even higher emission rates. In particular, it should not change the qualitative behavior of net stimulated emission when $v_D > v_s$.

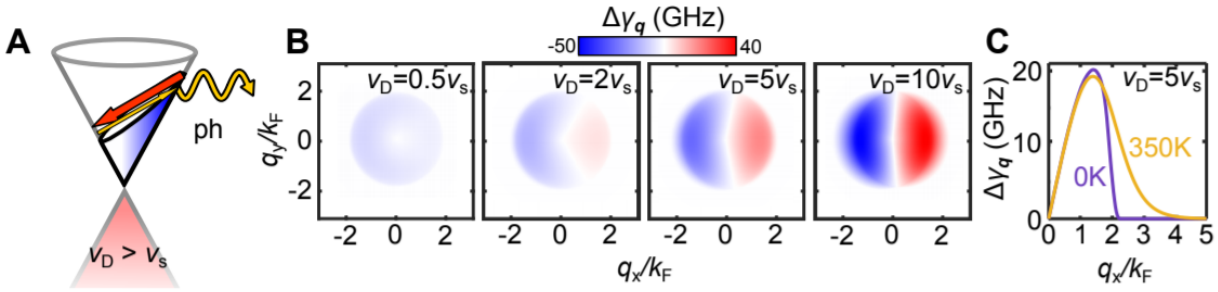


Figure 2.9: Onset of Cherenkov emission. (A) Cartoon showing Cherenkov criterion for graphene. When $v_D > v_s$, the electronic population becomes inverted with respect to phonon-induced transitions. As a result, the phonon emission rate (red arrow) becomes greater than the absorption rate (yellow arrow). (B) Net emission rate $\Delta\gamma_{\boldsymbol{q}}$ vs. phonon wavevector $\boldsymbol{q}$ at various electronic drift velocities in the x-direction, $n = 2 \cdot 10^{12}$ cm^{-2} and zero electronic temperature. Once the drift velocity exceeds the speed of sound ($v_s = 21$ km s$^{-1} = 0.021v_F$), we find regions of phononic phase space where $\Delta\gamma_{\boldsymbol{q}} > 0$ (red), indicating that stimulated emission dominates over absorption. This effect is strongest for the phonon modes moving along the current. The circle sector in which the amplification criterion is satisfied becomes wider as the drift velocity increases, and eventually saturates as a semi-circle. (C) Line cut along $q_y = 0$ for electronic temperatures $T_e = 0$ K and 350 K at $v_D = 5v_s$.

2.5.3 Phonon decay rate

As explained in Refs. (*64, 66, 72*), the acoustic phonon decay rate $\tau_{\boldsymbol{q}}^{-1}$ in graphene becomes very slow at low temperatures, especially for the small phonon energies relevant in our experiment ($\sim$ THz). Indeed, this is one of the main reasons graphene has such an exceptional thermal conductivity (*73*). Here, we discuss the three types of decay pathways considered in Ref. (*64*) for the relevant phonon modes, in order to demonstrate that Cherenkov amplification can easily occur ($\Delta\gamma_{\boldsymbol{q}} > \tau_{\boldsymbol{q}}^{-1}$) at the drift velocities reached in our experiment. Since the decay rate is found to be very small compared to $\Delta\gamma$, we emphasize that our fits depend only very weakly on the exact numerical value of the decay rate. First, we shall consider point-defect scattering, given by:

$$\gamma^{\mathrm{PD}} = \frac{S_0\omega^3}{v_s^2} \cdot \sum\nolimits_i p_i \left(1 - \frac{M_i}{\bar{M}}\right)^2, \tag{2.31}$$

where S_0 is the atomic cross-sectional area and $\bar{M}$ is the average atomic mass. p_i and $M_i$are the percentage and atomic mass of defect type *i*. Considering the contribution from 1% natural abundance of ^{13}C, one finds $\gamma^{\mathrm{PD}} \sim 1.5$ MHz at $\omega = 5$ THz, which is clearly much smaller than $\Delta\gamma$. Due to the low impurity content in our exfoliated graphene samples, we do not expect significantly larger contributions from other defect types. We then proceed to consider anharmonic decay, where our mode of interest interacts with two other modes, with wavevectors q' and q'', and energies ω' and ω''. These processes can be divided into two types, based on the hierarchy of the three phonon energies: I) $\omega'' > \omega, \omega'$, and II) $\omega > \omega', \omega''$. Following Ref. (*64*), the rate of the two processes are given by:

$$\gamma_{\boldsymbol{q}}^{\mathrm{I}} = \frac{2\pi}{\hbar} \sum_{\boldsymbol{b}} \sum_{s',s''} \sum_{\boldsymbol{q}',\boldsymbol{q}''} \left|C_{\omega,\omega',\omega''}\right|^2 [n(\omega') - n(\omega'')]\delta(\omega'' - \omega' - \omega)\delta_{\boldsymbol{q}'',\boldsymbol{q}+\boldsymbol{q}'+\boldsymbol{b}}, \tag{2.32}$$

$$\gamma_{\boldsymbol{q}}^{\mathrm{II}} = \frac{2\pi}{\hbar}\sum_{\boldsymbol{b}}\sum_{s',s''}\sum_{\boldsymbol{q}',\boldsymbol{q}''}\left|C_{\omega,\omega',\omega''}\right|^2[n(\omega')+n(\omega'')+1]\delta(\omega-\omega''-\omega')\delta_{\boldsymbol{q},\boldsymbol{q}''+\boldsymbol{q}'+\boldsymbol{b}'} \qquad (2.33)$$

where $\boldsymbol{b}$ is a lattice vector. Non-zero $\boldsymbol{b}$ correspond to Umklapp scattering, where total phonon momentum is not conserved. At the low temperatures and small $\boldsymbol{q}$ considered here, normal processes ($\boldsymbol{b} = 0$) are expected to dominate strongly, so we consider only these. While these do not reduce thermal conductivity (since they conserve momentum), they are still expected to affect Cherenkov amplification, since they can scatter phonon modes out of the amplified region of phononic phase space. s' and s'' represent the branches that our mode interacts with; as shown in Ref. (*64*), the small-$\boldsymbol{q}$ LA modes considered here are expected to predominantly interact with TA and LA modes in our hBN-encapsulated devices. $n(\omega)$ is the phonon distribution function. Since only a small part of the total phonon phase space experiences Cherenkov amplification, we here assume that the amplified modes mainly interact with non-amplified modes that remain close to thermal equilibrium. We therefore set $n(\omega)$ to be the Bose-Einstein distribution $n(\omega) = \left(e^{-\beta\hbar\omega}-1\right)^{-1}$ at bath temperature ($\beta = (k_{\mathrm{B}}T_{\mathrm{bath}})^{-1}$). Finally, $\left|C_{\omega,\omega',\omega''}\right|^2$ is the coupling matrix element:

$$\left|C_{\omega,\omega',\omega''}\right|^2 = \frac{2\gamma_{\mathrm{G}}\omega\omega'\omega''\hbar}{3\rho v_s^2 A}, \qquad (2.34)$$

where γ_{G} is the Gruneisen parameter. γ_{G} is in principle mode-dependent, but we have here replaced it with an average value ($\gamma_{\mathrm{G}} = 2$), as often done in the literature. As before, ρ is the (2D) mass density, and A is the device area, which we note is canceled out when turning the sum over wavevectors into an integral. We plot $\gamma_{\boldsymbol{q}}^{\mathrm{I}} + \gamma_{\boldsymbol{q}}^{\mathrm{II}}$ for a relevant range of phonon wavevectors in Figure 2.10, and find that these decay rates are faster than γ^{PD}, but still much slower than typical values of $\Delta\gamma$. The third decay pathway that we shall discuss is scattering off the rough device

edges. Indeed, we assume that the phonons decay when they have traversed the sample and reach the sample edge. This is not only due to the absorption at the edge, but also because the reflected (backwards-moving) modes are no longer in the amplified region of phonon phase space, and are thus quickly absorbed by the electronic system. Phonon amplification is strongest for modes moving at small angles with the source-drain axis, and the emission of these is expected to impact the current most strongly due to the large momentum transfer in the direction of current. Nevertheless, in the end of section 2.5.4, we discuss the treatment of modes that move at large enough angles to hit the side edges before traversing the whole device.

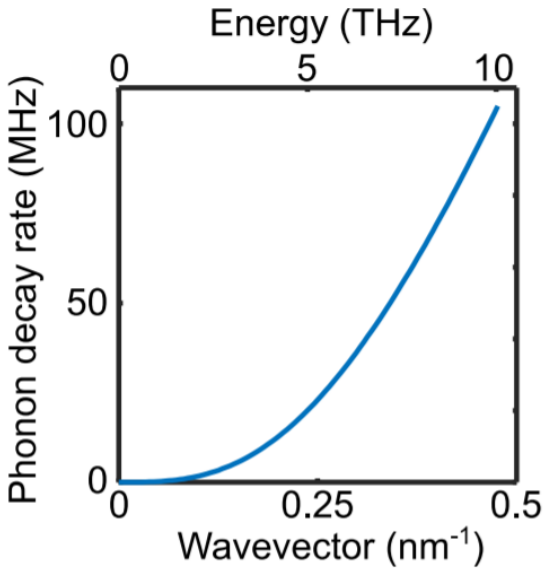


Figure 2.10: Phonon decay rate. Phonon decay rate (calculated from eqns. (2.32) and (2.33)) versus phonon wavevector q and energy $v_s q$.

2.5.4 AC conductivity in Cherenkov instability

In order to find the AC conductivity, we consider the current response to a voltage $V(t) = V_0 + \delta V e^{i\omega t}$. Since we are now concerned with only the field-induced (not stochastic) fluctuations, we can apply our argument about $\langle j \rangle$ and $\langle n_{\boldsymbol{q}} \rangle$ (section 2.5.1) to the oscillations δj and $\delta n_{\boldsymbol{q}}$ as well.

In other words, we have the simplifications $\delta \boldsymbol{j}(\boldsymbol{r},t) = \delta j(t)\hat{\boldsymbol{x}}$ and $\delta n_{\boldsymbol{q}}(\boldsymbol{r},t) = \delta n_{\boldsymbol{q}}(x,t)$, and can thus treat this as a 1D problem. Since $n_{\boldsymbol{q}}$ (and thus the scattering rate $\Gamma_{\mathrm{e}}(\{n_{\boldsymbol{q}}\})$) can vary with x, the electric field $\boldsymbol{E} = \left(E_0(x) + \delta E(x)e^{i\omega t}\right)$ can too. Analogously to a series of resistors, the applied potential difference is divided unequally across the resistors if they do not have the same resistance. Fortunately, this does not affect us for now, because we can only measure the global AC conductivity anyway:

$$\sigma = \frac{\delta j}{\delta V/L} = \frac{\delta j}{\frac{1}{L}\int_0^L \delta E(x)dx} = \frac{1}{\frac{1}{L}\int_0^L \sigma^{-1}(x)dx}, \tag{2.35}$$

where L is the length of the device. This is nothing but the spatially averaged conductivity (in reciprocal), and is completely equivalent to adding resistors in series. In order to make any sensible comparison with experiment, we should therefore integrate eqn. (2.26) over x:

$$\partial_t j = \frac{DV(t)}{L} - \overbrace{\frac{1}{L}\int_0^L \Gamma_{\mathrm{e}}\left(\{n_{\boldsymbol{q}}(\boldsymbol{r},t)\}\right)dx}^{\overline{\Gamma_{\mathrm{e}}}} \cdot j(t) \tag{2.36}$$

Here, and in what follows, barred quantities are spatially averaged, while brackets $\langle\ \rangle$ are used for temporal averages. The oscillating parts of $n_{\boldsymbol{q}}$ and j then evolve according to:

$$i\omega\delta j(\omega) = \frac{D\delta V}{L} - \overline{\langle\Gamma_{\mathrm{e}}\rangle}\delta j(\omega) - \sum_{\boldsymbol{q}} \overline{\frac{\partial\Gamma_{\mathrm{e}}}{n_{\boldsymbol{q}}} \cdot \delta n_{\boldsymbol{q}}(x,\omega)} \cdot \langle j\rangle \tag{2.37}$$

$$\begin{aligned} i\omega\delta n_{\boldsymbol{q}}(x,\omega) = {} & \overbrace{\left(\langle\gamma_{\boldsymbol{q}}^{\mathrm{em}}\rangle - \langle\gamma_{\boldsymbol{q}}^{\mathrm{abs}}\rangle - \langle\tau_{\boldsymbol{q}}^{-1}\rangle\right)}^{\langle\Gamma_{\boldsymbol{q}}^{\mathrm{amp}}\rangle} \cdot \delta n_{\boldsymbol{q}}(x,\omega) + \\ & \frac{\partial\Gamma_{\boldsymbol{q}}^{\mathrm{amp}}}{\partial j} \cdot \delta j(\omega)\langle n_{\boldsymbol{q}}(x)\rangle + \overbrace{\frac{\partial\gamma_{\boldsymbol{q}}^{\mathrm{em}}}{\partial j}\delta j(\omega)}^{\text{Spont. emission}} - v_{\mathrm{s}}\hat{\boldsymbol{q}} \cdot \hat{\boldsymbol{x}}\partial_x(\delta n_{\boldsymbol{q}}(x,\omega)) \end{aligned} \tag{2.38}$$

Since both absorption and stimulated emission of phonons are linear processes, we shall assume that Γ_{e} is linear in $n_{\boldsymbol{q}}$, and can therefore write:

$$\overline{\frac{\partial \Gamma_{\mathrm{e}}}{n_{\boldsymbol{q}}} \cdot \delta n_{\boldsymbol{q}}(x,\omega)} = \frac{\partial \Gamma_{\mathrm{e}}}{n_{\boldsymbol{q}}} \cdot \overline{\delta n_{\boldsymbol{q}}(x,\omega)} \tag{2.39}$$

Moreover, we note that although we use $\Gamma_{\boldsymbol{q}}^{\mathrm{amp}}$, our treatment also applies to the non-amplifying case ($\Gamma_{\boldsymbol{q}}^{\mathrm{amp}} < 0$). For now, we shall focus on phonon modes that move in parallel with the current ($\boldsymbol{q} \parallel \hat{\boldsymbol{x}}$). We will discuss the inclusion of larger-angle modes in the end of this section. We can immediately solve for $\delta n_{\boldsymbol{q}}(x,\omega)$ in terms of $\delta j(\omega)$:

$$\delta n_{\boldsymbol{q}}(x,\omega) = v_{\mathrm{s}}^{-1}\delta j(\omega)\int_0^x \left(\frac{\partial \Gamma_{\boldsymbol{q}}^{\mathrm{amp}}}{\partial j}\cdot\langle n_{\boldsymbol{q}}(x')\rangle + \frac{\partial \gamma_{\boldsymbol{q}}^{\mathrm{em}}}{\partial j}\right) e^{\frac{\left(\langle \Gamma_{\boldsymbol{q}}^{\mathrm{amp}}\rangle - i\omega\right)(x-x')}{v_{\mathrm{s}}}} dx' =$$

$$\left[\frac{C}{i\omega} e^{\frac{\langle \Gamma_{\boldsymbol{q}}^{\mathrm{amp}}\rangle x}{v_{\mathrm{s}}}} + \frac{i\omega B - \langle \Gamma_{\boldsymbol{q}}^{\mathrm{amp}}\rangle C}{i\omega\left(\langle \Gamma_{\boldsymbol{q}}^{\mathrm{amp}}\rangle - i\omega\right)} e^{\frac{\left(\langle \Gamma_{\boldsymbol{q}}^{\mathrm{amp}}\rangle - i\omega\right)x}{v_{\mathrm{s}}}} + \frac{C-B}{\langle \Gamma_{\boldsymbol{q}}^{\mathrm{amp}}\rangle - i\omega}\right]\delta j(\omega), \tag{2.40}$$

where

$$B = \frac{\partial \Gamma_{\boldsymbol{q}}^{\mathrm{amp}}}{\partial j}\cdot n_{\boldsymbol{q},0} + \frac{\partial \gamma_{\boldsymbol{q}}^{\mathrm{em}}}{\partial j}, \tag{2.41}$$

$$C = \frac{\partial \Gamma_{\boldsymbol{q}}^{\mathrm{amp}}}{\partial j}\cdot\left(n_{\boldsymbol{q},0} + \frac{n_{\boldsymbol{q},0}}{\langle \Gamma_{\boldsymbol{q}}^{\mathrm{amp}}\rangle \tau_{\boldsymbol{q}}} + \frac{\langle \gamma_{\boldsymbol{q}}^{\mathrm{em}}\rangle}{\langle \Gamma_{\boldsymbol{q}}^{\mathrm{amp}}\rangle}\right) \tag{2.42}$$

Before we can plug this back into the equation for δj, we need to calculate the spatial average:

$$\overline{\delta n_{\boldsymbol{q}}(\omega)} = \frac{1}{L}\int_0^L \delta n_{\boldsymbol{q}}(x,\omega)dx =$$

$$\overbrace{\left[\frac{C}{i\omega t_{\mathrm{T}}\langle \Gamma_{\boldsymbol{q}}^{\mathrm{amp}}\rangle}\left(e^{\langle \Gamma_{\boldsymbol{q}}^{\mathrm{amp}}\rangle t_{\mathrm{T}}} - 1\right) + \frac{i\omega B - \langle \Gamma_{\boldsymbol{q}}^{\mathrm{amp}}\rangle C}{i\omega t_{\mathrm{T}}\left(\langle \Gamma_{\boldsymbol{q}}^{\mathrm{amp}}\rangle - i\omega\right)^2}\left(e^{\left(\langle \Gamma_{\boldsymbol{q}}^{\mathrm{amp}}\rangle - i\omega\right)t_{\mathrm{T}}} - 1\right) + \frac{C-B}{\langle \Gamma_{\boldsymbol{q}}^{\mathrm{amp}}\rangle - i\omega}\right]}^{\tilde{\chi}(\boldsymbol{q},\omega)}\delta j(\omega), \tag{2.43}$$

where $t_{\mathrm{T}} = L/v_{\mathrm{s}}$ is the sample transit time. We have here introduced the current-phonon response function $\tilde{\chi}(\boldsymbol{q}, \omega)$, defined through $\delta n_{\boldsymbol{q}}(\omega) = \tilde{\chi}(\boldsymbol{q}, \omega)\delta j(\omega)$. Inserting this expression back into our expression for $\delta j(\omega)$, we find:

$$\sigma(\omega) = \frac{L\delta j(\omega)}{\delta V(\omega)} = \frac{D}{i\omega + \langle \Gamma_e \rangle + \sum_{\boldsymbol{q}} \frac{\partial \Gamma_{\mathrm{e}}}{\partial n_{\boldsymbol{q}}} \tilde{\chi}(\boldsymbol{q}, \omega)\langle j \rangle} \tag{2.44}$$

As expected, we retrieve the original Drude result if the phonons do not respond to the current ($\tilde{\chi}(\boldsymbol{q}, \omega) = 0$), or the scattering rate does not depend on the phonon occupation ($\frac{\partial \Gamma_{\mathrm{e}}}{\partial n_{\boldsymbol{q}}} = 0$). We note that so far, no mathematical approximations have been made. Eqn. (2.44) has a clear intuitive motivation. A fluctuation $\delta j(\omega)$ will not only decay due to $\langle \Gamma_e \rangle$, but also cause a change in phonon population $\delta n_{\boldsymbol{q}}$, which changes the scattering rate $\delta \Gamma_{\mathrm{e}}(\omega)$:

$$\delta \Gamma_e(\omega) = \sum_{\boldsymbol{q}} \frac{\partial \langle \Gamma_e \rangle}{\partial n_{\boldsymbol{q}}} \delta n_{\boldsymbol{q}}(\omega) = \sum_{\boldsymbol{q}} \frac{\partial \langle \Gamma_e \rangle}{\partial n_{\boldsymbol{q}}} \tilde{\chi}(\boldsymbol{q}, \omega)\delta j(\omega). \tag{2.45}$$

Let's now consider the low-frequency regime ($\omega \ll \Gamma_{\mathrm{e}} \sim$ THz), in the case where certain phonon modes are amplified strongly ($e^{\Gamma^{\mathrm{amp}} t_{\mathrm{T}}} \gg 1$). For these modes, the response function $\tilde{\chi}(\boldsymbol{q}, \omega)$ simplifies to:

$$\tilde{\chi}(\boldsymbol{q}, \omega) = \frac{C}{i\omega t_{\mathrm{T}} \langle \Gamma_{\boldsymbol{q}}^{\mathrm{amp}} \rangle} e^{\langle \Gamma_{\boldsymbol{q}}^{\mathrm{amp}} \rangle t_{\mathrm{T}}} \left(1 - e^{-i\omega t_T}\right) \tag{2.46}$$

Since the strongly amplified modes will have the dominant impact on the AC conductivity, we can apply the above simplifications to all the terms in the sum over $\boldsymbol{q}$ in eqn. (2.44). We then find:

$$\sigma^{\text{Cherenkov}}(\omega) = \frac{D}{\langle\Gamma_e\rangle + \sum_{\boldsymbol{q}} \frac{\partial\Gamma_e}{\partial n_{\boldsymbol{q}}}\langle j\rangle \frac{C}{i\omega t_T \langle\Gamma_{\boldsymbol{q}}^{\text{amp}}\rangle} e^{\langle\Gamma_{\boldsymbol{q}}^{\text{amp}}\rangle t_T}(1 - e^{i\omega t_T})}$$
$$= \frac{\sigma^{\text{Drude}}(0)}{1 + \frac{K}{i\omega t_T}(1 - e^{i\omega t_T})}, \tag{2.47}$$

where $\sigma^{\text{Drude}}(0) = D/\langle\Gamma_e\rangle$ is the regular DC Drude conductivity. Since the contributions from all the amplified phonon modes show the same ω-dependence, we could conveniently factor out the sum over $\boldsymbol{q}$ and define a single dimensionless parameter K:

$$K \equiv \sum_{\boldsymbol{q}} \frac{\partial\Gamma_e}{\partial n_{\boldsymbol{q}}} \frac{\langle j\rangle C e^{\langle\Gamma_{\boldsymbol{q}}^{\text{amp}}\rangle t_T}}{\langle\Gamma_e\rangle\langle\Gamma_{\boldsymbol{q}}^{\text{amp}}\rangle}. \tag{2.48}$$

As mentioned above, eqn. (2.47) was derived for phonon modes moving in the x-direction. Other phonon modes moving at an angle θ with the x-axis have different traversal times $t_T(\theta) = L/(v_s \cos\theta)$, and are thus expected to dampen the oscillations in $\sigma(\omega)$. Indeed, we find that eqn. (2.47) – although capturing the qualitative features of our data – overestimates the amplitude of the oscillations (top curve in Figure 2.11). To account for the spread in emission angles in 2D, we include more phonon modes in the second term of the denominator in eqn. (2.47). The contribution of phonon modes at different angles depends not only on the θ-dependent K, but also on reflections from the side edges of our finite-sized devices. The latter depends on the specularity of the graphene edges. As a first approximation, we average over θ with equal weights up to a maximum angle θ_{max}, and already find improving agreement with the data (Figure 2.11). We find that $\theta_{\text{max}} \sim 60°$ accounts for the spread in t_T well, and therefore use this value for fitting the data in section 2.4. Since this angle is slightly larger than $\tan^{-1}(L/W)$, it suggests that edge reflection plays a small, but not insignificant role. We note that the reported extracted traversal time is the shortest $t_T(\theta)$ in the average ($\min t_T(\theta) = t_T(\theta = 0)$), so that $t_T = L/v_s$ still holds. In order to derive a

more exact angular distribution, one could include the side edge reflection in the model, as well as other θ-dependent effects, including: 1) For a given $|\boldsymbol{q}|$, the amplification rate Γ_e is maximized for $\theta = 0$ and decreases monotonically with increasing angle. 2) Modes with larger θ take longer to traverse the sample, and are thus amplified for a longer time. 3) Phonons with large θ are expected to impact the current less than those moving in parallel with the current, since the large-angle modes remove less longitudinal momentum from the electronic population.

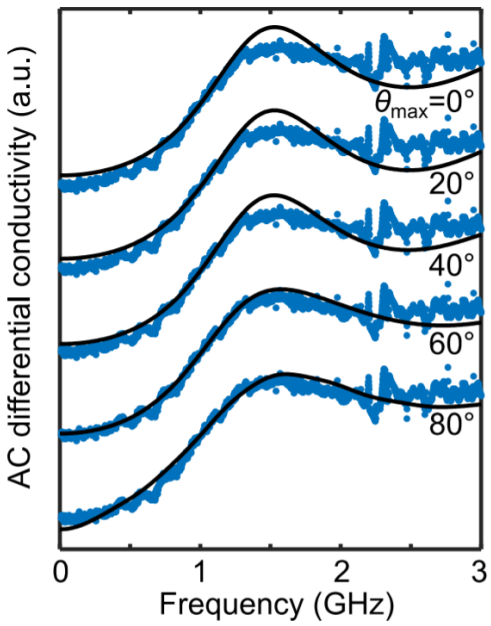


Figure 2.11: Including angular spread of phonon emission. Blue: Measured AC differential conductivity spectrum at 0.8 V bias and $n = 2 \cdot 10^{12}$ cm^{-2} (identical data shifted to show multiple fits). Black curves: Fits by averaging the phonon emission angle up to varying θ_{max}. We find best agreement at $\theta_{max} = 60°$.

2.5.5 Connection between global noise and phonon fluctuations

In order to relate the global noise to phonon fluctuations, we return to eqn. (2.37), but now without an oscillating field, since only a DC field is applied in noise measurements:

$$i\omega\delta j(\omega) = -\overline{\langle\Gamma_e\rangle}\delta j(\omega) - \sum_{\boldsymbol{q}} \overline{\frac{\partial\Gamma_e}{n_{\boldsymbol{q}}} \cdot \delta n_{\boldsymbol{q}}(\omega)} \cdot \langle j\rangle. \tag{2.49}$$

Note that we still operate with the spatially averaged phonon population $\delta n_{\boldsymbol{q}}$, since the global measurements are only sensitive to the uniform component of current fluctuations (other components do not contribute a net current). Solving for the current fluctuations at low frequencies $\omega \ll \Gamma_e \sim$ THz and assuming that the phonon modes are independent, we then find:

$$\langle\delta^2 j(\omega)\rangle = \overline{\langle\Gamma_e\rangle}^{-2} \sum_{\boldsymbol{q}} \left(\frac{\partial\Gamma_e}{\partial n_{\boldsymbol{q}}}\right)^2 \langle\overline{\delta n_{\boldsymbol{q}}(\omega)}^2\rangle \cdot \langle j\rangle^2. \tag{2.50}$$

We here observe that the current fluctuations mimic the behavior of $\delta n_{\boldsymbol{q}}$ at low frequencies, which can be intuitively thought of as the current response to slow variations in the total device resistance. The phonon fluctuations are here given by:

$$\langle\overline{\delta n_{\boldsymbol{q}}(\omega)}^2\rangle = \int_0^L \int_0^L \langle\delta n_{\boldsymbol{q}}(x_1,\omega)\delta n_{\boldsymbol{q}}(x_2,\omega)\rangle dx_1\, dx_2. \tag{2.51}$$

Since an emitted phonon can keep stimulating emission of subsequent phonons as it moves through the sample, we expect $\langle\delta n_{\boldsymbol{q}}(t)\delta n_{\boldsymbol{q}}(t+\tau)\rangle > 0$ for τ up to the traversal time t_T, causing roll-offs in both $\langle\overline{\delta n_{\boldsymbol{q}}(\omega)}^2\rangle$ and $\langle\delta^2 j(\omega)\rangle$ at low frequencies ($< 1/t_T$). We expect that the total phonon fluctuations (integrated over space and modes) scale with the total emission rate, due to the Poissonian nature of phonon emission.

2.5.6 Dependence of global noise on charge density

In order to understand the charge density dependence of phonon amplification, we need to consider the $\boldsymbol{q}$-distribution of phonon emission (Figure 2.12). At low $\boldsymbol{q}$, the net emission rate $\Delta\gamma_{\boldsymbol{q}} = \Delta\gamma_{\boldsymbol{q}}^{\mathrm{em}} - \Delta\gamma_{\boldsymbol{q}}^{\mathrm{abs}}$ increases with q, both because the electron-phonon coupling constant is linear in q, and

because larger q permits more accompanying electronic transitions for phonon emission. However, the emission rate starts decreasing again when q approaches the maximum momentum transfer $2k_{\mathrm{F}}\left(1+\frac{v_{\mathrm{D}}}{v_{\mathrm{F}}}\right) \sim 2k_{\mathrm{F}}$, corresponding to electronic transitions across the entire (shifted) Fermi surface. When the charge density n is increased through electrostatic gating (red to blue to green curve in Figure 2.12A), this upper bound is shifted according to $k_{\mathrm{F}} = \sqrt{\pi n}\left(1-\left(\frac{v_{\mathrm{D}}}{v_{\mathrm{F}}}\right)^2\right)^{3/4}$. This causes a blue-shift of the amplified phonon population, and increases the number of amplified modes. At the same time, however, the amplitude of $\Delta\gamma_{\boldsymbol{q}}$ decreases, because the drift velocity $v_{\mathrm{D}} = j/(ne)$ decreases with n at constant current density. In other words, increasing n causes the emission spectrum to become wider, but smaller in magnitude. We shall see that the competition between these two effects cause a non-monotonic dependence on charge density. As argued in section 2.4, the measured noise is expected to be due to the stochastic emission of phonons, and should scale with the total phonon emission rate due to the Poissonian nature. We thus integrate the phonon generation rate over both space and phonon modes:

$$\int\int_0^L \Delta\gamma_{\boldsymbol{q}} n_{\boldsymbol{q}}(x)dx \cdot qdq. \tag{2.52}$$

where the spatial profile $n_{\boldsymbol{q}}(x)$ is given in eqn. (2.28). We here integrate along the x-axis in q-space and account for the cone shaped emission pattern by weighting by q. This is the quantity plotted in Figure 2.7C. We plot the integrand of the q-integral in eqn. (2.52) in Figure 2.12B for $L = 2.5$ μm, and observe that the area is maximized at an intermediate doping level (blue curve), as argued in section 2.4. At this cross-over point, one achieves an optimal balance between the width and height of the gain profile for this particular device length. We turn to a longer (7 μm) sample in Figure 2.12C, and observe a more sharply peaked phonon spectrum. Intuitively, the

longer device allows for more nonlinear amplification, which acts as an active filter centered at the most amplified phonon mode. This filtering effect skews the competition between the width and height of the gain profile. Since the most amplified modes strongly dominate in the longer device, it is more favorable to have a few modes with high amplification rate (red curve) than many weakly amplified modes (blue and green curves). Thus, the integrated phonon emission is maximized at a lower doping level in longer devices. Another consequence of this filtering effect is that the cross-over behavior is predicted to be sharper in longer devices. As shown in Figure 2.7C, we find that our model agrees very well with the data, with regards to both the shifts and broadening of the cross-over peaks. Since the cut-off at $q = 2k_{\mathrm{F}}$ is less sharp at higher temperatures, it is expected that the nonmonotonic behavior will have some dependence on the electronic temperature. The latter is expected to be elevated above the lattice temperature due to Joule heating. Using no other fit parameters, we find best agreement with our data at an electronic temperature of 320 K. In order to evaluate whether this value is reasonable, we compare with an upper bound corresponding to the case where cooling only occurs through electronic conduction to the contacts. Using the thermal conductivity given by Wiedemann-Franz law and relevant bias voltages of $0.2 - 0.3$ V, we find temperatures of 340-500 K. Since in reality phonons also contribute to cooling, we expect that the electronic temperature should be somewhat lower than this. We thus consider the value used here to be reasonable. We finally note that the electronic temperature is expected to show some variation with charge density, which may explain the discrepancy between our model and the data at high charge densities.

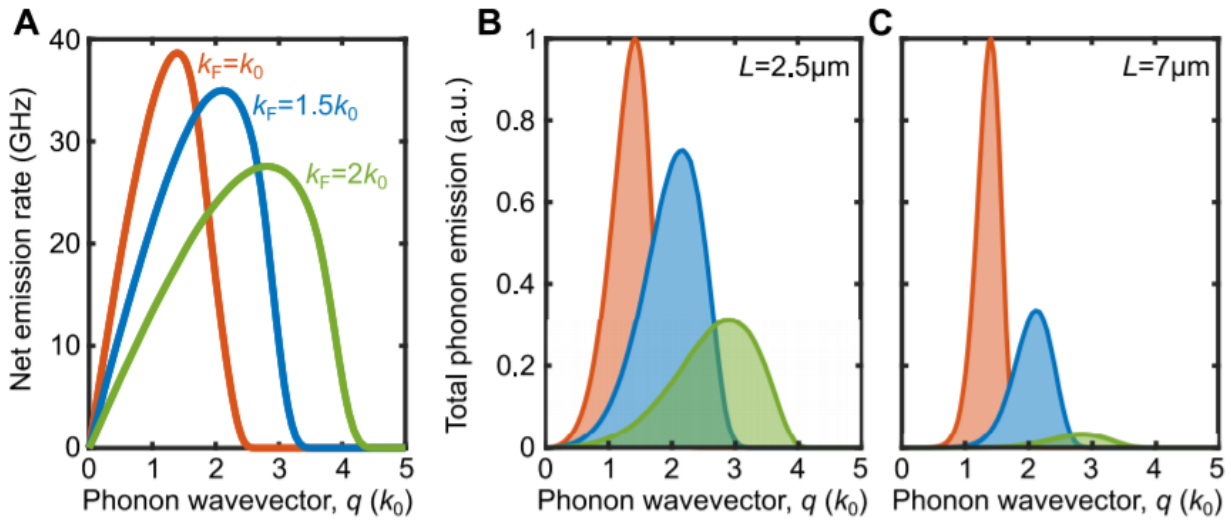


Figure 2.12: Non-monotonic charge density dependence of phonon amplification. (A) The net emission rate Δn_q at constant current density j = 0.6 mA/μm, for various k_F (k_0=165 meV/$\hbar v_F$). The corresponding charge densities are n = 2.1, 4.5 and 8.0 · 10^{12} cm^{-2}, including the effect of the non-zero v_D on n. Δn_q becomes zero near $2k_F$. (B) The integrand of eqn. (2.52), which is expected to be strongly related to the measured noise. The blue curve has the biggest area and thus corresponds to the highest expected noise, for device length L = 2.5 μm. (C) Same as (B), but for L = 7 μm. The longer device allows for more filtering, causing the noise to be maximized at a lower k_F (red curve).

2.5.7 Local noise

The NV center measures magnetic noise due to local current fluctuations, which are intuitively expected to be determined by the local phonon fluctuations. However, if one considers the 1D case, where the current has to be constant along the whole device, one quickly finds this not to be the case. This comes from the fact that we can no longer integrate eqn. (2.26) over the device length to remove local fluctuations in the electric field. A change in the resistance in one part of the device will thus affect the electric field in other parts of the device, due to the division of the bias potential along the device. Here, we show that this non-local effect is negligible in two dimensions, and that the local current fluctuations are indeed determined by the local phonon fluctuations. We do this by dividing the sample into small squares of size corresponding to the NV

sensing area, and then think of the sample as a grid of $N \times N$ resistors with resistance $R(x,y,t) \propto \Gamma_e(n_q(x,y,t))$. We here remind that Γ_e is the electronic scattering rate. The NV sampling dimension is approximately given by its depth $d_{NV} \sim 50$ nm, so the number of resistors $N^2 = \frac{A_{sample}}{A_{NV}} \sim 10^5$ is very large. We now switch to discretized subscripts instead of x and y to represent position, and consider an NV center located just below position (m,n) in the grid. The current moving right above the NV center is then given by:

$$j_{mn} = \frac{j_{tot} R_m}{R_{mn}} \propto \frac{R_m}{R_{mn} R_{tot}} \tag{2.53}$$

$$R_{tot} = \sum_i R_i = \sum_i \left(\sum_j R_{ij}^{-1} \right)^{-1} \tag{2.54}$$

where the first subscript is the position along the current (x), and the second is in the transverse direction (y). When only one subscript i is used, it refers to the total cross-sectional resistance at $x = i$ ($R_i = 1/\Sigma_j R_{ij}^{-1}$). We see that all resistors affect the total current j_{tot}, but only resistors on the same transverse plane as the NV affect the portion of j_{tot} that goes through the NV sensing area. The local current fluctuations probed by the NV are then given by the sum:

$$\delta j_{mn} = \langle j_{mn} \rangle \left(-\frac{\delta R_{tot}}{\langle R_{tot} \rangle} + \frac{\delta R_m}{\langle R_m \rangle} - \frac{\delta R_{mn}}{\langle R_{mn} \rangle} \right) \tag{2.55}$$

There are thus three candidates for which resistors we have to consider, corresponding to the three terms above: 1) All of them, 2) The ones on the same transverse plane as the NV, or 3) Only the resistor at the NV location, R_{mn}. In order to determine which effect is larger, we for now assume that all resistors have the same rms fluctuations δR_{rms} and mean resistance $\langle R \rangle$, so:

$$1)\ (\delta R_{\mathrm{tot}})_{\mathrm{rms}} = \left(\sum_{ij} \frac{R_i^2}{R_{ij}^2}\delta R_{ij}\right)_{\mathrm{rms}} = \frac{\delta R_{\mathrm{rms}}}{N} \quad \rightarrow \quad \left(\frac{\delta R_{\mathrm{tot}}}{\langle R_{\mathrm{tot}}\rangle}\right)_{\mathrm{rms}} = \frac{1}{N}\frac{\delta R_{\mathrm{rms}}}{\langle R\rangle} \tag{2.56}$$

$$2)\ (\delta R_m)_{\mathrm{rms}} = \left(\sum_{j} \frac{R_m^2}{R_{mj}^2}\delta R_{mj}\right)_{\mathrm{rms}} = \frac{\delta R_{\mathrm{rms}}}{N^{3/2}} \quad \rightarrow \quad \left(\frac{\delta R_m}{\langle R_m\rangle}\right)_{\mathrm{rms}} = \frac{1}{\sqrt{N}}\frac{\delta R_{\mathrm{rms}}}{\langle R\rangle} \tag{2.57}$$

$$3)\ (\delta R_{mn})_{\mathrm{rms}} = \delta R_{\mathrm{rms}} \ \rightarrow \ \left(\frac{\delta R_{mn}}{\langle R_{mn}\rangle}\right)_{\mathrm{rms}} = \frac{\delta R_{\mathrm{rms}}}{\langle R\rangle} \tag{2.58}$$

Assuming the phonon fluctuations at each site are independent, we find that the rms values of the three terms scale as $1/N$, $1/\sqrt{N}$ and 1, respectively. It is the parallel connections that prevent δR_{tot} and δR_m from simply scaling with the square root of the number of resistors involved. We thus only have to consider the phonon fluctuations right above the NV center to determine the local current fluctuations. We here stress that this is only the case for fluctuations; the mean local current depends on the total phonon population (all resistors in the grid). This justifies our argument that the spatial current noise profile (Figure 2.5D) is representative of the local phonon fluctuations. Moreover, it is now clear that the NV center is only sensitive to correlations within its sampling area. This means that the locally measured fluctuations should have a frequency cut-off given by the inverse transit time of the NV sampling area ($\frac{v_{\mathrm{s}}}{d_{\mathrm{NV}}} \sim$ THz), not the total device, consistent with our observations in Appendix A5.1.

2.5.8 Alternative mechanisms

We include here an accounting of other known processes that may occur in highly biased graphene and comment on their inconsistency with our observations. By contrast, as shown in section 2.4, the electron-phonon Cherenkov instability agrees very well with all of our observations.

2.5.8.1 Optical phonon scattering

When biased to very large drift velocities, electrons in graphene can relax by emitting optical phonons, eventually leading to current saturation (*74-76*). In particular, this behavior is often observed in devices fabricated directly on SiO_2, where the optical phonon energy is only $\sim$ 50 meV. The anomalous noise and conductivity features investigated in section 2.4 are only observed in fully hBN-encapsulated devices, where the relevant low-lying optical phonon mode is in the hBN itself (*77*). This mode has a higher energy of $\sim$ 100 meV, which is only accessible at biases far beyond the onset of the anomalous behavior. In particular, we observe that the AC conductivity spectrum has developed clear low-frequency features and that the noise is superlinear in power when the available excitations ($k_{\mathrm{B}}T, 2\hbar k_{\mathrm{F}} v_{\mathrm{D}}$) are less than 20 meV. This is clearly too low for substantial optical phonon emission. Besides being outside the parameter range required to excite optical phonons, it is not expected that optical phonon scattering will lead to the observed strong noise signal and its growth across the sample. Indeed, noise measurements in disordered samples on SiO_2 clearly show that the noise signal is simply dominated by thermal (white) noise when the graphene sample is biased strongly enough to access optical phonons. Furthermore, the velocity extracted from Figure 2.6 matches well with the acoustic phonon velocity, while optical phonons have orders of magnitude lower group velocities. Lastly, due to the high energy of optical phonons, it is not expected that their effects should be as dependent on lattice temperature as we observe in the 10-300 K range (Figure 2.7A).

2.5.8.2 Plasmonic effects

A plasmonic analogue to phonon Cherenkov amplification in graphene has also been proposed (58). While plasmons in graphene have far too high velocities ($\sim$10 times higher than the drift velocities in our experiment) to match well with our observations (*78*), losses could allow for

accessing lower velocity modes below the dispersion. However, we operate in a parameter regime that is far from that required to achieve this. As analyzed in Ref. (*79*), intra-band transitions are only accessed by very high initial electronic excitations of ~2000 meV above the Fermi energy, which is two orders of magnitude higher than the excitations reached in our experiment at the onset of the anomalous observations ($k_{\mathrm{B}}T, 2\hbar k_{\mathrm{F}} v_{\mathrm{D}} < 20$ meV).

Another plasmonic effect of interest is the Dyakonov-Shur (DS) instability (*40*). We also exclude this mechanism based on many considerations: 1) This mechanism relies on carefully chosen boundary conditions not satisfied in our experiment. 2) The DS instability requires much longer electronic mean free paths than what we observe when applying high bias. 3) Since DS plasmon amplification occurs at the sample edge and the plasmons are damped in the channel, the signal is expected to be higher in shorter samples. In clear contrast, we observe that the signal increases with device length (Appendix A4.3). 4) The DS instability is expected to cause oscillations at much higher frequencies (~THz) than what is observed in our experiment. Moreover, there is another critical difference between phonons and plasmons: while the speed of sound does not depend on electronic parameters, the plasmon velocity is highly dependent on charge density (*78*). Thus, if plasmonic emission were driving the instability, the timescale (device traversal time) observed in noise and AC conductivity measurements should change with gating. As explained in the manuscript and shown in Appendix A4.5, we show that this is not the case. Based on these arguments, we conclude that plasmons are not connected with our observations.

2.5.8.3 Hydrodynamic instabilities

When electron-electron interactions are the dominant scattering mechanism in the device, graphene enters the hydrodynamic regime and may exhibit instabilities such as vortex shedding and preturbulent flow (*38*). We discount such hydrodynamic instabilities as an explanation for our

observations for the following reasons: 1) The rate of electron-phonon scattering in driven graphene-hBN heterostructures is too high to realize long-range hydrodynamic instabilities. This was recently discussed in Ref. (*80*). 2) The frequency of vortex shedding in pre-turbulent oscillations should be highly dependent on drift velocity, in contrast to our observations in Figure 2.3, where the observed timescales are independent of electronic parameters. 3) The extent to which hydrodynamic instabilities occur increases with the Reynolds number, $Re = v_D L/\eta$, where η is the kinematic viscosity. The Reynolds number is expected to decrease monotonically with incrasing carrier density n for two reasons: The kinematic viscosity of the electron fluid increases with n, and at constant current density, the drift velocity decreases with n. Thus, we do not expect hydrodynamic instabilities to show the non-monotonic doping dependence observed in Figure 2.7C.

3

VALLEYTRONICS IN TWISTED TRANSITION METAL DICHALCOGENIDES

3.1 Transition metal dichalcogenides (TMDs)

Another very interesting two-dimensional material is the transition metal dichalcogenides (TMDs), which consist of one atomic plane of transition metal atoms (Mo, W,…) between two planes of chalcogen (S, Se, Te,..) atoms. In contrast to graphene, where the valence and conduction bands touch at the K-point, the TMDs are semiconductors with bandgaps in the 1-2 eV range, enabling strong light-matter interactions in the visible regime. Specifically, the TMDs host tightly bound electron-hole pairs known as excitons, which are formed when an electron is optically excited to the conduction band and binds to the resultant hole in the valence band through Coulomb interaction. As we shall see later in this chapter, the constituent electron and hole can either reside in the same or different layers, known as intra- and inter-layer excitons, respectively. The energy of an exciton is given by the band gap of the TMD, minus the Coulomb energy, often referred to as the exciton binding energy. Importantly, excitons in TMDs have very large binding energies on the order of 100s of meV, due to the large effective carrier masses and reduced screening in two dimensions (*81*). In comparison, excitons in conventional III-IV semiconductors, such as GaAs, have binding energies down to just a few meV (*82*). In this and the next chapter, I will present three studies of excitons in bilayer TMDs, in which we utilize the twist angle between the two layers to engineer new exciton properties.

3.2 Band structure and the valley degree of freedom

The honeycomb lattice of TMDs gives rise to a hexagonal Brillouin zone (BZ), with high-symmetry points at the K-points (vertices of BZ) and Γ-point (center of BZ), as well as at the Q-points, which are located at the midpoints between the K- and Γ-points. As in graphene, the K-points are divided into alternating K and K’ points, which are internally equivalent. The band

structure depends strongly on the number of layers. Monolayers exhibit a direct bandgap with the valence band maximum and conduction band minimum at the K-points (*2*). In multilayer TMDs, on the other hand, interlayer hybridization effects cause energy shifts that are larger at the Γ- and Q-points than at the K-points, thus inducing indirect bandgaps (*83*). For instance, bilayer WSe_2 has its conduction band minimum (CBM) at the Q-point (*84*), while bilayer $MoSe_2$ has its valence band maximum at the Γ-point (*83*). Since photons carry negligible momentum, monolayer TMDs exhibit much stronger photoluminescence due to their momentum-direct band gap at the K-point.

In order to understand the full optical selection rules at the K-point, one needs to consider both spin-orbit coupling and the quantum numbers of the orbital wavefunctions. In particular, the orbital wavefunction can be described by an angular momentum quantum number *m* and parity *p*, defined through its response to the symmetry operations of the lattice, namely in-plane rotation by 120° (*R*) and inversion in *z* (*P*), respectively:

$$R\psi = e^{-i2\pi m/3}\psi \tag{3.1}$$

$$P\psi = (-1)^p\psi \tag{3.2}$$

Due to the three-fold rotational symmetry of the TMD lattice, m is only defined modulo 3. At the K-point, the conduction band states consist mainly of d_{z^2}-orbitals with orbital quantum number m=0, while the valence band states are predominantly composed of $d_{x^2-y^2} \pm id_{xy}$ orbitals with $m = \pm 2$ (∓ 1) at the K and K' points, respectively (*85*). All of these states have even parity. Spin-orbit coupling causes a considerable spin splitting of the valence band of ~ 150 (450) meV in molybdenum (tungsten)-based TMDs (*86*). Due to the Kramers degeneracy theorem, the spin splittings are opposite at the K and K' points. In contrast to the valence band states, the dominant d_{z^2}-orbitals of the conduction band states do not contribute spin-orbit coupling. However, second-

order contributions from other orbitals give rise to a small non-zero spin splitting of a few 10s of meV (*87*).

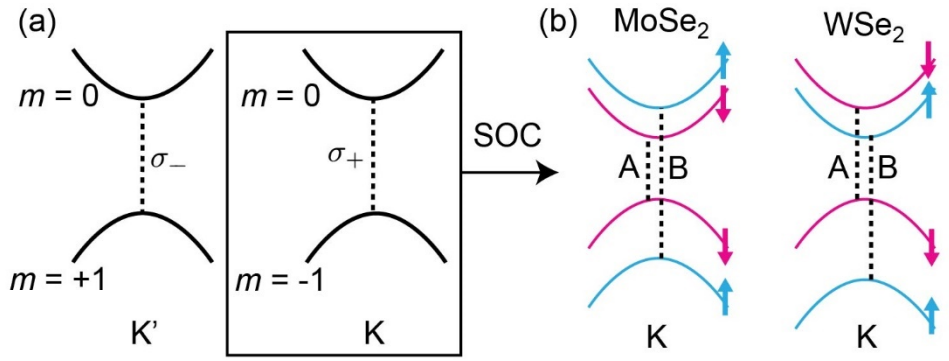


Figure 3.1: Optical selection rules of TMDs. (a) Band edges at the K' and K points. Circularly polarized excitation with σ_- (σ_+) only couples to the K' (K) valley. (b) Spin-orbit coupling causes splitting of the bands (spin-up and spin-down indicated in cyan and magenta, respectively), giving rise to two spin-conserving transitions, A and B. While the lowest energy transition is spin-conserving in $MoSe_2$, it is not in WSe_2, causing stronger photoluminescence from the former.

The optical selection rules dictate that right-handed (left-handed) circularly polarized photons only couple bands with the same spins, the same parities *p,* and angular momentum quantum numbers *m* that differ by +1 (-1) (see Figure 4.2a). In order to increase *m* by +1, right-handed circularly polarized photons can only cause excitations at the K-point, where the valence band state has $m = +2 = -1 \bmod 3$. Similarly, left-handed circularly polarized photons can only cause excitations at the K'-point. As shown in Figure 4.2b, spin-orbit coupling gives rise to two "bright" (spin-conserving) transitions, known as the A and B excitons. For each transition, the chirality of the photon not only determines the valley of the exciton, but also its spin since the spin splittings have opposite signs at the K and K' points. This is commonly referred to as spin-valley locking (*88*). Interestingly, the spin splittings of the valence and conduction bands are of opposite signs in molybdenum-based TMDs, but not in tungsten-based ones. This causes the lowest lying

transition to be bright in MoX_2, but not in WX_2, resulting in brighter photoluminescence from the former.

3.3 Gate control of excitons

A very useful feature of excitons in TMDs is that their properties can be tuned in-situ via electrostatic gating (*89*). This is achieved by fabricating field effect transistors (FET), in which a conducting gate and the TMD are separated by a gate dielectric. While such a FET structure can be realized by simply placing the TMD on a standard Si/SiO_2 substrate, higher quality devices (such as the ones studied in this thesis) typically make use of a graphite gate and hBN dielectric to provide a cleaner, atomically flat interface with the TMD. Through the application of a voltage between the gate and the TMD, the latter can be electrostatically doped, which dramatically affects the exciton properties.

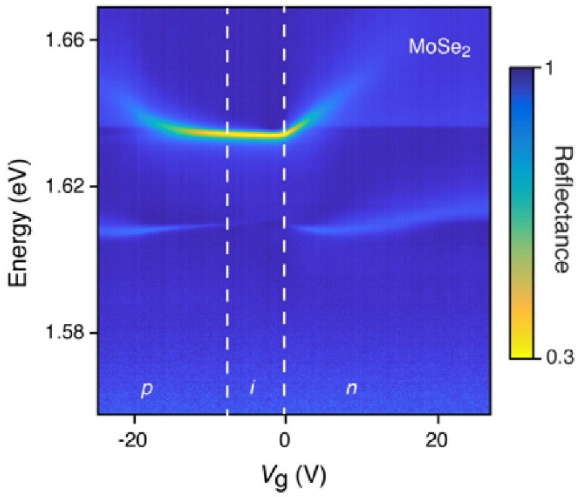


Figure 3.2: Gate-tunable exciton reflection in $MoSe_2$. The application of a gate voltage V_g allows for tuning the TMD out of the intrinsic (*i*) regime, into the *p*- and *n*-doped regimes. In the doped regimes, the intrinsic exciton resonance blue-shifts due to Pauli blocking and repulsive polaron formation, and a new red-shifted resonance appears due to attractive polarons.

For example, Figure 3.2 shows gate-dependent reflection spectra of intralayer excitons in monolayer $MoSe_2$, demonstrating that the exciton resonance blue-shifts and becomes weaker upon the introduction of additional charges. This is attributed to Pauli blocking and the formation of repulsive polarons – a quasiparticle mode involving excitons dressed by the surrounding sea of electrons or holes (*90*). Simultaneously, another resonance appears at lower energies due to attractive polarons – the bonding counterpart to the (anti-bonding) repulsive polaron.

So far, we have considered the case of single-gated FET structures, where the modulation of the doping level in the TMD is accompanied by a vertical electric field. However, by fabricating dual-gated FETs, the doping level and vertical electric field can be tuned independently. Interlayer excitons have non-zero vertical dipole moment and therefore experience a DC Stark shift under the application of an electric field E, given by $\hbar\Delta\omega = E \cdot ed$, where e is the elementary charge and d is the vertical electron-hole separation of the exciton. Besides modulation of the resonance energy, electrostatic gating also enables tuning of several other exciton properties, including the exciton lifetime, linewidth, and intervalley mixing rate. We shall see several examples of such tunability in this and the following chapter.

3.4 Valleys for information storage: promises and challenges

Due to the different selection rules of the K and K' valleys in TMDs, the valley degree of freedom presents a promising alternative to conventional, charge-based information storage and processing. Analogously to the binary levels (0 and 1) in a traditional computer, the K and K' valleys could be used as a new way to store information. While it is quite challenging to manipulate and read out the valley population of single charge carriers (electrons or holes), valley excitons represent a

promising alternative, since information could be "written" by exciting excitons with circularly polarized photons, and retrieved at a later point from the resulting photoluminescence. Due to the coupling with photons, such an approach also features great opportunities for information transfer. Moreover, TMDs could facilitate new routing schemes based on the valley degree of freedom. Since the K and K' valleys have Berry curvature of opposite sign, charges in the two valleys become deflected in opposite directions when electrically biased, an effect known as the valley Hall effect (*91, 92*). An analogous effect was demonstrated with excitons driven by diffusion (*93*), referred to as the exciton Hall effect. Another appealing feature of exciton valleytronics is the excellent in-situ tunability via electrostatic gating that was discussed in section 3.3. Specifically, as we show in section 3.5, the rate at which excitons transition from one valley to another depends dramatically on the doping level.

Despite these promising capabilities, a major obstacle to using TMDs for valleytronic information storage is that the exciton lifetime in monolayer TMDs is limited to a few picoseconds, due to a large overlap between the electron and hole wavefunctions (*94, 95*). Hence, the information storage time is much shorter than that required for most applications. While interlayer excitons in bilayer TMDs have longer lifetimes, these feature a separate important limitation: since the top and bottom layers are rotated 180° relative to each other, the K valley in one layer has the same momentum (and energy) as the K' valley in the other, thus allowing the excitons to quickly scatter between valleys, causing scrambling of the stored information. In the following, we demonstrate that twisted bilayer TMDs represent a promising platform for overcoming these shortcomings.

3.5 Electrically tunable valley dynamics in twisted WSe_2/WSe_2 bilayers

The following is reproduced from the manuscript "Electrically tunable valley dynamics in twisted WSe_2/WSe_2 bilayers" by Giovanni Scuri, Trond I. Andersen, You Zhou *et al*. (*96*)

The twist degree of freedom provides a powerful new tool for engineering the electrical and optical properties of van der Waals heterostructures. Here, we show that the twist angle can be used to control the spin-valley properties of transition metal dichalcogenide bilayers by changing the momentum alignment of the valleys in the two layers. Specifically, we observe that the interlayer excitons in twisted WSe_2/WSe_2 bilayers exhibit a high (>60%) degree of circular polarization (DOCP) and long valley lifetimes (>40 ns) at zero electric and magnetic fields. The valley lifetime can be tuned by more than 3 orders of magnitude via electrostatic doping, enabling switching of the DOCP from ~80% in the n-doped regime to <5% in the p-doped regime. These results open up new avenues for tunable chiral light-matter interactions, enabling novel device schemes that exploit the valley degree of freedom.

Valleys represent the crystal momentum states where bands have an extremum (*88, 97-101*). Charge carriers or excitons in different valleys can exhibit markedly distinct properties (*88*), including different spin, optical selection rules, and Berry curvature, leading to a wealth of new physical phenomena such as the valley Hall (*92, 102*) and Nernst effects (*103, 104*). Moreover, the valley degree of freedom can enable new ways of encoding and processing information beyond traditional schemes based purely on charge (*105-107*). The realization of such applications relies on efficiently initializing a large valley polarization and achieving long valley and exciton lifetimes.

Transition metal dichalcogenides (TMDs) are a promising platform for valleytronics as they host tightly bound excitons with coupled spin-valley properties that can be optically addressed via circularly polarized light (*2, 7, 97, 108, 109*). A major obstacle to harnessing these properties in monolayer TMDs is the short lifetimes of intralayer excitons (0.1-1 ps) resulting from the sizeable electron-hole wavefunction overlap (*94, 95*), as well as rapid valley mixing caused by exchange interactions (*110-114*). Interlayer excitons in bilayer TMDs (*10, 107, 115*), consisting of an electron and a hole residing in two distinct TMD layers, present a promising route for overcoming these limitations. Because of the reduced wavefunction overlap, interlayer excitons can exhibit enhanced lifetimes that are 3 to 4 orders of magnitude longer than their intralayer counterparts (*10, 115*) and tunable by electric field (*84*).

Unfortunately, interlayer excitons in naturally occurring TMD bilayers exhibit rapid valley mixing because valleys of opposite chirality are degenerate in energy and momentum (Figure 3.3(a), top) (*84, 88, 116, 117*). Moreover, natural bilayers are inversion symmetric (the two layers are rotated 180^{o} relative to each other), thus as a whole they do not exhibit net valley polarization (*116, 118*) unless the symmetry is broken, *e.g.*, with an electric field (*119*). Consequently, most valleytronic studies involving interlayer excitons have focused on heterobilayers made of two different materials, such as WSe_2/MoS_2 (*120*) and $MoSe_2/WSe_2$ (*106, 107, 121, 122*).

Here, we show that the introduction of a twist angle between the layers can provide a new avenue for engineering the spin-valley properties of TMD bilayers, including homobilayers. Previously, the twist angle has been used to modify the resonance energy of excitons (*123, 124*) and alter their properties due to moiré-induced spatial confinement and hybridization of bands (*125-130*). Here, we tune the twist angle between the layers to control the momentum alignment of their respective valleys (Figure 3.3(a), bottom), permitting long-lived interlayer exciton states

with slow valley depolarization even at zero electric and magnetic fields. Importantly, we also demonstrate that the exciton and valley dynamics of twisted bilayers can be tuned via electrostatic doping.

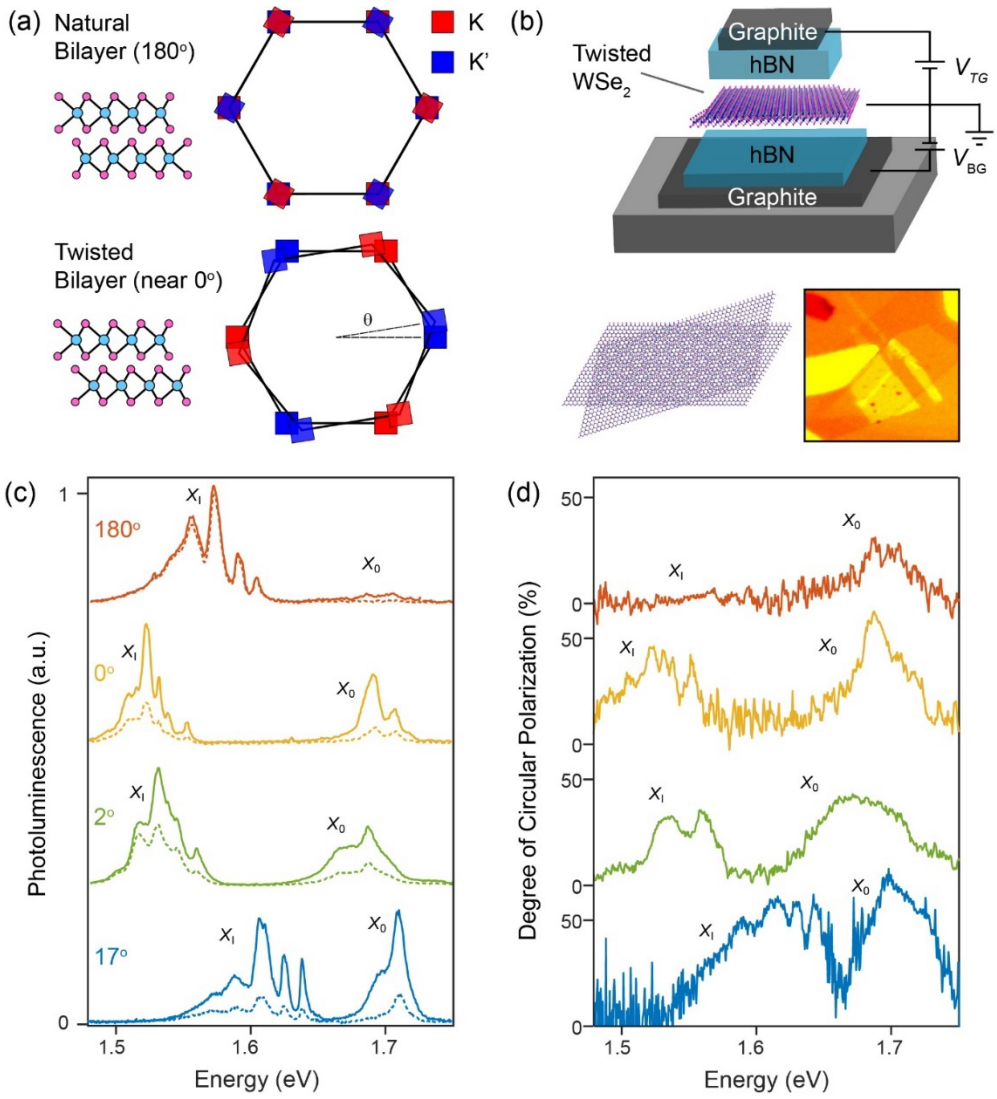


Figure 3.3: Band engineering through twisting. (a) Side view and Brillouin zone alignment of natural (2H-stacked, top) and twisted homobilayer (bottom). The K and K' points are aligned in natural bilayers, but not in twisted structures. (b) Device schematic (top), illustration of a moiré pattern in a twisted WSe_2/WSe_2 bilayer (bottom left) and optical image of a device (bottom right). (c) Polarization-resolved PL spectra from bilayers with varying twist angle. All spectra are collected in the intrinsic regime. Solid (dashed) lines represent co- (cross-) polarized emission. X_0 and X_I indicate intra- and interlayer excitons, respectively. (d) Degree of circular polarization calculated from PL spectra in (c). While the natural bilayer (red) exhibits almost zero interlayer DOCP, the twisted devices show DOCP as high as 60%.

To experimentally demonstrate twist-based spin-valley engineering, we fabricate optically addressable field-effect transistors that incorporate twisted WSe_2/WSe_2 bilayers (t-WSe_2/WSe_2) encapsulated in hexagonal boron nitride (hBN, Figure 3.3(b)). The devices feature top and bottom graphene gates for independent control of doping and vertical electric field (*84*). Using the tear-and-stack technique (*11, 131*), we fabricate multiple such devices from high-quality exfoliated flakes, with target twist angles ranging from 0^o to 17^o. For comparison, we also make a device using a 2H-stacked natural bilayer (labeled as 180^o twist angle).

Figure 3.3(c) shows polarization-resolved photoluminescence (PL) spectra from t-WSe_2/WSe_2 at different twist angles (see Figure B.3 in Appendix B6 for additional twist angles). These spectra are obtained with both of the graphene gates grounded, so that the TMD layers are intrinsic and under zero vertical electric field. At all twist angles, including the natural 2H bilayer, the spectra show two sets of peaks: the higher energy peaks near 1.7 eV (X_0) are assigned to momentum direct (K-K) intralayer transitions (*84, 116, 118*), and the lower energy peaks between 1.5 and 1.6 eV (X_I) are attributed to interlayer transitions (*2, 84, 132, 133*). This assignment is based on our out-of-plane electric field dependence measurements (Figure 3.4(a), Appendix B2 and Figure B.4), which show a zero (non-zero) linear Stark shift for intralayer (interlayer) excitons, consistent with previous studies (*10, 84*). Despite their weaker binding energies (*10*), the interlayer excitons have lower energies than the K-K intralayer excitons, indicating that they do not originate from the momentum direct K-K transition. Instead, the interlayer excitons arise from lower-energy transitions that are momentum indirect, as previously predicted for multilayer TMDs (*2*). In particular, the interlayer exciton PL in natural bilayer WSe_2 was previously attributed to the K-Q transition (*84*).

As the twist angle is increased from 0° to 17°, the interlayer exciton peaks blueshift by almost 80 meV, consistent with reduced interlayer coupling (*123, 124, 134-136*) (Figure 3.3(c)). In all twisted structures, we observe four or five interlayer exciton peaks separated by 15-17 meV. We note that similar multi-peak structures in twisted $MoSe_2/WSe_2$ heterostructures have been attributed to the confinement of interlayer excitons in moiré supercells (*126*). In t-WSe_2/WSe_2 studied here, the multiple peaks are observed even in natural bilayers (as in Ref. (*84*)) and their spacing is independent of twist angle, suggesting a different origin. Since their energy separation is similar to the optical phonon energy in WSe_2 (*84, 137*), one possibility is that the peaks are phonon replicas (*84*). Further experimental and theoretical studies are necessary to confirm this hypothesis, however.

The spin-valley properties of the interlayer excitons change drastically with the introduction of a twist angle between the two layers, as evidenced by the contrast between co- and cross-polarized emission signals (I_{co} and I_{cross}, respectively) in PL measurements. Upon illumination with circularly polarized light, the natural bilayer emits almost equal I_{co} and I_{cross}, whereas t-WSe_2/WSe_2 emits much stronger co-polarized light (Fig. 1(c)). Defining the degree of circular polarization (DOCP) as $\frac{I_{\mathrm{co}}-I_{\mathrm{cross}}}{I_{\mathrm{co}}+I_{\mathrm{cross}}}$, we find that while the neutral interlayer exciton DOCP remains close to zero in natural bilayers, it reaches values as high as 60% in twisted bilayers (Figure 3.3(d), see also Appendix B3 for spatial mapping of DOCP in a device that contains both natural and twisted bilayers). Such high DOCP suggests much slower valley depolarization dynamics in t-WSe_2/WSe_2.

Next, we investigate the gate dependence of the interlayer excitons and their valley properties in the 17°-twisted bilayer device. Figure 3.4(a) and (b) show the electric field dependence of PL and the corresponding DOCP, obtained by applying equal and opposite voltages

to the top and bottom graphene gates to eliminate effects of doping. From the Stark shift of the interlayer excitons, we extract an electron-hole separation of 0.37 nm, significantly smaller than the interlayer spacing, thus indicating that at least one of the carrier wavefunctions is partially delocalized between the layers. Importantly, both the extracted *e*-*h* separation and the DOCP are robust to electric field, suggesting that the same interlayer exciton state dominates the PL signal at all fields explored here.

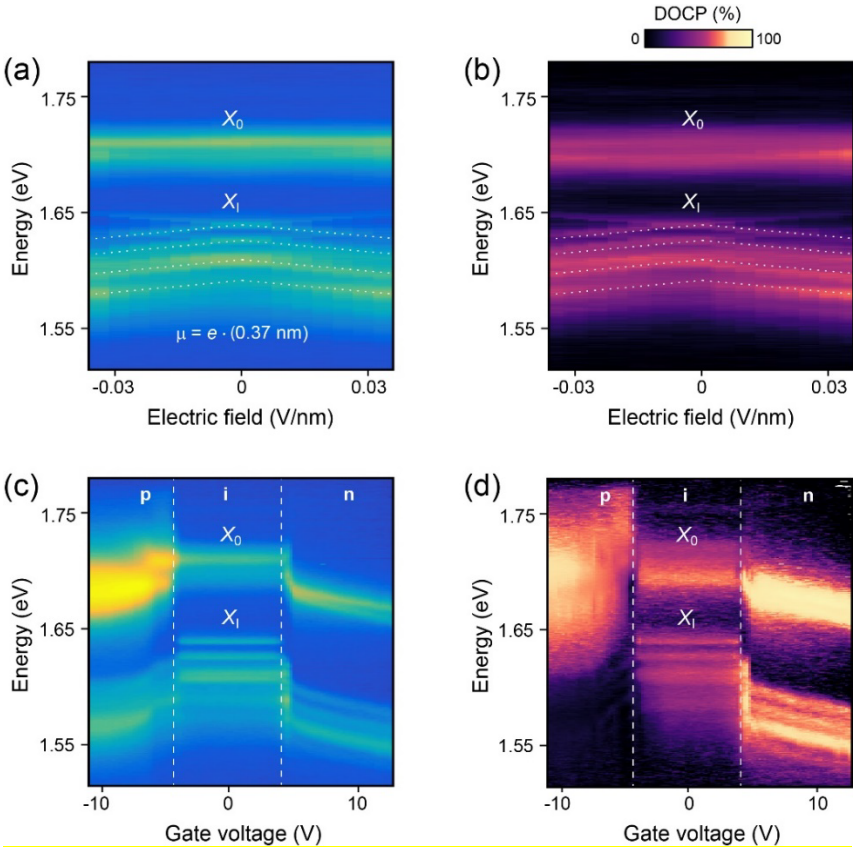


Figure 3.4: Gate tunability of DOCP. (a) Out-of-plane electric field dependence of intra- and interlayer exciton PL from the 17°-twisted bilayer. While the intralayer excitons (X_0) do not shift with electric field, the interlayer excitons (X_I) exhibit a Stark shift equivalent to an electron-hole separation of 0.37 nm. Opposite voltages are applied to the two gates (the hBN flakes have the same thickness) to apply an electric field while keeping the TMD intrinsic. (b) Electric field dependence of DOCP, showing that the DOCP is largely insensitive to electric field. (c) Doping dependence of PL emission for intra- and interlayer excitons. The same voltages are applied to the two gates to dope the sample without applying an electric field. (d) Doping dependence of DOCP, showing switching from large (>80%) values in the *n*-doped regime, to almost zero (<5%) in the *p*-doped regime.

By instead applying equal voltages to the gates, we investigate the dependence on electrostatic doping in the absence of vertical electric field (Figure 3.4(c-d), see Figure B.4 for similar behavior at a twist angle of 2°). In stark contrast to the electric field dependence, the DOCP is strongly dependent on doping. While the interlayer exciton DOCP exceeds 80% in the *n*-doped regime, it can be switched to almost zero (<5%) in the *p*-doped regime (Figure 3.4(c)). The DOCP stays relatively constant within each of the doping regimes and switches abruptly at their boundaries (Figure 3.4(c)). As in previous studies, the intralayer excitons do not exhibit this strong asymmetry (*116*).

Time-resolved PL measurements of the 17° twisted bilayer sample provide further insight into the exciton and valley dynamics (Figure 3.5(a)-(c), corresponding DOCP in Fig. 3(d)). In the intrinsic regime, we fit the data with a biexponential decay (*138*) convoluted with the instrument response (dotted lines in Figure 3.5(a) and (d)), and extract fast and slow time scales of τ_1=0.1 ns and τ_2=0.9 (1.0) ns for co- (cross-) polarized emission. Long interlayer exciton lifetimes are also observed for twist angles of 0° and 5°, which exhibit τ_2=2.0 ns and τ_2=3.3 ns, respectively (Figure B.6). Similar to previous studies (*114, 139*), we observe a 15 ps delay between the co- and cross-polarized emission, which causes a dip in the DOCP until both polarization branches reach the slow decay regime (Figure 3.5(d)). Fitting the DOCP in this regime with a linear coupled model (see Appendix B4), we extract a very long valley lifetime of 44 ns (dashed line in inset of Figure 3.5(d), lines corresponding to 5 ns and 10 ns shown for comparison), comparable to the best reported values in TMD heterobilayers (*121*).

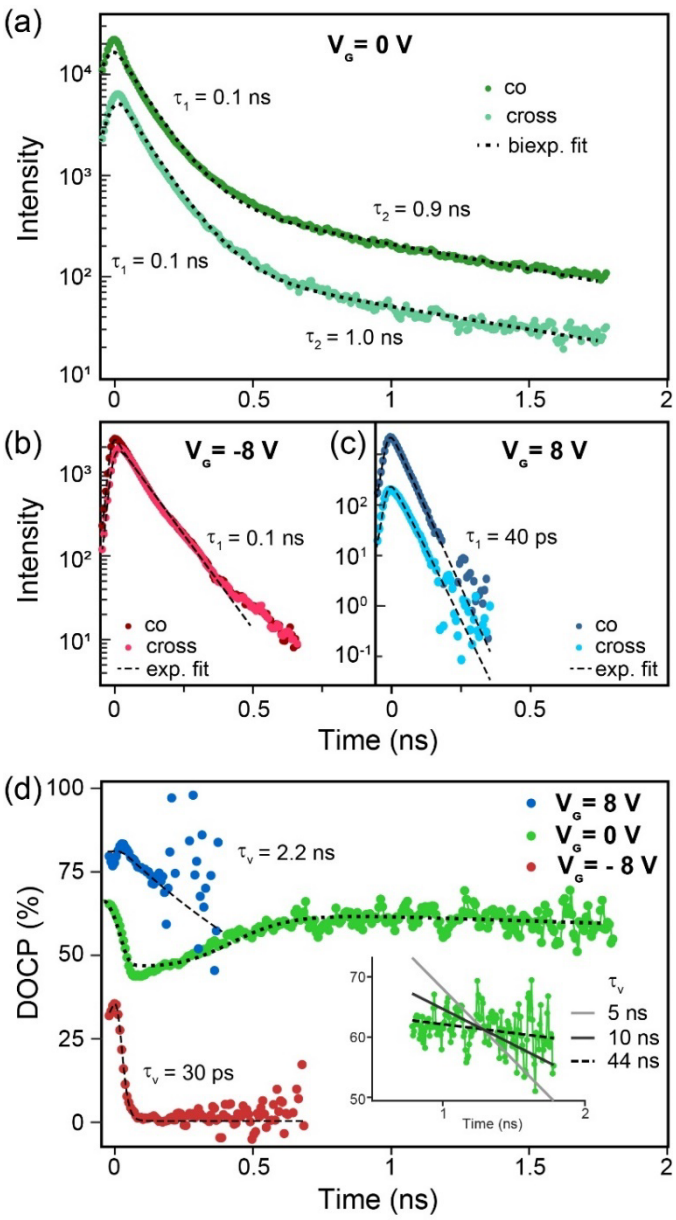


Figure 3.5: Exciton and valley dynamics in twisted WSe_2. (a) Time-resolved measurements of co- and cross-polarized photoluminescence (dark and light green markers, respectively) from the 17° twisted bilayer in the intrinsic regime. Black dotted lines are bi-exponential fits convolved with the instrument response (Appendix B4). The extracted slow and fast time scales are $\tau_1 = 0.1$ ns and $\tau_2 = 0.9$ (1.0) ns for co- (cross-) polarized emission. (b) and (c) Same as in (a), but at V_G=-8 V and V_G=8 V. Black dashed lines are fits based on the coupled linear model (Appendix B4). The extracted exciton and valley lifetimes are $\tau_1 = 0.1$ ns and $\tau_v = 30$ ps at $V_G = -8$ V, and $\tau_1 = 40$ ps and $\tau_v = 2.2$ ns at $V_G = 8$ V. (d) Time-resolved DOCP corresponding to measurements in (a)-(c). Black dotted and dashed curves are calculated from fits in (a)-(c). Inset: Zoomed-in version of long tail in intrinsic regime, fitted with the linear coupled model (dashed line). The extracted valley lifetime is $\tau_v = 44$ ns. Lines corresponding to $\tau_v = 5$ ns (light grey) and $\tau_v = 10$ ns (dark grey) are shown for comparison.

In the doped cases, we focus on shorter time scales, because the exciton population and DOCP decay very rapidly in the *n*- and *p*-doped regimes, respectively. Fitting the data with the linear coupled model (*139*) (dashed lines in Figure 3.5(b)-(d)), we find that the initial exciton decay rate is faster in the *n*-doped regime (τ_1 =40 ps) than in the intrinsic and *p*-doped regimes (τ_1 =0.1 ns). Conversely, the valley lifetime is longer in the *n*-doped regime (τ_v =2.2 ns) than in the *p*-doped regime (τ_v =30 ps, similar to instrument response time).

The observed polarization properties and their doping dependence can be understood from the band structure of t-WSe_2/WSe_2 bilayers. In natural (2H) bilayer WSe_2, recent angle-resolved photoemission spectroscopy measurements (*140, 141*) and density functional theory calculations (*83, 84*) suggest that the conduction band minimum (CBM) and valence band maximum (VBM) are located at the Q and K points, respectively. Our results suggest that these band extrema are conserved in t-WSe_2/WSe_2, consistent with recent studies in 3R-stacked bilayer WS_2 (*142*). The extracted electron-hole separation of d =0.37 nm (Figure 3.4(a)) is smaller than the interlayer separation of d_0 =0.6 nm (*10*) but larger than d_0/2, as expected for a K (hole) to Q (electron) transition, where the hole is localized in a single layer and the electron is partially delocalized between the layers (see Appendix B2 for further discussion). In particular, the extracted dipole moment is in excellent agreement with recent DFT calculations for 0° twisted bilayer WSe_2 (*143*), where the wavefunction at the Q-point was predicted to have a 62%-38% distribution between the two layers (see Appendix B5 for further discussion).

A key difference in the band structures of natural and twisted WSe_2 bilayers is that the Q and K points are spin-degenerate in the former, but not in the latter (*144*). Therefore, electrons and holes in natural bilayer WSe_2 do not need to acquire any energy or momentum to change spin, enabling rapid depolarization (Figure 3.6(a)). In contrast, valley depolarization of neutral

interlayer excitons in twisted structures requires both carriers to scatter with phonons, acquire energy and flip their spins (*114, 138*) (Figure 3.6(b)). This is a much slower process, and the dynamics are instead likely governed by electron-hole exchange interactions (*106, 138, 145*). However, since the interlayer excitons are indirect both in real and momentum space, even exchange interactions are expected to be slow (*106, 107, 146*). In particular, they should be substantially slower than for momentum direct intralayer excitons, where such processes cause very short valley lifetimes (1-10 ps) in the intrinsic regime (*114, 147, 148*).

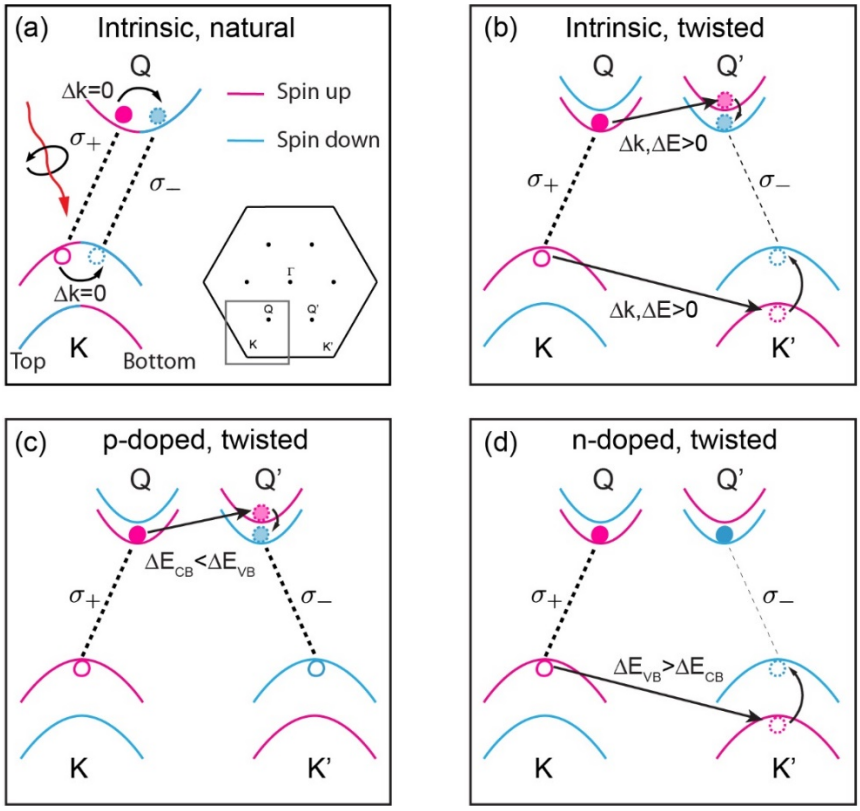


Figure 3.6: Depolarization mechanisms in natural and twisted WSe_2/WSe_2 bilayers. (a) Depolarization in natural bilayer WSe_2 occurs simply through two spin-flip transitions (curved arrows), causing low DOCP. Magenta (cyan) bands indicate spin up (down) for electrons. The thickness of the dashed lines qualitatively represents the relative dominance of the σ_+ and σ_- recombination processes. Inset: Brillouin zone showing location of the degenerate K and Q points of a natural bilayer as a whole. (b) Depolarization in twisted bilayer WSe_2 requires both a phonon-induced momentum kick (straight arrows) and a spin-flip transition (curved arrows) for both carriers, resulting in high DOCP and long τ_v. (c)-(d) Since positively (negatively) charged excitons already have holes (electrons) at both the K and K' (Q and Q') points, only the electron (hole) must flip spin and shift in *k*-space.

The observed hierarchy of valley lifetimes in the three doping regimes, *i.e.* τ_v(intrinsic) > τ_v(*n*-doped) > τ_v(*p*-doped), is also well described by our band-structure considerations. In the *p*- and *n*-doped regimes, the depolarization dynamics of charged interlayer excitons are dominated by intervalley scattering (*106, 138, 145*), and in contrast to the intrinsic regime, only one of the carriers needs to scatter, due to the additional resident charge in the opposite valley. Positively charged excitons, which already have resident holes in both the K and K' valleys, only require scattering of the electron to depolarize (Figure 3.6(c)). Conversely, only the hole needs to scatter in negatively charged excitons (Figure 3.6(d)). These considerations indicate that the valley lifetime should be shorter in the doped regimes than in the intrinsic regime, as observed here. Our results in Figure 3.5(d) suggest that the depolarization mechanism for holes is slower than for electrons in our twisted structures, consistent with the large spin-orbit coupling at the K point VBM and the resultant strong spin-valley locking for holes (*116*). This is also in good agreement with a recent study on 3R-stacked bilayer WS_2 (*142*). We note that the doping dependence of the interlayer exciton lifetimes depends on various recombination processes, including both radiative and non-radiative ones. Further experimental and theoretical studies will be necessary to obtain a full understanding of the underlying microscopic phenomena that determine the doping dependence of exciton lifetimes.

The strong asymmetry in degree of circular polarization shown in Figure 3.4 is a result of the interplay between the depolarization and exciton decay dynamics, as implied from the expression $\mathrm{DOCP_{tot}} = \mathrm{DOCP_0} \,/\, (1 + 2\tau_1/\tau_v)$, where $\mathrm{DOCP_{tot}}$ and $\mathrm{DOCP_0}$ are the total (time-integrated) and initial DOCP, respectively. In the hole doped regime, the depolarization timescale is shorter than τ_1 (30 ps and 0.1 ns, respectively), resulting in a low DOCP (<5%). In the electron doped regime, on the other hand, τ_v is much longer than τ_1 (2.2 ns and 40 ps, respectively) so the

observed DOCP is very large (>80%). Additionally, $\mathrm{DOCP_{tot}}$ is also affected by variations in $\mathrm{DOCP_0}$, which causes $\mathrm{DOCP_{tot}}$ to be higher in the *n*-doped regime than in the intrinsic regime, despite the fact that $\tau_1/\tau_\mathrm{v} \ll 1$ in both regimes.

In conclusion, we have shown that the twist angle provides a new route for engineering the chiral optical properties of interlayer excitons in WSe_2/WSe_2 bilayers. Specifically, by changing the momentum separation of the valleys in the two layers, we achieved large valley polarization for long-lived interlayer excitons in t-WSe_2/WSe_2, in contrast to natural bilayers. Such valley polarization, which can be initialized and read out optically, is a direct consequence of the valley lifetime greatly exceeding the exciton lifetime. Moreover, in agreement with band structure considerations, the valley dynamics are highly tunable by electrostatic doping, enabling switching of DOCP from more than 80% in the *n*-doped regime to <5% in the *p*-doped regime. Our results exemplify the power of twist-based engineering in van der Waals heterostructures and demonstrate that twisted TMD bilayers are a new promising platform for tunable chiral photonics and electrically switchable spin-valley based devices. The coupling to functional structures, such as plasmonic metasurfaces (*149-151*), can further enhance chiral light-matter interactions and enable routing of electrically switchable chiral photons, thus opening up avenues for applications in quantum information storage and processing.

4

CORRELATION OF MOIRÉ STRUCTURE AND EXCITON PROPERTIES IN TWISTED TMDS

4.1 Moiré patterns

When two 2d-materials are stacked on top of each other with a small relative twist angle and/or a non-zero lattice mismatch, a periodic pattern appears with periodicity:

$$a_{\mathrm{m}} = \frac{a_0}{\sqrt{\theta^2+\delta^2}}, \tag{4.1}$$

where a_0 is the average lattice constant of the two materials, θ is the relative twist angle, and δ is the relative lattice mismatch. This pattern, known as a moiré pattern, can be thought of as the spatial "beating" of the local atomic alignment of the two lattices. Importantly, the potential experienced by charge carriers depends sensitively on the local atomic environment, so the moiré pattern introduces a periodic potential landscape with peak-to-peak variations of up to 100s of meV (*152*). This moiré potential can induce bandfolding near the band edges, potentially inducing very flat bands in parts of the band structure at particular twist angles. Famously, this was shown to cause superconductivity (*11*) and Mott-like insulating states (*153*) in so-called "Magic angle" twisted bilayer graphene with a twist angle near 1.1°. Besides graphene, moiré physics in twisted TMDs has also received wide attention, with a particular focus on the effects of the moiré potential on excitons. For instance, twisted heterobilayers were found to exhibit localized exciton states trapped in the moiré potential (*126*), as well as twist-angle dependent interlayer hybridization between the two layers (*128*). More recently, Hubbard model physics, Mott insulator and generalized Wigner states were observed in these systems (*154, 155*). Twisted homobilayer TMDs, which can have larger moiré periodicities due to their zero lattice mismatch, have also proven to be very interesting, with experimental demonstrations of superconductivity (*156*).

4.2 Imaging moiré patterns – an important challenge

A major obstacle to fully understanding the rich physics of twisted 2D-materials has been the limited ability to image the moiré structure and correlate it with measurements of optical and electronic properties. This is crucial to our understanding of moiré physics, because the lattices can rotate both locally and globally during the stacking process, so the actual moiré pattern can be vastly different from that expected from the target twist angle. While transmission electron microscopy (TEM) has been used to image moiré patterns with great success (*157*), the thin substrate required for such imaging has prevented optoelectronic measurements on the same sample. This has sparked a recent interest in new imaging techniques, including scanning nearfield optical microscopy (SNOM) (*158*), piezoresponse force microscopy (PFM) (*159*) and conductive atomic force microscopy (CAFM) (*160, 161*). In our work, we have taken two other paths to address the challenge of imaging moiré patterns. In one effort, described in section 4.4, we developed an imaging technique based on Scanning Electron Microscopy (SEM) that allows for imaging moiré patterns with periodicities down to 10s of nm. Crucially, this technique is fully compatible with standard devices on regular substrates, and therefore enables correlating the imaged moiré structure with optoelectronic measurements in the same device. In the other effort (*162*), we studied the local exciton properties in individual moiré domains by fabricating twisted homobilayer devices with domains that were sufficiently large to be optically resolved in conventional confocal microscopy (see section 4.3).

4.3 Interlayer excitons in small-angle twisted homobilayer $MoSe_2$

When two different 2D materials are stacked on top of each other into a heterobilayer, the moiré periodicity is limited by their relative lattice mismatch, typically resulting in moiré periodicities below 30 nm. On the other hand, homobilayers, which consist of two layers of the same 2D material, can in principle exhibit much larger moiré periodicities provided that the twist angle is sufficiently small. In Ref. (*162*), we studied homobilayer $MoSe_2$ devices with very small twist angles in order to achieve optically resolvable moiré domains. In such devices, transmission electron microscopy (TEM) imaging shows that the moiré pattern exhibits strong lattice reconstruction (Fig. 4.1a), where the lattices rotate and stretch locally to maximize the area of energetically favorable AB- and BA-domains. We note that such TEM imaging is incompatible with optoelectronic measurements, thus the imaging was conducted in a different device than the following measurements of the exciton properties.

Figure 4.1b,c show the electric field dependence of the photoluminescence from interlayer excitons in two different spots in one of our devices, demonstrating that the Stark shift has a different sign in the two spots. These observations can be explained by the fact that the AB and BA domains have broken inversion symmetry and resultant (opposite) preferential dipole moments. Specifically, in AB (BA)-stacked domains, electrons have a lower energy in the top (bottom) layer. Holes, on the other hand, have a much weaker layer preference, since the valence band maximum is at the Γ-point, where the wavefunction is almost equally distributed between the two layers. We thus assign spot 1 (2) to a BA (AB) domain, where the lowest energy interlayer exciton species has a dipole moment pointing up and thus a negative (positive) Stark shift with positive vertical electric field. Importantly, the extracted electron-hole separation of 0.26 nm is

slightly smaller than half the interlayer distance, which is consistent with the electron localized in one layer and the hole almost perfectly delocalized between the layers. At the border between two domains or in areas where the domains are very small, the optical spot covers several domains, and thus both interlayer exciton species are observed (Fig. 4.1d).

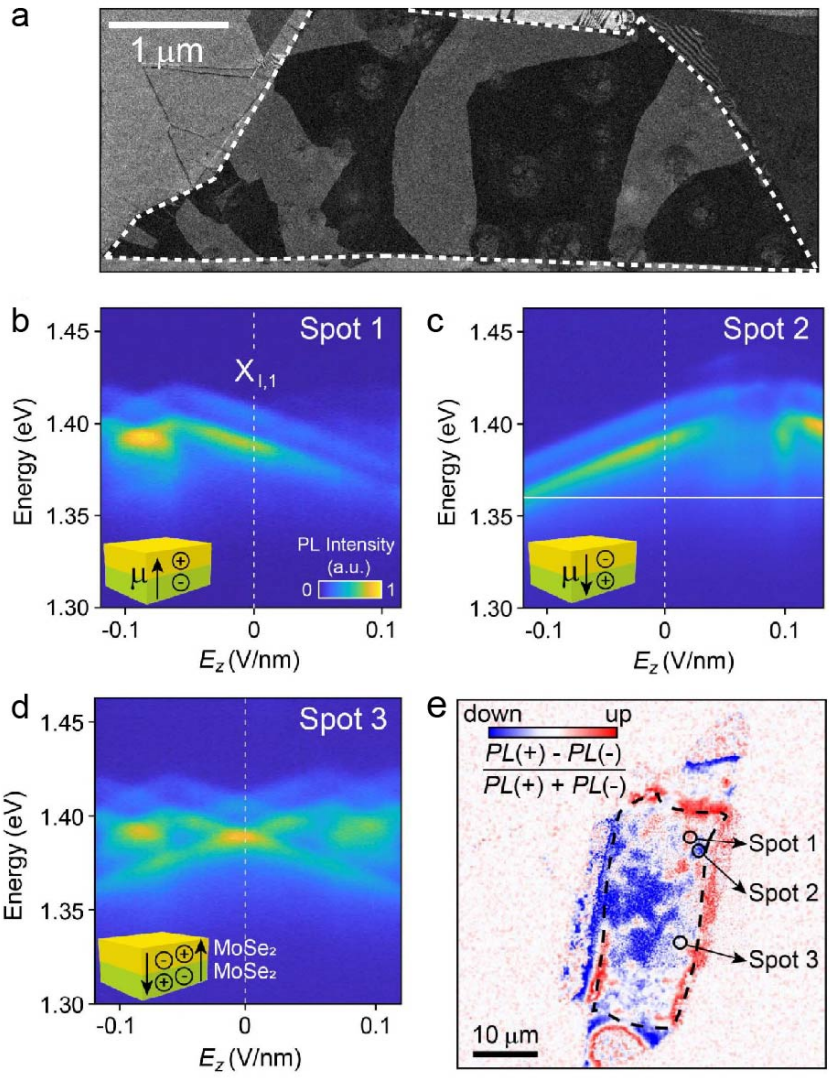


Figure 4.1: Optically resolvable moiré domains with broken mirror symmetry in twisted $MoSe_2/MoSe_2$. **a**, TEM image of twisted $MoSe_2/MoSe_2$, showing large reconstructed AB- and BA-domains. **b**,**c**, Electric field dependence of photoluminescence from interlayer excitons in two different spots. Opposite Stark shifts in the two spots are explained by (opposite) preferential dipole moments in AB and BA domains. **d,** Same as **b** and **c**, but in location where both exciton species are observed. **e**, Mapping of $\eta = ((PL(+)-PL(-))/(PL(+)+PL(-))$ (see definition in text), demonstrating confocal imaging of the moiré domains.

By collecting the photoluminescence below 1.36 eV and mapping out $\eta = \big((PL+) - (PL-)\big)/\big((PL+) + (PL-)\big)$ (where $(PL\pm)$ is the photoluminescence at $E_z = \pm 0.15\ \mathrm{Vnm}^{-1}$), we create a spatial map of the domain structure in the device (Fig. 4.1e). While this works very well in devices with such large moiré domains, devices with larger twist angles (smaller domains) require alternative techniques to correlate moiré structure with exciton properties. In section 4.4, we address this challenge.

4.4 Correlated moiré imaging and exciton spectroscopy in twisted bilayer WSe_2

The following is reproduced from the manuscript "Excitons in a reconstructed moiré potential in twisted WSe_2/WSe_2 homobilayers" by Trond I. Andersen, Giovanni Scuri, Andrey Sushko, Kristiaan De Greve *et al*. (*163*)

Moiré superlattices in twisted van der Waals materials have recently emerged as a promising platform for engineering electronic and optical properties. A major obstacle to fully understanding these systems and harnessing their potential is the limited ability to correlate direct imaging of the moiré structure with optical and electronic properties. Here we develop a secondary electron microscope technique to directly image stacking domains in fully functional van der Waals heterostructure devices. After demonstrating the imaging of AB/BA and ABA/ABC domains in multilayer graphene, we employ this technique to investigate reconstructed moiré patterns in twisted WSe_2/WSe_2 bilayers and directly correlate the increasing moiré periodicity with the emergence of two distinct exciton species in photoluminescence measurements. These states can be tuned individually through electrostatic gating and feature different valley coherence properties. We attribute our

observations to the formation of an array of two intralayer exciton species that reside in alternating locations in the superlattice, and open up new avenues to realize tunable exciton arrays in twisted van der Waals heterostructures, with applications in quantum optoelectronics and explorations of novel many-body systems.

Engineered moiré superlattices arising from lattice mismatch or relative twist angle between layers can induce periodic potentials for charge carriers and excitons. While conceptually related to quantum simulation experiments such as those in optical lattices (*164*), these systems feature the advantages of on-chip integrability, electronic tunability, and small (nm) length scales. Moiré superlattices in semiconductor van der Waals (vdW) materials, such as transition metal dichalcogenides (TMDs), are attractive for this purpose due to the presence of optically active, tightly bound excitons (*2*). Theoretical studies predict that these systems can be used to create topologically nontrivial states (*165, 166*), atomically thin mirrors for quantum optical applications (*167*), and Hubbard model simulators (*168*) analogous to those based on trapped atom arrays (*169*). Recent experiments have explored the effects of moiré patterns in heterobilayers of TMDs, including $MoSe_2/WSe_2$ (*126, 129, 170, 171*), $MoSe_2/WS_2$ (*128*), $MoSe_2/MoS_2$ (*125*), and WS_2/WSe_2 (*127*). Photoluminescence and absorption measurements in those experiments suggest that the periodic moiré potential can cause trapping of interlayer exciton states (*126, 129*), hybridization between bands in opposite layers (*128*), and multiple intralayer exciton states (*127*). Most recently, there has been growing interest in twisted TMD homobilayers (*96, 156, 166, 172, 173*), where the moiré lattice is governed only by the relative twist angle and not lattice constant mismatch, enabling experimental access to a larger range of superlattice length-scales. This system was shown to exhibit superconductivity (*156*), and theoretically predicted to display topological insulator behavior as well as two-orbital Hubbard physics (*166, 172*).

A major challenge within this field involves correlating the optical response with imaging of the moiré lattice, which is necessary to draw unambiguous conclusions, disentangle extraneous effects, and investigate the role of moiré length scales. Although direct imaging of the small ($\lesssim$100 nm) moiré domains can be achieved through transmission electron microscopy (TEM) (*127*) or scanning probe microscopy (*174*), such imaging techniques require special sample preparation, which has previously prevented optoelectronic measurements of the same device. Therefore, there have recently been substantial efforts to develop new imaging techniques, including Piezoresponse Force Microscopy (PFM) (*159*), Conductive Atomic Force Microscopy (CAFM) (*160, 161*) and Scanning Nearfield Optical Microscopy (SNOM) (*158*).

An alternative route to these scanning probe methods involves different forms of electron microscopy. While scanning electron microscopy (SEM) techniques have been used extensively for crystallographic imaging, the typical mode of operation relies on detection of backscattered primary electrons (*175, 176*), which is not efficient enough to probe mono- or bilayer materials. Nevertheless, in recent studies of conventional, covalently bonded semiconductors, it was pointed out that a subtle interplay between the channeling of primary electrons through a lattice and the extreme depth dependence of the generation of secondary electrons (*177*) allows for direct imaging of the surface lattice ordering of SiC.

Here, we demonstrate SEM-based imaging of local atomic stacking order in a range of 2D materials. This technique, which we refer to as "channeling modulated secondary electron imaging", is compatible with typical devices used widely in the field, including complete hBN-encapsulation, electrostatic gates, generic (*e.g.* Si/SiO_2) substrates, and no special sample fabrication. Crucially, it enables us to correlate imaged moiré patterns with optoelectronic measurements in twisted WSe_2/WSe_2 bilayers.

4.4.1 Channeling modulated secondary electron imaging technique

Our approach, illustrated in Figure 4.2a, is based on measuring secondary electron emission, which depends on the scattering cross section experienced by the incident primary electron beam as well as the escape depth of the secondary electrons. By placing the device at an angle, different stacking orders exhibit different channeling conditions, thus giving rise to signal contrast between them.

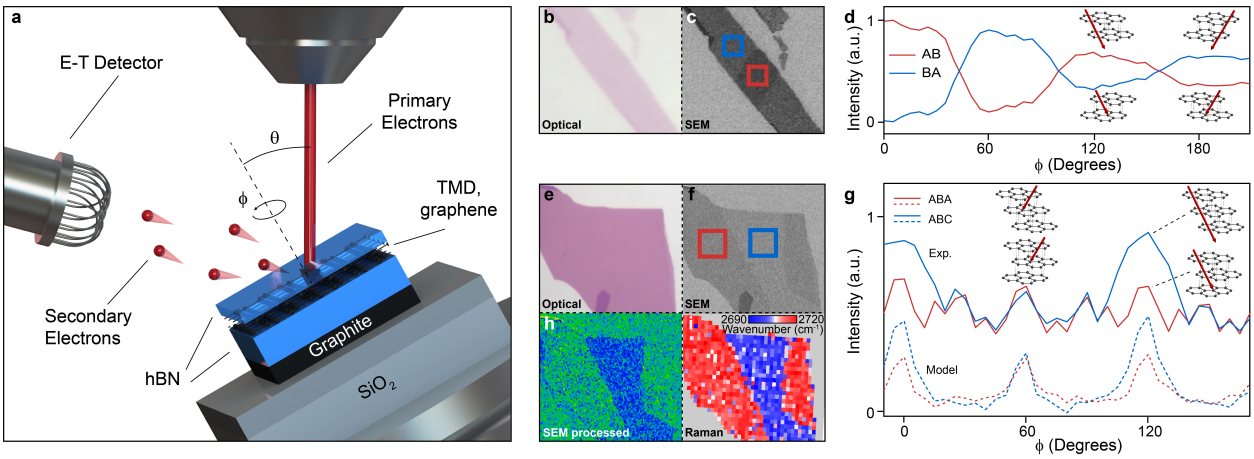


Figure 4.2: SEM based imaging of stacking order in vdW heterostructures. a, Schematic of operating principle: an accelerated electron beam is focused onto the device at an azimuthal (polar) angle, ϕ (θ). Channeling of the incident electrons and subsequent secondary electron generation depend on the local stacking order. **b,c,** Optical (**b**) and SEM (**c**) images of a natural bilayer graphene flake ($\theta = 24°, \phi = 5°$). SEM reveals areas of different contrast. **d**, Dependence of SEM signal on ϕ in boxed locations in **c** (normalized to the mean). The two regions display 120° symmetry and 180° phase offset, consistent with AB and BA domains (inset schematics). The contrast decays due to gradual charging of the substrate. **e-g**, Same as **b-d**, in a few (~ 6) layer graphene flake. The more complex ϕ-dependence is consistent with our model of ABC and ABA stacking (dashed line, Appendix C2): while ABC stacking exhibits fully open channels every 120°, ABA stacking shows only partially open channels every 60°. **h**, Difference between two SEM images with a 60° offset in azimuthal angle. **i,** Spatial map of Raman 2D-peak position, confirming the ABC/ABA stacking order.

To illustrate how the technique resolves atomic stacking order in vdW heterostructures, we first consider naturally occurring stacking domains in graphene. Besides representing a simple model system due to its monoatomic and purely 2D structure, stacking domains in graphene have been shown to exhibit exciting novel physical phenomena, including the observation of Mott

insulator and superconducting states in ABC-stacked trilayer graphene (*178*), and topologically protected states along the AB/BA boundaries in bilayer graphene (*158, 179, 180*).

Figure 4.2b-c show images of a bilayer graphene flake on a Si/SiO_2 substrate, acquired with optical microscopy and SEM, respectively. While the former is homogeneous, confirming that the flake has uniform thickness, SEM imaging at a 24° tilt angle and a small acceleration voltage of 500 eV uncovers two types of distinct domains. As the stage is rotated azimuthally, the number of collected secondary electrons exhibits 120°-periodic oscillations, with a 60° phase shift between the two domain types (Figure 4.2d). The contrast is found to gradually decrease when the polar angle (θ) is moved away from 24° and to reappear near 40° (Appendix C1). We attribute the observed domains to different levels of electron channeling through naturally occurring regions of AB- and BA- stacked graphene (*179-181*). Such channeling arises at particular polar and azimuthal angles (ϕ), when the incoming electron beam is oriented parallel to the open cavities or "channels" within the atomic lattice (inset of Figure 4.2d), allowing the electrons to travel through the material with minimal scattering. Consistent with our observations, the open cavities are expected to appear when $\theta = \tan^{-1}\left(\frac{na_{\mathrm{gr}}}{d_{\mathrm{gr}}}\right) = 24°$, where n is an integer ($n = 1$ here), a_{gr} is the graphene atom-atom spacing and d_{gr} is the interlayer spacing. Moreover, optimal channeling conditions appear when ϕ is aligned with one of the three in-plane displacement vectors between the top and bottom layers, thus causing the observed 120° periodicity and the 60° relative angle between AB and BA domains. Since graphene has a lower atomic number, Z, than the substrate (SiO_2), it generates fewer secondary electrons (*182*). Thus, for graphene on oxide substrates, the secondary yield maxima occur when channeling is maximized.

Turning to a thicker (approx. 6 layer) graphene flake, which also exhibits domains in SEM imaging that are not observable optically (Figure 4.2e-f), we find a more complex azimuthal dependence (Figure 4.2g). While one domain type (red) is 60°-periodic in ϕ, the other (blue) exhibits a period of 120°, reflecting a lower inherent symmetry (Figure 4.2h). Based on a simple channeling model (dashed line, Figure 4.2g; see Appendices C2 and C3), we attribute this more complex pattern to ABA- and ABC-stacking orders (*183*), as independently verified with Raman spectroscopy (*184*) through the position of the Raman 2D peak (Figure 4.2i, see AppendixC4 for representative spectra). Indeed, consistent with our observations, the two domain types are expected to have similar scattering cross sections at certain azimuthal angles (Figure 4.2g, left inset), while at other angles, the ABC domain allows for "complete channeling" (Figure 4.2g, right inset), giving rise to enhanced SEM signal every 120°.

Having demonstrated the ability to differentiate different stacking orders in few-layer graphene, we turn to a twisted WSe_2/WSe_2 bilayer device (D1), motivated by the fact that moiré patterns are periodic variations between AB and BA stacking orders (*127, 129*). We fabricate a fully functional device (Figure 4.3a), including few-layer graphene gates for electrostatic tuning and encapsulation in hexagonal BN (hBN), which is widely used to improve the optical and electronic properties of 2D materials. In order to image the TMD layers embedded in the heterostructure, we find that the acceleration voltage must be increased to 3 keV so that secondaries can escape from within the heterostructure (see Appendices C5 and C6 for further discussion of escape depth and acceleration voltage dependence). Moreover, since the lattice constant and interlayer spacing is different in WSe_2 from graphene, a different polar angle must be used. To simultaneously maximize the interaction volume, we use a shallow angle $\theta = \tan^{-1}\left(\frac{3a_{WSe_2}}{d_{WSe_2}}\right) \sim 40\,°$, corresponding to three lattice shifts.

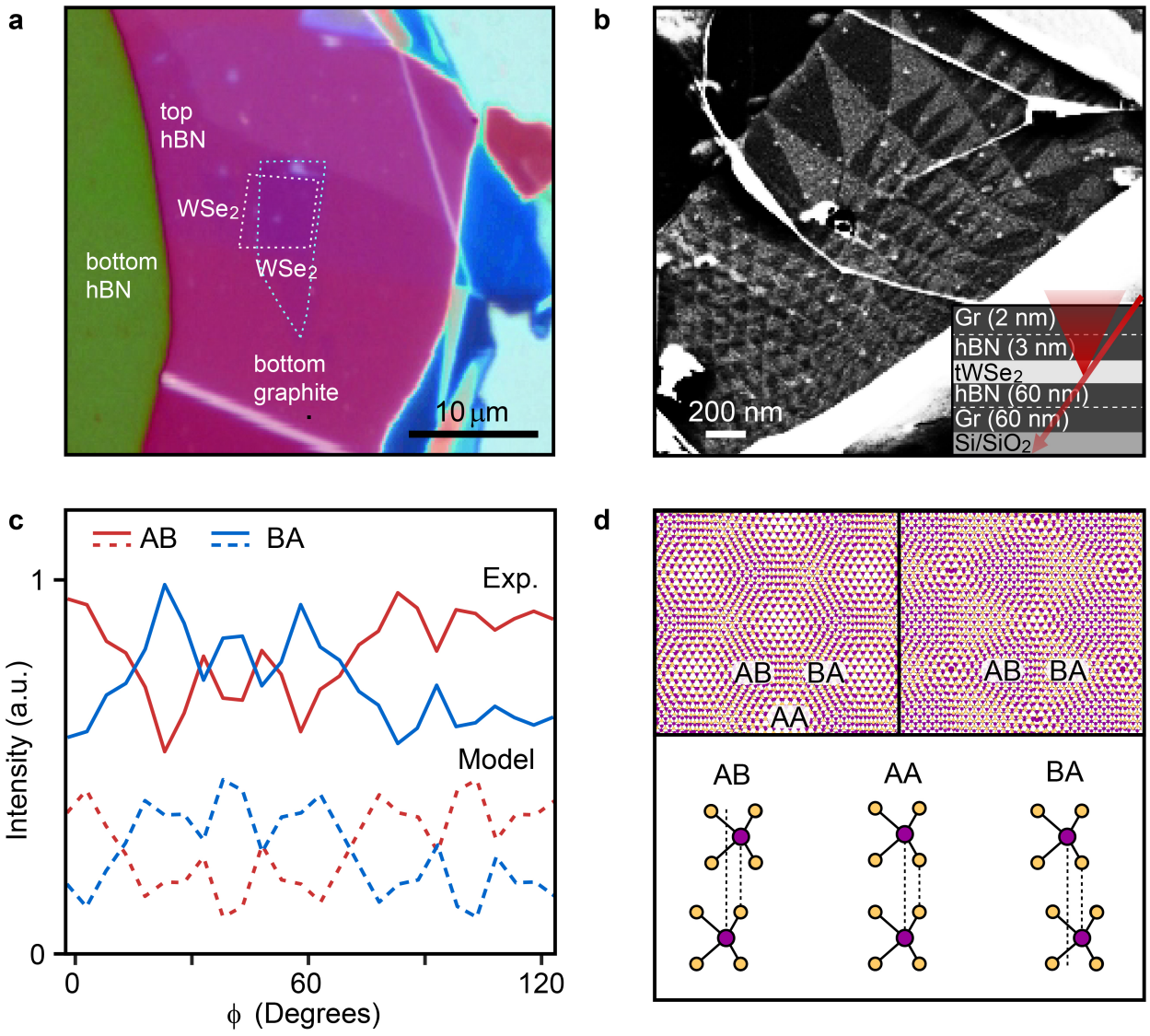


Figure 4.3: Moiré superlattices in twisted homobilayers. a, Optical image of hBN-encapsulated twisted WSe_2 bilayer (device D1). Dashed white and teal lines indicate top and bottom TMD layer, respectively. **b**, SEM image of device D1, showing a reconstructed moiré pattern with triangular AB and BA (3R) stacking domains. ($\theta = 40°$). **c**, ϕ-dependence of signal from AB and BA domains (solid red and blue curves), along with model predictions (dashed curves). **d,** Top: Top view schematic of moiré pattern (5° twist angle) with and without reconstruction (right and left). Reconstruction was illustrated by reducing the local twist angle near AB and BA sites. Bottom: Side view of AB, AA and BA stacking orders. Purple: W, yellow: Se.

Following these considerations, the SEM technique enables imaging of a moiré pattern in the small (<1°) twist angle WSe_2/WSe_2 bilayer (Figure 4.3b). Due to the 3D structure of TMDs,

we observe a more complex ϕ-dependence than in graphene (Figure 4.3c), which is nevertheless captured well by our model, which takes the full lattice structure into account (dashed line, see also Appendix C2). Moreover, the bright regions now correspond to less channeling because in contrast to graphene, the constituent elements of WSe_2 have higher Z than the SiO_2 substrate and therefore a higher secondary electron yield.

Crucially, the imaged moiré pattern exhibits atomic reconstruction, where the lattices are strained locally to maximize the size of energetically favorable AB and BA (3R) stacking domains (Figure 4.3d, right) (*157, 159-161, 174*). This reconstruction mechanism results in a triangular array of alternating AB/BA regions, as opposed to gradual transitions between the two domain types in a canonical moiré picture (Figure 4.3d, left) (*157*) – the latter being more prevalent at larger twist angles and in heterobilayers with intrinsic lattice mismatch (*127, 169*).

The SEM imaging directly demonstrates that the local moiré periodicity varies considerably across and within each of our devices, highlighting the necessity of imaging. This inhomogeneity is also observed in a similar hBN-encapsulated and gated device (D2, Figure 4.4a), with a target twist angle of 2.5°, close to the theoretically proposed critical angle for reconstruction (*160, 161*). In particular, SEM imaging shows that the reconstructed moiré wavelength is $\lambda_m \sim 60$ nm on the right side of the device, and gradually decreases towards the left until the reconstructed moiré pattern is no longer observed (λ_m<10 nm, left side of the dashed line). Since a domain size of 10 nm is near the threshold for reconstruction, it is likely that the moiré pattern is not fully reconstructed in this left region, which may also play a part in its reduced visibility.

4.4.2 Correlating reconstructed moiré patterns with optical measurements

Because the SEM-based imaging technique is compatible with fully functional devices, we can now explore correlations between the moiré wavelength observed in SEM and the local optoelectronic properties. In particular, device D2 also enables us to explore excitonic properties in the structural transition from the reconstructed to non-reconstructed regime. After co-aligning the SEM image with a map of photoluminescence (PL) intensity (see Appendix C9 for details), we collect gate-dependent PL spectra from both sides of the device (boxed crosses in Figure 4.4a), in locations where λ_m<10 nm and λ_m=25±10 nm (Figure 4.4b and c, respectively). Due to the diffraction limited spot size and the aforementioned inhomogeneity, we note that each optical measurement probes a finite range of domain sizes, as indicated by the uncertainty range in λ_m.

In both spots, we observe two sets of emission features: the peaks near 1.5 eV are attributed to momentum indirect interlayer excitons based on their energy (*96, 123*), whereas the higher energy peaks near 1.7 eV are attributed to K-valley momentum direct intralayer excitons, consistent with previous studies (*7, 123, 185*) and absorption measurements (Appendix C10). While only one intralayer exciton peak (peak I) is observed on the left side of the device (Figure 4.4b, λ_m<10 nm), an additional higher energy peak (peak II) emerges in the right part (Figure 4.4c, λ_m=25±10 nm). Their splitting is 36 meV in the *p*-doped regime, where the two peaks are most pronounced, and decreases to 16 meV in the intrinsic regime (Appendix C11). Besides their resonance energies, the doping dependence of peak I and II is also distinct: with increasing hole doping, peak I broadens and intensifies strongly, while peak II is much less affected.

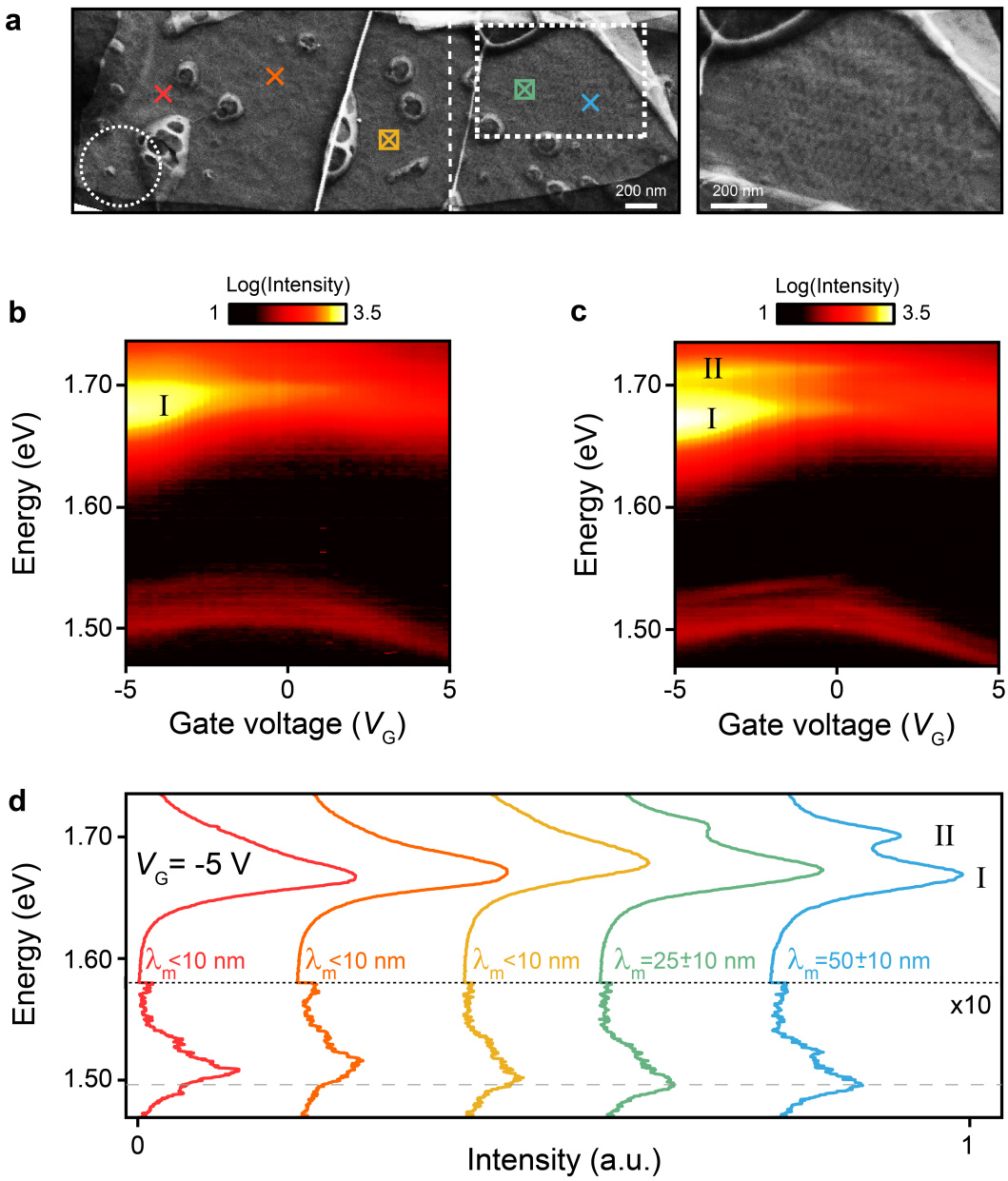


Figure 4.4: Correlating local superlattice structure and optical properties. a, Left: SEM image ($\theta = 40°$) of device D2, displaying reconstructed moiré pattern. λ_m increases from <10 nm to 60 nm from left to right. The moiré pattern is not visible left of the vertical dashed line. Dashed circle indicates optical beam spot size, crosses indicate beam spot centers. Right: Zoom-in of area indicated by dotted lines. **b**,**c**, Gate-dependent PL spectra collected from locations with $\lambda_m <$ 10 nm (**b**) and $\lambda_m = 25 \pm 10$ nm (**c**), indicated by boxed crosses in **a**. While the left region only exhibits one intralayer peak in the *p*-doped regime, the right (larger λ_m) region exhibits two peaks. **d**, Raw PL spectra collected from the locations marked with crosses in **a**, at $V_G = -5$ V. The spectra are offset for clarity and the intensity is multiplied by 10 below 1.58 eV. The higher energy (type II) exciton peak emerges with increasing λ_m, and the interlayer exciton emission is blue-shifted for $\lambda_m < 10$ nm.

Inspecting more locations (crosses in Figure 4.4a) at V_G=-5 V, we find that a single dominant intralayer peak appears in all spots investigated on the left side of the device ($\lambda_m <$ 10 nm), and that the higher energy peak only emerges with the larger λ_m in the right region (Figure 4.4d), where the reconstructed moiré domains are observed. Consistent with these observations, the two intralayer exciton peaks are also observed in all of our devices with small twist angles ($0° - 0.5°$, Appendix C12), and the higher-energy peak is absent in all large-angle devices (5°-22°, Appendix C12). We also find that the interlayer exciton peak is blue-shifted in the left (small λ_m) region. This is not expected to be due to interlayer contamination (further details in Appendix C13), but rather the weaker interlayer coupling in the small-domain regime (*96, 123, 124, 135*), which is also expected to cause less lattice reconstruction (*160, 161*).

Previous studies of non-reconstructed moiré patterns in twisted heterobilayers (*126, 127, 186, 187*), as well as recent theoretical predictions for twisted homobilayer WSe_2 (*188*), have considered exciton multiplets that arise from the moiré-induced mixing of exciton Bloch states k=0 and k=k_m (where k_m is a moiré wavevector), due to band folding and miniband formation. In that case, the splitting between the states, $E(k_m) - E(0) \sim \lambda_m^{-2}$, is strongly dependent on domain size (*127, 186-188*). In order to investigate whether this is the case for the two exciton states observed here, we turn to the smaller angle device D1, which has both larger moiré domains and a greater variation in their size (Figure 4.5a). Importantly, this device exhibits the same two-peak structure as device D2 (Figure 4.5b, inset), with a very similar splitting in both the *p*-doped (36 meV) and intrinsic (16 meV) regimes (see Appendix C11). By spatially correlating the PL signal with SEM imaging (Figure 4.5b), we find that the splitting is independent of domain size over a 30-fold range (25-670 nm, Figure 4.5c), in stark contrast to previous observations in TMD heterostructures (*126, 127*).

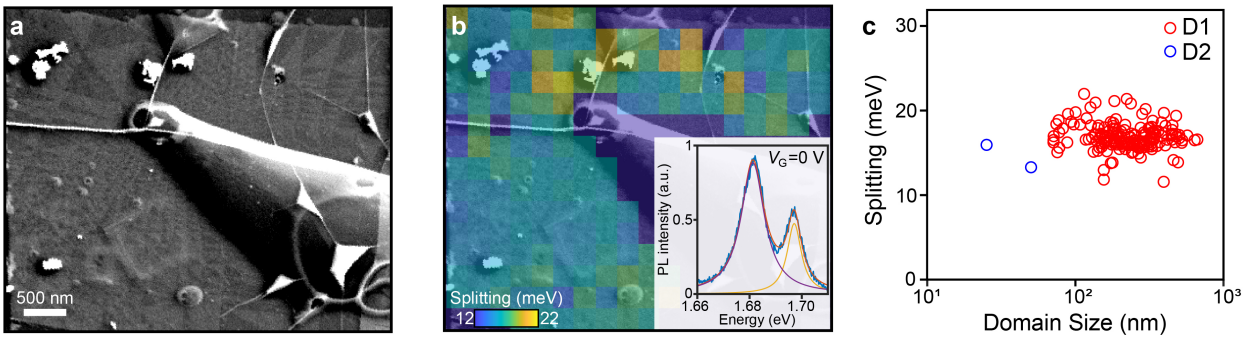


Figure 4.5: SEM correlation of PL peak splitting. a, Zoomed-out SEM image of D1 showing large (70-670 nm) reconstructed moiré domains in the entire twisted bilayer region. ($\theta = 40°$). **b,** Map of extracted exciton peak splitting overlaid with the SEM image from **a**. Inset: Example PL spectrum (blue) with double Lorentzian fit. **c**, Correlation of SEM and PL shows that the peak splitting is independent of domain size over a 30-fold range. Red: device D1, blue: device D2.

Device D1 also exhibits more pronounced features in the *n*-doped regime, which shows very different behavior from the *p*-doped regime. While peak I red-shifts much more than peak II at the onset of the *p*-doped regime ($E_{\mathrm{h}}^{\mathrm{I}}$ =20 meV, $E_{\mathrm{h}}^{\mathrm{II}} \sim 0$ meV), peak II exhibits a larger red-shift in the *n*-doped regime ($E_{\mathrm{e}}^{\mathrm{II}} = 16$ meV, $E_{\mathrm{e}}^{\mathrm{I}} = 11$ meV; green arrows in Figure 4.6a), thus reducing the splitting to only 10 meV (see Appendix C10 for equivalent behavior in absorption measurements and Appendix C11 for fitting procedure).

In order to further explore the origin of the two exciton peaks, we conduct polarization-resolved photoluminescence spectroscopy. By illuminating with linearly polarized light, we excite a superposition of K and K' valley excitons (excited by the superposition of σ^+ and σ^- photons), and subsequently measure the quantum coherence between these valley states by comparing the parallel and perpendicular emission components (*116*). Importantly, we note that this measurement is very distinct from circularly polarized PL measurements, which probe the valley depolarization rate, not the quantum coherence (*116, 189*) (see further explanation in Appendix C14).

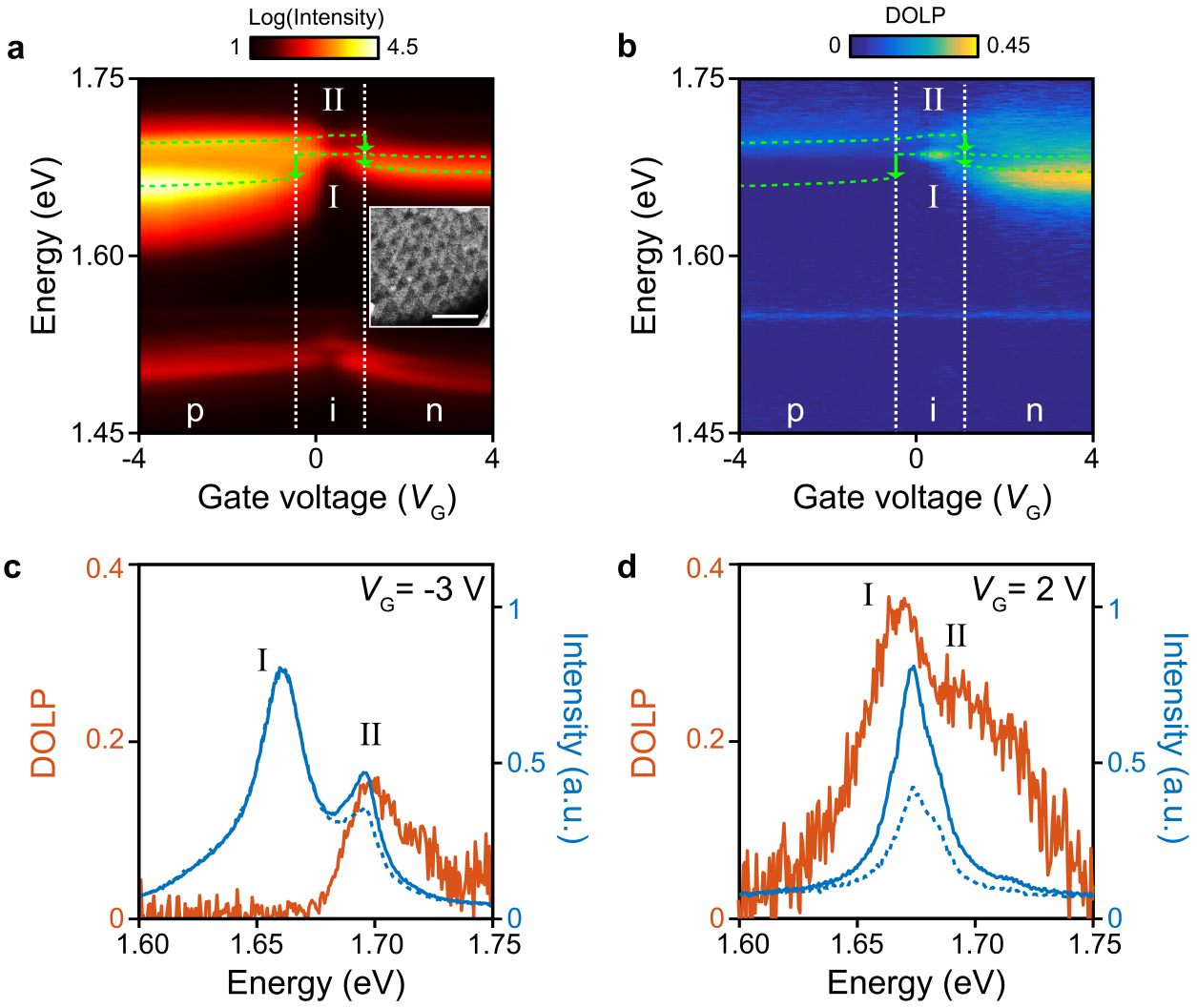


Figure 4.6: Valley coherence of the two exciton species. a, Gate-dependent PL spectra from device D1. Green dashed lines show fitted peak positions (Appendix C11). Inset: SEM image of measured spot ($\theta = 40°$). Scale bar: 200 nm. **b**, Gate-dependent DOLP, showing that type I excitons have nearly zero DOLP in the *p*-doped regime. **c**,**d**, Co- and cross-polarized PL (blue solid and dashed curves), and corresponding DOLP (orange) at $V_G = -3$ V (**c**) and $V_G = 2$ V (**d**).

Defining the degree of linear polarization, DOLP $= (I_{\parallel} - I_{\perp})/(I_{\parallel} + I_{\perp})$, where $I_{\parallel(\perp)}$ is the intensity of emission with parallel (perpendicular) polarization, we find that the two exciton species have very distinct coherence properties. The lower-energy (type I) exciton has almost zero DOLP in the *p*-doped regime, while the higher-energy (type II) exciton exhibits a DOLP of up to

18% (Figure 4.6b and c). When entering the neutral regime, the DOLP of the type I exciton increases strongly and exceeds that of type II, which exhibits much less change. In the *n*-doped regime, the DOLP of both exciton types is found to be even higher, reaching 44% (Figure 4.6b and d). We note that very similar doping dependent behavior and valley coherence properties were also observed in several other small twist angle WSe_2/WSe_2 devices (see Appendices C15 and C16).

4.4.3 Properties of the reconstructed superlattice

We here show that all our observations are consistent with two spatially alternating, individually controllable exciton species in the reconstructed superlattice. Our model is based on the local band structure differences in the observed AB- and BA-stacked domains of t-WSe_2/WSe_2. Since AB and BA domains are vertical mirror images of each other, we refer to the top layer in BA domains and the equivalent bottom layer in AB domains as type I locations (Figure 4.7a, maroon squares), and the opposite locations as type II (Figure 4.7a, orange squares). We conduct density functional theory calculations (DFT, see further details in Appendix C17), which show that the global valence band maximum (VBM) at the K-point is $\Delta E_{\mathrm{VB}} = 73$ meV higher in type II locations than in type I locations (Figure 4.7b). Conversely, the local conduction band minimum at the K-point is $\Delta E_{\mathrm{CB}} = 60$ meV higher in type I locations. These observations in essence reflect the different electronic environment of the respective layers. In addition, and consistent with previous studies, our DFT calculations indicate that the wavefunctions at the K-point are localized in the individual layers (insets, Figure 4.7b) (*190*).

These results give rise to two effects that split the energies of type I and type II excitons in the namesake locations. First, the two locations are expected to possess different optical band gaps,

causing excitons in type II locations to be higher in energy by $\Delta E_0 = \Delta E_{\mathrm{VB}} - \Delta E_{\mathrm{CB}} = 13$ meV in the intrinsic regime (Figure 4.7c). This is in very good agreement with our observations for all devices ($\Delta E_0 \sim 16$ meV; Figure 4.6 and Appendices C11 and C12). Importantly, since $\Delta E_0 < \max(\Delta E_{\mathrm{VB}}, \Delta E_{\mathrm{CB}})$, our results suggest a staggered band gap at the domain boundaries.

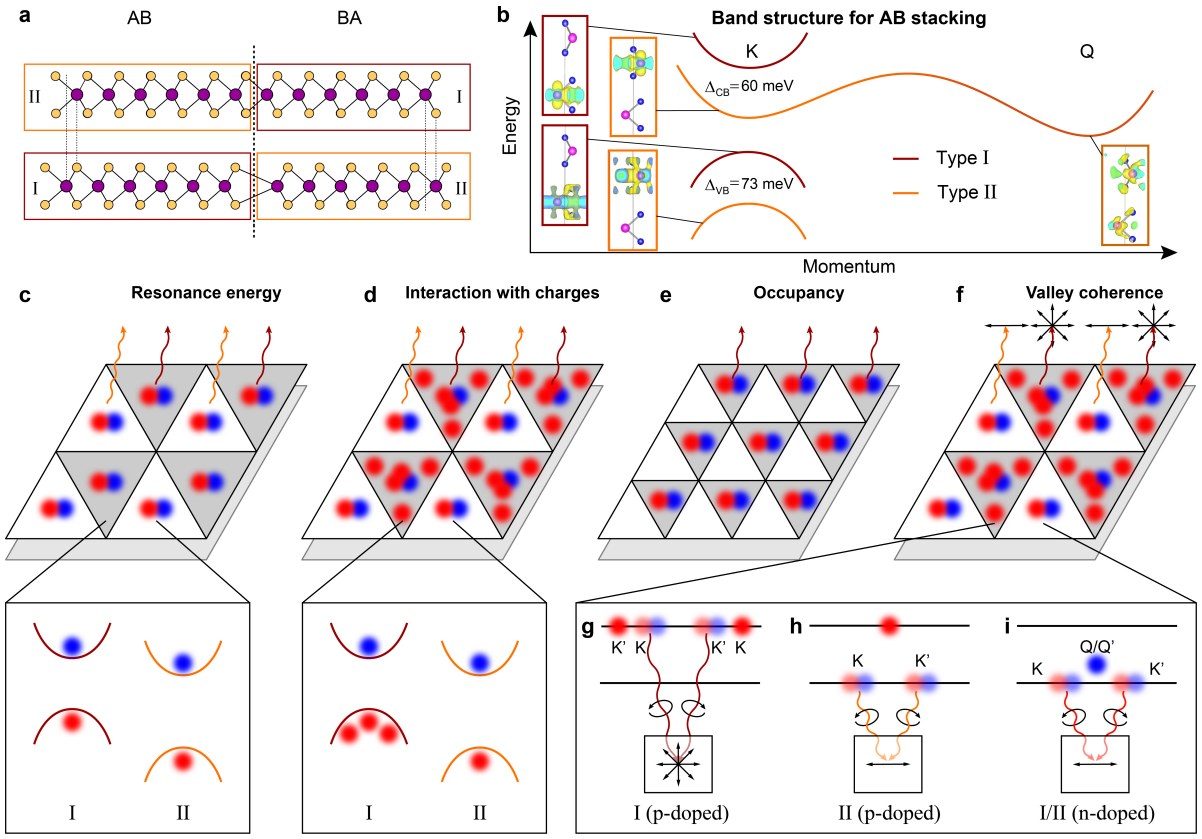


Figure 4.7: Periodic exciton and doping landscape in reconstructed superlattice. a, Side view of AB and BA domains. Maroon and orange boxes indicate type I and II locations, respectively. **b**, Band structure schematic and wavefunction distribution at important points in *k*-space. **c-f**, Schematic of alternating properties in the two-dimensional triangular exciton array. For clarity, only excitons in the top layer are shown. **c**, Excitons have higher energies in type II locations due to larger optical band gap. **d**, Type I excitons are preferentially *p*-doped due to higher VBM. **e**, Only the type I exciton is observed in the small-domain regime due to relaxation of the higher energy exciton. **f**, The two alternating exciton species also have different valley coherence properties. **g-i**, Schematics of K/K' exciton recombination. Black horizontal lines indicate top and bottom layer. **g**, Since the resident hole must be in the opposite valley of the type I exciton, it becomes correlated with the photon and breaks coherence. **h**, For the type II exciton, the resident hole is in a different layer and carries no information about the exciton valley, allowing for non-zero DOLP. **i**, DOLP is non-zero for both exciton types in the *n*-doped regime, because the electron is in a different valley (Q/Q') than the exciton (K/K').

Second, in the doped regimes, the two exciton types are expected to have an additional energy difference because of different interactions (*191*) with the additional charges (Figure 4.7d). In particular, our calculations predict that type I locations should be preferentially *p*-doped due to their higher VBM (Figure 4.7b) (*144, 166*). Thus, it is indeed expected that type I excitons can bind strongly to a nearby hole to form charged excitons with reduced energy, while type II excitons only interact weakly with the holes in the other layer, as found in our measurements (Figure 4.4a). In the *n*-doped regime, our calculations indicate that the induced carriers are less layer-localized than in the *p*-doped regime, because the global conduction band minimum is at the Q-point instead of the K-point (Figure 4.7b) (*83, 140*). Both exciton species are therefore expected to interact with the electrons, consistent with our observations in Figure 4.6a.

The higher energy (type II) peak is only expected to be observed if the excitons are unable to relax to a lower energy state in a different location type before recombining (τ_X ~1-10 ps, Figure 4.7e) (*192, 193*). While interlayer tunneling is symmetry forbidden at the K-point in 3R (AB/BA-stacked) bilayers (*166, 194*), moving laterally to an oppositely stacked domain within the same layer is a faster process (*192, 193*), especially for small domains (Figure 4.7e). The estimated exciton diffusion length in our system is 10-100 nm (see discussion in section 4.5.1), consistent with the observed disappearance of the higher energy peak as the domains decrease from λ_m= 50 nm to λ_m<10 nm. We note that for very small domains, such as in the left side of device D2 (see also large-angle devices D8-D10 in Appendix C12), additional effects may appear due to reduced effects of lattice reconstruction (*126, 127, 157, 160, 161*). When the lattices are not reconstructed into perfect AB/BA domains, interlayer tunneling is no longer symmetry forbidden (see section 4.5.2) and could therefore provide an additional relaxation pathway for the higher energy state. Moreover, in the small-domain limit, the exciton wavefunction is expected to become delocalized

over multiple moiré domains (*126, 127, 186-188*). In this case, higher energy excitons can more easily relax to lower energy states due to their increased spatial overlap (see section 4.5.3 for further details).

Finally, our model also explains why the two species have such different coherence properties (Figure 4.7f). In the case of type I excitons in the *p*-doped regime, the additional hole is in the same layer as the exciton and must therefore be in the opposite valley due to the Pauli exclusion principle (Figure 4.7g). Thus, the exciton (X) and hole (h) form an entangled state $|\mathrm{K}\rangle_{\mathrm{X}}|\mathrm{K}'\rangle_{\mathrm{h}} \pm |\mathrm{K}'\rangle_{\mathrm{X}}|\mathrm{K}\rangle_{\mathrm{h}}$. Since $|\mathrm{K}\rangle_{\mathrm{h}}$ and $|\mathrm{K}'\rangle_{\mathrm{X}}$ are orthogonal, linearly polarized emission is not possible (*195*), as observed in our experiment. For type II excitons, on the other hand, the additional holes are in the opposite layer compared to the exciton and thus carry no information about its valley, allowing for higher coherence than that of type I (Figure 4.7h) (*116, 195*). In the intrinsic regime, there are no additional holes, and the DOLP of both exciton types is therefore non-zero. Finally, in the *n*-doped regime, the K-K exciton and resident Q-valley electron are in different valleys. Thus, there is no Pauli exclusion principle at play, allowing for non-zero DOLP regardless of which layer the exciton resides in (Figure 4.7i).

4.4.4 Outlook

We have demonstrated that the SEM-based technique can be used to directly image stacking domains in bi- and few-layer graphene, and importantly, moiré patterns in twisted vdW heterostructures. This versatile technique, which can be applied to a wide range of 2D material based systems (see Appendices C3 and C7), can also become an important tool in the pursuit of large-area synthesis of high quality 2D materials through techniques such as chemical vapor deposition (CVD) (*196*). The ability to directly resolve angle-misalignment between subsequently

grown layers, as well as AB, BA, and AA' stacking orders, can provide structural information on as-grown samples without dedicated preparation for TEM, thus significantly accelerating the rate of process development for material synthesis (see Appendix C7.4).

Crucially, we have demonstrated that our technique can be used to correlate local moiré structure with optical properties. Our observations can be understood as resulting from the emergence of two spatially alternating exciton species in the reconstructed moiré superlattice, with distinct gate tunability and valley coherence properties. We note that although the bilayer system as a whole is expected to exhibit the same optical response in AB and BA domains, the two layers can be treated independently due to strongly suppressed interlayer tunneling in AB/BA domains at the K-point (*166*). Furthermore, a modest vertical electric field (~0.1 V/nm) can lift the degeneracy in AB/BA optical response in the doped regimes. Our experiments therefore indicate that this system can be an attractive solid-state platform for engineering arrays of emitters, and open the door to new quantum optoelectronic applications (*165-167, 169*). In particular, the large range of attainable moiré wavelengths in homobilayers, combined with electrostatic control of the individual regions, can be used to develop new types of moiré-based metasurfaces (*167*). Specifically, we have shown that the splitting between type I and II excitons can be electrostatically tuned from 36 meV in the *p*-doped regime to 10 meV in the *n*-doped regime. Moreover, the tunable quantum coherence properties demonstrated in our system can enable controlled, spatially patterned entangled states of light, essential for the development of quantum metasurfaces (*167*).

One particularly intriguing direction involves realizing one-dimensional localized exciton states, where the electron and hole reside at opposite sides of the sharp moiré domain boundaries in twisted homobilayers. These have been predicted to exhibit large in-plane dipole moments, as well as quantum confinement effects in 10-100 nm sized triangles (*197*). Besides featuring

triangular domains with ideal band alignment and length scales, our platform provides regular arrays of such systems, which could permit tunable interactions. This may be utilized for engineering strongly correlated states with strong optical response, potentially enabling the realization of interacting excitons for applications such as quantum nonlinear optics (*167*).

4.5 Extended discussion of exciton properties in the small-domain limit

As the moiré wavelength decreases to length scales smaller than 10 nm, the exciton properties are expected to change due to the interplay of multiple effects. First, the decreasing domain size enables more diffusion of the higher energy state to the lower energy domains. Second, atomic reconstruction also becomes less prevalent with larger twist angle (smaller λ_{m}), thus increasing interlayer tunneling, which is only symmetry forbidden in fully reconstructed 3R-stacked AB/BA domains. Finally, for moiré periodicities below the coherence length of the intralayer excitons, the exciton wavefunction becomes delocalized across multiple moiré unit cells. Below, we expand on these effects.

4.5.1 Enhanced exciton diffusion to lower energy states

As the reconstructed domains become smaller, higher energy excitons can move laterally to an adjacent domain and relax to a lower energy state before recombining. Assuming a thermalized ensemble of excitons, we estimate the distance that an exciton moves before recombining as $\ell = \sqrt{k_{\mathrm{B}}T/M_{\mathrm{X}}} \cdot \tau_{\mathrm{X}} \sim 10 - 100$ nm, where k_B is the Boltzmann constant, $M_{\mathrm{X}} \sim 0.8\, m_{\mathrm{e}}$ (*198*) is the exciton translational mass, and T=4 K is the exciton temperature. This estimated range is consistent with our PL measurements, which show that the higher energy peak disappears as the domain size decreases from 50 nm to <10 nm. Since the intralayer excitons are short-lived ($\tau_{\mathrm{X}} \sim 1 - 10$ ps)

(*94, 192*), the lifetime is expected to be comparable to the mean free scattering time, τ_{mfp}. Their motion should therefore be between the diffusive ($\ell \propto \sqrt{\tau_{\mathrm{X}}\tau_{\mathrm{mfp}}}$) and ballistic ($\ell \propto \tau_{\mathrm{X}}$) regimes, and the two pictures give similar estimates ($\sqrt{\tau_{\mathrm{X}}\tau_{\mathrm{mfp}}} \sim \tau_{\mathrm{X}}$). We also note that the exciton temperature can be slightly elevated due to laser heating. Nevertheless, since we use a low-power continuous wave laser and have not observed any heating-induced exciton peak shifts, we expect that the exciton temperature remains below 10 K, thus not impacting the conclusions in section 3.5.

4.5.2 Reduced lattice reconstruction

For twist angles larger than the critical twist angle of ~ 2° (λ_{m} ~10 nm) (*160, 161*), reconstruction effects are expected to be less prominent. It is therefore likely that the moiré pattern is not fully reconstructed in the left side of device D2 (2.5°), and even less in devices D8-10 (5°, 17° and 22°). In this case, the moiré pattern features a more continuous variation of atomic registry, as opposed to sharp transitions between AB and BA domains. Crucially, this implies that a larger portion of the moiré unit cell is not perfectly AB- or BA-stacked, but rather has an atomic registry that is somewhere in between the two. While interlayer tunneling is symmetry forbidden in AB- and BA-stacked domains (*117, 166, 187, 199, 200*), this is no longer the case for intermediary atomic registries (*116, 127, 166, 199*).

In order to analyze how the interlayer tunneling rate changes with reduced levels of lattice reconstruction, we consider the tunneling rate $w(\boldsymbol{r})$ at the valence band K-point (*166*):

$$w(\boldsymbol{r}) = w_0(1 + \exp(-iu_2) + \exp(-iu_3)), \text{ where } u_i = \boldsymbol{G}_{\mathrm{i}} \cdot \boldsymbol{s}(\boldsymbol{r}), \tag{4.2}$$

Here, $\boldsymbol{G}_{\mathrm{i}}$ is the reciprocal lattice vector $4\pi/(\sqrt{3}a_0)\hat{\boldsymbol{y}}$ rotated counter-clockwise by $(n-1)\pi/3$, and $\boldsymbol{s}(\boldsymbol{r})$ is the local misalignment between the two layers. w_0 was determined to be 9.7 meV for

WSe_2 in Ref. (*166*). We write $\boldsymbol{s}(\boldsymbol{r}) = \boldsymbol{s}_0(\boldsymbol{r}) + 2d\boldsymbol{s}(\boldsymbol{r})$, where $\boldsymbol{s}_0 = \theta\hat{\boldsymbol{z}} \times \boldsymbol{r}$ is the misalignment in the absence of reconstruction and the factor 2 accounts for the fact that both lattices relax in equal and opposite directions due to symmetry. In order to determine $d\boldsymbol{s}$ in equilibrium, we solve the Navier-Cauchy equation computationally:

$$\boldsymbol{f}_{\text{inter}} + \boldsymbol{f}_{\text{intra}} = -\partial_{d\boldsymbol{s}} U(\boldsymbol{s}_0 + 2d\boldsymbol{s})/2 + \mu\nabla^2 d\boldsymbol{s} + (\lambda + \mu)\nabla(\nabla \cdot d\boldsymbol{s}) = 0, \tag{4.3}$$

where $\mu_{\text{WSe2}} = 26.4 \frac{\text{eV}}{\text{unit cell}}$ and $\lambda_{\text{WSe2}} = 14.8 \frac{\text{eV}}{\text{unit cell}}$ are the (2D) shear modulus and the first Lamé constant, respectively (*168*). U is the stacking fault energy, which represents the energy cost of different stacking orders, and is given in Ref. (*160*), as:

$$\begin{aligned} U(\boldsymbol{s}) = c_0 + c_1 \cdot [\cos(u_5) + \cos(u_1) + \cos(u_5 + u_1)] + \\ c_2 \cdot [\cos(u_5 + 2u_1) + \cos(u_5 - u_1) + \cos(2u_5 + u_1)] + \\ c_3 \cdot [\cos(2u_5) + \cos(2u_1) + \cos(2u_5 + 2u_1)]. \end{aligned} \tag{4.4}$$

Since the goal of the present analysis is not to provide an exact spatial profile of the tunneling rate, but rather to qualitatively illustrate the changes in interlayer tunneling with reconstruction, we use the parameters c_i calculated for near-0° stacked MoS_2 in Ref. (*160*). Seeing as WSe_2 has relatively similar lattice properties, we do not expect this to significantly affect our results.

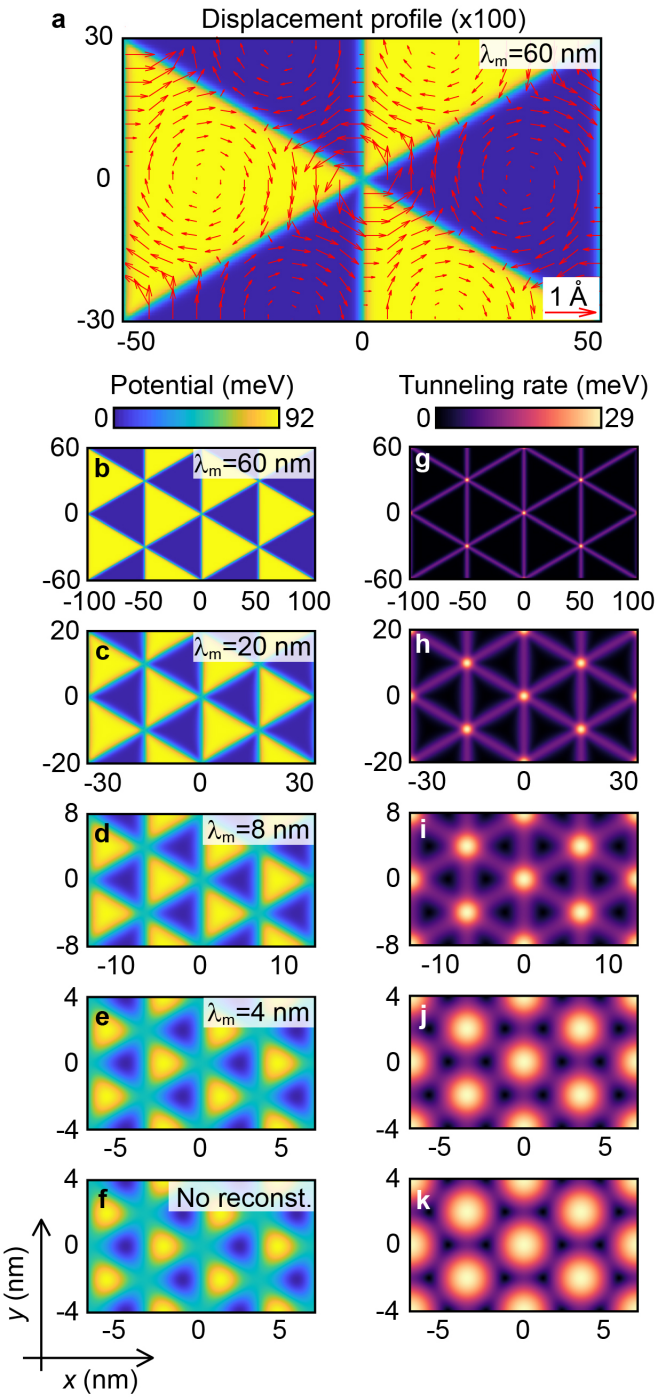


Figure 4.8: Effects of reconstruction. a, Lattice displacement profile for λ_m = 60 nm (twist angle 0.3°), showing that the lattice rotates locally to approach 3R-stacking. **b-k**, Calculated potential (**b-h**) and interlayer tunneling rate (**g-k**) at the valence band K-point for λ_m = 60 nm (**b,g**), 20 nm (**c,h**), 8 nm (**d,i**) and 4 nm (**e,f,j,k**). **b-e** and **g-j** are modeled based on the stacking fault energy, while **f** and **k** are fully non-reconstructed for reference. Weaker reconstruction effects are observed for smaller λ_m (larger twist angle), causing a smoother moiré potential and more interlayer tunneling.

Plotting the displacement profile $d\boldsymbol{s}(\boldsymbol{r})$ for λ_{m}=60 nm (Figure 4.8a), we observe that the lattice rotates locally around AB and BA centers in order to reduce the local twist angle and approach the more energetically favorable 3R-stacking order. Figure 4.8b-k shows the hole potential $V(\boldsymbol{r}) = 2V_0 \sum_{i=1,3,5} \sin(u_i)$ and tunneling rate $w(\boldsymbol{r})$ as λ_{m} decreases from 60 nm to 4 nm (twist angle increasing from 0.3° to 4.7°). We also include a completely non-reconstructed scenario for reference (Figure 4.8f,k). As expected from recent studies (*160*), we find that the level of reconstruction decreases rapidly over this range in λ_{m}, as indicated by the smoother moiré potential (Figure 4.8b-f). Importantly, the tunneling profiles (Figure 4.8g-k) show that while tunneling is strongly suppressed in reconstructed moiré patterns (except at the narrow domain boundaries), it becomes much more substantial in the less reconstructed case. In the fully non-reconstructed scenario, the tunneling rate exceeds 14 meV in more than 50% of the completely non-reconstructed pattern. Since this value is comparable to the layer splitting of the valence band (~92 meV in AB-sites, smaller in other locations), it is expected that interlayer tunneling may provide an additional relaxation pathway in the less reconstructed regime. Moreover, the enhanced interlayer tunneling in the small-domain limit suggests that the hole wavefunction may be less layer localized in this regime. We note, of course, that this discussion only considers the hole wavefunction, and that a more sophisticated analysis could consider the complete exciton wavefunction including binding energy effects.

4.5.3 Exciton delocalization

Finally, when the domains become smaller than the coherence length of the excitons, the exciton center of mass wavefunction is expected to be delocalized across multiple of the small moiré cells (*126, 188*). While it is challenging to experimentally determine the coherence length for intralayer

excitons in our system, we estimate it to be 15-30 nm based on the typical homogeneous linewidths of intralayer excitons (*95, 201*). It is therefore expected that delocalization effects may play a role in the left side of device D2, and in our large twist angle devices D8-10 (twist angles 5°, 17° and 22°). In the delocalized case, a bandfolding picture becomes relevant: exciton Bloch states with momenta $\boldsymbol{k} = \boldsymbol{k}_{\mathrm{m},i}$ (where $\boldsymbol{k}_{\mathrm{m},i}$ are moiré wavevectors) can hybridize with the bright $\boldsymbol{k} = 0$ state due to the periodic moiré potential, thus becoming optically active, depending on the level of hybridization.

In the weak coupling regime, the first two hybridized delocalized states, ψ_+ and ψ_-, should exhibit a splitting of $E_{\mathrm{m}} = \hbar^2 k_{\mathrm{m}}^2/(2m_X^*)$, which is strongly domain size dependent, since $k_{\mathrm{m}} \propto \lambda_{\mathrm{m}}^{-1}$. Importantly, in the regime where we observe two peaks ($\lambda_{\mathrm{m}} > 25\ \mathrm{nm}$), no such λ_{m}-dependence was observed, consistent with the excitons residing within (not delocalized across) the reconstructed domains. In the smaller domain regime ($\lambda_{\mathrm{m}} < 10\ \mathrm{nm}$), where delocalization across moiré domains may occur, the hybridization effects are expected to be weak in our system (*188*). This is because the level of hybridization depends on the ratio of the coupling strength to the moiré kinetic energy (E_{m}), the latter of which is large (>30 meV) for small domains ($\lambda_{\mathrm{m}} < 10\ \mathrm{nm}$). The moiré potential strength can be determined from $V_{\mathrm{X},0} = \frac{E_0}{6\sqrt{3}}$ (*127, 166*), where E_0 is the energy splitting between sites with AB- and BA-stacked atomic registry. Since the non-reconstructed moiré potential is expected to be approximately just a smoother version of the reconstructed potential, we use the splitting $E_0 \sim 15$ meV determined from our measurements to find $V_{\mathrm{X},0} = 1.4$ meV. It is evident that $V_{\mathrm{X},0} \ll E_{\mathrm{m}}$ in our system, suggesting that the delocalized excitons in the small-domain limit should only hybridize weakly.

Due to the weak level of hybridization, the higher energy states are expected to have very small population in $|\boldsymbol{k} = \boldsymbol{0}\rangle$ and should therefore have very weak oscillator strength. In our system, we find that $(V_{\mathrm{X},0}/E_{\mathrm{m}})^2 < 0.002$, which is more than 2 orders of magnitude smaller than estimates for heterobilayers (*127*). The weak hybridization also causes the hybridized states to predominantly consist of one Bloch state, thus causing the probability density distributions $|\psi_+|^2$ and $|\psi_-|^2$ to have a substantial spatial overlap. This increased spatial overlap is expected to enable more rapid relaxation of $|\psi_+\rangle$ into $|\psi_-\rangle$.

Therefore, due to the weak oscillator strength and fast relaxation of the higher energy state $|\psi_+\rangle$, we only expect to observe one intralayer exciton state when the exciton becomes delocalized across multiple domains, consistent with our observations.

A

ADDITIONAL DETAILS FOR GRAPHENE NOISE EXPERIMENT

A1 Device fabrication

A1.1 Devices on diamond substrate

To fabricate the devices on diamond substrates, we exfoliated flakes of hexagonal boron nitride (hBN) and graphene onto a Si/SiO_2 substrate (Fig. A.1B), and used optical microscopy as well as atomic force microscopy (AFM) to pick clean flakes of the desired thicknesses. We then used the hot polycarbonate (PC) assembly technique (34) ($T_{\text{engage}} \sim 100$ °C) to assemble the flakes into stacks (Fig. A.1A). These consisted of fully hBN-encapsulated single layer graphene flakes, with two graphite contacts, and a few-layer graphene topgate. The top graphene was 3-5 layers thick to ensure uniform doping while still allowing us to optically address the NV centers through the stack. The top hBN flake was relatively thick ($\sim$ 90 nm) to minimize the doping effect of the source-drain voltage, while the bottom layer was thinner ($\leq$ 20 nm) to minimize the graphene-NV distance. The graphite contacts were used to ensure that the contact interface was under the topgate electrode. Upon assembling the stack, we transferred it onto a Si/SiO_2 substrate ($T_{\text{transfer}} \sim 180$ °C) and vacuum annealed at 350 °C for 2 minutes. Next, the stack was picked up again and transferred onto the diamond substrate (Fig. A.1C). The vacuum annealing was not done on the diamond substrate, since we consistently observed that this caused a strong background fluorescence signal. We then used e-beam lithography (JEOL JSM-7000F) and thermal evaporation (10 nm Cr + 100 nm Au) to construct bonding pads and contacts (Fig. A.1D). During lithography steps, Aquasave was deposited on top of the PMMA layer to prevent charging effects. We also fabricated a thick wire surrounding the stack for delivering reference microwave noise to the NV centers. Next, we defined the geometry of the device (Fig. A.1E) using a reactive ion etch (CHF_3, Ar, O_2), carefully choosing the cleanest region of the stack based on AFM images. Using a new PMMA etch mask, we gently O_2-etched the two edges of the device that were to be

contacted, in order to make sure the graphite contacts were well exposed. We then evaporated 2 nm Cr and 120 nm Au to create edge contacts (Fig. A.1F). This procedure is further described in Ref. (*20*). Finally, another gentle O_2 etch was used to create two ~ 200 nm cuts in the topgate graphene (Fig. A.1G) in order to disconnect it from the source-drain contacts. The complete, wire bonded device on diamond is shown in Fig. A.1H.

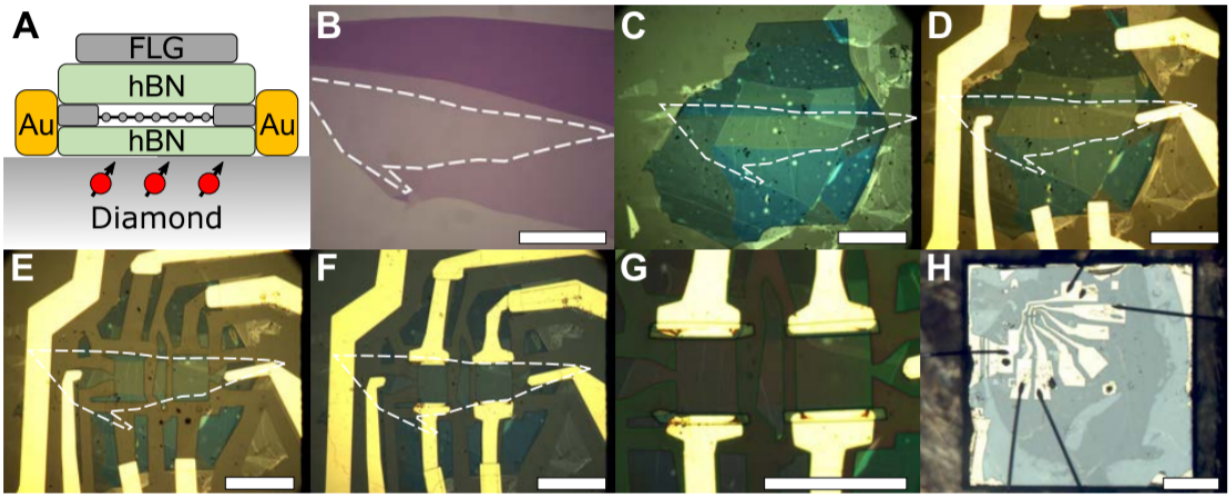


Figure A.1: Device fabrication on diamond substrate. (A) Device schematic: Monolayer graphene (grey chain) was graphite contacted and encapsulated with hexagonal boron nitride (hBN). Few-layer graphene (FLG) was used as topgate. (B-H) Micrographs of device fabrication, with 40 μm scalebar in (B)-(G) and 500 μm in (H). (B) Exfoliated graphene. White dashed line indicates monolayer region. (C) Complete stack on diamond substrate with shallow implanted (40 − 60 nm deep) NV centers. (D) Initial contacts and wire for delivering reference noise (left-most electrode). (E) Device after etch to define geometry. (F) Edge contacts constructed through etching and subsequent thermal evaporation. (G) Device with etch mask for disconnecting topgate from edge contacts. Note that ripples visible in the image are entirely contained in the top gate graphene and are not expected to affect the transport properties of the channel graphene, due to the thick (~ 90 nm) hBN dielectric. (H) Entire (2×2 mm^2) single crystal diamond, with wire bonded device.

A1.2 Devices on Si/SiO_2 substrate

In fabricating devices on Si/SiO_2 -substrates, we used the same exfoliation and stacking technique as outlined in the previous section. However, these samples were gated using a global backgate through the 1 μm thick SiO_2 (Fig. A.2A), and therefore did not need a topgate and graphite

contacts. Thus, the stacks simply consisted of an hBN-encapsulated graphene channel. The remaining fabrication process (Fig. A.2B-F) was identical to the procedure on diamond substrate, except without the reference noise wire and the final topgate etch step.

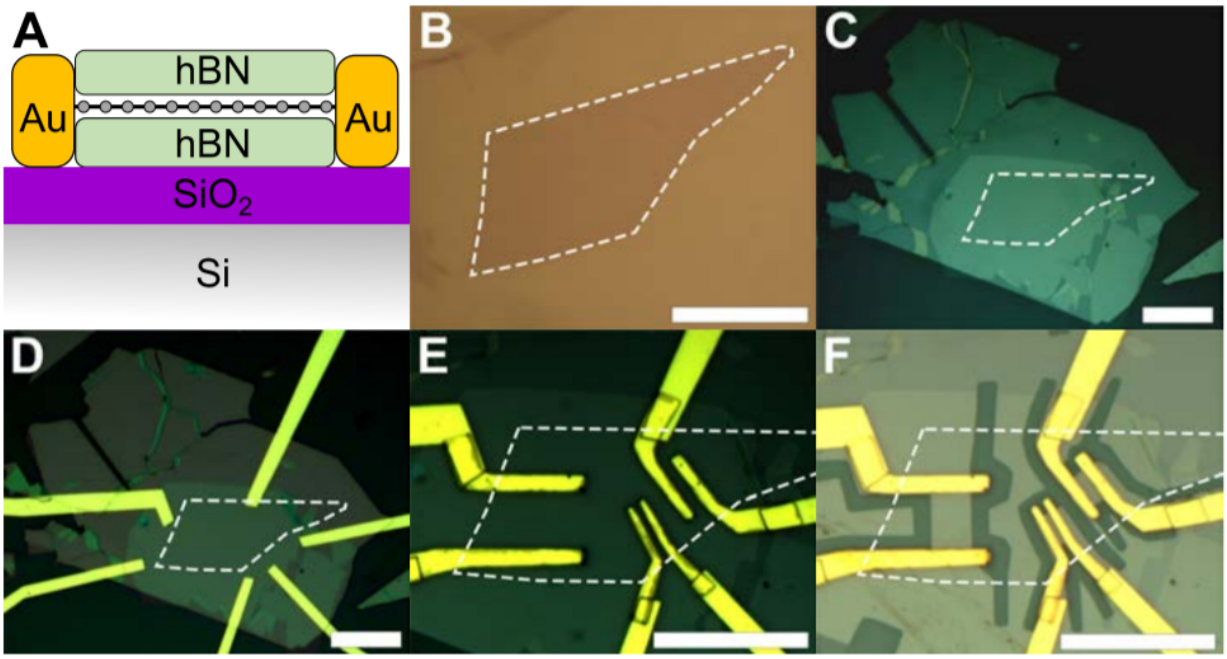


Figure A.2: Device fabrication on Si/SiO_2 substrate. (A) Device schematic: Monolayer graphene (grey chain) was encapsulated with hexagonal boron nitride (hBN). Silicon substrate was used as a global backgate. (B)-(F) Micrographs of device fabrication, with 20 µm scalebar. (B) Exfoliated graphene. (C) Complete stack on substrate. (D) Initial contacts. (E) Edge contacts constructed through etching and subsequent thermal evaporation. (F) Device after geometry-defining etch.

A2 NV measurement setup

For local noise measurements, the graphene devices were fabricated on single crystal E-grade diamonds with a (100) major face (Element Six). Prior to device fabrication, the substrates were plasma etched, implanted, and annealed as in Reference (*202*), but without the oxygen annealing step. This process resulted in a very smooth surface (<200 pm rms roughness). ^{15}N ions were

implanted at 20 keV, which corresponds to an approximate depth of 40-60 nm (calculated by Stopping and Range of Ions in Matter simulation).

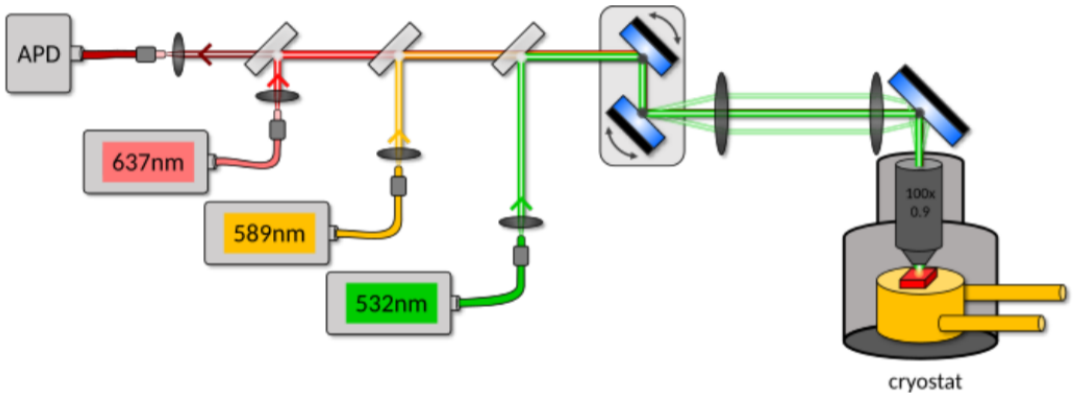


Figure A.3: NV measurement setup. The three laser beams used for spin-to-charge readout are combined before the galvonometric mirrors located at one focal point of a 4f system. Lasers are switched by acousto-optic modulators, except for the 637 nm high-powered ionization laser, which is a directly driven diode laser. The objective and sample are located inside a Janis ST-500 cryostat, which is used to keep the sample at ~70 K by a combination of flowing liquid helium and a resistive heater in a PID loop.

NV center measurements were performed in a Janis ST-500 flow cryostat (see Fig. A.3). Cryogenic temperatures allowed for resonant excitation of the NV center at low powers to reduce background. A scanning mirror-based confocal microscope was used to address, track and read out the NV centers during measurements. The full initialization and readout sequence required lasers of wavelengths 532 nm, 594 nm, and 637 nm that were separately switched with acousto-optic modulators. One of the 637 nm lasers (NewFocus Velocity TLB6704) was an external cavity diode laser that was tuned to each NV zero phonon line. The other red laser was a high-powered diode laser that was used to apply short >70 mW pulses to ionize NV centers. Photons emitted in the phonon side-band were collected with a fiber-coupled single photon counting module (Excelitas Technologies). Timings were orchestrated by a SpinCore PulseBlaster ESRPro with 2.5

ns timing resolution. The cryostat was equipped with coax lines, both for driving microwave pulses to manipulate the NV center, and to perform high-frequency measurements of the graphene device as described in the previous sections. Microwave signals for NV center manipulations were generated on an SRS SG384 signal generator and amplified with a Minicircuits ZHL-16W-43+ amplifier. For microwave noise references, phase noise was introduced by applying 200 MHz bandwidth white noise to the IQ modulation input on the SRS. Non-zero magnetic field measurements were achieved by positioning large rare earth magnets outside the cryostat, approximately aligned with one of the NV axes.

A3 High-frequency measurements

High-frequency noise and conductivity measurements were performed in a Janis ST-400 cryostat equipped with coax lines (see Fig. A.4). To improve high-frequency signal transmission, we used a PCB with co-planar waveguides that were connected to the device with short wire bonds. The DC bias was applied through an external bias tee (Minicircuits ZBT-4R2GW+) that directed AC signals to either two 34 dB low-noise amplifiers (Fairview SLNA-030-34-14-SMA) and spectrum analyzer (Keysight N9322C) for noise measurements, or to a network analyzer (Keysight N5222A) for AC conductivity measurements.

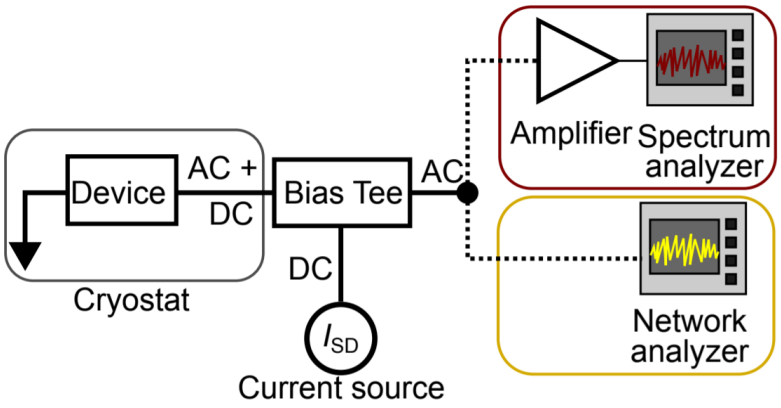


Figure A.4: High frequency transport setup. Circuit diagram for the measurement of noise (red box) and AC differential conductivity (yellow box).

A3.1 AC conductivity calibration

For the sake of clarifying terminology, it should be noted that the (intensive) conductivity spectrum $\sigma(\omega) = \frac{L}{W} \cdot G'(\omega)$ was found by first determining the (extensive) differential conductance $G'(\omega)$ and then multiplying by the aspect ratio L/W. Moreover, we consistently refer to the differential conductance $G'(\omega) = \frac{dI(\omega)}{dV(\omega)}$, not the chord conductance $G = I/V$. In order to determine the AC conductance spectrum, we used a bias tee to measure the reflection coefficient $r = |r|e^{i\phi}$ with a network analyzer, while simultaneously DC-biasing the sample. The reflection coefficient depends on not only the impedance matching to the sample, but also the external cabling leading up to it:

$$|r|e^{i\phi} = r_{\text{ext}}(\omega) + t_{\text{ext}}^2(\omega) \cdot \frac{50\ \Omega - Z(\omega, G')}{50\ \Omega + Z(\omega, G')}, \tag{A.5}$$

where $r_{\text{ext}}(\omega)$ is the reflection from external components between the network analyzer and the sample (e.g. connectors, cables), and $t_{\text{ext}}(\omega)$ is the transmission through these. We note that r_{ext} and t_{ext} are completely independent of the sample conductance, and one would observe $r = r_{\text{ext}} - t_{\text{ext}}^2$ if the cable was open instead of connected to the sample. $Z(\omega, G')$ is the complex impedance

of the sample, which depends on its differential conductance, but also on parasitic reactance. The latter comes predominantly from two sources: 1) Capacitance from the $\sim 75 \times 75\ \mu m^2$ source bonding pad on 1 μm SiO_2 dielectric ($C \sim 0.2$ pF) 2) Inductance from ~ 10 mm wirebond ($L \sim 10$ nH) We thus use the circuit model shown in Fig. A.5, which gives the impedance:

$$Z(\omega, G') = i\omega L + \frac{1}{G'(\omega) + i\omega C}, \tag{A.6}$$

In what follows, we assume that the parasitic *L* and *C* do not change with the graphene doping or the current flowing through the sample.

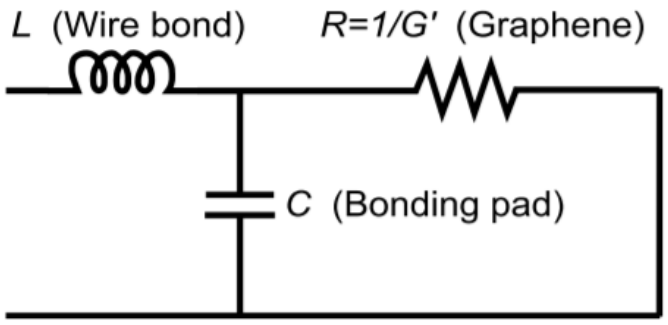


Figure A.5: Circuit diagram of wire bonded device. Wire bonds and bonding pads give rise to parasitic reactance.

A key observation is that the reflection coefficient $r(\omega, G')$ depends on only one graphene property, namely the differential conductance $G'(\omega)$. The latter depends on both the graphene current density (*j*) and doping (*n*), but if two pairs of parameters (j_A, n_A) and (j_B, n_B) give the same $G'_A(\omega) = G'_B(\omega)$ at a given ω, then their reflection coefficients must also be the same at that ω. An important result in our study is that the AC differential conductivity of clean graphene devices becomes frequency-dependent in the GHz-range when a strong DC bias is applied. This can be seen clearly in the raw reflection measurements shown in Fig. A.6.

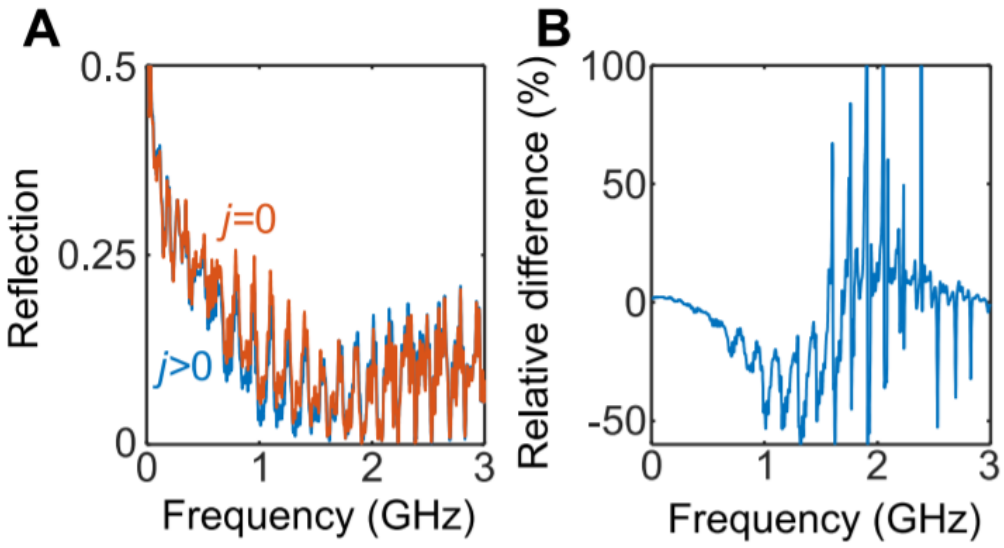


Figure A.6: Changes in reflection during biasing. (A) Reflection spectrum in the biased (blue) and unbiased (orange) case. (B) Relative difference in reflection. The gate is used to keep the DC conductance equal (3.1 mS) in the two cases, and as expected, the DC reflection is approximately equal. At higher frequencies, however, the reflection coefficients differ significantly, indicating that the conductance varies with frequency.

We have here chosen to compare a biased measurement (j_A = 0.56 mA/µm, $n_A = 2 \cdot 10^{12}\text{cm}^{-2}$) to an unbiased one ($j_A$ = 0.56 mA/µm, $n_A = 0.24 \cdot 10^{12}\text{cm}^{-2}$), that have the same DC conductance $G'_A(0) = G'_B(0) = 3.1$ mS. As expected, we therefore also find that these two pairs have the same DC reflection $r_A(0) = r_B(0)$. However, at higher frequencies, one finds $r_A(\omega > 0) \neq r_B(\omega > 0)$, which indicates that $G'_A(\omega > 0) \neq G'_B(\omega > 0)$. Since it is theoretically expected and previously experimentally established that the unbiased $G'_B(\omega)$ is frequency-independent at the low frequencies considered here (*60, 61*), we conclude that the biased $G'_A(\omega)$ develops a frequency dependence. In order to determine $G'(\omega)$ at non-zero bias, one must determine C, L, $r_{ext}(\omega)$ and $t_{ext}(\omega)$. This was done by measuring $|r|e^{i\phi}$ at zero bias, while sweeping G' using the electrostatic gate. We note that since no DC bias was applied during this calibration step, it was assumed that the graphene conductance G' was frequency-independent

through the entire frequency range used here (< 3 GHz). In other words, we could simply measure the DC conductance $G'(0)$, and use $G'(\omega) = G'(0)$. We stress that this only applies to the conductance of the graphene itself, not the total impedance, which also contains the frequency-dependent reactance due to parasitic capacitance and inductance. Using eqn. (A.5), we fit both the real and imaginary parts of $r(\omega, G')$ (examples in Fig. A.7A-B), and find $C = 0.24\ (0.22)$ pF and $L = 11\ (16)$ nH for device A2 (A1) (Fig. A.7C), in excellent agreement with the expected parasitic reactance components. The extracted parameters were used to determine the frequency-dependent conductance $G'(\omega; j, n)$ in the biased case, using the measured $r(\omega; j, n)$. Finally, we filtered out a small spurious periodic signal whose period was found to vary with cable length l according to l/c.

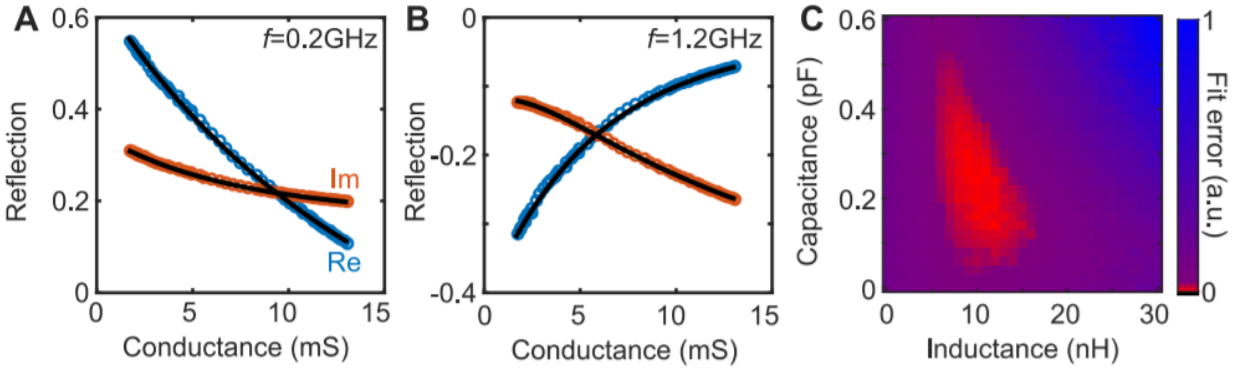


Figure A.7: AC conductivity calibration. (A-B) Real (blue) and imaginary (orange) parts of the reflection coefficient at $\omega = 2\pi \cdot 0.2$ GHz (A) and $2\pi \cdot 1.2$ GHz (B), as a function of the conductance (swept through electrostatic gating at zero bias). Using L = 11 nH and C = 0.24 pF, we extract $r_{ext}(0.2\ \text{GHz}) = -0.011 + 0.085i$, $t^2_{ext}\ (0.2\ \text{GHz}) = 0.66 + 0.29i$, $r_{ext}(1.2\ \text{GHz}) = 0.041 - 0.048i$, and $t^2_{ext}(1.2\ \text{GHz}) = -0.43 - 0.17i$. (C) Total fit error (summed over all ω) as a function of parasitic capacitance and inductance. The error is minimized at $L \sim 11$ nH and $C \sim 0.24$ pF.

A3.2 Noise calibration

To measure the noise from our graphene device, we used an external bias tee (Minicircuits ZBT-4R2GW+) that allowed for simultaneously biasing the graphene and measuring the high-frequency noise. The latter was amplified with two low-noise 34 dB amplifiers in series (Fairview SLNA-030-34-14-SMA) before its spectrum was recorded with a spectrum analyzer. The recorded noise $S_{\mathrm{rec}}(\omega)$ is a transformed version of the device noise $S_{\mathrm{dev}}(\omega)$, due to both background noise $S_0(\omega, G')$ and the gain function $A(\omega, G')$ of the total setup:

$$S_{\mathrm{rec}}(\omega; j, n) = S_0\big(\omega, G'(\omega; j, n)\big) + A\big(\omega, G'(\omega; j, n)\big) \cdot S_{\mathrm{dev}}\big(\omega, G'(\omega; j, n)\big). \tag{A.7}$$

Both S_0 and A depend on the sample differential conductance spectrum $G'(\omega; j, n)$, which depends on the current and charge densities, j and n. The background S_0 has a weak dependence on G' because part of the external background noise is reflected off the sample before reaching the spectrum analyzer. Indeed, we observe a higher background signal when the differential conductance G' is further away from the impedance-matched value. The gain A depends more strongly on G', because the impedance matching determines the transmission of the noise signal from the sample to the 50 Ω cable. In addition, A also depends on external factors, such as amplifier gain and cable attenuation (represented by $A_{\mathrm{ext}}(\omega)$ below):

$$A(\omega, G') = A_{\mathrm{ext}}(\omega) \cdot \left(1 - \left|\frac{50\Omega - Z(\omega, G')}{50\Omega + Z(\omega, G')}\right|^2\right), \tag{A.8}$$

Here, Z is the (complex) impedance of the sample, which depends on the differential conductance G' of the sample, as well as parasitic reactive components. In order to characterize $S_0(\omega, G')$ and $A(\omega, G')$, we need two known (preferably white) noise signals from the sample. Thus, we used a heating stage to record the Johnson noise (spectral density $k_{\mathrm{B}}T$) from the graphene at an elevated temperature T_{H} and at the base temperature T_{C}, while sweeping the gate through a wide range of

G'. To minimize heating effects on $S_0(\omega)$ (from heating up other noisy components), or on $A(\omega, G')$ (through temperature-induced changes in parasitic reactive components), we used a local heater that only heats the silicon substrate supporting the graphene device, keeping the rest of the cryostat cold. We could then find $S_0(\omega, G')$ and $A(\omega, G')$ from:

$$A(\omega, G') = \frac{S_{\mathrm{rec}}^{\mathrm{H}}(\omega, G') - S_{\mathrm{rec}}^{\mathrm{C}}(\omega, G')}{k_{\mathrm{B}}(T_{\mathrm{H}} - T_{\mathrm{C}})}, \tag{A.9}$$

$$S_0(\omega, G') = \frac{S_{\mathrm{rec}}^{\mathrm{C}}(\omega, G') \cdot T_H - S_{\mathrm{rec}}^{\mathrm{H}}(\omega, G') \cdot T_{\mathrm{C}}}{T_{\mathrm{H}} - T_{\mathrm{C}}}, \tag{A.10}$$

where $S_{\mathrm{rec}}^{\mathrm{H(C)}}(\omega, G')$ is the noise recorded at $T_{\mathrm{H(C)}}$. We remind that no bias was applied during these calibration measurements, so the conductance spectrum was flat and could be easily determined from DC measurements. The procedure to find $S_0(\omega, G')$ and $A(\omega, G')$ is shown as a function of G' in Fig. A.8A-C, and as a function of ω in Fig. A.8D-F.

As shown in Fig. A.8F, we finally corrected for the effect of the frequency-dependent G' on the gain (the effect on S_0 is much smaller $\sim 0.1\%$). This was done by also measuring the reflection coefficient (plotted against initial gain calibration in Fig. A.9), and utilizing the near-linear relationship between reflection and transmission:

$$A(\omega, G') \sim A_{\mathrm{ext}}\left(1 - \frac{|r(\omega, G')|^2}{|t_{\mathrm{ext}}(\omega)|^4}\right), \tag{A.11}$$

where r is the measured reflection coefficient with the network analyzer and t_{ext} is the transmission through external cabling (section A3.1). Reflections from external components were here ignored, since reflections predominantly come from the sample. A key point is that while the gain $A(\omega, G')$ must be measured at $j = 0$, the reflection $|r(\omega, G')|^2$ can be measured while applying a non-zero current. Thus we can measure $|r\big(\omega, G'(\omega; j, n)\big)|^2$ and translate it to

$A\big(\omega, G'(\omega; j, n)\big)$, using the fits of $A(\omega, G')$ vs. $|r(\omega, G')|^2$ at each ω. The corrected gain profile $A(\omega, G'(\omega; j, n))$ at a particular (non-zero) current density $j = 0.56$ mA/μm and $n = 2 \cdot 10^{12}$ cm^{-2} is shown in Fig. A.8F (green curve).

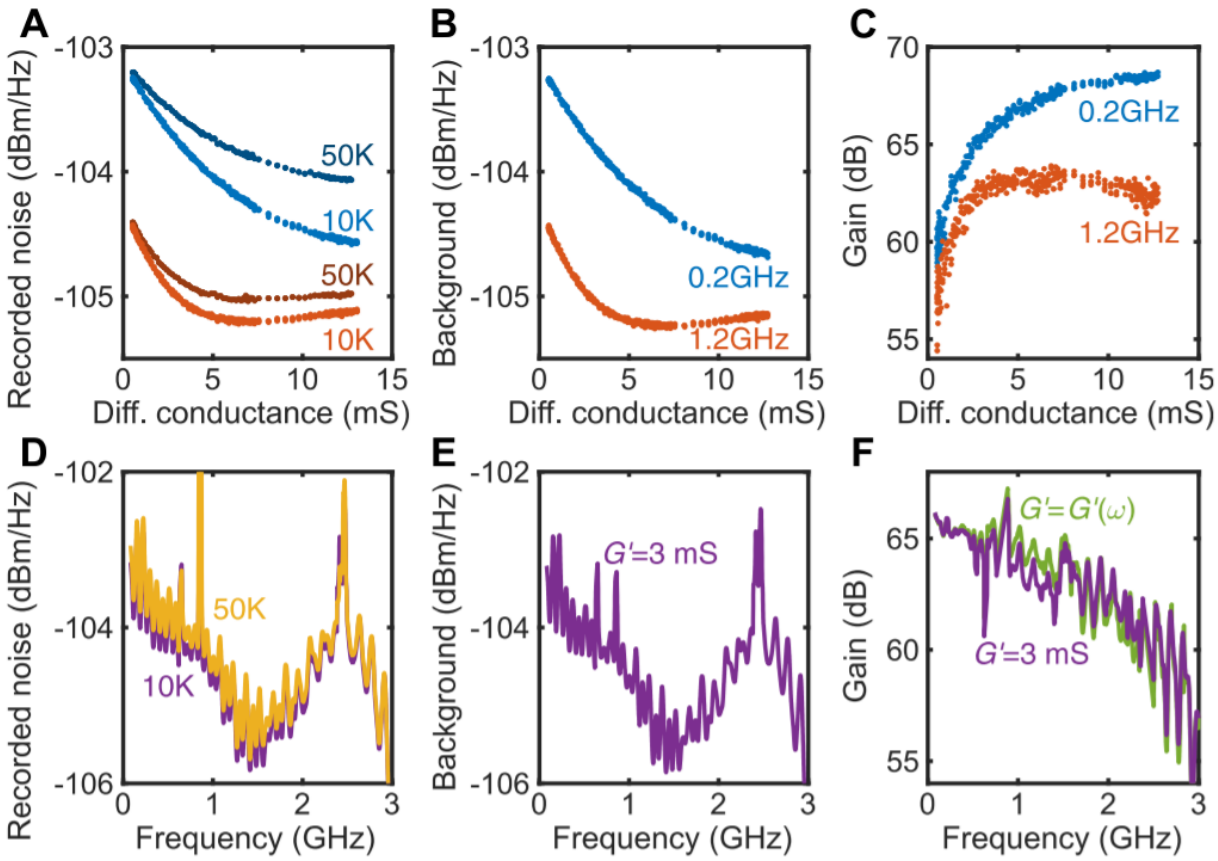


Figure A.8: Noise calibration. In A-C, blue and orange dots represent data at f = 0.2 GHz and f = 1.2 GHz, respectively. (A) Measured noise S_{rec} vs. differential conductance $Z(G')$, at base temperature T_C = 10 K (bright dots) and an elevated temperature T_H = 50 K (dark dots). The noise is minimized when $Z(G')$ is closest to matching 50 Ω, because at such low temperatures, the noise is dominated by background noise reflected off the sample. As expected, the matching value of G' is above 12 mS (below ~ 80 Ω) at low frequencies, but shifts to ~ 6 mS (~ 150 Ω) at f=1.2 GHz, due to the emerging parasitic reactance. (B) Background noise S_0 calculated according to eqn. (A.10). (C) Total gain A calculated according to eqn. (A.9). Sub-unity transmission and losses in the cables bring A below the 68 dB amplifier gain. (D-F) Same as (A)-(C), except as a function of frequency, $f = \omega/2\pi$. Purple and yellow curves show measurements at fixed G' = 3 mS. Green curve in (F) accounts for the frequency-dependence of $G'(\omega; j, n)$ for the particular driven case, j = 0.56 mA/μm and $n = 2 \cdot 10^{12}$ cm^{-2}. This is achieved using the technique outlined in the text.

After these calibration steps, we finally applied a current j through the device and measured the noise $S_{\mathrm{rec}}(\omega; j, n)$. We could then use $S_0(\omega, G')$ and $A(\omega, G'(\omega; j, n))$ to determine the device noise $S_{\mathrm{dev}}(\omega; j, n)$ from eqn. (A.7). Telecom signals at $f = 800$ MHz were removed, as well as regions where the linear relationship in eqn. (A.11) broke down due to strong external reflections.

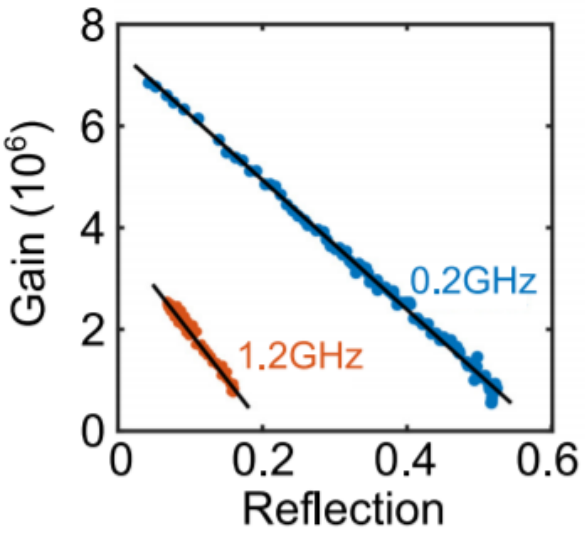


Figure A.9: Linear relationship between gain and reflection. Gain $A(\omega, G')$ plotted against the reflection, $|r(\omega, G')|^2$ at $\omega = 2\pi \cdot 0.2$ GHz (blue) and $\omega = 2\pi \cdot 1.2$ GHz (orange). The different points are obtained by sweeping the charge density n (and thus also G') at zero bias. As expected, the two quantities are linearly related. The gain in the biased case $A(\omega, G'(\omega; j, n))$ can now be found by measuring the reflection $|r(\omega, G'(\omega; j, n))|^2$ while applying current, and inserting it into the fit.

A4 Additional noise and conductivity measurements

A4.1 Noise power vs. drift velocity

In Figure 2.4 in section 2.4, we show the noise power as a function of bias power P for a limited range of P, to facilitate comparison between clean and disordered devices and highlight their contrasting behavior. Here, we show the dependence of global noise on electronic drift velocity

for the full range of bias drives (Fig. A.10A). As expected, no anomalous noise is observed below $v_D = v_s$ (Fig. A.10B). We note that no sharp transition is expected at $v_D = v_s$, since at this point, only one phonon mode satisfies the Cherenkov criterion, and with a negligible amplification rate. Thus, one should instead observe a smooth transition into the excess noise regime, as the number of amplified modes and the amplification rate increase.

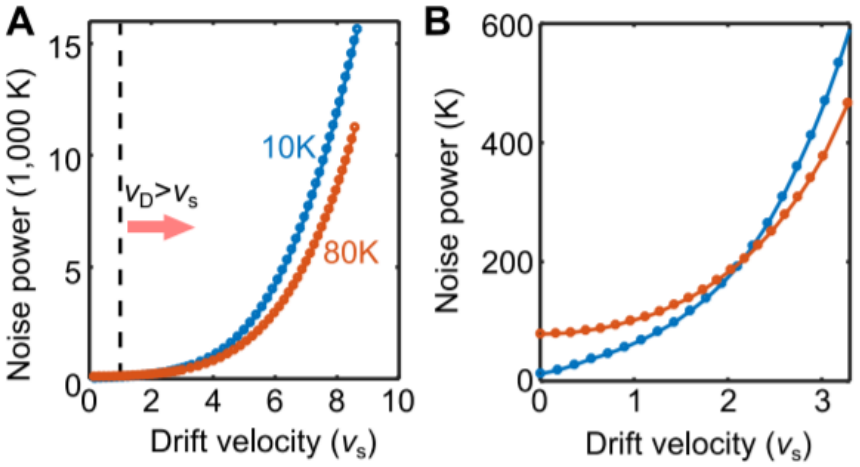


Figure A.10: Noise versus drift velocity. (A) Measured noise power spectral density (averaged over 0.1-0.3 GHz) as a function of electronic drift velocity in clean device A1, at bath temperatures 10 K and 80 K (blue and red, respectively). We observe equivalent noise temperatures in excess of 15,000 K. (B) Zoomed-in version of (A) to highlight smooth transition into the excess noise regime. Lines are guides to the eye.

A4.2 Disordered device noise

To model the thermal noise observed in a disordered device, we need to consider the balance between Joule heating P and phonon cooling. The rate of the latter is typically given by $\Sigma\left(T_e^{\delta} - T_{\text{bath}}^{\delta}\right)$, where Σ is a cooling constant and T_e and T_{ph} are the electron and phonon temperatures, respectively (*53*). Solving for the electronic temperature, one finds:

$$T_e = \left(T_{\text{bath}} + \frac{P}{\Sigma}\right)^{1/\delta}, \tag{A.12}$$

where we have assumed that the phonon temperature remains close to the base temperature T_{bath}, as normally observed. In samples with high impurity density, phonon cooling is usually dominated by "supercollision" scattering, in which electrons scatter with phonons with the assistance of defects (*53*). In that case, one finds $\delta = 3$ and $\Sigma = 9.62 g^2 \mathrm{DoS}^2(\epsilon_{\mathrm{F}}) k_{\mathrm{B}}^3/(\hbar k_{\mathrm{F}} \ell)$, where $g = D/\sqrt{2\rho v_{\mathrm{s}}}$ is the electron-phonon coupling and ℓ is the mean-free path. Fitting our data with eqn. (A.12), we find good agreement (Fig. A.11) and find $\delta = 3.04$. We also extract the deformation potential from the fitted value of Σ, and find $D = 39$ eV ($\epsilon_{\mathrm{F}} = 165$ meV). This is consistent with a previous study on disorder-assisted cooling in graphene $D = 39$ eV (*53*) and the typically reported range of $\sim 10 - 30$ eV (*203*). (We note that we use the more accepted value of $D = 20$ eV for all other fits pertaining to Cherenkov emission in clean devices.) This confirms that the dominant noise in our driven disordered devices is thermal Johnson-Nyquist noise.

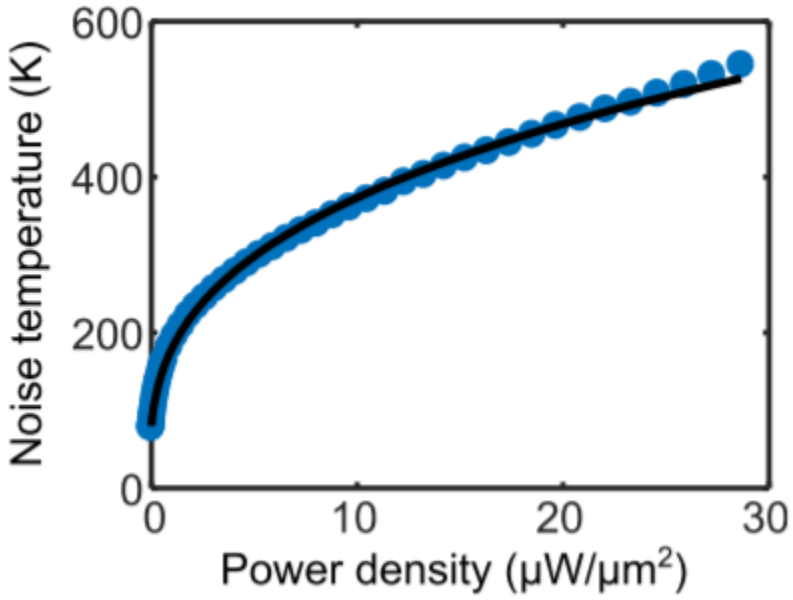


Figure A.11: Johnson noise in a disordered device. Measured noise temperature (blue circles) as a function of input power for disordered device B1. The data agrees well with a fit based on disorder-assisted phonon cooling (black curve), and confirms that the dominant noise source is thermal Johnson-Nyquist noise.

A4.3 Length dependence in global noise measurements

Local (NV) noise measurements indicate that the noise grows across the device in the direction of carrier flow. By measuring devices of different lengths, we find a similar trend in the global noise. At a constant electronic drift velocity ($v_D = 3.3v_s$) and charge density ($n = 2 \cdot 10^{12}\text{cm}^{-2}$), the noise initially grows superlinearly with device length (Fig. A.12A, inset). Our longest device does not appear to follow the initial length dependence, hinting at the role of saturation effects that prevent unbounded exponential growth of the phonon population (Fig. A.12A).

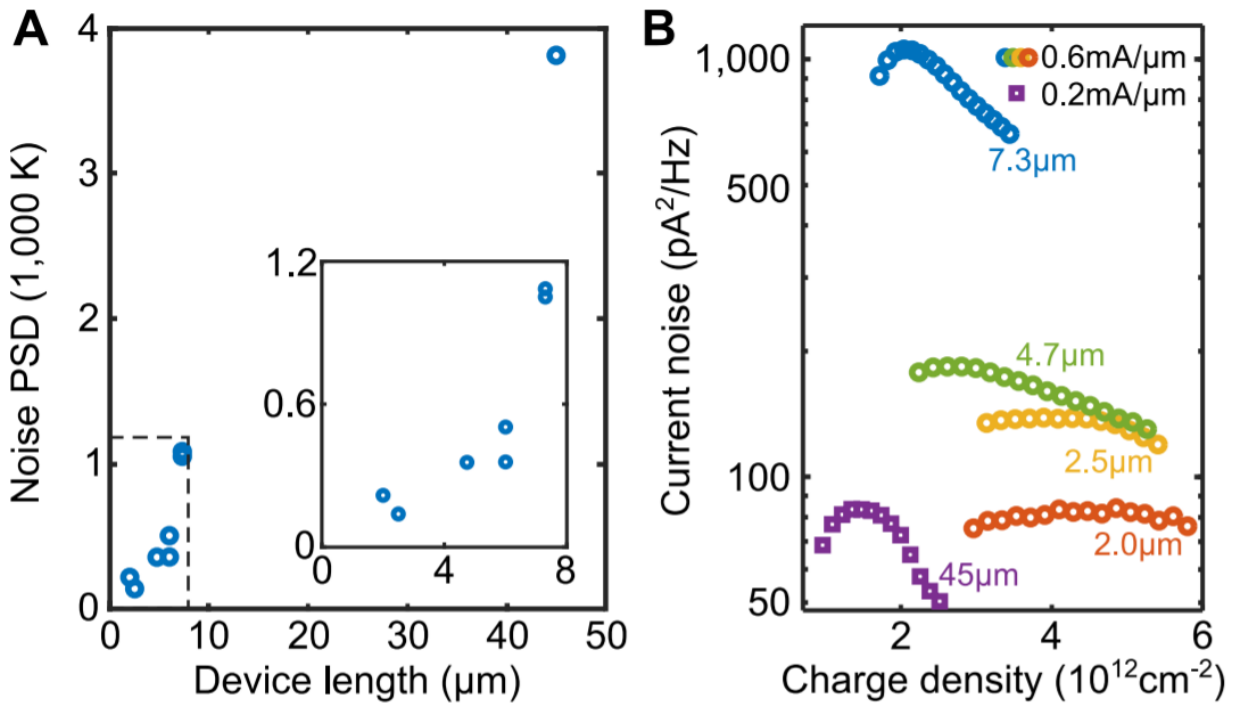


Figure A.12: Dependence of noise on device length. (A) Measured noise power spectral density from devices of different lengths, at $v_D = 3.3v_s$ and $n = 2 \cdot 10^{12}$ cm^{-2}. The noise power initially increases superlinearly with device length (inset), but appears to saturate in longer devices. (B) Current noise versus carrier density at constant current density $j = 0.6$ mA/μm (circles) and $j = 0.2$ mA/μm (squares). As shown in Figure 2.7, the cross-over density decreases with device length.

We here also show the charge density dependence before normalization (Fig. A.12B). In addition to the data shown in Figure 2.7, we have also included measurements of our longest ($L =$

45 μm) device (purple squares), which broke down before we could reach the current density used for Figure 2.7. As expected from our theory (section 2.5), this longer device shows a cross-over at an even lower charge density than the other devices. As in Figure 2.7, we show the density dependence in terms of current noise $\delta^2 I$, which is similar to noise power, but divided by the differential resistance. This was done to allow for comparison with the model, but we note that the non-monotonic dependence is also observed when plotted in terms of noise power.

A4.4 Global noise independent of carrier flow direction

In chapter 2, we demonstrate that the local noise measured far from the middle of the device exhibits strong asymmetry with respect to carrier flow direction (Figure 2.5). Here, we show that no such asymmetry is observed in *I-V* transport or global noise measurements (Fig. A.13A and B, respectively).

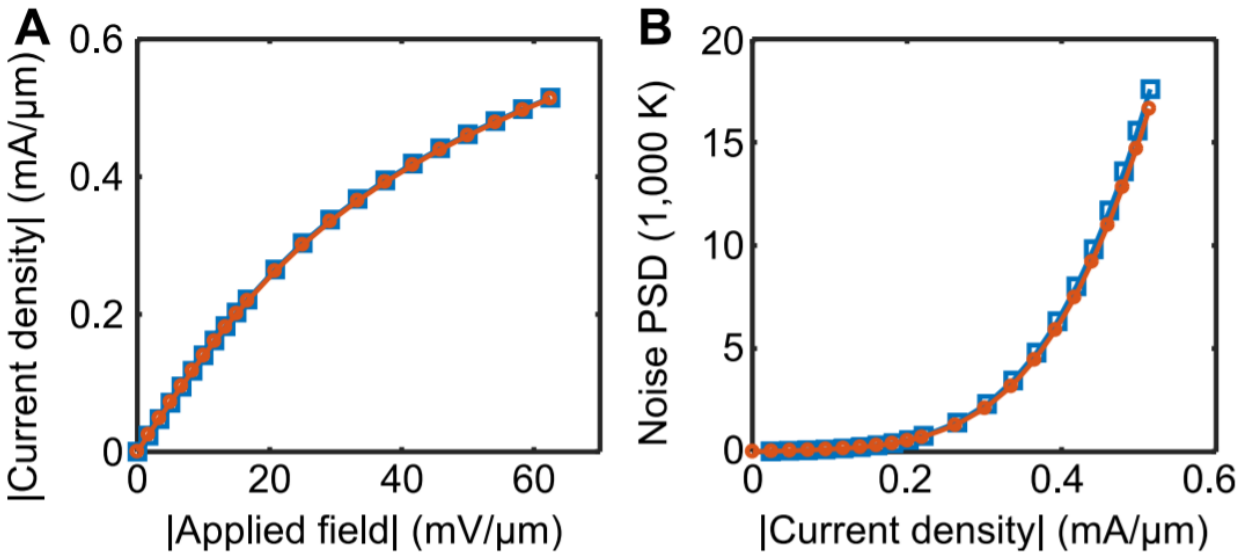


Figure A.13: Global electronic transport and noise under current inversion. (A) Absolute value of current density versus absolute applied field at $n = 2 \cdot 10^{12}$ cm^{-2} and $T = 10$ K, for positive (orange) and negative (blue) fields. The $I - V$ curve is observed to be highly symmetric. (B) Global noise power spectral density as a function of (absolute) current density. Changing the sign of the current has almost no effect on the measured noise power. Lines are guides to the eye.

A4.5 Independence of conductivity time scales on charge density and temperature

As shown in section 2.4, the time scale extracted from conductivity measurements is independent of drift velocity. We here show that the time scale does not depend on charge density (Fig. A.14A-B) and sample temperature (Fig. A.14C) either.

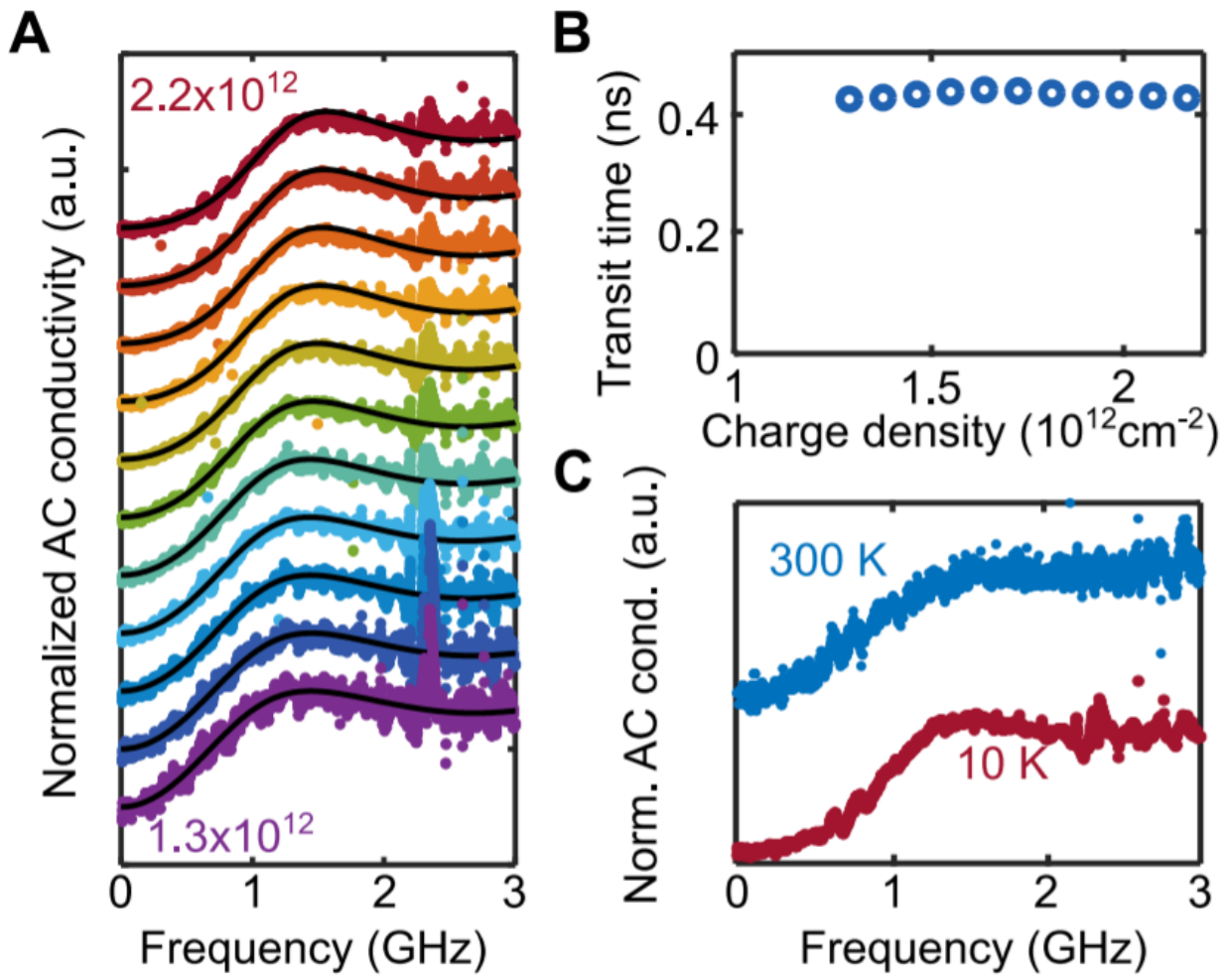


Figure A.14: Global conductivity for different charge densities and temperatures. (A) The normalized real part of the conductivity spectrum for $v_D = 0.125v_F$ at different doping levels. The curves are normalized to have the same vertical spread, and are offset to avoid overlap. The general shape of the conductivity spectrum, as well as the extracted time scales (B) are unchanged by varying the charge density. (C) The normalized real part of the conductivity spectrum measured at bath temperatures of 300 K (blue) and 10 K (red), at $v_D = 0.125v_F$ and $n = 2.2 \cdot 10^{12}$ cm^{-2}. We again observe no clear frequency shifts, but the effect is much ($\sim$ 4 times) weaker at room temperature than at 10 K.

Fig. A.14A shows normalized AC conductivity spectra measured at charge densities ranging from $n = 1.3$ to $2.2 \cdot 10^{12}\mathrm{cm}^{-2}$, with the extracted time scales displayed in Fig. A.14B. Evidently, no dependence on charge density is observed. We also compare the conductivity spectra obtained at 10 K and room temperature (Fig. A.14C), and again observe no clear change in the time scale. The independence of these parameters is consistent with our model, since the time scale is expected to be determined by the phonon traversal time $t_\mathrm{T} = L/v_\mathrm{s}$. We emphasize that this is only the case for the time scale; the magnitude of both the conductivity and noise features depend strongly on drift velocity, charge density and bath temperature.

A5 Additional NV measurements

A5.1 Local noise spectroscopy

Spectroscopy of the local noise can be performed by varying the spin flip transition frequency of the NV center. We tuned the level-splitting of the two transitions to $\omega = 2.87 \pm 1.01$ GHz by applying an external magnetic field of 363 Gauss, and found no significant change in the relaxation rate of NV centers (Figure A.15). We note that when measuring the decay into both the $m_\mathrm{s} = +1$ and $m_\mathrm{s} = -1$ states, cancellation effects can occur since the two transition frequencies are changed by equal and opposite amounts. In the worst case, $\Gamma(\omega)$ decreases linearly, and the relaxation rates of the two transitions change from Γ_0 to $\Gamma_0 \pm \delta\Gamma$. It can then be shown that the measured relaxation rate Γ_meas out of the initial $m_\mathrm{s} = 0$ state should increase, with a relative change given by $\frac{\delta\Gamma_\mathrm{meas}}{\Gamma_\mathrm{meas}} = \frac{\delta\Gamma^2}{6\Gamma_0^2}$. Considering the < 10% change observed here, we conclude that the local noise varies by $< \sqrt{6 \cdot 10\%} \sim 80\%$ over 1 GHz. The difference from the much sharper frequency dependence observed in globally measured spectra is expected: the global measurements are sensitive to phonon-mediated electronic correlations across the entire device,

and should thus show a roll-off corresponding to the (inverse) sample traversal time ($\frac{v_s}{L} \sim$ GHz). The NV center, on the other hand, is primarily sensitive to correlations that occur within its $\sim 50 \times 50\ \mathrm{nm}^2$ sampling area. Thus, the NV centers are expected to observe a significantly higher frequency cut-off ($\frac{v_s}{d_{\mathrm{NV}}} \sim 100$ GHz) and very weak spectral dependence around 2.87 GHz.

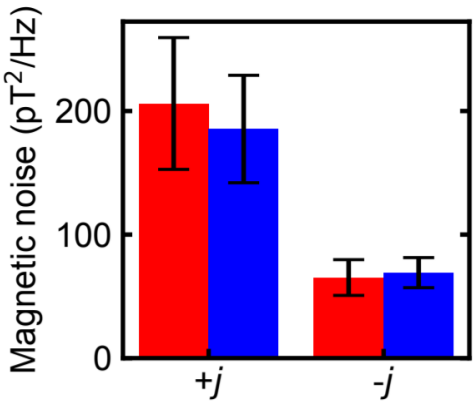


Figure A.15: Noise measured at different applied magnetic fields. Relaxation rates of an NV center at B = 0 (red) and B = 363 Gauss (blue), for positive and negative bias ($|j|$ = 0.2 mA/μm) at $n = 0.92 \cdot 10^{12}$ cm^{-2}.

A5.2 NV measurement of lattice temperature

When large source-drain voltages are applied to the device, a significant amount of power is dissipated (~5 mW). Since the relaxation rate of an NV center is temperature-dependent, it is important to consider the temperature change of the diamond lattice from this power dissipation. This can be done by measuring the linewidth of the NV zero-phonon line, which is very sensitive to temperature and scales as T^5 (*204*). We measure the fluorescence of an NV center as a function of excitation wavelength and find a slight change in linewidth for the highest applied biases (Fig. A.16). By heating the cryostat from 70 to 80 K, we achieve a similar level of broadening at zero bias. This shows that the bias-induced increase in the diamond temperature near the NV is very small (~ 10 K), consistent with the high thermal conductivity of diamond. Since the spin relaxation

rate is proportional to T in the regime considered here (*205*), and the intrinsic spin relaxation rate was measured to be very low (< 0.2 Hz), this slight temperature increase should have a negligible effect compared to the high levels of noise from the graphene. Moreover, the clear gate dependence observed at constant power (section A5.3) further shows that the increased spin relaxation rate is due to noise from the graphene. Nevertheless, to keep the diamond temperature as constant as possible, we lowered the cryostat base temperature by 10 K while measuring at the highest biases.

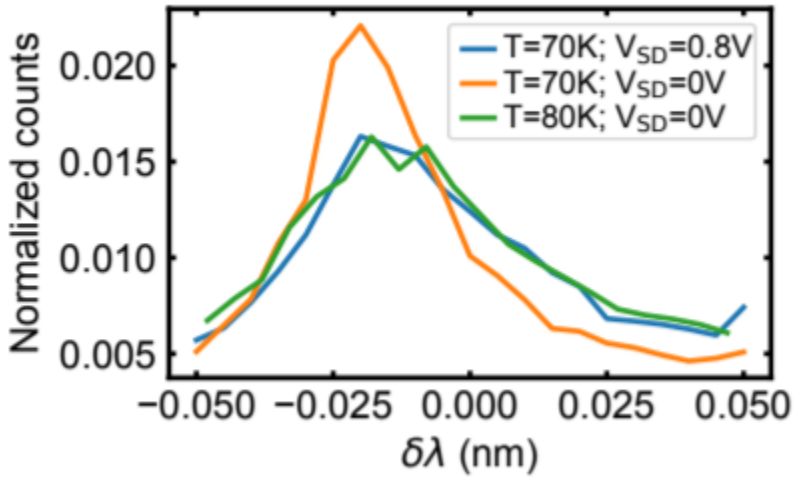


Figure A.16: Lattice heating during NV measurements. Scans of the optical line of an NV center located below device C2. The NV center zero phonon line is broadened by approximately the same amount when a high bias is applied (blue) as when the bath temperature is increased by 10 K at zero bias (green), suggesting that the increase in temperature near the NV during device operation is approximately 10 K. $\delta\lambda$ is approximate and is inferred from cavity piezo voltage and laser manufacturer's specifications (New Focus Velocity 6300). Center wavelength corresponds to ~ 637.4 nm

A5.3 Local doping dependence

By focusing on a single NV center and measuring its relaxation rate while sweeping the topgate voltage, we map out the charge density dependence of the Cherenkov noise on the nanoscale (Fig. A.17). As with the current dependence, the anomalous noise is only observed when the charge

carrier sign is such that the NV center is downstream with respect to the carrier flow. These measurements were done at constant power, so the drift velocity increases with doping level, leading to an abrupt increase in noise once the Cherenkov condition is satisfied.

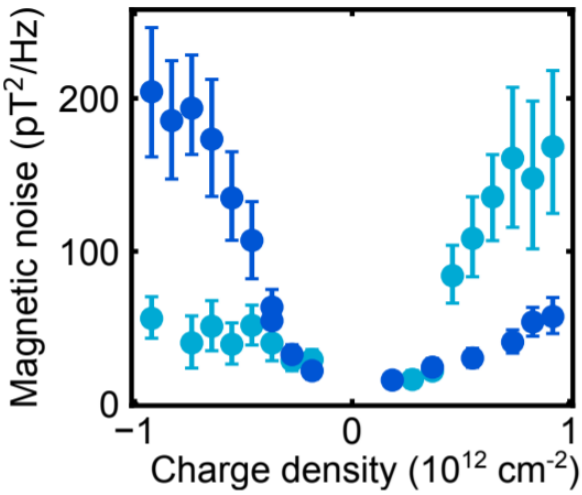


Figure A.17: Doping dependence of local magnetic noise. Locally probed magnetic noise as a function of graphene charge density. Light and dark blue points represent positive and negative source-drain current, respectively. The bias power was kept constant at 14 ± 0.1 mW.

A5.4 NV center orientation

Our diamond samples were all cut such that the devices are fabricated on the (100) surface. The diamond crystal structure entails that each NV axis (the vector connecting nitrogen and vacancy sites) points in one out of four directions. The four possible NV axes all make the same angle $\sim$ 54.7° with the surface normal vector (Fig. A.18A), but have four different projections onto the *xy*-plane (Fig. A.18B). We align our devices to be parallel with the *xy*-projection of two axes (red, group II), and perpendicular to the other two (blue, group I) (Fig. A.18B). The NV centers can be used to sense DC currents by measuring the Zeeman splitting of the $m_s = \pm 1$, $2\gamma_e B_{\parallel}$, where $B_{\parallel}$ is the projected field onto the NV-axis (22). Thus, aligning our devices in this way enables us to determine the NV groupings by measuring the DC current response. When flowing a source-drain

current through the device, the magnetic field projection onto group I is large, but nearly zero for group II, as shown in Fig. A.18C. We also note that the consistency of the field measured by group I NVs suggests that the current is very uniform. In section A5.5, we comment on a few NVs that showed discrepancy. Spin relaxation, on the other hand, is determined by the perpendicular component of the noise on the NV axis, which should in principle allow for observing effects of anisotropic noise. However, we do not observe a significant difference in relaxation rates under driven graphene for nearby NVs in different orientation groups (Fig. A.18D), suggesting that the induced noise is relatively isotropic.

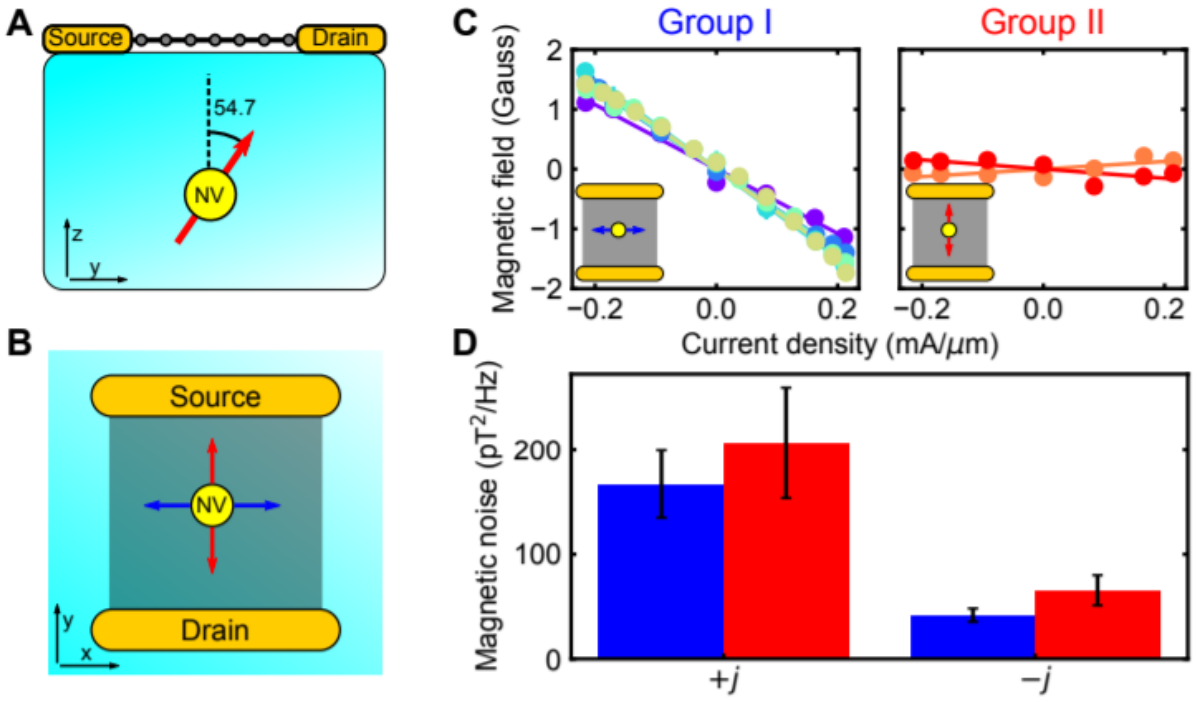


Figure A.18: NV center orientation. (A) NV center orientation with respect to diamond surface. (B) Projection of the four possible NV axes onto the device plane. Our device is closely aligned along two of the projections, giving rise to two distinctive groupings of NV centers: those with *xy*-projections that are perpendicular to current flow (group I, blue) and those with *xy*-projections parallel to current flow (group II, red). (C) DC field measurements. Group I NVs measure a significant current-induced magnetic field, while group II NVs do not. (D) Relaxation rates of NVs in group I (blue) and II (red). The noise sensed by nearby NVs from different orientation groups is similar, despite measuring very different DC magnetic fields. $|j| = 0.2$ mA/μm, $n = 0.92 \cdot 10^{12}$ cm^{-2}.

A5.5 DC measurements of local current distribution

Our devices are not implanted at a high density, which precludes vector reconstruction of the DC current distribution at all points, but the NV density is high enough to measure general trends. Overall, we observe that the DC magnetic field shift of the NV centers is uniform and consistent with the applied global current density (Fig. A.18C). However, we observe some small departures at discrete locations that are likely due to local disorder. Current imaging in graphene samples has shown that edges, folds, and defects can cause the current density to vary across the sample (*206*). At these locations in our samples, the field sensed by the NV is not linear in the applied current: at some threshold current density, the slope of the current-field curve changes (Fig. A.19A, blue).

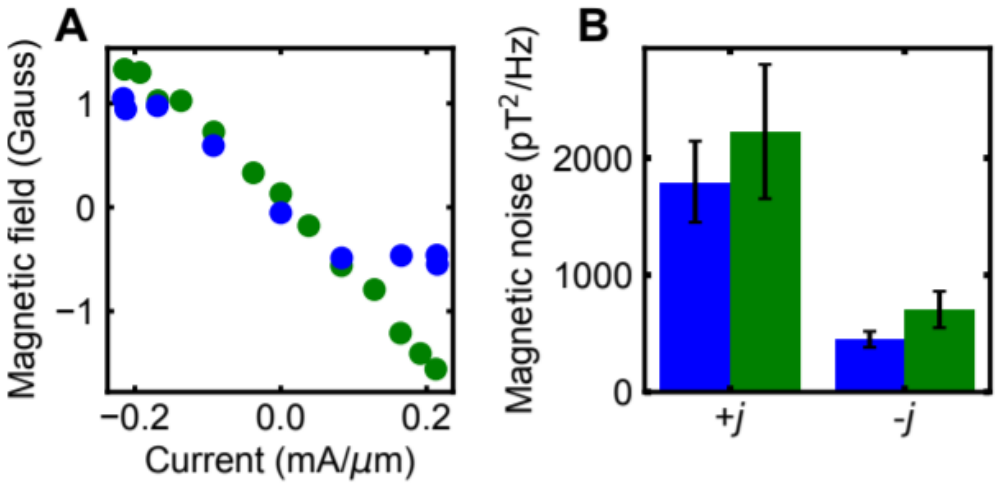


Figure A.19: DC and AC current measurements. (A) DC current response of two NVs located a similar distance from the source electrode. While one of the NVs shows the expected linear local field dependence on global current (green), the other shows non-linear behavior at high drives (blue). (B) Local noise measurements for same NVs as in (A). Noise measurements taken at $|j| = 0.2$ mA/μm, $n = 0.92 \cdot 10^{12}$ cm^{-2}.

We emphasize that this non-linear behavior is not expected to be related to the observed anomalous noise effects, since it is only observed in a few discrete locations. This is further supported in Fig. A.19B, where we show that two NVs at similar distances from the source electrode both show the asymmetric noise behavior, despite their different DC current profiles. As

expected, the outlier NV that measures a lower local current than the global average also measures slightly less noise. Along with variations in NV depth, such discrete discrepancies in local current may have caused some of the departures from the overall trends observed in Figure 2.5.

A6 Device overview

In table A.1, we present an overview of all the devices employed in the study of the electron-phonon Cherenkov instability in biased graphene.

Device name	hBN-encapsulation	Substrate	$L \times W (\mu m^2)$	Abnormal noise
A1	Fully	SiO_2	6×5.4	Yes
A2	Fully	SiO_2	9.5×11	Yes
A3	Fully	SiO_2	2.5×11	Yes
A4	Fully	SiO_2	2.0×3.3	Yes
A5	Fully	SiO_2	4.7×2.3	Yes
A6	Fully	SiO_2	7.3×5.3	Yes
A7	Fully	SiO_2	7.3×5.3	Yes
A8	Fully	SiO_2	45×15	Yes
A9	Fully	SiO_2	1.3×5.0	Unclear*
A10	Fully	SiO_2	1.0×5.0	Unclear*
B1	Bottom Only	SiO_2	7×18	No
B2	None	SiO_2	10×15	No
B3	None	SiO_2	12×19	No
B4	Top Only	SiO_2	10×15	No
B5	Top Only	SiO_2	12×19	No
C1	Fully	Diamond	6×22	Yes
C2	Fully	Diamond	17×20	Yes
C3	Fully	Diamond	20×23	Yes
C4	Fully	Diamond	6×8.4	Yes

Table A.1: Device overview. Here, we give a brief overview of the numerous samples measured. The key observation is that the anomalous noise signal is found in all the 12 clean (fully encapsulated) devices with lengths ≥ 2 μm. The disordered (partially or not encapsulated) devices, on the other hand, never exhibit this signal. The devices that are extensively discussed in section 2.4 appear in bold. *Unclear: Higher noise temperature than expected from thermal model, but the other signatures are missing: The spectrum is white, and the noise depends sub-linearly on power. We propose that this is due to shot noise, commonly observed in short devices.

B

ADDITIONAL DETAILS FOR TWISTED TMD VALLEYTRONICS EXPERIMENT

B1 Materials and methods

Flakes of hBN, graphene and WSe_2 were mechanically exfoliated from bulk crystals onto Si wafers (with 285 nm SiO_2). Monolayer and bilayer WSe_2 were identified using optical microscopy and later confirmed in photoluminescence measurements. The thicknesses of hBN flakes were determined with atomic force microscopy. The heterostructures were then assembled with the dry-transfer method, using the tear-and-stack technique (*11, 131*) to form twisted bilayer WSe_2. Next, electrical contacts to the WSe_2 and graphite gates were defined with electron-beam lithography and deposited through thermal evaporation (10 nm Cr+90 nm Au). Optical measurements were conducted in a 4 K cryostat (Montana Instruments), using a self-built confocal setup with an 0.75 NA objective. The DOCP was measured with two polarizers in the excitation and collection paths, and a quarter wave plate directly above the objective. To eliminate any polarization-dependent instrument response, all DOCP measurements included excitation with (and collection of) both σ_+ and σ_- light. PL measurements were carried out using a 660 nm diode laser. A sub-picosecond pulsed laser (Coherent) and a streak camera (Hamamatsu) were used in the time-resolved PL measurements.

B2 Exciton characterization based on DC Stark shift

Upon applying a vertical electric field, excitons experience a Stark shift given by $\Delta E = E \cdot e \cdot d$, where E is the applied electric field, d is the (vertical) electron-hole separation, and e is the elementary charge. Since interlayer excitons have an out-of-plane dipole moment (d), unlike intralayer excitons, the two species can be distinguished through electric field dependent PL measurements (Figure 3.4(a)). In all of our devices, the higher-energy feature ($\sim$ 1.7 eV) exhibits

no Stark shift, and is therefore attributed to intralayer excitons. The lower-energy peaks, on the other hand, show a clear shift, and are therefore assigned to interlayer excitons.

The interlayer excitons are expected to be momentum indirect, because their PL energy is lower than that of the direct intralayer exciton, even with their weaker binding energy (*10*). This is further supported by the fact that the extracted electron-hole separation, $d = 0.37$ nm (0.36 nm in 2° twist device), is significantly smaller than the full interlayer separation ($d_0 = 0.6$ nm) (*10*) that would be expected if both carriers were at the K point. It is also not consistent with the Γ-K transition, because the wavefunction at the Γ-point is completely delocalized between the two layers (*123, 207*), causing $d \sim d_0/2$. Instead, the extracted electron-hole separation is consistent with the K to Q transition, where the hole is localized in a single layer and the electron is partially delocalized (*143*).

B3 Spatial map of DOCP in a sample containing natural and twisted bilayer regions

To confirm the stark contrast in DOCP between natural and twisted bilayer WSe_2, we fabricate an hBN-encapsulated TMD heterostructure that contains both natural (180°) and twisted (~0°) bilayer regions (Fig. B.1(a)). The device was made from a single exfoliated WSe_2 flake that had both a bilayer and a monolayer region, the latter of which was torn and stacked on top of itself. Integrating only the interlayer exciton emission (photon energies below 1.6 eV), we find that the natural bilayer area exhibits almost no DOCP, while the twisted region has a DOCP close to 50% almost everywhere, except in sporadic defect spots (Fig. B.1(b)).

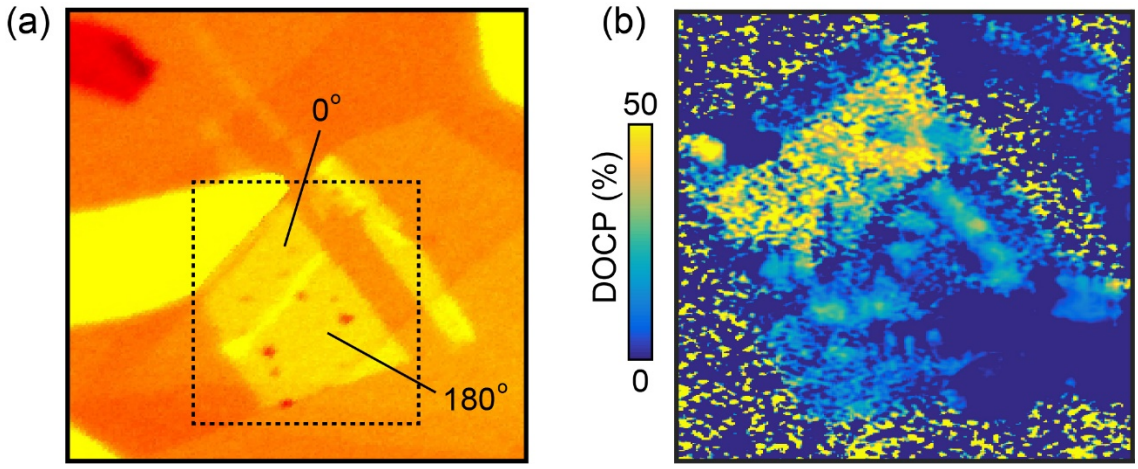


Figure B.1: Spatial map of DOCP. (a) Optical image of an hBN-encapsulated heterostructure that contains both natural (180°, lower right) and twisted (~0°, upper left) bilayer regions. (b) Spatial dependence of average interlayer exciton DOCP (photon energy below 1.6 eV). Consistent with PL spectra shown in Chapter 3, the twisted bilayer region exhibits much higher DOCP than the natural bilayer region.

B4 Fitting of lifetime data

To fit the full time-dependence of the photoluminescence in the intrinsic regime, we use a biexponential decay convoluted with the system response, $s(t)$, as measured from the response of our sub-picosecond laser:

$$p(t) = \left(A_1 e^{-t/\tau_1} + A_2 e^{-t/\tau_2}\right) * s(t - t_0). \tag{B.13}$$

Here, τ_1 and τ_2 are the fast and slow decay timescales, with corresponding amplitudes A_1 and A_2. This model is used for both the co- and cross-polarized emission components (with separate fit parameters), and t_0 accounts for the observed delay between the two. The fits are shown as dotted lines in Figure 3.5(a), with corresponding DOCP in Figure 3.5(d).

In the *n*- and *p*-doped regimes, we focus on shorter timescales due to their shorter exciton and valley lifetimes, respectively. At these timescales, we only observe a single exponential decay

and therefore fit with a linear coupled model, which also allows for extracting the valley lifetime, τ_v:

$$\dot{p}_{co} = -\frac{p_{co}}{\tau_1} - \frac{p_{co} - p_{cross}}{\tau_v} + (1-\alpha)\cdot s(t), \tag{B.14}$$

$$\dot{p}_{cross} = -\frac{p_{cross}}{\tau_1} - \frac{p_{cross} - p_{co}}{\tau_v} + \alpha \cdot s(t). \tag{B.15}$$

Here, p_{co} and p_{cross} are the co- and cross-polarized exciton populations, and α is the proportion of cross-polarized excitons due to imperfect excitation. In order to account for the system response, we use the measured laser pulse, $s(t)$, as the laser input. The fits and corresponding DOCP are shown with dashed lines in Figure 3.5(b)-(d). This model was also used for fitting in the intrinsic regime at longer timescales (inset of Figure 3.5(d)).

B5 Intra- and interlayer K-Q excitons

The wavefunction at the Q-point in twisted bilayer WSe_2 is expected to be more layer delocalized than that at the K-point, but still not fully delocalized as in the case of natural bilayers (Fig. B.2). Hence, there are two candidate K-Q exciton species: the intralayer species, where the electron wavefunction is more localized in the same layer as the hole (Fig. B.2(b)), and the interlayer species where the electron is more localized in the opposite layer (Fig. B.2(c)). The intra- (inter-) layer K-Q exciton is expected to exhibit an electron-hole separation that is smaller (greater) than $\frac{d_0}{2} = 0.3$ nm. Thus, the extracted electron-hole separation of 0.37 nm in section 3.5 indicates that the interlayer K-Q exciton dominates in PL. In this section, we explain why this is also to be expected theoretically.

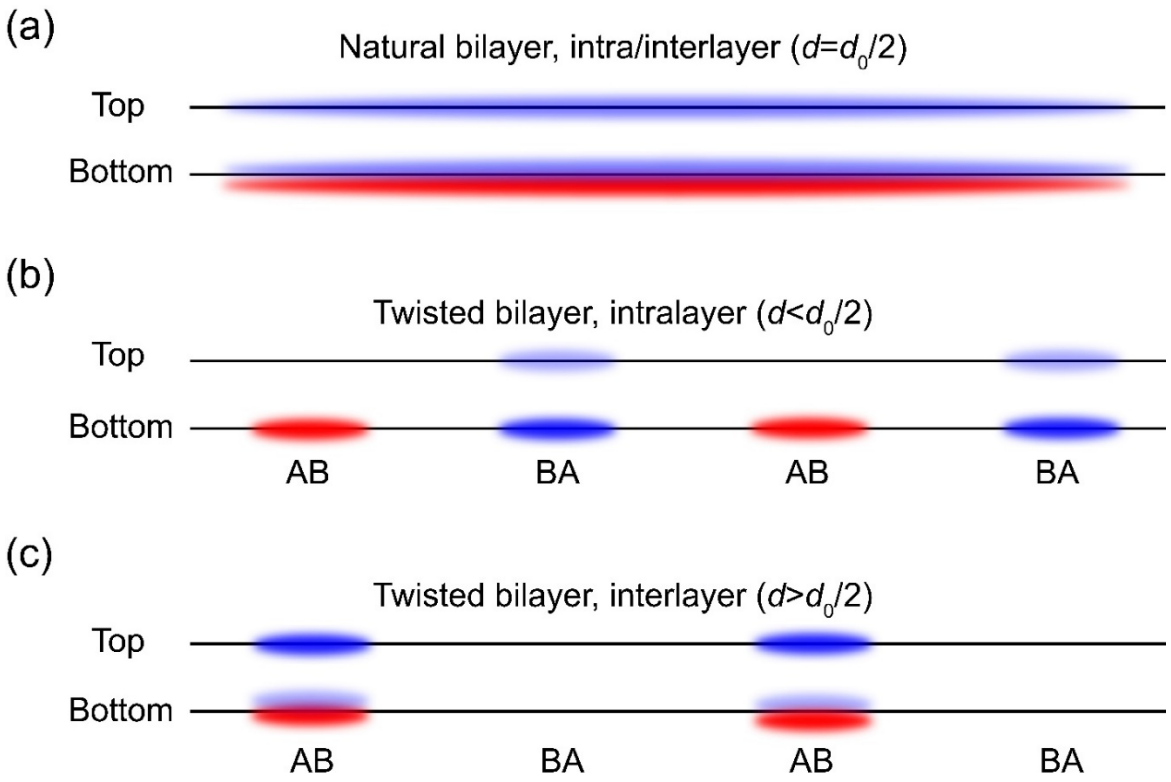


Figure B.2: Electron (blue, Q-point) and hole (red, K-point) wavefunctions in natural and twisted bilayers (only the bottom layer hole wavefunction is shown for simplicity). (a) In natural bilayers, the wavefunction at the Q-point is completely delocalized between the layers, causing the inter- and intralayer K-Q exciton to be equivalent. The expected electron-hole separation is half the interlayer spacing ($d = d_0/2$). (b)-(c) In twisted bilayers, the hole wavefunction is concentrated near the AB(BA)-stacked sites in the bottom (top) layer. In contrast, the electron wavefunction is concentrated near the AB(BA)-stacked sites in the top (bottom) layer, although more layer delocalized. Thus, the electron-hole wavefunction overlap can be larger for the interlayer exciton (c) than the intralayer exciton (b).

Crucially, the bands are not layer degenerate in twisted bilayers, even at zero electric field. This important difference from natural bilayers arises from the broken inversion symmetry, and is most easily understood by starting from the limit of zero twist angle, i.e. AB (3R) stacking. In that case, the W-atoms in the top layer are vertically aligned with Se-atoms in the other layer, while the W-atoms in the bottom layer are not. This difference in atomic environment renders the bands non-degenerate between the two layers, as shown both theoretically (*143, 208, 209*) and

experimentally (*160, 161*). In particular, theoretical studies suggest that the lowest conduction band at the Q-point and the highest valence band at the K-point are preferentially localized in opposite layers. Hence, the interlayer K-Q exciton is expected to be the lower energy state and to dominate in photoluminescence measurements.

Proceeding to non-zero twist angles, the system now exhibits a smooth periodic variation between AB- and BA-stacked points (the moiré pattern), and at large twist angles, the wavefunctions become delocalized over multiple moiré cells. Nevertheless, as shown in Refs. (*166, 210*), the delocalized hole wavefunction of the highest band at the K-point is still concentrated near the AB(BA)-stacked sites in the bottom (top) layer. Conversely, the lowest CB Q-bands are expected to be preferentially concentrated near the BA(AB)-stacked sites in the bottom (top) layer. Since the intralayer exciton consists of an electron and hole that are concentrated in different parts of the sublattice, the wavefunction overlap is very small (Fig. B.2(b)). In the case of interlayer excitons, on the other hand, the electron is predicted to be in the same domain and layer as the hole almost 40% of the time (Fig. B.2(c)). Hence, it is expected that the interlayer K-Q species has both higher binding energy and stronger oscillator strength than the intralayer counterpart, and is thus the exciton species responsible for the lower energy peaks observed in our experiment.

B6 Data from additional devices

In this section, we provide data from other devices to show the reproducibility of the results shown in section 3.5.

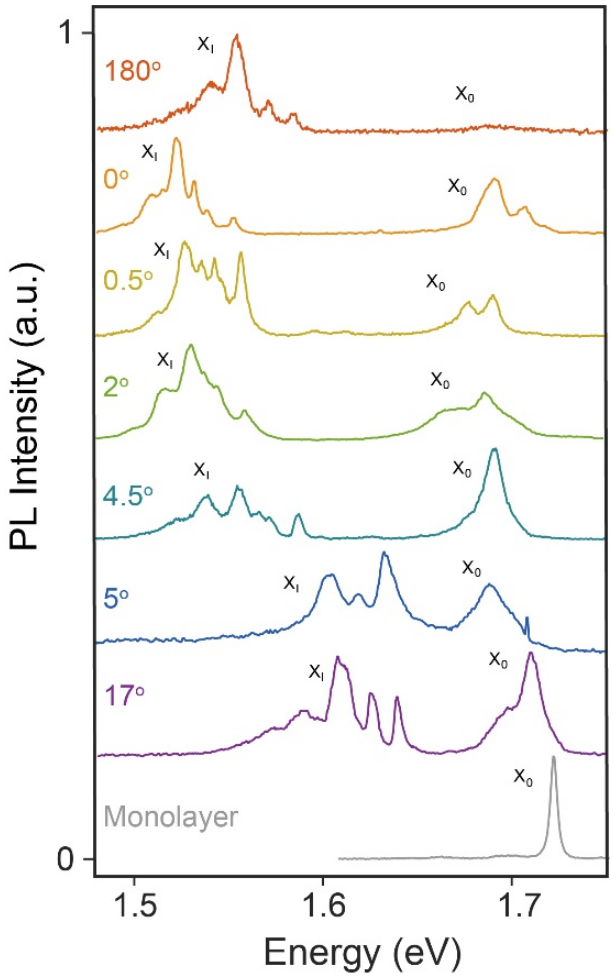


Figure B.3: Photoluminescence from additional samples. Colored (grey) curves show PL from bilayer (monolayer) WSe_2, including additional twist angles of 0.5°, 4.5° and 5° not displayed in section 3.5. The devices with 4.5° and 5° twist angles show the same interlayer exciton blue-shift as was presented for the 17° sample in section 3.5.

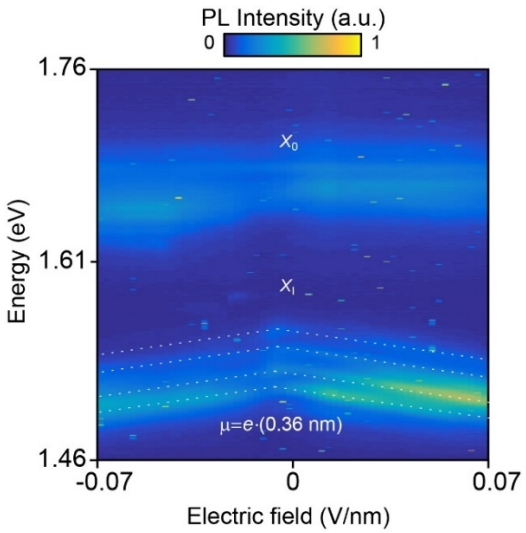


Figure B.4: Electric field dependence of PL in device with 2° twist angle. While the intralayer exciton (~ 1.7 eV) does not shift observably with electric field, the interlayer excitons (~ 1.5 – 1.6 eV) exhibit a clear Stark shift (dashed white lines). The corresponding electron-hole separation is 0.36 nm, similar to the value extracted in the 17° device (0.37 nm).

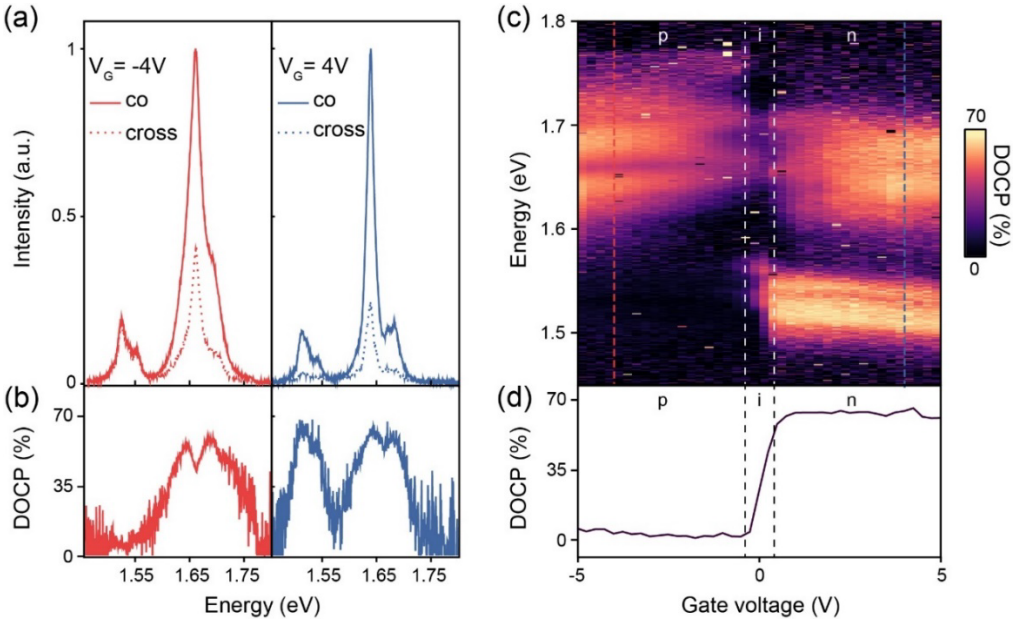


Figure B.5: Doping dependence of DOCP in device with 2° twist angle. (a) Polarization-resolved photoluminescence spectra from 2°-twisted bilayer WSe_2 at gate voltages V_G = -4 V (left) and V_G=4 V (right). Solid and dashed curves show co- and cross-polarized emission, respectively. (b) DOCP calculated from PL spectra in (a). As in the 17° device presented in in section 3.5, the interlayer DOCP is much higher in the *n*-doped regime than in the *p*-doped regime. (c) Full gate dependence of DOCP. (d) DOCP of the brightest interlayer exciton peak as a function of gate voltage. Since this device exits the intrinsic regime at relatively low gate voltages, plateaus are only observed in the *p*- and *n*-doped regimes.

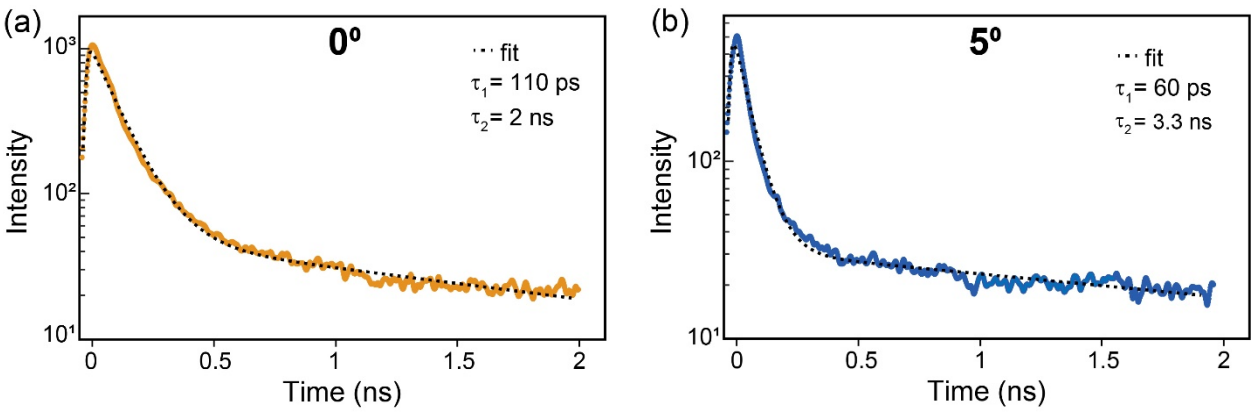


Figure B.6: Exciton lifetime in additional samples. (a)-(b) Time-resolved PL measurements from devices with 0° (a) and 5° (b) twist angles (colored dots). Dotted black lines are biexponential fits convoluted with the system response. The extracted fast and short timescales are τ_1=110 (60) ps and τ_2=2.0 (3.3) ns for the device with 0° (5°) twist angle.

C

ADDITIONAL DETAILS FOR MOIRÉ IMAGING EXPERIMENT

C1 Polar angle dependence of imaging contrast

The SEM contrast depends on both the azimuthal and polar angle of the incident electron beam, since these determine whether the electrons can channel through open "cavities" in the lattice. The SEM data for graphene in Fig. 1 is collected at a polar angle of $\theta = 24°$, since this approximately corresponds to the interlayer displacement of one carbon-carbon bond length per layer, thus enabling complete channeling for particular azimuthal angles.

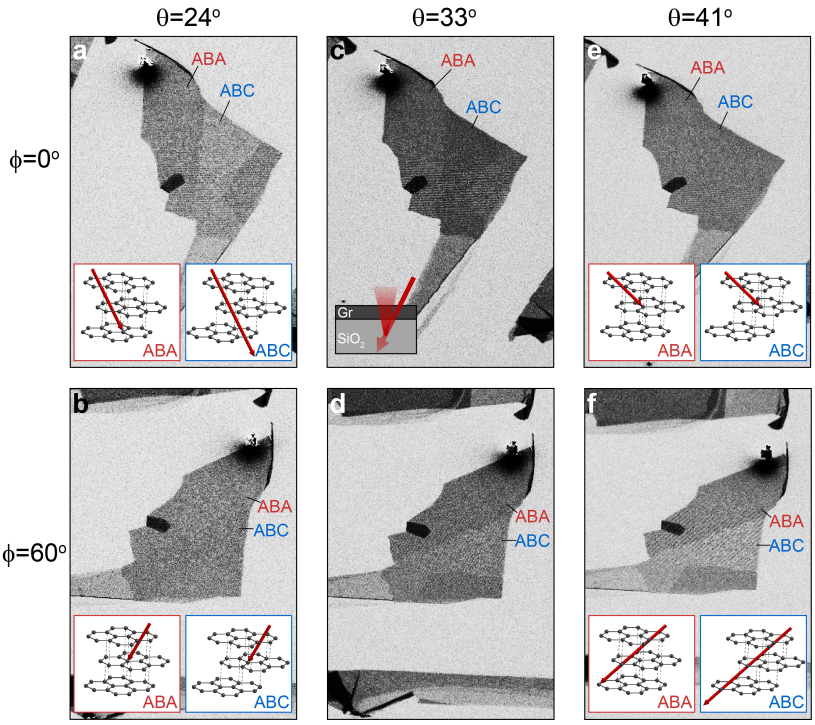


Figure C.1: Polar angle variation. a-f, SEM images of few-layer graphene containing ABA- and ABC-stacked regions, at different polar ($\theta = 24°, 33°, 41°$) and azimuthal ($\phi = 0°, 60°$) angles. Schematics show channeling paths for ABA (red) and ABC (blue) stacking order at the different angle combinations. Since $\theta = 24°(41°)$ corresponds to a shift of one (two) carbon-carbon bond lengths per layer, these polar angles enable complete channeling in the ABC region (causing bright SEM signal), but at different azimuthal angles. Less contrast is observed at $\theta = 33°$, since this does not correspond to an integer number of bond lengths.

This is exemplified in Fig. C.1a,b, which shows strong domain contrast at ϕ=0° due to complete channeling through the ABC-stacked domain, and no contrast at ϕ=60°, where neither

domain exhibits optimal channeling conditions. Moving away from $\theta = 24°$, complete channeling is not possible at any azimuthal angle, thus causing weaker domain contrast and less dependence on azimuthal angle (Fig. C.1c,d). However, the contrast re-appears near $\theta \sim 41°$ (Fig. C.1e,f), because this angle corresponds to a displacement of two bond-lengths per layer. In this case, the signal exhibits a 60° phase shift in ϕ relative to that at $\theta = 24°$, as expected from the symmetry of the lattice (Fig. C.1, insets). In general, optimal channeling can occur for $\theta = \tan^{-1}(n\,a/d)$, where n is an integer, a is the bond length and d is the interlayer spacing.

C2 Modelling of SEM signal

Our observations can be understood from a simple, semi-classical model of channeling physics (*175, 176*). For TMD bilayers encapsulated in lighter elements with lower secondary yield, contrast mainly results from the difference in direct secondary generation in the bilayer. Hence, it is sufficient to model the secondary emission as proportional to the scattering probability in the bilayer in order to reconstruct an azimuthal dependence that closely resembles the experimental data (Figure 4.3c). Few-layer graphene, on the other hand, has a lower secondary yield than the SiO_2 substrate and therefore produces a "negative" signal, in the sense that enhanced channeling through the top layer and into the substrate increases overall detected secondary yield. In this scenario, we model the yield as proportional to the transmission probability and accurately recover the dominant features of ABA/ABC stacked few-layer graphene (Figure 4.2g).

To compute primary electron transmission, atomic nuclei for the 2D material of interest are represented as points in 3D (Fig. C.2). Owing to the translational symmetry of the lattice, we consider incoming electrons across a hexagonal region corresponding to one lattice cell. A set of

10,000 to 250,000 coordinates within the hexagon is selected as entry points for the electron beams into the material, either at random with uniform probability or via a uniform grid. For each value of polar and azimuthal angle, a line through each point is considered, and the distance between the line and every lattice atom (*i.e.*, the impact parameter, b) is calculated. A transmission probability of the form $1 - \frac{A}{(b/B)^2}$ is then used, with the product over all lattice atoms giving the overall transmission probability for the line in question. Averaging over all lines then gives the overall transmission at the given θ and ϕ. Notably, though we only consider transmission across one lattice cell, the tails of the scattering probability mean that we must consider atoms outside of a one-cell-wide path. Typically, calculations were done considering atoms up to 4 inter-atomic distances away from the electron beam.

The calculations for Figure 4.2g and Figure 4.3d were performed using empirical values of A=0.1 and B=0.18 Å. Computations for ABA/ABC graphene in Figure 4.2 were performed for 5 layers stacked in ABCAB and ABABA orderings, using 100,000 lines within the lattice cell, with Monte Carlo coordinates. WSe_2 AB/BA computations were performed with 100,000 lines arranged on a grid, and verified with an equivalent model using 250,000 Monte Carlo generated lines. To represent the difference in atomic number in the WSe_2 lattice, the tungsten atoms were modelled as two overlapping selenium atoms. Notably, the computed output that most closely resembles the data is at a polar angle of 43° rather than 40° at which the data was taken. This is most likely due to differences in interlayer spacing in AB/BA stacked TMD compared to the natural AA' stacking lattice constants used for the computation. The $MoSe_2$ computation in Figure 4.3 was performed with a grid of 100,000 lines, at a polar angle of 27.5° and reproduces the periodicity but differs in some features. The difference could be attributed to the simplification of the multilayer to a model

of only the top two layers, and also potential differences in secondary yield between molybdenum and selenium. Attenuation effects due to the 10 nm gold encapsulation may also play a role.

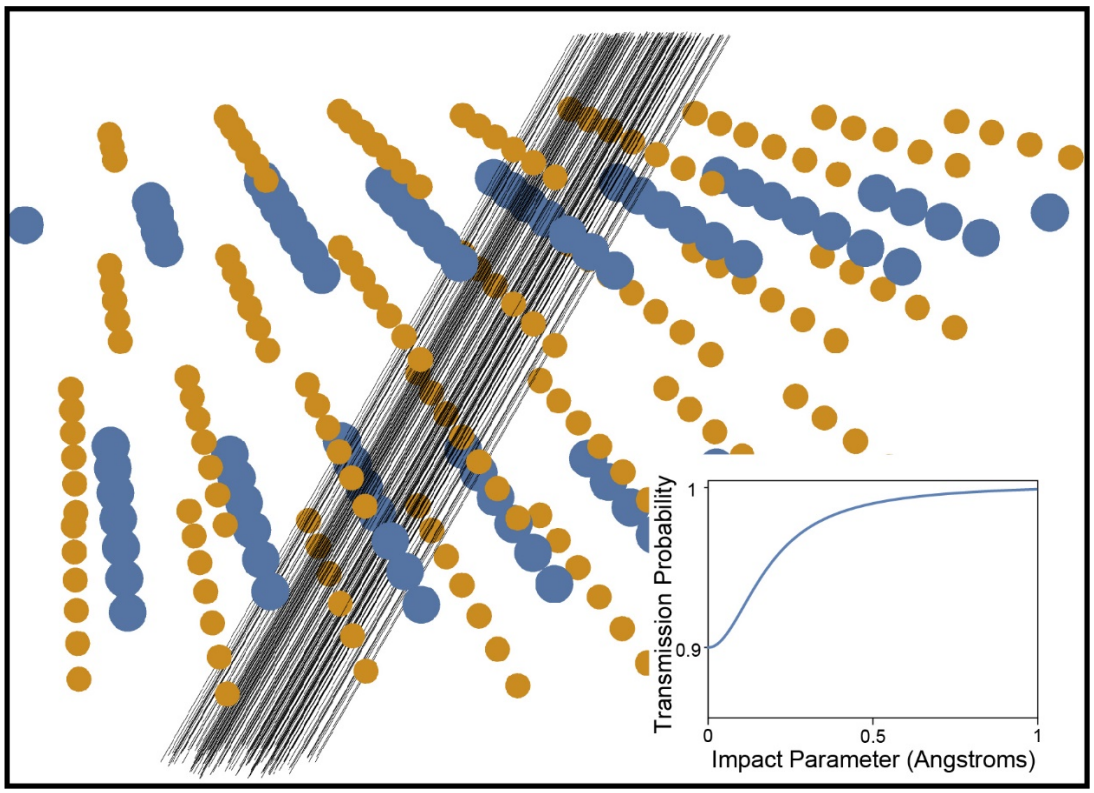


Figure C.2: Computational modeling of SEM imaging. Parallel primary beams (black lines) are positioned at Monte Carlo generated positions within an area corresponding to one unit cell, and their transmission probability through the lattice is calculated using a Lorentzian shaped scattering potential (inset) at each atom site.

C3 Distinguishing multilayer polytypes

While the stacking order of thin (2-3 layer) flakes is typically easy to determine based on the symmetries of their SEM azimuthal dependence, this becomes more challenging in thicker flakes due to the possibility of mixed polytypes. Nevertheless, pure and mixed polytypes are still expected to exhibit somewhat different channeling conditions. For instance, a multilayer graphene structure with pure ABC stacking will present fully open channels, which cause a 120° periodic

component with higher amplitude than a mixed polytype with less pronounced channels. Computational modelling of pure and mixed stacking orders in 5-layer graphene demonstrates substantial contrast between pure ABC stacking and other polytypes (Fig. C.3), and suggests that the domain observed in Figure 4.2e-i has pure ABC-stacking, not a mixture. For increasingly thick structures it becomes more challenging to identify with certainty a pure polytype, though the relative amplitude of channeling at 60° and 120° periodicities provides some indication of the degree of purity.

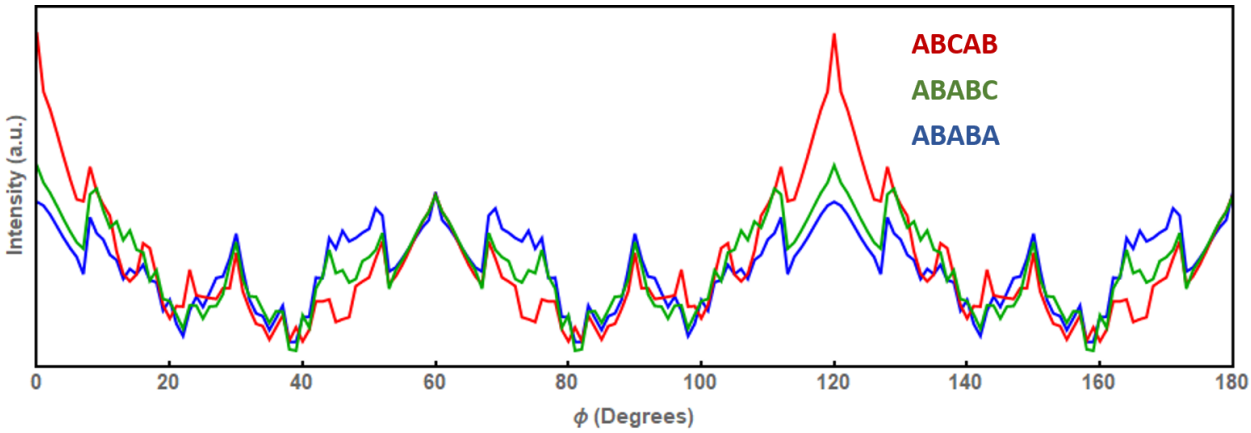


Figure C.3: Modelling signal from 5-layer graphene polytypes. Computational model of pure ABABA and ABCAB stacking orders along with the mixed ABABC ordering in graphene, modelled at $\theta = 24°$.

C4 Representative Raman spectra in multilayer graphene

In Fig. C.4, we show representative Raman spectra from the ABA- and ABC-stacked regions of the few-layer graphene flake investigated in Figure 4.2e-i. Consistent with Ref. (*184*), the 2D Raman peak for 532 nm (2.33 eV) excitation is shifted to lower wavenumbers for ABC stacking compared to ABA stacking.

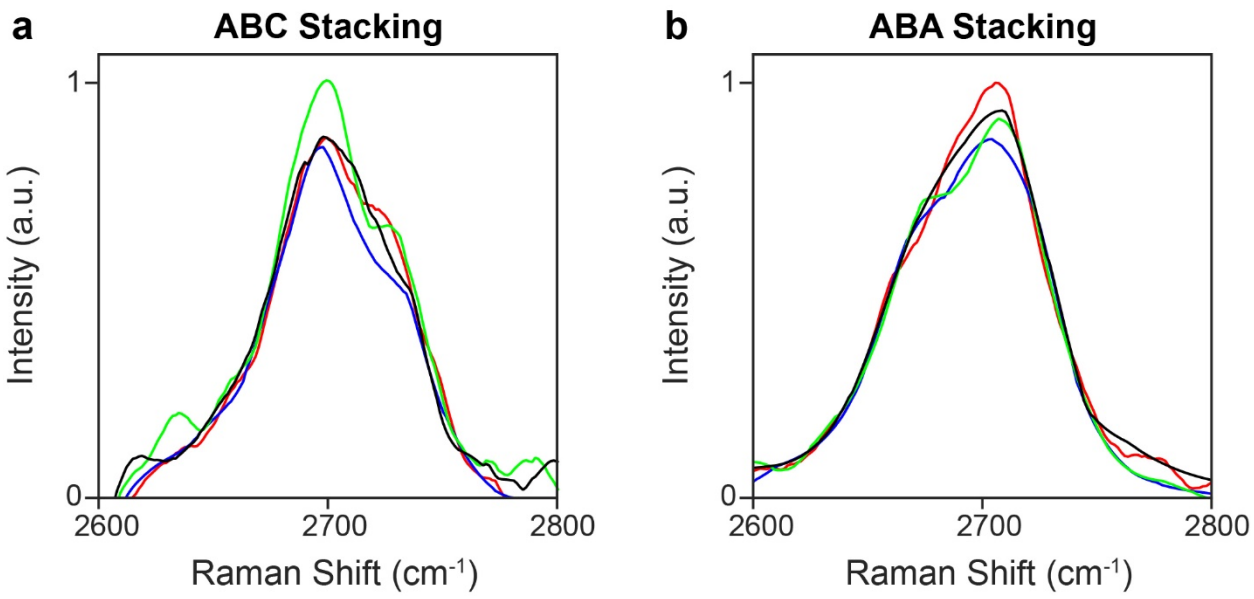


Figure C.4: Representative Raman spectra for ABC stacking **(a)** and ABA stacking (**b**) in four different locations within each domain.

C5 Dependence of SEM signal on acceleration voltage and hBN thickness

A key feature of our technique is the ability to image 2D materials fully encapsulated in hBN, which is known to enhance both optical and electronic properties (*203*). In Fig. C.5, we explore the dependence of the SEM contrast on hBN thickness, by imaging a heterostructure composed of a stepped WSe_2 flake under a perpendicularly stepped hBN flake. An optical image of the sample and the hBN thickness profile (acquired with AFM) are shown in Fig. C.5a. As with general secondary electron techniques, the depth to which we can image is determined not by the total penetration of the primary beam (typically on the order of microns) but rather by the ability of secondary electrons to escape the material. Increasing the acceleration voltage increases the energy of the secondary electrons (*183*), corresponding to a greater imaging depth, as illustrated in Fig. C.5b. At primary energies below 1.5 keV (left) the secondary electrons are only collected from the

top layers of hBN, with no WSe_2 signal through hBN thicker than ~10 nm. At an energy of 3 keV (right), the imaging depth exceeds the thickness of the heterostructure, revealing the complete thickness variation in the hBN and underlying WSe_2. Increased imaging depth, however, reduces individual layer contrast, as can be seen in the mono-, bi- and tri-layer WSe_2 steps along the right edge of the image. Nevertheless, at a reasonable acceleration voltage, monolayer steps in the TMD are clearly visible through more than 27 nm of hBN.

To determine the visibility of different stacking orders through increasingly thick hBN encapsulation, we consider the azimuthal angle dependence from natural AA'-stacked WSe_2. The azimuthal dependence of the bi- and tri-layer SEM signal for different hBN thicknesses and the corresponding contrast (root mean square amplitude) are displayed in Fig. C.5c-e, respectively. Due to the crystalline nature of the top hBN, the raw secondary yield of the bilayer is convolved with channeling effects in the hBN. Yet, we can conveniently correct for this convolution by dividing by the secondary yield from an adjacent region of equal hBN thickness but without underlying TMD (further details in Appendix C6). We observe that the contrast indeed decreases with hBN thickness, but nevertheless persists through to 27 nm. Our ability to resolve signals at large depth is mainly limited by uncertainty in this background deconvolution, as the amplitude of the channeling effect in thick hBN significantly exceeds that of the bilayer. Spatially resolvable contrast, for instance between AB/BA domains in a bilayer, can of course be imaged directly without such compensation. Since 27 nm thick top-layer hBN is sufficient for most device applications, our observations suggest that our technique is applicable to a wide range of encapsulated vdW heterostructures.

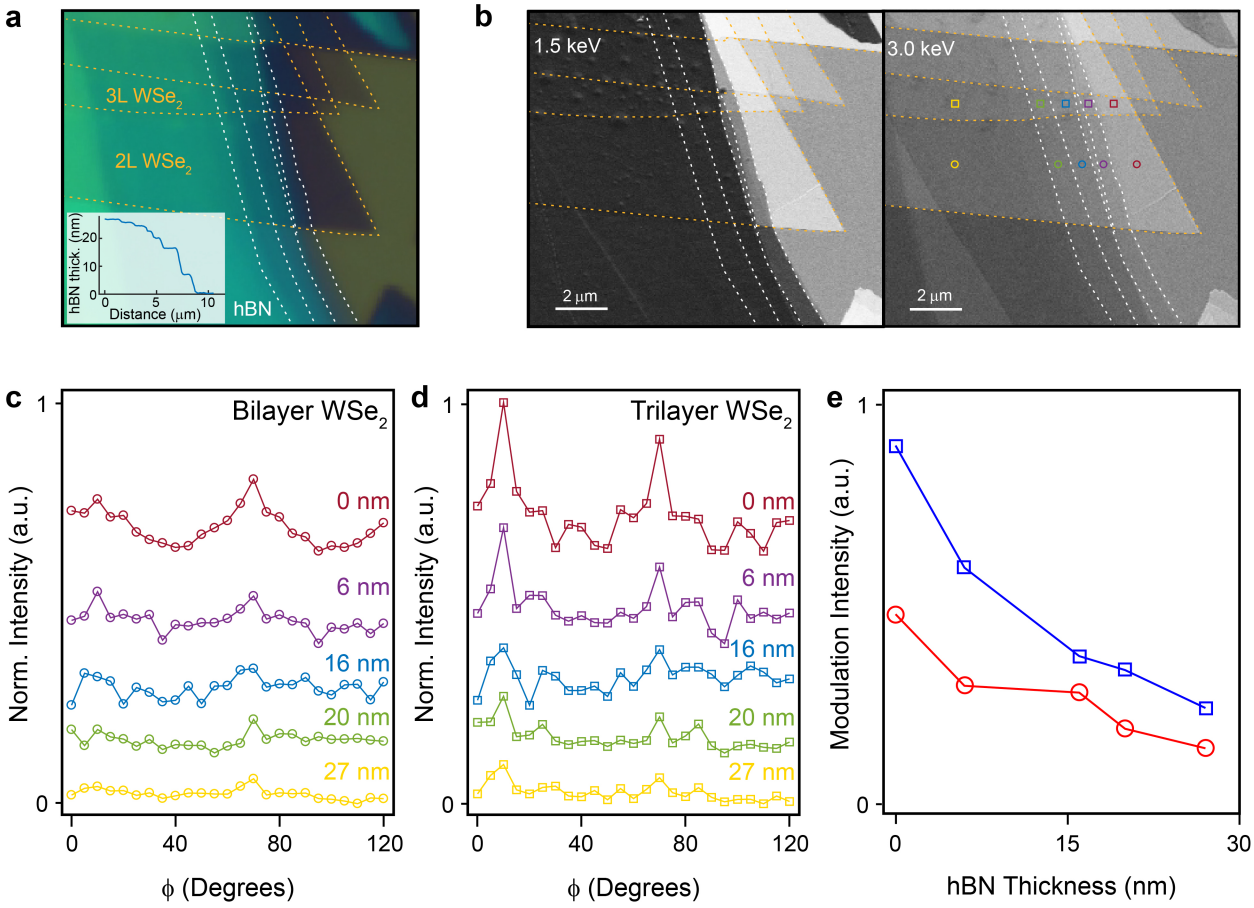


Figure C.5: Acceleration voltage and hBN thickness dependence of SEM contrast. a, Optical image of a naturally stepped WSe_2 flake stacked underneath a stepped hBN flake. Inset: AFM of stepped hBN thickness. **b,** SEM images of the sample in **a** at 1.5 keV (left) and 3 keV (right) primary acceleration voltage. Tuning the primary voltage alters the secondary electron energy spectrum, allowing for greater escape depth at higher acceleration voltage. For 1.5 keV, the escape depth is ~10 nm, restricting collected secondary signal to the hBN. At 3 keV, the depth exceeds 30 nm, revealing the underlying stepped WSe_2 structure. **c,d**, Azimuthal angle dependence of secondary yield from bilayer (**c**) and trilayer (**d**) WSe_2 under varying thickness of hBN. The curves are normalized by dividing by the yield of bare silicon oxide underneath an equal thickness of hBN. **e**, RMS amplitude of the modulation signal for bi- and tri-layer WSe_2 (red and blue squares, respectively) as a function of encapsulating layer thickness. Our data indicate that domain contrast in bilayer TMDs is resolvable even through 27 nm of hBN.

C6 Background compensation of SEM data

During azimuthal angle dependent measurements, there can be fluctuations in the level of secondary emission due to effects such as substrate charging and angle-dependent channeling of

the encapsulant or substrate. For systems with natural contrast, such as AB/BA domains in graphene or twisted WSe_2, we compensate for these effects by normalizing to the mean of the two regions. In the case of materials without domain contrast, such as AA' stacked natural WSe_2 bilayers, we instead normalize the SEM signal to that of only the encapsulant and substrate. Figure C.6 shows the azimuthal dependence for the bilayer part of the device discussed in section C5, before and after compensating for channeling in the top encapsulation.

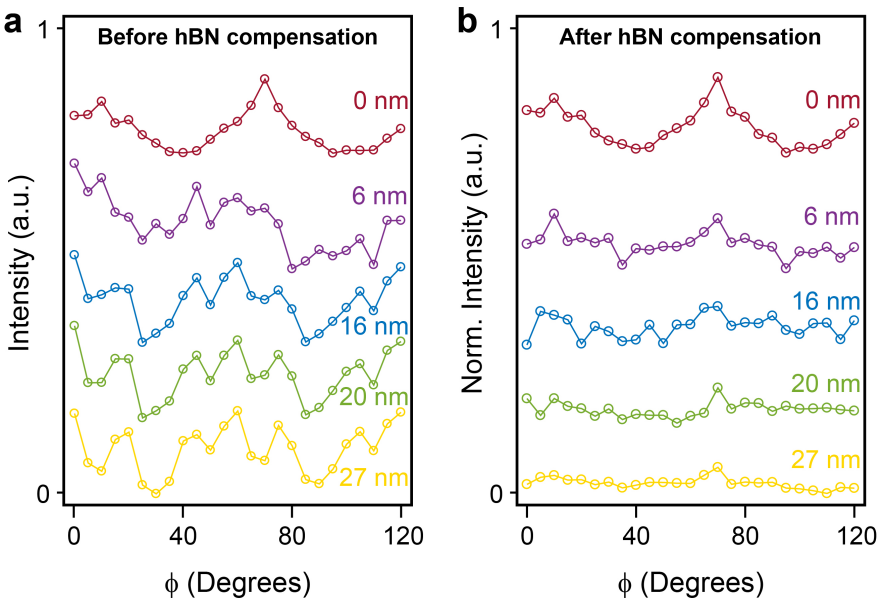


Figure C.6: Compensation for channeling effects through top hBN. a,b, Azimuthal dependence of SEM signal from bi-layer TMD under hBN of varying thickness, before (**a**) and after (**b**) compensation for channeling effects in the hBN. We note that **b** is also shown in Fig. C.5.

C7 Additional SEM data

C7.1 Monolayer TMD signal

Due to the three-dimensional atomic structure of TMD layers, it is possible to measure the secondary yield modulation with azimuthal angle of a monolayer when imaging at a sufficiently shallow polar angle. Fig. C.7a-c show an SEM image, a schematic and the azimuthal dependence

of a WSe_2 monolayer on an SiO_2 substrate at a polar angle of 40°. These data indicate that the SEM technique can be used to extract the lattice orientation of an exfoliated monolayer flake - information that is valuable for the assembly of twisted heterobilayer devices.

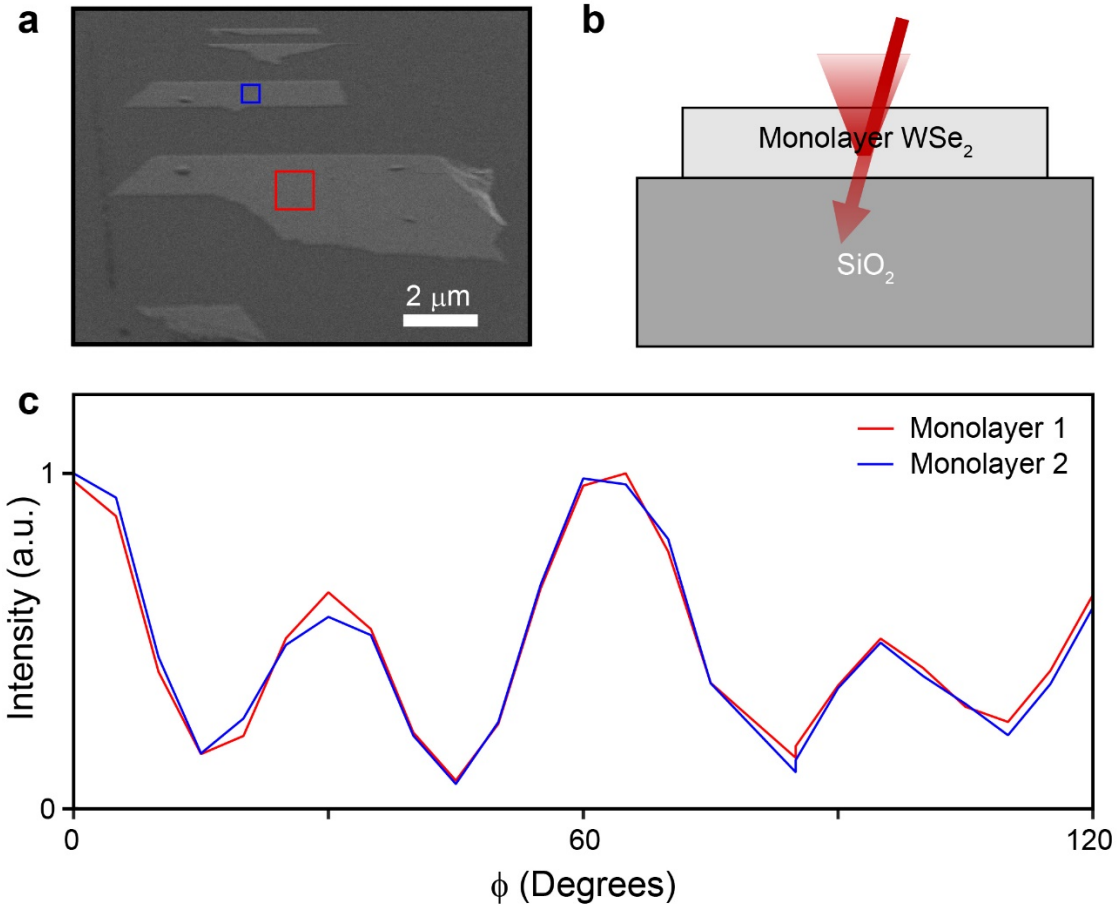


Figure C.7: Imaging of monolayer TMD. a, SEM image of monolayer WSe_2 flakes on SiO_2 substrate, using acceleration voltage of 1 keV and $\theta = 40°$. **b,** Schematic of secondary emission in this system, showing stronger secondary signal from the TMD, due to its higher atomic mass. **c,** Azimuthal dependence of SEM signal from two separate monolayer WSe_2 flakes, indicated by boxes in **a**. Due to the 3D structure of TMDs, amplitude modulation can be observed even from monolayers.

C7.2 Imaging of monolayer on bulk TMD

Fig. C.8a shows an SEM image of a monolayer $MoSe_2$ flake stacked at a random angle on a thick multilayer $MoSe_2$ substrate (schematic in Fig. C.8b). While the azimuthal rotation signal of the

bulk is relatively symmetric (Fig. C.8c), the signal from the monolayer region displays a more complex pattern due to the partial channels between the monolayer and bulk. Taking the difference signal (Fig. C.8d) reveals a roughly 60°-periodic structure, with strong asymmetry due to the partial channels.

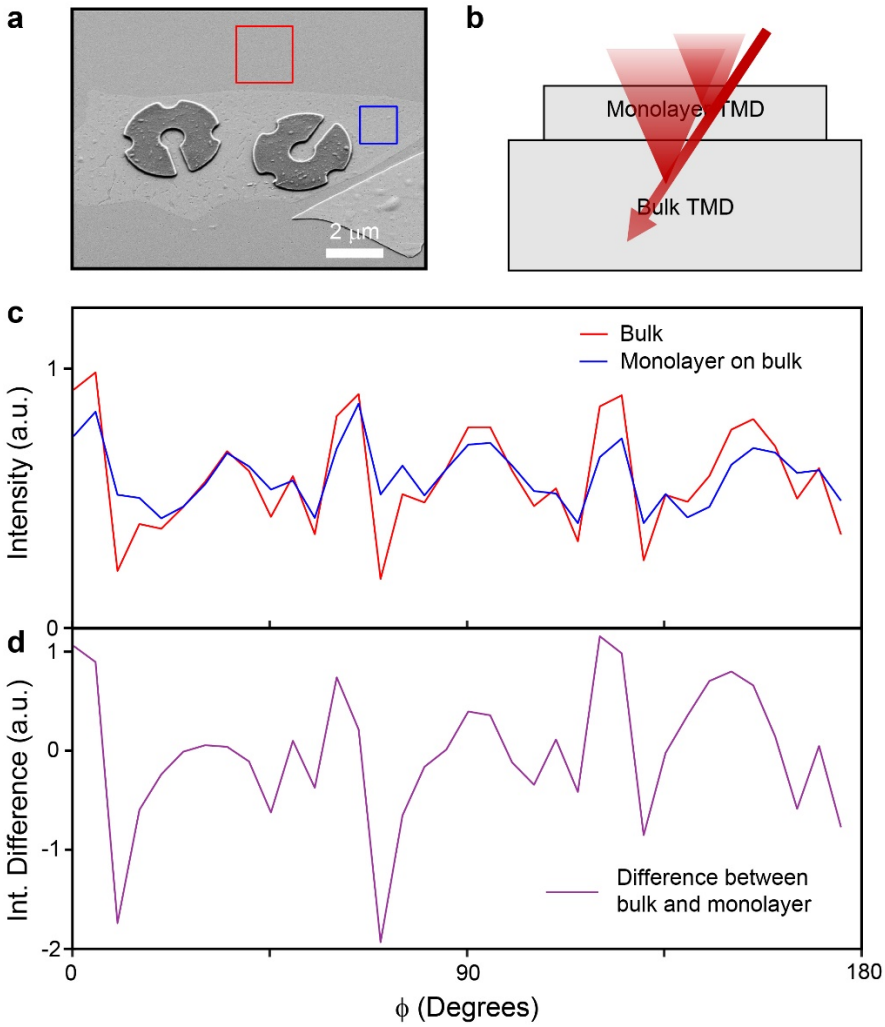


Figure C.8: Imaging TMD monolayer on bulk. a, SEM image of a monolayer $MoSe_2$ flake placed on top of a thick $MoSe_2$ flake. **b**, Schematic of secondary generation from both the monolayer and bulk flake. **c**, Azimuthal dependence of SEM signal from monolayer on bulk (blue) and only the bulk (red), collected from the boxed regions in **a**. The more complex structure of the former is due to the partial channels of the combined system. **d**, Difference between the two curves in **c**.

C7.3 Imaging of stepped graphene and TMD flakes

In order to explore the ability to differentiate stacking orders of graphene on top of materials with similar secondary yield (e.g. graphite, hBN), we image thick, stepped graphite flakes (Fig. C.9a-c). By using a relatively small acceleration voltage (500 eV), the flake is sufficiently thick that the secondary yield depends on the stacking order of the surface layers, rather than the total thickness. In particular, the SEM signal depends on whether the top two layers are AB- or BA-stacked, and therefore alternates across steps of monotonically changing thickness (Fig. C.9a). Similar to in Figure 4.2d, the two stacking orders exhibit 120º contrast oscillations with a 60º offset.

Similar measurements were also conducted in a stepped multilayer $MoSe_2$ flake underneath a 10 nm layer of gold (Fig. C.9d-f). Again, the SEM contrast depends on the stacking order of the top two layers, and thus alternates with the parity of the number of layers (Fig. C.9d). In this case, the angular dependence (Fig. C.9f) is more complex than in graphene, due to the 3D nature of the $MoSe_2$ layers, and also because the polar angle used here (30°) is not commensurate with the dominant channels in $MoSe_2$, thus not allowing for maximal channeling.

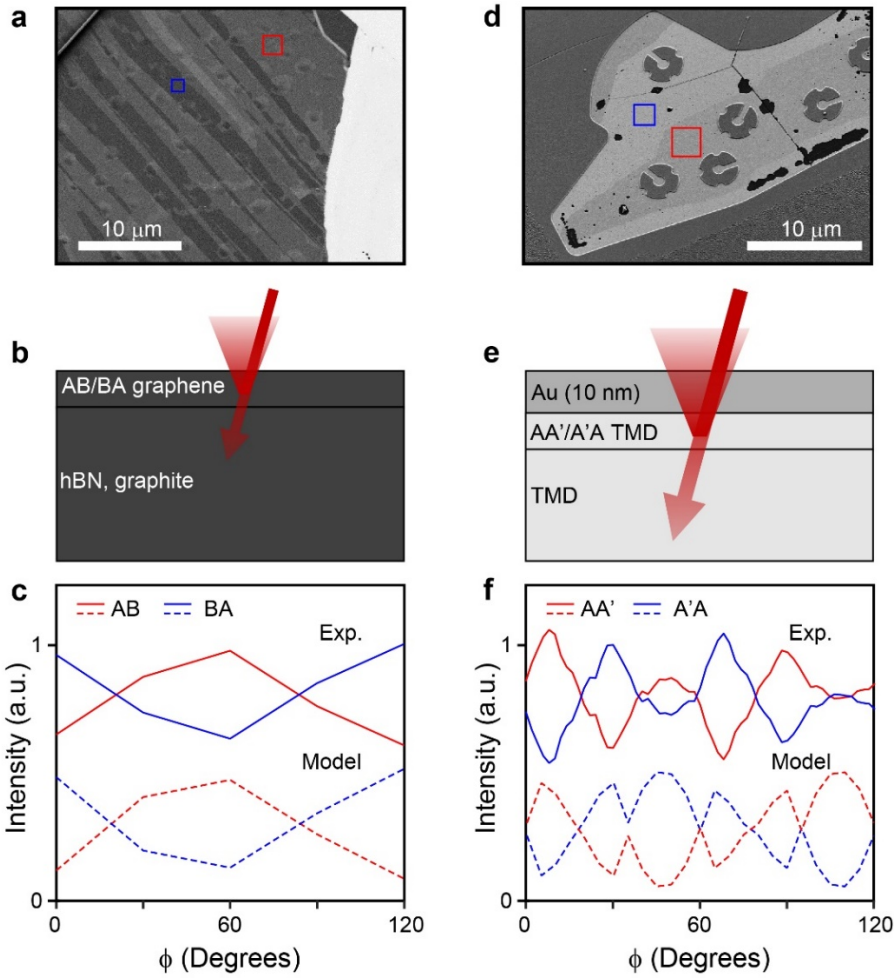


Figure C.9: Imaging of stepped graphite and $MoSe_2$. **a**, SEM image of stepped graphite flake using acceleration voltage of 500 eV and $\theta = 24°$. Alternating contrast is observed as the top two layers change between AB and BA stacking across the steps. **b,** Schematic of secondary generation, highlighting the sensitivity to the stacking order of the top few layers, which enables imaging of AB/BA domains on top of thick low-Z materials such as graphite or hBN. **c,** Azimuthal angle dependence of SEM signal in regions with AB (red) and BA (blue) surface stacking (solid lines). Dashed lines show predictions of model presented in Appendix C2. **d-f**, Same as **a-c**, but in stepped $MoSe_2$ underneath 10 nm Au. The more complex azimuthal dependence (**f**) is due to the 3D nature of the $MoSe_2$ layers, and also because the polar angle used here (30°) does not allow for maximal channeling.

C7.4 Applications to CVD-grown materials

An interesting application of SEM imaging is rapid identification of layer stacking in CVD-grown 2D materials. We consider the ability to resolve a series of common stacking orders via the same computational methods used for AB/BA stacking orders in WSe_2, but applied to AA', AB, and 15°

misaligned moiré bilayers (Fig. C.10). A clear contrast between different stacking orders was found for a polar angle of 24°, with AA' dominated by a 60°-periodic signal, compared to a large 120°-periodic component for AB. Computations for 15° moiré stacking were performed in a similar manner but averaging transmission over the full superlattice cell rather than that of the monolayer lattice.

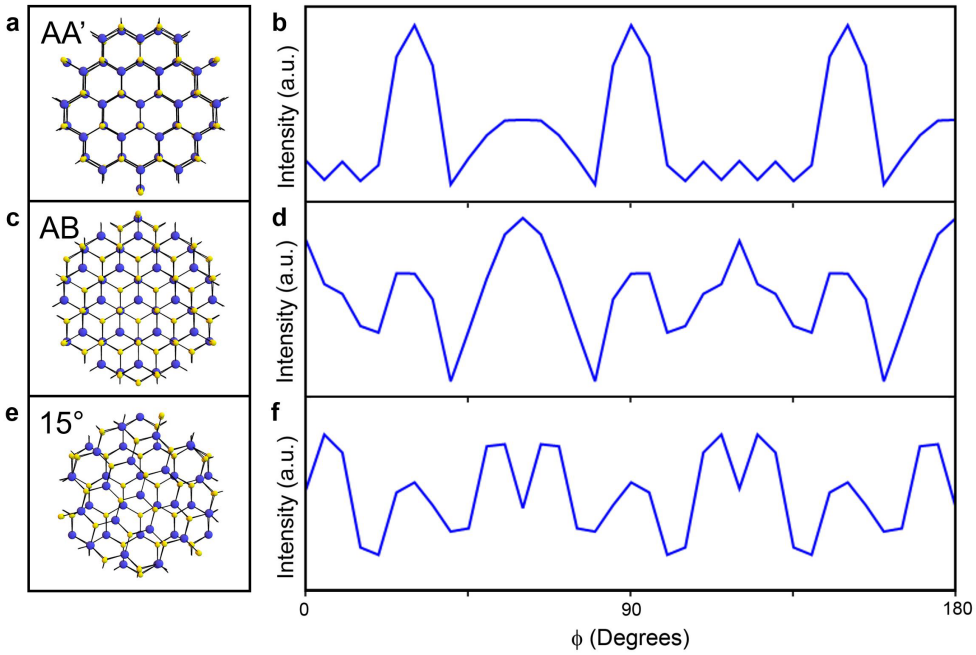


Figure C.10: Modelling signal from TMD bilayer stackings. **a**, Schematics of three of the stacking orders that can be found in CVD-grown TMD bilayers (**a**,**c**,**e**), with corresponding computed azimuthal dependence (**b**,**d**,**f**). Computational modelling is performed for WSe_2 at $\theta = 24°$.

C8 Parameters used for SEM imaging

The SEM images shown in section 4.4 were captured with a Zeiss Ultra Plus FESEM (Ultra55 and Supra55VP were also confirmed to show domain contrast). The following is a table of the parameters used with the Zeiss Ultra Plus:

Figure	Device Type	Acceleration Voltage (keV)	Polar Angle	Bias on Secondary Electron Detector (V)	Aperture size (μm)
Figure 4.2c,d	Bilayer graphene	0.5	24°	300	30
Figure 4.2f,g	Few-layer graphene	1	24°	300	30
Figure 4.3b,c	hBN-encapsulated twisted TMD bilayer	3	40°	300	30
Figure 4.4a	hBN-encapsulated twisted TMD bilayer	2	40°	300	30
Figure 4.5a	hBN-encapsulated twisted TMD bilayer	3	40°	300	30

Table C.1: List of parameters used for SEM imaging of the devices presented in section 4.4.

C9 Procedure for co-alignment of SEM imaging and optical measurements

In order to correlate the moiré wavelength with our optical measurements, we co-align an SEM image of the device (Fig. C.11a) with a photoluminescence (PL) intensity scan (Fig. C.11b). The latter is obtained by spatially rastering a 660 nm laser (1.88 eV) using galvo mirrors, and collecting the PL emission for wavelengths greater than 700 nm (<1.77 eV). The SEM and PL images are co-aligned (Fig. C.11c) based on features with easily identifiable PL signal. A good example is surrounding monolayer WSe_2 regions (dotted blue lines in Fig. C.11), which exhibit a substantially stronger PL signal and are also easily identifiable in the SEM images. After aligning, the galvo

mirrors are used to select spots with known position relative to the original PL scan, where we perform gate-dependent optical experiments.

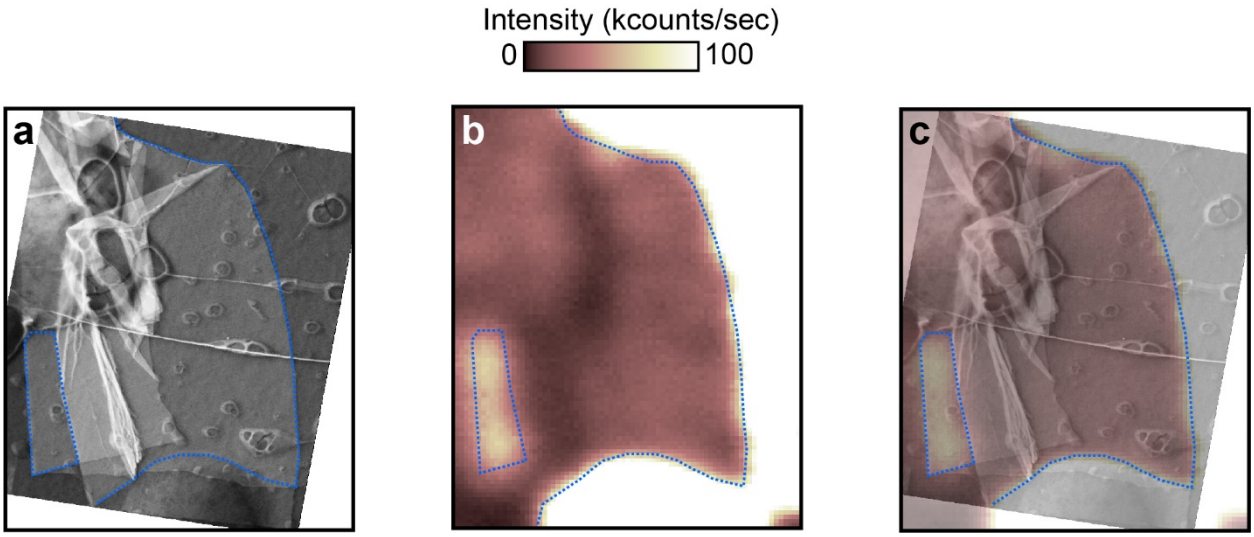


Figure C.11: Co-alignment of SEM and photoluminescence device images. **a**, SEM image of a twisted TMD device (D2). Dashed blue line indicates the border of features recognizable in both PL and SEM. **b,** Photoluminescence intensity scan showing that the twisted TMD area is darker than the surrounding monolayer TMD section. Once the scan is performed, one can select any spot within the sample to perform optical measurements. **c,** Overlaid PL and SEM images, which allow for correlation of moiré periodicity with optical signal.

C10 Comparison of PL and absorption spectroscopy

We also conduct gate-dependent absorption spectroscopy of device D4, shown as the derivative of differential reflection in Fig. C.12a (PL spectra are shown in Fig. C.12b for comparison). While interlayer exciton absorption is too weak to be observed, we observe strong absorption features from the intralayer excitons (*7, 191*). This is consistent with our assignment of the intralayer excitons to the momentum direct K-K transition.

The doping dependence observed in absorption measurements is also consistent with PL. While the type I exciton exhibits much stronger doping effects (blue-shift and weakening of neutral state) than the type II exciton at the onset of the *p*-doped regime, the type II exciton exhibits

stronger doping effects at the onset of the n-doped regime. In the *n*-doped regime, the type I exciton also shows clear signs of doping, as expected from the fact that the electrons are more delocalized than the holes. The absorption spectra also show the red-shifted charged exciton states that were observed in PL.

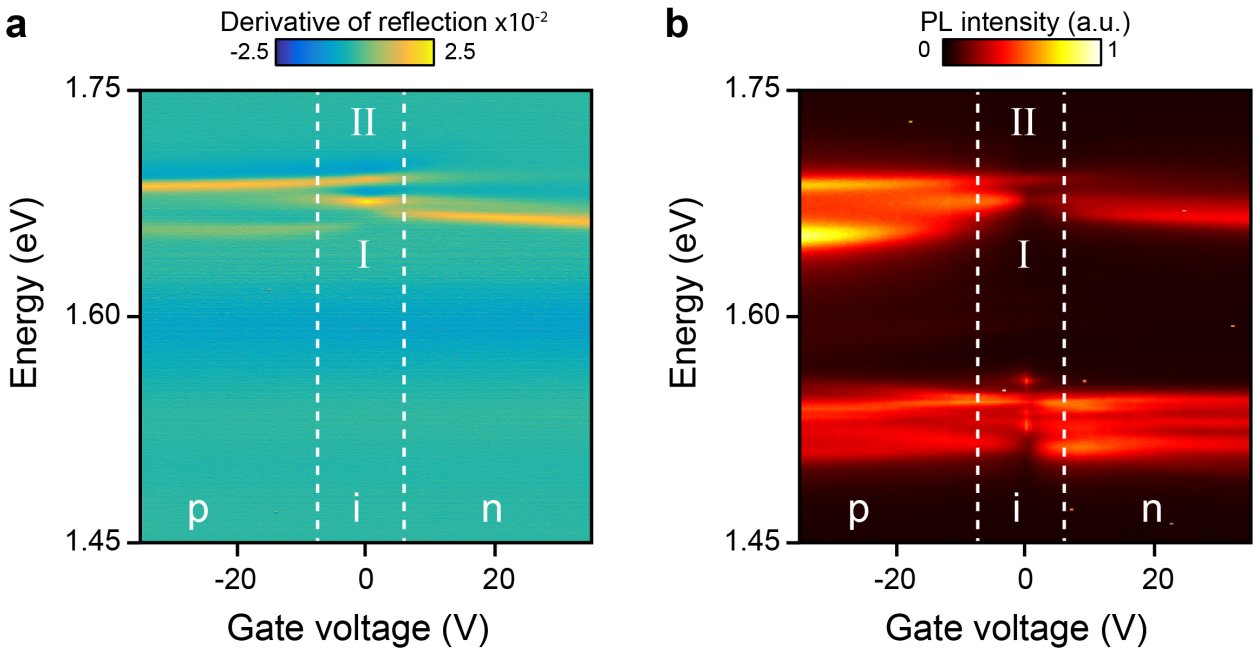


Figure C.12: Comparison of absorption and photoluminescence spectra. a, Derivative of differential reflectance vs. gate voltage in device D4, showing strong intralayer exciton absorption, consistent with the momentum direct K-K transition. **b**, Corresponding gate-dependent photoluminescence spectra from device D4.

C11 Extracting energy splitting between the exciton species

In order to extract the different energy scales, we fit the gate-dependent PL spectra with a double Lorentzian of the form:

$$I(E) = \frac{A_{\mathrm{I}}}{(E - E_{\mathrm{I}})^2/\Gamma_{\mathrm{I}}^2 + 1} + \frac{A_{\mathrm{II}}}{(E - E_{\mathrm{II}})^2/\Gamma_{\mathrm{II}}^2 + 1}, \tag{C.16}$$

where $A_{I(II)}$, $E_{I(II)}$ and $\Gamma_{I(II)}$ are the amplitude, resonance energy and linewidth of peak I(II). In some devices, the doped and neutral excitons are found to coexist at the transition between the doping regimes. Moreover, in D2 the charged type I exciton peak extends out of the *p*-doped regime, likely due to localized charge (defect) states, as previously observed (*211-215*). In these cases, we fit the spectra with a triple Lorentzian.

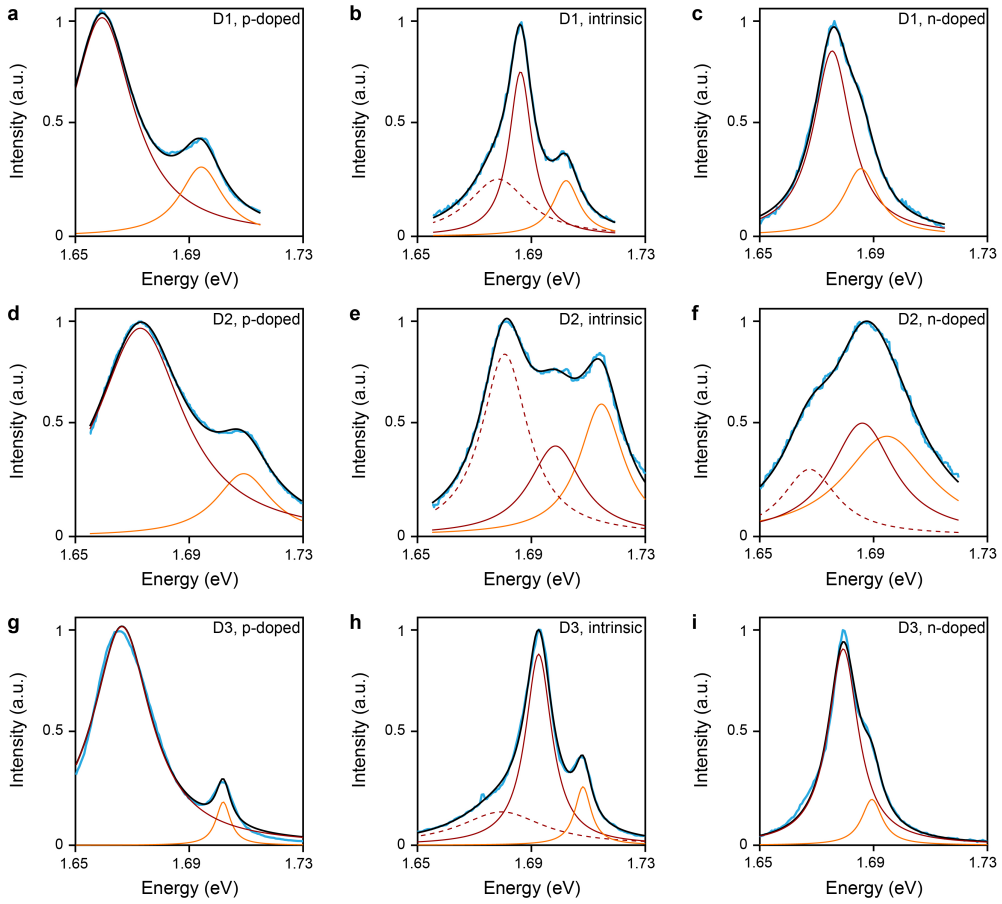


Figure C.13: Peak fitting in different doping regimes. a-c, Photoluminescence spectra (light blue lines) from devices D1 (**a-c**), D2 (**d-f**) and D3 (**g-i**) in the p-doped, intrinsic and n-doped regimes. In **a,c,d,i,g**, the spectra are fit with double Lorentzians (black), with contributions from the type I (II) excitons shown in maroon (orange). In **b,e,f,h** the positively charged type I exciton is observed even outside the p-doped regime (dashed maroon), likely due to localized charge defects. We therefore fit with a triple Lorentzian (black). The extracted peak splittings are 36 meV, 16 meV and 10 meV in **a-c**, and 36 meV, 16 meV and 9 meV in **d-f**, 35 meV, 16 meV and 10 meV in **g-i**.

Fig. C.13 shows fitting examples for device D1-D3 in the three doping regimes, and Fig. C.17 displays the full gate dependence of the extracted values of E_{I} and E_{II} in D1-D4 and D6. The red-shifts, $E_{\mathrm{h(e)}}^{\mathrm{I(II)}}$, of the type I(II) exciton due to interactions with holes (electrons) are extracted from the change in E_{I} and E_{II} at the onset of doping (Fig. C.17).

C12 PL measurements of additional devices

In order to confirm the reproducibility of the observed two-peak structure, as well as the disappearance of the higher energy (type II) exciton in the small-domain regime, we have conducted PL measurements in a total of 10 devices with a wide range of twist angles. Consistent with the picture presented in Chapter 4.4, we find that the two-peak structure:

-is not visible in any of our large (5°, 17° and 22°) twist angle devices (Fig. C.14a-c).

-is visible in some spots (but not everywhere) in intermediate twist angle (2°-4.5°) devices (Fig. C.14d-f), in good agreement with our results from the 2.5° twisted device (D2) presented in Figure 4.4.

-persists everywhere in all small angle (<1°) devices (Fig. C.14g-i), consistent with the data shown in Figure 4.4 and Figure 4.5.

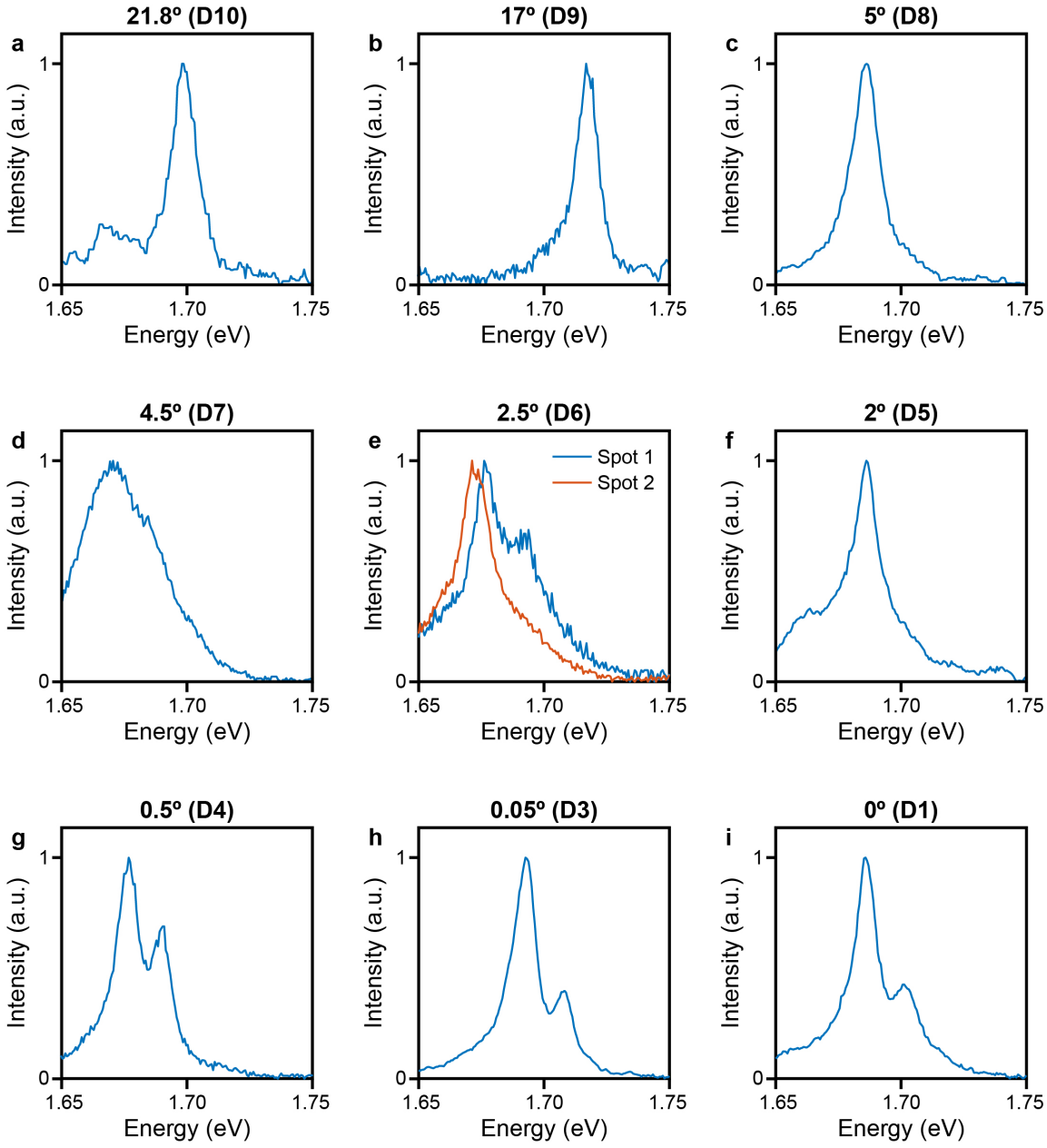


Figure C.14: Photoluminescence measurements of devices with varying target twist angle in the intrinsic regime. The higher energy (type II) exciton is not observed in large angle devices (**a-c**), appears sporadically in intermediate twist angle devices (**d-f**), and is seen everywhere in small angle devices (**g-i**).

C13 Prevention of interlayer contamination

In order to minimize interlayer contamination, we first clean the Si/SiO_2 substrates with acetone, isopropyl alcohol and then O_2 Plasma (100 W for 10 min). Next, the 2D material flakes are exfoliated with low-residue scientific tape, and the hBN flakes are vacuum annealed at high temperatures (>200 °C). Finally, all stacks are assembled using the pick-up technique (*20, 131, 216*), in which the flakes only come in contact with each other, and not with any polymer or solvent (except for the top part of the top flake). All flakes are engaged slowly at temperatures exceeding 100 °C, which is known to effectively reduce interfacial contamination as shown in Ref. (*217*). We also do the final transfer step at even higher temperatures (T=150-180 °C), which has been shown to further remove interlayer contamination (*218*).

Due to these measures, the majority of the contamination features observed in our SEM images (red boxes in Fig. C.15a) are not between the TMD layers, but rather on top of the heterostructure. Additional SEM images show that similar features are observed in all parts of the sample (red boxes in Fig. C.15a), and even on single (not stacked) flakes (Fig. C.15b). The latter observation unambiguously indicates that these contamination features must be on the top surface, and not within the heterostructure. Since the flakes were confirmed to be pristine prior to stacking via AFM, we expect that the top surface contamination arises from the polycarbonate/PDMS stamp used for stacking. The top surface contamination is most visible in regions that are otherwise uniform, such as the left side of device D2, where the moiré domains are very small and not resolvable. In the right region of D2, on the other hand, the top surface contamination is seen as a modulation of the moiré contrast, because it lightly distorts the SEM signal. Similar variation in moiré contrast due to top surface contamination is also observed in device D1 (Fig. C.15c,d), and we also observe the surface contamination in AFM (Fig. C.15e). We note that the top surface

contamination is separated from the TMD bilayer by both hBN and a screening graphene gate, and is thus not expected to affect its optoelectronic properties.

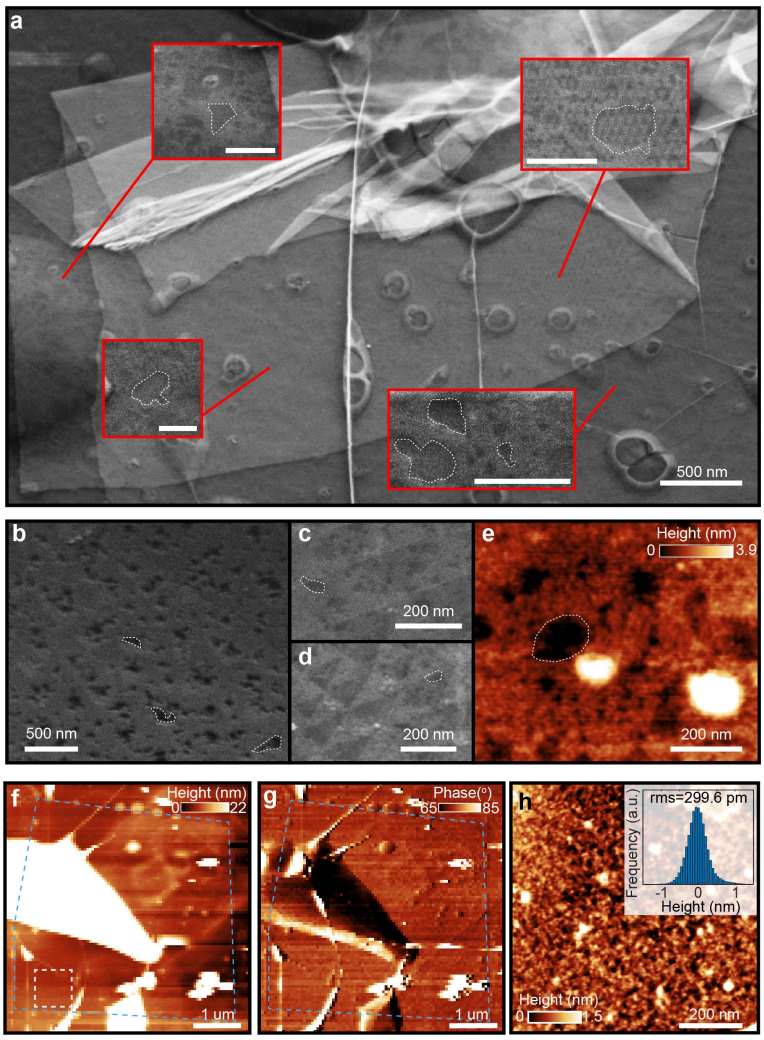


Figure C.15: Surface contamination. a, Zoomed-out SEM image of device D2. Red boxes show zoomed-in, contrast-enhanced versions of top surface contamination, and include a 200 nm scale bar. In the reconstructed moiré region (top right), top surface contamination causes variation in moiré contrast. **b**, SEM image of a single hBN flake, showing the same type of surface features. **c,d,** Variation in moiré contrast due to surface contamination is also observed in D1. **e**, Top surface contamination can also be seen with AFM. **f,g,** AFM images of device D1, including height (**f**) and phase (**g**) profiles. Blue dashed lines indicate twisted bilayer region. **h**, AFM height profile of region indicated by white box in **f**. Inset: Histogram of height profile, showing rms roughness of ~300 pm.

We also observe some "bubble"- and "wrinkle"-like features in our devices (Fig. C.15a,f,g). As can be seen from the zoomed-out SEM image in Fig. C.15a, these also appear

outside the twisted TMD region, and some features even extend across the twisted TMD boundary. Based on these observations, we expect that many of these features are not due to contamination between TMD layers, but rather on other interfaces within the heterostructure. Nevertheless, a few of the features may be between the TMD layers, and even features on TMD-hBN interfaces may affect the optoelectronic properties. In between such features, we observe that the heterostructure is very flat (Fig. C.15a,h).We therefore used the SEM images to make sure that the inspected locations avoid major features and show clear moiré domains.

C14 Linear vs circular polarization measurements

In order to illustrate the important difference between linearly and circularly polarized PL measurements, we compare the two in the p-doped regime in Fig. C.16 (device D3). While the DOLP of the type I exciton is very close to zero, the DOCP is very high for both exciton species. This suggests that the reduced DOLP is not simply due to enhanced valley depolarization, but rather a valley decoherence effect, as predicted in our theoretical picture.

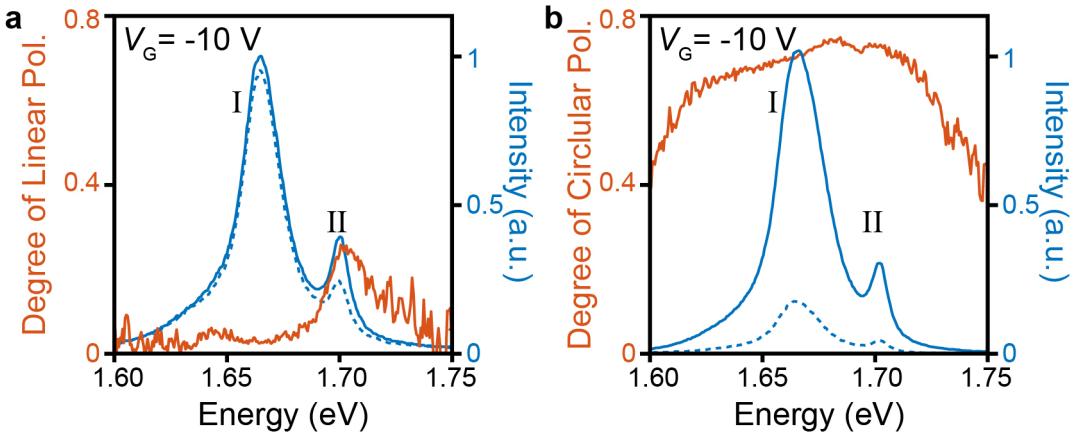


Figure C.16: Comparison of DOLP and DOCP. a,b, Orange: Line cuts of DOLP (**a**) and DOCP (**b**) at $V_G = -10$ V. Blue: Co- and cross-polarized emission components (solid and dashed curves).

C15 Doping dependence of additional small-angle devices

Figure C.17 displays gate-dependent photoluminescence spectra (top) and extracted peak splittings (bottom) from the small-angle devices D1, D2, D3, D4 and D6, which all show very similar behavior. We here list the main common features, which are explained in Chapter 4.4:

-In the *p*-doped regime, the type I exciton intensifies, broadens and red-shifts more than the type II exciton.

-At the onset of the *n*-doped regime, both exciton types red-shift, but the type II exciton red-shifts more.

-The splittings are (±3 meV) 35 meV, 15 meV and 10 meV in the *p*-doped, intrinsic and *n*-doped regimes, respectively.

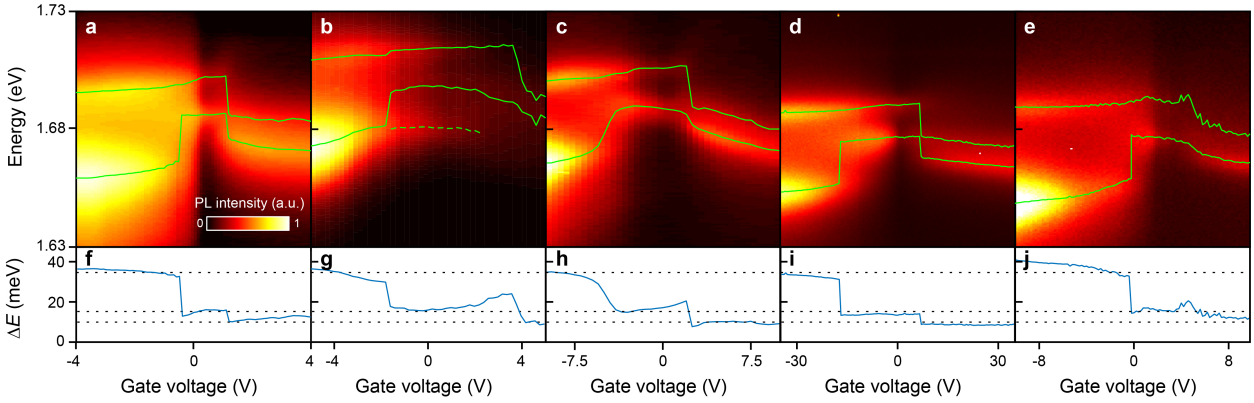


Figure C.17: Doping dependent PL measurements of additional devices. a-e, Gate dependent photoluminescence from devices D1, D2, D3, D4 and D6 (left to right). Green lines show the extracted peak positions from double or triple Lorentzian fits. The dashed green line in **b** indicates that the charged type I exciton emission persists into the intrinsic regime, likely due to localized charge defects. The width of the intrinsic regime varies due to differences in contact quality and hBN thickness. **f-j**, Peak splitting calculated from green lines in **a-e**. Dashed horizontal lines highlight that the splitting is very similar across all five devices.

C16 DOLP measurements of additional small-angle device

To confirm the reproducibility of the DOLP results shown in Figure 4.6, we conduct equivalent measurements of device D3 (Fig. C.18) and observe the same behavior.

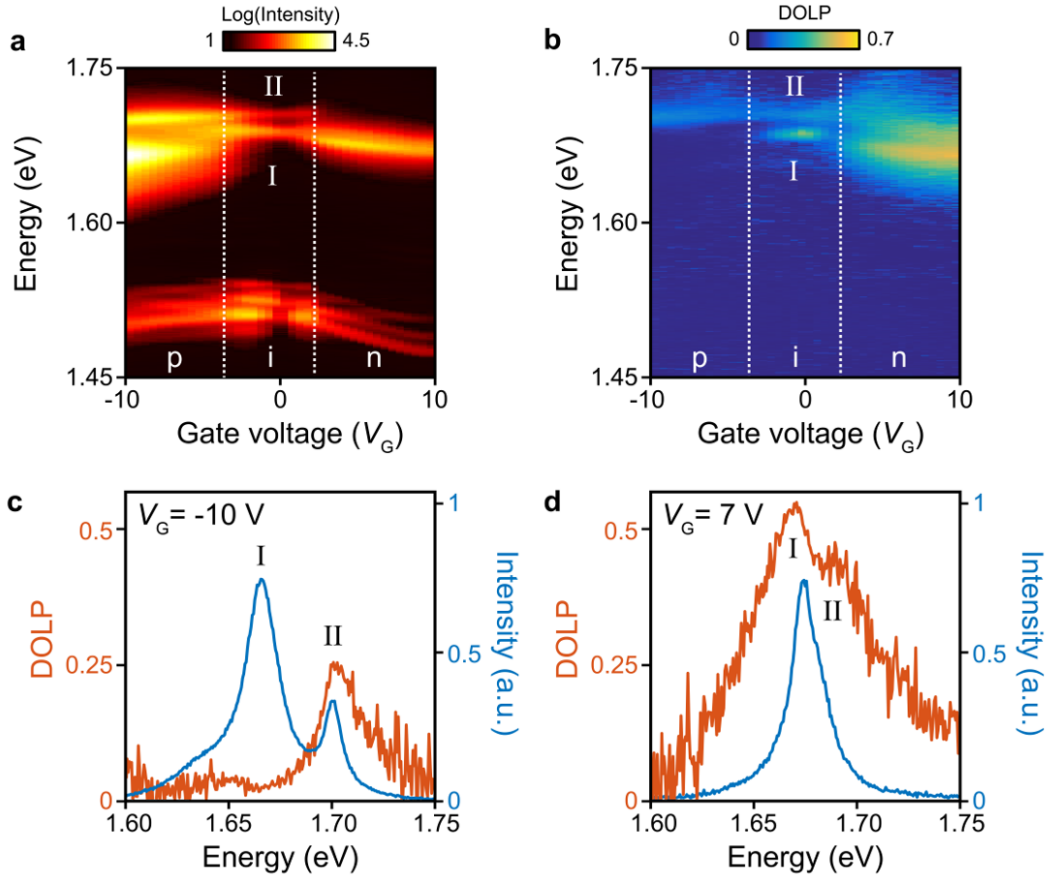


Figure C.18: DOLP measurements in device D3. a, Gate-dependent PL spectra from device D3. **b**, Corresponding DOLP, showing the same behavior as device D1 presented in Figure 4.6. **c**,**d**, Photoluminescence (blue) and corresponding DOLP (orange) at $V_G = -10$ V (**c**) and $V_G = 7$ V (**d**).

C17 Density functional theory

Electronic properties of 3R-stacked (AB/BA) bilayer WSe_2 were computed using the Quantum ESPRESSO plane-wave DFT package (*219, 220*) with fully relativistic norm-conserving pseudopotentials and the Perdew-Zunger LDA parametrization. The cutoff energy used was 60 Ry, and the Brillouin-zone was sampled with a 15x15x1 Monkhorst-Pack *k*-points mesh. A 30 Å vacuum region was added to avoid interactions between repeated images.

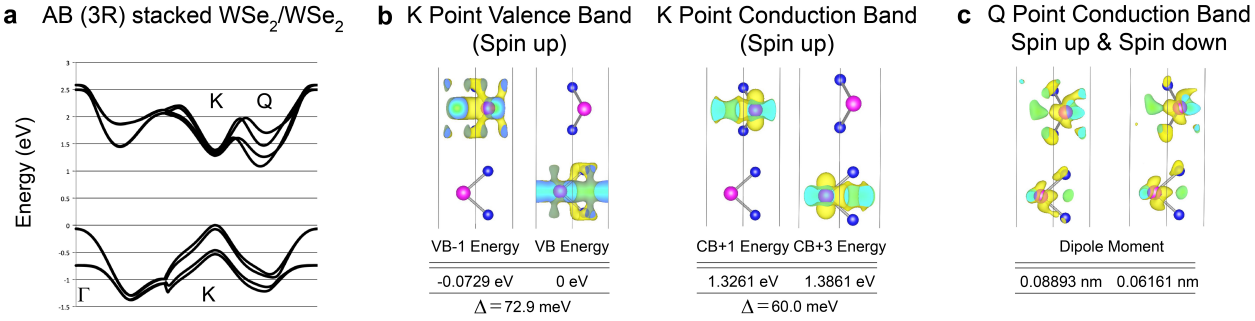


Figure C.19: Density functional theory calculations of AB (3R) stacked WSe_2 bilayers. a, Calculated band structure for 3R-stacked WSe_2 bilayers, with indicated Γ, K, and Q points. **b,** Top: electron density plots of the same-spin K-point valence and conduction bands, showing that the wavefunctions are localized in different layers and around the tungsten atoms. Below: calculated energy differences from the plot in **a**. **c,** Top: electron density plots of the conduction band minima at the Q point showing that the wavefunctions are more delocalized between the two layers than at the K point. Bottom: calculated dipole moments indicate that the wavefunctions at the Q points are still slightly preferentially localized in one of the two layers.

References

1. K. S. Novoselov *et al.*, Electric Field Effect in Atomically Thin Carbon Films. *Science* **306**, 666-669 (2004).

2. K. F. Mak, C. Lee, J. Hone, J. Shan, T. F. Heinz, Atomically thin MoS_2: A new direct-gap semiconductor. *Phys. Rev. Lett.* **105**, 136805 (2010).

3. K. Zhang, Y. Feng, F. Wang, Z. Yang, J. Wang, Two dimensional hexagonal boron nitride (2D-hBN): synthesis, properties and applications. *Journal of Materials Chemistry C* **5**, 11992-12022 (2017).

4. S. Y. F. Zhao *et al.*, Sign-Reversing Hall Effect in Atomically Thin High-Temperature Bi2.1Sr1.9CaCu2.0O8+δ Superconductors. *Physical Review Letters* **122**, (2019).

5. B. Huang *et al.*, Layer-dependent ferromagnetism in a van der Waals crystal down to the monolayer limit. *Nature* **546**, 270-273 (2017).

6. K. S. Novoselov *et al.*, Two-dimensional gas of massless Dirac fermions in graphene. *Nature* **438**, 197-200 (2005).

7. G. Scuri *et al.*, Large Excitonic Reflectivity of Monolayer $MoSe_2$ Encapsulated in Hexagonal Boron Nitride. *Phys. Rev. Lett.* **120**, 037402 (2018).

8. S. Dai *et al.*, Tunable Phonon Polaritons in Atomically Thin van der Waals Crystals of Boron Nitride. *Science* **343**, 1125-1129 (2014).

9. B. Hunt *et al.*, Massive Dirac Fermions and Hofstadter Butterfly in a van der Waals Heterostructure. *Science* **340**, 1427 (2013).

10. L. A. Jauregui *et al.*, Electrical control of interlayer exciton dynamics in atomically thin heterostructures. *Science* **366**, 870-875 (2019).

11. Y. Cao *et al.*, Unconventional superconductivity in magic-angle graphene superlattices. *Nature* **556**, 43 (2018).

12. J. A. Sulpizio *et al.*, Visualizing Poiseuille flow of hydrodynamic electrons. *Nature* **576**, 75-79 (2019).

13. M. J. H. Ku *et al.*, Imaging viscous flow of the Dirac fluid in graphene. *Nature* **583**, 537-541 (2020).

14. D. Halbertal *et al.*, Imaging resonant dissipation from individual atomic defects in graphene. *Science* **358**, 1303-1306 (2017).

15. T. P. Darlington *et al.*, Imaging strain-localized excitons in nanoscale bubbles of monolayer WSe2 at room temperature. *Nature Nanotechnology* **15**, 854-860 (2020).

16. M. Yi, Z. Shen, A review on mechanical exfoliation for the scalable production of graphene. *Journal of Materials Chemistry A* **3**, 11700-11715 (2015).

17. C. Lee, X. Wei, J. W. Kysar, J. Hone, Measurement of the Elastic Properties and Intrinsic Strength of Monolayer Graphene. *Science* **321**, 385-388 (2008).

18. A. A. Balandin *et al.*, Superior Thermal Conductivity of Single-Layer Graphene. *Nano Letters* **8**, 902-907 (2008).

19. V. Berry, Impermeability of graphene and its applications. *Carbon* **62**, 1-10 (2013).

20. L. Wang *et al.*, One-dimensional electrical contact to a two-dimensional material. *Science* **342**, 614-617 (2013).

21. C.-H. Liu, Y.-C. Chang, T. B. Norris, Z. Zhong, Graphene photodetectors with ultra-broadband and high responsivity at room temperature. *Nature Nanotechnology* **9**, 273-278 (2014).

22. H. Kim, K.-Y. Park, J. Hong, K. Kang, All-graphene-battery: bridging the gap between supercapacitors and lithium ion batteries. *Scientific Reports* **4**, (2014).

23. A. Balandin, The Heat Is On: Graphene Applications. *IEEE Nanotechnology Magazine* **5**, 15-19 (2011).

24. D. Cohen-Tanugi, J. C. Grossman, Water Desalination across Nanoporous Graphene. *Nano Letters* **12**, 3602-3608 (2012).

25. A. H. Castro Neto, F. Guinea, N. M. R. Peres, K. S. Novoselov, A. K. Geim, The electronic properties of graphene. *Reviews of Modern Physics* **81**, 109-162 (2009).

26. Y. M. Blanter, M. Büttiker, Shot noise in mesoscopic conductors. *Physics Reports* **336**, 1-166 (2000).

27. J. Crossno *et al.*, Observation of the Dirac fluid and the breakdown of the Wiedemann-Franz law in graphene. *Science* **351**, 1058-1061 (2016).

28. G. Iannaccone, G. Lombardi, M. Macucci, B. Pellegrini, Enhanced Shot Noise in Resonant Tunneling: Theory and Experiment. *Physical Review Letters* **80**, 1054-1057 (1998).

29. F. M. D. Pellegrino, G. Falci, E. Paladino, 1/f critical current noise in short ballistic graphene Josephson junctions. *Communications Physics* **3**, (2020).

30. H. Nyquist, Thermal Agitation of Electric Charge in Conductors. *Physical Review* **32**, 110-113 (1928).

31. V. J. Goldman, B. Su, Resonant Tunneling in the Quantum Hall Regime: Measurement of Fractional Charge. *Science* **267**, 1010-1012 (1995).

32. X. Jehl, M. Sanquer, R. Calemczuk, D. Mailly, Detection of doubled shot noise in short normal-metal/ superconductor junctions. *Nature* **405**, 50-53 (2000).

33. A. Gruber *et al.*, Scanning Confocal Optical Microscopy and Magnetic Resonance on Single Defect Centers. *Science* **276**, 2012-2014 (1997).

34. N. B. Manson, J. P. Harrison, M. J. Sellars, Nitrogen-vacancy center in diamond: Model of the electronic structure and associated dynamics. *Physical Review B* **74**, (2006).

35. D. Redman, S. Brown, S. C. Rand, Origin of persistent hole burning of N–V centers in diamond. *Journal of the Optical Society of America B* **9**, (1992).

36. T. I. Andersen *et al.*, Electron-phonon instability in graphene revealed by global and local noise probes. *Science* **364**, 154-157 (2019).

37. K. S. Novoselov, A. Mishchenko, A. Carvalho, A. H. Castro Neto, 2D materials and van der Waals heterostructures. *Science* **353**, (2016).

38. M. Mendoza, H. J. Herrmann, S. Succi, Preturbulent Regimes in Graphene Flow. *Physical Review Letters* **106**, (2011).

39. R. Krishna Kumar *et al.*, Superballistic flow of viscous electron fluid through graphene constrictions. *Nature Physics* **13**, 1182-1185 (2017).

40. M. Dyakonov, M. Shur, Shallow water analogy for a ballistic field effect transistor: New mechanism of plasma wave generation by dc current. *Physical Review Letters* **71**, 2465-2468 (1993).

41. A. Tomadin, M. Polini, Theory of the plasma-wave photoresponse of a gated graphene sheet. *Physical Review B* **88**, (2013).

42. Y. M. Lin *et al.*, 100-GHz Transistors from Wafer-Scale Epitaxial Graphene. *Science* **327**, 662-662 (2010).

43. Y. D. Kim *et al.*, Ultrafast Graphene Light Emitters. *Nano Letters* **18**, 934-940 (2018).

44. R.-H. Kim *et al.*, Stretchable, Transparent Graphene Interconnects for Arrays of Microscale Inorganic Light Emitting Diodes on Rubber Substrates. *Nano Letters* **11**, 3881-3886 (2011).

45. A. B. Pippard, Acoustic amplification in semiconductors and metals. *Philosophical Magazine* **8**, 161-165 (1963).

46. H. N. Spector, Amplification of Acoustic Waves through Interaction with Conduction Electrons. *Physical Review* **127**, 1084-1090 (1962).

47. S. M. Komirenko, K. W. Kim, A. A. Demidenko, V. A. Kochelap, M. A. Stroscio, Generation and amplification of sub-THz coherent acoustic phonons under the drift of two-dimensional electrons. *Physical Review B* **62**, 7459-7469 (2000).

48. C. X. Zhao, W. Xu, F. M. Peeters, Cerenkov emission of terahertz acoustic-phonons from graphene. *Applied Physics Letters* **102**, (2013).

49. A. R. Hutson, J. H. McFee, D. L. White, Ultrasonic Amplification in CdS. *Physical Review Letters* **7**, 237-239 (1961).

50. M. Pomerantz, Amplification of Microwave Phonons in Germanium. *Physical Review Letters* **13**, 308-310 (1964).

51. M. Eizenberg, B. Fisher, X-ray Brillouin scattering and electrical measurements of acoustoelectric gain and lattice attenuation in semidegeneraten-GaAs. *Journal of Applied Physics* **49**, 5260-5269 (1978).

52. K. Shinokita *et al.*, Strong Amplification of Coherent Acoustic Phonons by Intraminiband Currents in a Semiconductor Superlattice. *Physical Review Letters* **116**, (2016).

53. A. C. Betz *et al.*, Supercollision cooling in undoped graphene. *Nature Physics* **9**, 109-112 (2012).

54. W. Yang *et al.*, A graphene Zener–Klein transistor cooled by a hyperbolic substrate. *Nature Nanotechnology* **13**, 47-52 (2017).

55. J. R. Maze *et al.*, Nanoscale magnetic sensing with an individual electronic spin in diamond. *Nature* **455**, 644-647 (2008).

56. S. Kolkowitz *et al.*, Probing Johnson noise and ballistic transport in normal metals with a single-spin qubit. *Science* **347**, 1129-1132 (2015).

57. K. Agarwal *et al.*, Magnetic noise spectroscopy as a probe of local electronic correlations in two-dimensional systems. *Physical Review B* **95**, (2017).

58. F. Casola, T. van der Sar, A. Yacoby, Probing condensed matter physics with magnetometry based on nitrogen-vacancy centres in diamond. *Nature Reviews Materials* **3**, (2018).

59. A. A. Balandin, Low-frequency 1/f noise in graphene devices. *Nature Nanotechnology* **8**, 549-555 (2013).

60. J. Horng *et al.*, Drude conductivity of Dirac fermions in graphene. *Physical Review B* **83**, (2011).

61. S. A. Awan *et al.*, Transport conductivity of graphene at RF and microwave frequencies. *2D Materials* **3**, (2016).

62. H. Hartnagel, Katilius, R., and Matulionis, A. , *Microwave noise in semiconductor devices.*, (John Wiley & Sons., 2001).

63. S. A. Mikhailov, Graphene-based voltage-tunable coherent terahertz emitter. *Physical Review B* **87**, (2013).

64. D. L. Nika, E. P. Pokatilov, A. S. Askerov, A. A. Balandin, Phonon thermal conduction in graphene: Role of Umklapp and edge roughness scattering. *Physical Review B* **79**, (2009).

65. K. Kaasbjerg, K. S. Thygesen, K. W. Jacobsen, Unraveling the acoustic electron-phonon interaction in graphene. *Physical Review B* **85**, (2012).

66. P. G. Klemens, D. F. Pedraza, Thermal conductivity of graphite in the basal plane. *Carbon* **32**, 735-741 (1994).

67. M. Freitag, H.-Y. Chiu, M. Steiner, V. Perebeinos, P. Avouris, Thermal infrared emission from biased graphene. *Nature Nanotechnology* **5**, 497-501 (2010).

68. K. L. Grosse, M.-H. Bae, F. Lian, E. Pop, W. P. King, Nanoscale Joule heating, Peltier cooling and current crowding at graphene–metal contacts. *Nature Nanotechnology* **6**, 287-290 (2011).

69. E. H. Hwang, S. Das Sarma, Acoustic phonon scattering limited carrier mobility in two-dimensional extrinsic graphene. *Physical Review B* **77**, (2008).

70. T. Stauber, N. M. R. Peres, F. Guinea, Electronic transport in graphene: A semiclassical approach including midgap states. *Physical Review B* **76**, (2007).

71. E. Mariani, F. von Oppen, Temperature-dependent resistivity of suspended graphene. *Physical Review B* **82**, (2010).

72. R. Saito, M. Mizuno, M. S. Dresselhaus, Ballistic and Diffusive Thermal Conductivity of Graphene. *Physical Review Applied* **9**, (2018).

73. A. A. Balandin, Thermal properties of graphene and nanostructured carbon materials. *Nature Materials* **10**, 569-581 (2011).

74. I. Meric *et al.*, Current saturation in zero-bandgap, top-gated graphene field-effect transistors. *Nature Nanotechnology* **3**, 654-659 (2008).

75. A. M. DaSilva, K. Zou, J. K. Jain, J. Zhu, Mechanism for Current Saturation and Energy Dissipation in Graphene Transistors. *Physical Review Letters* **104**, (2010).

76. V. Perebeinos, P. Avouris, Inelastic scattering and current saturation in graphene. *Physical Review B* **81**, (2010).

77. M. A. Yamoah, W. Yang, E. Pop, D. Goldhaber-Gordon, High-Velocity Saturation in Graphene Encapsulated by Hexagonal Boron Nitride. *ACS Nano* **11**, 9914-9919 (2017).

78. M. B. Lundeberg *et al.*, Tuning quantum nonlocal effects in graphene plasmonics. *Science* **357**, 187-191 (2017).

79. I. Kaminer *et al.*, Efficient plasmonic emission by the quantum Čerenkov effect from hot carriers in graphene. *Nature Communications* **7**, (2016).

80. A. Gabbana, M. Polini, S. Succi, R. Tripiccione, F. M. D. Pellegrino, Prospects for the Detection of Electronic Preturbulence in Graphene. *Physical Review Letters* **121**, (2018).

81. A. Chernikov *et al.*, Exciton Binding Energy and Nonhydrogenic Rydberg Series in Monolayer WS2. *Phys. Rev. Lett.* **113**, 076802 (2014).

82. S. B. Nam *et al.*, Free-exciton energy spectrum in GaAs. *Physical Review B* **13**, 761-767 (1976).

83. G.-B. Liu, D. Xiao, Y. Yao, X. Xu, W. Yao, Electronic structures and theoretical modelling of two-dimensional group-VIB transition metal dichalcogenides. *Chemical Society Reviews* **44**, 2643-2663 (2015).

84. Z. Wang, Y.-H. Chiu, K. Honz, K. F. Mak, J. Shan, Electrical Tuning of Interlayer Exciton Gases in WSe_2 Bilayers. *Nano Letters* **18**, 137-143 (2018).

85. S. Fang *et al.*, Ab initiotight-binding Hamiltonian for transition metal dichalcogenides. *Physical Review B* **92**, (2015).

86. Z. Y. Zhu, Y. C. Cheng, U. Schwingenschlögl, Giant spin-orbit-induced spin splitting in two-dimensional transition-metal dichalcogenide semiconductors. *Physical Review B* **84**, (2011).

87. K. Kośmider, J. W. González, J. Fernández-Rossier, Large spin splitting in the conduction band of transition metal dichalcogenide monolayers. *Physical Review B* **88**, (2013).

88. D. Xiao, G.-B. Liu, W. Feng, X. Xu, W. Yao, Coupled Spin and Valley Physics in Monolayers of MoS2 and Other Group-VI Dichalcogenides. *Physical Review Letters* **108**, 196802 (2012).

89. J. S. Ross *et al.*, Electrical control of neutral and charged excitons in a monolayer semiconductor. *Nat. Commun.* **4**, 1474 (2013).

90. C. Fey, P. Schmelcher, A. Imamoglu, R. Schmidt, Theory of exciton-electron scattering in atomically thin semiconductors. *Physical Review B* **101**, (2020).

91. J. Lee, K. F. Mak, J. Shan, Electrical control of the valley Hall effect in bilayer MoS2 transistors. *Nature Nanotechnology* **11**, 421-425 (2016).

92. K. F. Mak, K. L. McGill, J. Park, P. L. McEuen, The valley Hall effect in MoS_2 transistors. *Science* **344**, 1489 (2014).

93. M. Onga, Y. Zhang, T. Ideue, Y. Iwasa, Exciton Hall effect in monolayer MoS2. *Nature Materials* **16**, 1193-1197 (2017).

94. C. Robert *et al.*, Exciton radiative lifetime in transition metal dichalcogenide monolayers. *Physical Review B* **93**, 205423 (2016).

95. G. Moody *et al.*, Intrinsic homogeneous linewidth and broadening mechanisms of excitons in monolayer transition metal dichalcogenides. *Nat. Commun.* **6**, 8315 (2015).

96. G. Scuri *et al.*, Electrically Tunable Valley Dynamics in Twisted WSe_2/WSe_2 Bilayers. *Physical Review Letters* **124**, 217403 (2020).

97. X. Xu, W. Yao, D. Xiao, T. F. Heinz, Spin and pseudospins in layered transition metal dichalcogenides. *Nat. Phys.* **10**, 343 (2014).

98. L. J. Sham, S. J. Allen, A. Kamgar, D. C. Tsui, Valley-Valley Splitting in Inversion Layers on a High-Index Surface of Silicon. *Physical Review Letters* **40**, 472-475 (1978).

99. A. Rycerz, J. Tworzydło, C. W. J. Beenakker, Valley filter and valley valve in graphene. *Nature Physics* **3**, 172-175 (2007).

100. Y. P. Shkolnikov, E. P. De Poortere, E. Tutuc, M. Shayegan, Valley Splitting of AlAs Two-Dimensional Electrons in a Perpendicular Magnetic Field. *Physical Review Letters* **89**, 226805 (2002).

101. O. Gunawan *et al.*, Valley Susceptibility of an Interacting Two-Dimensional Electron System. *Physical Review Letters* **97**, 186404 (2006).

102. D. Xiao, W. Yao, Q. Niu, Valley-Contrasting Physics in Graphene: Magnetic Moment and Topological Transport. *Physical Review Letters* **99**, 236809 (2007).

103. M.-T. Dau *et al.*, The valley Nernst effect in WSe_2. *arXiv preprint arXiv:1910.08070*, (2019).

104. X.-Q. Yu, Z.-G. Zhu, G. Su, A. P. Jauho, Thermally Driven Pure Spin and Valley Currents via the Anomalous Nernst Effect in Monolayer Group-VI Dichalcogenides. *Physical Review Letters* **115**, 246601 (2015).

105. W. Yao, D. Xiao, Q. Niu, Valley-dependent optoelectronics from inversion symmetry breaking. *Physical Review B* **77**, 235406 (2008).

106. J. R. Schaibley *et al.*, Valleytronics in 2D materials. *Nature Reviews Materials* **1**, 16055 (2016).

107. P. Rivera *et al.*, Interlayer valley excitons in heterobilayers of transition metal dichalcogenides. *Nature Nanotechnology* **13**, 1004-1015 (2018).

108. K. F. Mak, K. He, J. Shan, T. F. Heinz, Control of valley polarization in monolayer MoS_2 by optical helicity. *Nature Nanotechnology* **7**, 494 (2012).

109. H. Zeng, J. Dai, W. Yao, D. Xiao, X. Cui, Valley polarization in MoS2 monolayers by optical pumping. *Nature Nanotechnology* **7**, 490 (2012).

110. M. M. Glazov *et al.*, Exciton fine structure and spin decoherence in monolayers of transition metal dichalcogenides. *Physical Review B* **89**, 201302 (2014).

111. T. Yu, M. W. Wu, Valley depolarization due to intervalley and intravalley electron-hole exchange interactions in monolayer MoS_2. *Physical Review B* **89**, 205303 (2014).

112. C. Mai *et al.*, Many-Body Effects in Valleytronics: Direct Measurement of Valley Lifetimes in Single-Layer MoS2. *Nano Letters* **14**, 202-206 (2014).

113. C. R. Zhu *et al.*, Exciton valley dynamics probed by Kerr rotation in WSe_2 monolayers. *Physical Review B* **90**, 161302 (2014).

114. A. Singh *et al.*, Long-Lived Valley Polarization of Intravalley Trions in Monolayer WSe_2. *Physical Review Letters* **117**, 257402 (2016).

115. P. Rivera *et al.*, Observation of long-lived interlayer excitons in monolayer $MoSe_2$–WSe_2 heterostructures. *Nat. Commun.* **6**, 6242 (2015).

116. A. M. Jones *et al.*, Spin–layer locking effects in optical orientation of exciton spin in bilayer WSe_2. *Nature Physics* **10**, 130 (2014).

117. Z. Gong *et al.*, Magnetoelectric effects and valley-controlled spin quantum gates in transition metal dichalcogenide bilayers. *Nature Communications* **4**, 2053 (2013).

118. G. Wang *et al.*, Exciton dynamics in WSe2 bilayers. *Applied Physics Letters* **105**, 182105 (2014).

119. S. Wu *et al.*, Electrical tuning of valley magnetic moment through symmetry control in bilayer MoS_2. *Nature Physics* **9**, 149 (2013).

120. J. Kim *et al.*, Observation of ultralong valley lifetime in WSe_2/MoS_2; heterostructures. *Science Advances* **3**, e1700518 (2017).

121. P. Rivera *et al.*, Valley-polarized exciton dynamics in a 2D semiconductor heterostructure. *Science* **351**, 688 (2016).

122. A. Ciarrocchi *et al.*, Polarization switching and electrical control of interlayer excitons in two-dimensional van der Waals heterostructures. *Nature Photonics* **13**, 131-136 (2019).

123. A. M. van der Zande *et al.*, Tailoring the Electronic Structure in Bilayer Molybdenum Disulfide via Interlayer Twist. *Nano Letters* **14**, 3869-3875 (2014).

124. K. Liu *et al.*, Evolution of interlayer coupling in twisted molybdenum disulfide bilayers. *Nature Communications* **5**, 4966 (2014).

125. N. Zhang *et al.*, Moiré Intralayer Excitons in a $MoSe_2/MoS_2$ Heterostructure. *Nano Letters* **18**, 7651-7657 (2018).

126. K. Tran *et al.*, Evidence for moiré excitons in van der Waals heterostructures. *Nature* **567**, 71-75 (2019).

127. C. Jin *et al.*, Observation of moiré excitons in WSe_2/WS_2 heterostructure superlattices. *Nature* **567**, 76-80 (2019).

128. E. M. Alexeev *et al.*, Resonantly hybridized excitons in moiré superlattices in van der Waals heterostructures. *Nature* **567**, 81-86 (2019).

129. K. L. Seyler *et al.*, Signatures of moiré-trapped valley excitons in $MoSe_2/WSe_2$ heterobilayers. *Nature* **567**, 66-70 (2019).

130. C. Jin *et al.*, Identification of spin, valley and moiré quasi-angular momentum of interlayer excitons. *Nature Physics* **15**, 1140-1144 (2019).

131. K. Kim *et al.*, van der Waals Heterostructures with High Accuracy Rotational Alignment. *Nano Letters* **16**, 1989-1995 (2016).

132. A. Splendiani *et al.*, Emerging photoluminescence in monolayer MoS_2. *Nano Lett.* **10**, 1271-1275 (2010).

133. J. Lindlau *et al.*, The role of momentum-dark excitons in the elementary optical response of bilayer WSe2. *Nature Communications* **9**, 2586 (2018).

134. P. K. Nayak *et al.*, Probing Evolution of Twist-Angle-Dependent Interlayer Excitons in $MoSe_2/WSe_2$ van der Waals Heterostructures. *ACS Nano* **11**, 4041-4050 (2017).

135. J. Kunstmann *et al.*, Momentum-space indirect interlayer excitons in transition-metal dichalcogenide van der Waals heterostructures. *Nature Physics* **14**, 801-805 (2018).

136. K. Wang *et al.*, Interlayer Coupling in Twisted WSe_2/WS_2 Bilayer Heterostructures Revealed by Optical Spectroscopy. *ACS Nano* **10**, 6612-6622 (2016).

137. Z. Jin, X. Li, J. T. Mullen, K. W. Kim, Intrinsic transport properties of electrons and holes in monolayer transition-metal dichalcogenides. *Physical Review B* **90**, 045422 (2014).

138. G. Wang *et al.*, Colloquium: Excitons in atomically thin transition metal dichalcogenides. *Reviews of Modern Physics* **90**, 021001 (2018).

139. R. Bertoni *et al.*, Generation and Evolution of Spin-, Valley-, and Layer-Polarized Excited Carriers in Inversion-Symmetric WSe_2. *Physical Review Letters* **117**, 277201 (2016).

140. P. V. Nguyen *et al.*, Visualizing electrostatic gating effects in two-dimensional heterostructures. *Nature* **572**, 220-223 (2019).

141. E. J. Sie, T. Rohwer, C. Lee, N. Gedik, Time-resolved XUV ARPES with tunable 24–33 eV laser pulses at 30 meV resolution. *Nature Communications* **10**, 3535 (2019).

142. L. Du *et al.*, Robust circular polarization of indirect Q-K transitions in bilayer 3R WS_2. *Physical Review B* **100**, 161404 (2019).

143. V. Enaldiev, V. Zólyomi, C. Yelgel, S. Magorrian, V. Fal'ko, Stacking domains and dislocation networks in marginally twisted bilayers of transition metal dichalcogenides. *arXiv preprint arXiv:1911.12804*, (2019).

144. A. Kormányos, V. Zólyomi, V. I. Fal'ko, G. Burkard, Tunable Berry curvature and valley and spin Hall effect in bilayer MoS_2. *Physical Review B* **98**, 035408 (2018).

145. K. F. Mak, D. Xiao, J. Shan, Light–valley interactions in 2D semiconductors. *Nature Photonics* **12**, 451-460 (2018).

146. F. Wu, T. Lovorn, A. H. MacDonald, Theory of optical absorption by interlayer excitons in transition metal dichalcogenide heterobilayers. *Physical Review B* **97**, 035306 (2018).

147. K. Shinokita *et al.*, Continuous Control and Enhancement of Excitonic Valley Polarization in Monolayer WSe_2 by Electrostatic Doping. *Advanced Functional Materials* **29**, 1900260 (2019).

148. T. Yan, J. Ye, X. Qiao, P. Tan, X. Zhang, Exciton valley dynamics in monolayer WSe_2 probed by the two-color ultrafast Kerr rotation. *Physical Chemistry Chemical Physics* **19**, 3176-3181 (2017).

149. A. A. High *et al.*, Visible-frequency hyperbolic metasurface. *Nature* **522**, 192 (2015).

150. L. Sun *et al.*, Separation of valley excitons in a MoS_2 monolayer using a subwavelength asymmetric groove array. *Nature Photonics* **13**, 180-184 (2019).

151. G. Hu *et al.*, Coherent steering of nonlinear chiral valley photons with a synthetic Au–WS_2 metasurface. *Nature Photonics* **13**, 467-472 (2019).

152. S. Brem, C. Linderälv, P. Erhart, E. Malic, Tunable Phases of Moiré Excitons in van der Waals Heterostructures. *Nano Letters* **20**, 8534-8540 (2020).

153. Y. Cao *et al.*, Correlated insulator behaviour at half-filling in magic-angle graphene superlattices. *Nature* **556**, 80 (2018).

154. Y. Tang *et al.*, Simulation of Hubbard model physics in WSe_2/WS_2 moiré superlattices. *Nature* **579**, 353-358 (2020).

155. E. C. Regan *et al.*, Mott and generalized Wigner crystal states in WSe_2/WS_2 moiré superlattices. *Nature* **579**, 359-363 (2020).

156. L. Wang *et al.*, Correlated electronic phases in twisted bilayer transition metal dichalcogenides. *Nature Materials*, (2020).

157. H. Yoo *et al.*, Atomic and electronic reconstruction at the van der Waals interface in twisted bilayer graphene. *Nature Materials* **18**, 448-453 (2019).

158. L. Xiong *et al.*, Photonic crystal for graphene plasmons. *Nature Communications* **10**, 4780 (2019).

159. L. J. McGilly *et al.*, Visualization of moiré superlattices. *Nature Nanotechnology* **15**, 580-584 (2020).

160. S. Carr *et al.*, Relaxation and domain formation in incommensurate two-dimensional heterostructures. *Physical Review B* **98**, 224102 (2018).

161. A. Weston *et al.*, Atomic reconstruction in twisted bilayers of transition metal dichalcogenides. *Nature Nanotechnology*, (2020).

162. J. Sung *et al.*, Broken mirror symmetry in excitonic response of reconstructed domains in twisted MoSe2/MoSe2 bilayers. *Nature Nanotechnology* **15**, 750-754 (2020).

163. T. I. Andersen *et al.*, Excitons in a reconstructed moiré potential in twisted WSe2/WSe2 homobilayers. *Nature Materials* **20**, 480-487 (2021).

164. A. Mazurenko *et al.*, A cold-atom Fermi–Hubbard antiferromagnet. *Nature* **545**, 462 (2017).

165. J. Perczel *et al.*, Topological Quantum Optics in Two-Dimensional Atomic Arrays. *Phys. Rev. Lett.* **119**, 023603 (2017).

166. F. Wu, T. Lovorn, E. Tutuc, I. Martin, A. H. MacDonald, Topological Insulators in Twisted Transition Metal Dichalcogenide Homobilayers. *Physical Review Letters* **122**, 086402 (2019).

167. R. Bekenstein *et al.*, Quantum metasurfaces with atom arrays. *Nature Physics* **16**, 676-681 (2020).

168. F. Wu, T. Lovorn, E. Tutuc, A. H. MacDonald, Hubbard Model Physics in Transition Metal Dichalcogenide Moiré Bands. *Physical Review Letters* **121**, 026402 (2018).

169. H. Yu, G.-B. Liu, J. Tang, X. Xu, W. Yao, Moiré excitons: From programmable quantum emitter arrays to spin-orbit–coupled artificial lattices. *Science Advances* **3**, e1701696 (2017).

170. W. Li, X. Lu, S. Dubey, L. Devenica, A. Srivastava, Dipolar interactions between localized interlayer excitons in van der Waals heterostructures. *Nature Materials* **19**, 624-629 (2020).

171. M. Brotons-Gisbert *et al.*, Spin–layer locking of interlayer excitons trapped in moiré potentials. *Nature Materials* **19**, 630-636 (2020).

172. C. Schrade, L. Fu, Spin-valley density wave in moiré materials. *Physical Review B* **100**, 035413 (2019).

173. L. Xian *et al.*, Realization of nearly dispersionless bands with strong orbital anisotropy from destructive interference in twisted bilayer MoS_2. *arXiv preprint arXiv:2004.02964*, (2020).

174. A. Kerelsky *et al.*, Moiré-less Correlations in ABCA Graphene. *arXiv preprint arXiv:1911.00007*, (2019).

175. A. J. Schwartz, M. Kumar, B. L. Adams, D. P. Field, *Electron backscatter diffraction in materials science*. (Springer, 2009), vol. 2.

176. D. Coates, Kikuchi-like reflection patterns obtained with the scanning electron microscope. *The Philosophical Magazine: A Journal of Theoretical Experimental and Applied Physics* **16**, 1179-1184 (1967).

177. K. Ashida, T. Kajino, Y. Kutsuma, N. Ohtani, T. Kaneko, Crystallographic orientation dependence of SEM contrast revealed by SiC polytypes. *Journal of Vacuum Science & Technology B, Nanotechnology and Microelectronics: Materials, Processing, Measurement, and Phenomena* **33**, 04E104 (2015).

178. G. Chen *et al.*, Signatures of tunable superconductivity in a trilayer graphene moiré superlattice. *Nature* **572**, 215-219 (2019).

179. I. Martin, Y. M. Blanter, A. Morpurgo, Topological confinement in bilayer graphene. *Physical Review Letters* **100**, 036804 (2008).

180. L. Ju *et al.*, Topological valley transport at bilayer graphene domain walls. *Nature* **520**, 650-655 (2015).

181. A. Vaezi, Y. Liang, D. H. Ngai, L. Yang, E.-A. Kim, Topological edge states at a tilt boundary in gated multilayer graphene. *Physical Review X* **3**, 021018 (2013).

182. D. Joy, M. Prasad, H. MEYER III, Experimental secondary electron spectra under SEM conditions. *Journal of microscopy* **215**, 77-85 (2004).

183. K. F. Mak, J. Shan, T. F. Heinz, Electronic structure of few-layer graphene: experimental demonstration of strong dependence on stacking sequence. *Physical review letters* **104**, 176404 (2010).

184. T. A. Nguyen, J.-U. Lee, D. Yoon, H. Cheong, Excitation energy dependent Raman signatures of ABA-and ABC-stacked few-layer graphene. *Scientific reports* **4**, 4630 (2014).

185. A. M. Dibos *et al.*, Electrically Tunable Exciton–Plasmon Coupling in a WSe_2 Monolayer Embedded in a Plasmonic Crystal Cavity. *Nano Letters* **19**, 3543-3547 (2019).

186. F. Wu, T. Lovorn, A. H. MacDonald, Topological Exciton Bands in Moiré Heterojunctions. *Physical Review Letters* **118**, 147401 (2017).

187. Y. Wang, Z. Wang, W. Yao, G.-B. Liu, H. Yu, Interlayer coupling in commensurate and incommensurate bilayer structures of transition-metal dichalcogenides. *Physical Review B* **95**, 115429 (2017).

188. S. Brem *et al.*, Hybridized intervalley moiré excitons and flat bands in twisted WSe_2 bilayers. *Nanoscale*, (2020).

189. K. Hao *et al.*, Direct measurement of exciton valley coherence in monolayer WSe_2. *Nature Physics* **12**, 677-682 (2016).

190. E. Cappelluti, R. Roldán, J. A. Silva-Guillén, P. Ordejón, F. Guinea, Tight-binding model and direct-gap/indirect-gap transition in single-layer and multilayer MoS_2. *Physical Review B* **88**, 075409 (2013).

191. K. F. Mak *et al.*, Tightly bound trions in monolayer MoS_2. *Nature Materials* **12**, 207 (2012).

192. M. Kulig *et al.*, Exciton Diffusion and Halo Effects in Monolayer Semiconductors. *Physical Review Letters* **120**, 207401 (2018).

193. F. Cadiz *et al.*, Exciton diffusion in WSe_2 monolayers embedded in a van der Waals heterostructure. *Applied Physics Letters* **112**, 152106 (2018).

194. R. Pisoni *et al.*, Absence of Interlayer Tunnel Coupling of K-Valley Electrons in Bilayer MoS_2. *Physical Review Letters* **123**, 117702 (2019).

195. K. Hao *et al.*, Trion valley coherence in monolayer semiconductors. *2D Materials* **4**, 025105 (2017).

196. S. V. Mandyam *et al.*, Controlled Growth of Large-Area Bilayer Tungsten Diselenides with Lateral P–N Junctions. *ACS Nano* **13**, 10490-10498 (2019).

197. K. W. Lau, Calvin, Z. Gong, H. Yu, W. Yao, Interface excitons at lateral heterojunctions in monolayer semiconductors. *Physical Review B* **98**, 115427 (2018).

198. A. V. Stier *et al.*, Magnetooptics of Exciton Rydberg States in a Monolayer Semiconductor. *Phys. Rev. Lett.* **120**, 057405 (2018).

199. I. Paradisanos *et al.*, Controlling interlayer excitons in MoS_2 layers grown by chemical vapor deposition. *Nature Communications* **11**, 2391 (2020).

200. D. A. Ruiz-Tijerina, V. I. Fal'ko, Interlayer hybridization and moiré superlattice minibands for electrons and excitons in heterobilayers of transition-metal dichalcogenides. *Physical Review B* **99**, 125424 (2019).

201. M. Selig *et al.*, Excitonic linewidth and coherence lifetime in monolayer transition metal dichalcogenides. *Nat. Commun.* **7**, 13279 (2016).

202. S. Sangtawesin *et al.*, Origins of Diamond Surface Noise Probed by Correlating Single-Spin Measurements with Surface Spectroscopy. *Physical Review X* **9**, (2019).

203. C. R. Dean *et al.*, Boron nitride substrates for high-quality graphene electronics. *Nat. Nanotech.* **5**, 722 (2010).

204. K.-M. C. Fu *et al.*, Observation of the Dynamic Jahn-Teller Effect in the Excited States of Nitrogen-Vacancy Centers in Diamond. *Physical Review Letters* **103**, (2009).

205. A. Norambuena *et al.*, Spin-lattice relaxation of individual solid-state spins. *Physical Review B* **97**, (2018).

206. J.-P. Tetienne *et al.*, Quantum imaging of current flow in graphene. *Science Advances* **3**, (2017).

207. J. E. Padilha, H. Peelaers, A. Janotti, C. G. Van de Walle, Nature and evolution of the band-edge states in MoS_2: From monolayer to bulk. *Physical Review B* **90**, 205420 (2014).

208. W. Li *et al.*, Bandgap engineering of different stacking WS_2 bilayer under an external electric field. *Solid State Communications* **225**, 32-37 (2016).

209. X. Fan *et al.*, Modulation of electronic properties from stacking orders and spin-orbit coupling for 3R-type MoS_2. *Scientific Reports* **6**, 24140 (2016).

210. H. Yu, M. Chen, W. Yao, Giant magnetic field from moiré induced Berry phase in homobilayer semiconductors. *arXiv preprint arXiv:1906.05499*, (2019).

211. G.-H. Lee *et al.*, Highly Stable, Dual-Gated MoS_2 Transistors Encapsulated by Hexagonal Boron Nitride with Gate-Controllable Contact, Resistance, and Threshold Voltage. *ACS Nano* **9**, 7019-7026 (2015).

212. A. Raja *et al.*, Dielectric disorder in two-dimensional materials. *Nature Nanotechnology* **14**, 832-837 (2019).

213. F. Cadiz *et al.*, Excitonic Linewidth Approaching the Homogeneous Limit in MoS_2-Based van der Waals Heterostructures. *Phys. Rev. X* **7**, 021026 (2017).

214. Y. Zhou *et al.*, Controlling Excitons in an Atomically Thin Membrane with a Mirror. *Physical Review Letters* **124**, 027401 (2020).

215. Y. Zhou *et al.*, Probing dark excitons in atomically thin semiconductors via near-field coupling to surface plasmon polaritons. *Nat. Nanotech.* **12**, 856-860 (2017).

216. P. J. Zomer, M. H. D. Guimarães, J. C. Brant, N. Tombros, B. J. van Wees, Fast pick up technique for high quality heterostructures of bilayer graphene and hexagonal boron nitride. *Appl. Phys. Lett.* **105**, 013101 (2014).

217. F. Pizzocchero *et al.*, The hot pick-up technique for batch assembly of van der Waals heterostructures. *Nature Communications* **7**, 11894 (2016).

218. D. G. Purdie *et al.*, Cleaning interfaces in layered materials heterostructures. *Nature Communications* **9**, 5387 (2018).

219. P. Giannozzi *et al.*, QUANTUM ESPRESSO: a modular and open-source software project for quantum simulations of materials. *Journal of Physics: Condensed Matter* **21**, 395502 (2009).

220. P. Giannozzi *et al.*, Advanced capabilities for materials modelling with Quantum ESPRESSO. *Journal of Physics: Condensed Matter* **29**, 465901 (2017).